

09/28/95

09:47

DUKE UNIV SPONSORED PROGRAMS

002

JUN-30-1995

13:27

DTIC

## REPORT DOCUMENTATION PAGE

Form Approved

OMB No. 0704-0188

Public reporting burden for this collection of information is estimated to average 1 hour per response, including the time for reviewing instructions, searching existing data sources, gathering and maintaining the data needed, and completing and reviewing the collection of information. Send comments regarding this burden estimate or any other aspect of the collection of information, including suggestions for reducing this burden, to Washington Headquarters Services, Directorate for Information Operations and Reports, 1215 Jefferson Davis Highway, Suite 1204, Arlington, VA 22202-4302, and to the Office of Management and Budget, Paperwork Reduction Project (0704-0188), Washington, DC 20503.

1. AGENCY USE ONLY (Leave blank) 2. REPORT DATE May, 1991 3. REPORT TYPE AND DATES COVERED Final January, 1987 - June, 1990

4. TITLE AND SUBTITLE Gas Bubble Detection and Decompression Sickness Prevention By Noninvasive Bioelectrical Impedance Spectroscopy 5. FUNDING NUMBERS C - N00014-87-C-0166

6. AUTHOR(S) Wayne A. Gerth, Ph.D.

7. PERFORMING ORGANIZATION NAME(S) AND ADDRESS(ES) F.G. Hall Center for Hypobaric and Hyperbaric Medicine Box 3823 - Duke University Medical Center Durham, N.C. 27710

8. SPONSORING/MONITORING AGENCY NAME(S) AND ADDRESS(ES) Office of Naval Research Department of the Navy 800 N. Quincey Street Arlington, VA 22217-3000

11. SUPPLEMENTARY NOTES CDR Peter D. Kent Code 401 Naval Medical Research & Development Command Naval Medical Command, National Capital Region, Bethesda, MD

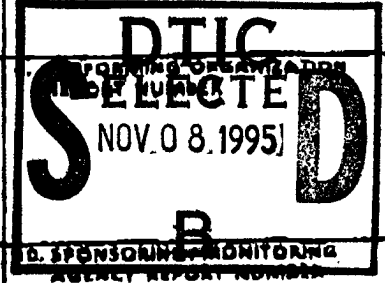
12a. DISTRIBUTION/AVAILABILITY STATEMENT DISTRIBUTION STATEMENT A Approved for public release Distribution Unlimited DTIC QUALITY INSPECTED 6 12b. DISTRIBUTION CODE A

13. ABSTRACT (Maximum 200 words) Excessively rapid decompression causes bubble formation in the blood and tissues, which can in turn cause Decompression Sickness (DCS) through a variety of mechanisms that include direct mechanical damage to tissue and perfusion impairment. Noninvasive computer-driven Electrical Impedance Spectroscopic (EIS) and Impedance Plethysmographic (IPG) methods were developed and used to track such bubble formation and its attendant hemodynamic effects. Studies of bubble formation in gelatin confirmed theoretical indications that bubble formation and growth should cause systemic changes in the electrical impedance spectrum of the host liquid through effects of solute adsorption at the bubble gas liquid interfaces. Using these changes as indices for bubble formation in vivo EIS technology was applied to detect bubble formation in the tails of rats decompressed to simulated altitudes. The tails were also monitored for bubble-induced hemodynamic changes using more conventional IPG techniques. Results were correlated with the incidence of DCS, which was judged to have occurred with the exhibition of respiratory distress, convulsions or death. Because the decompressions used in these animal experiments were severe, further work remains to determine whether EIS and IPG monitoring can provide noninvasive, objective and premonitory indices of DCS in man.

14. SUBJECT TERMS Decompression Sickness; Electrical Impedance Spectroscopy; Rats; Gelatin; Bubble Detection; Impedance Plethysmography; Hemodynamics 15. NUMBER OF PAGES 228 16. PRICE CODE

17. SECURITY CLASSIFICATION OF REPORT UNCLAS 18. SECURITY CLASSIFICATION OF THIS PAGE UNCLAS 19. SECURITY CLASSIFICATION OF ABSTRACT UNCLAS 20. LIMITATION OF ABSTRACT UL

Post-it brand fax transmittal memo 7671  
 Mary Johnson  
 684-5134



19951107 002

GAS BUBBLE DETECTION AND DECOMPRESSION SICKNESS PREVENTION BY  
NONINVASIVE BIOELECTRICAL IMPEDANCE SPECTROSCOPY

Final Report

ONR Contract

N00014-87-C-0166

Wayne A. Gerth, Ph.D.

May 1991

F.G. Hall Hypo-Hyperbaric Center  
Department of Cell Biology, Division of Physiology  
and  
Department of Anesthesiology

Box 3823  
Duke University Medical Center  
Durham, North Carolina 27710  
Ph. (919) 684-5902

# FOREWARD

The work presented in this report was undertaken and completed with the close collaboration of Dr. Leslie D. Montgomery of LDM Associates, San Jose, CA, who was a Co-Investigator in this program. Dr. Montgomery provided much of the electronic test equipment that was used in the initial phases of the program. He also provided the BioImpedance Analyzer that was used in later phases to make electrical impedance plethysmographic measurements on animal and human subjects.

The software used to analyze the impedance plethysmographic data was originally written by Dr. Richard L. Montgomery of Management Analytics, Corvallis, OR, in collaboration with Dr. Leslie D. Montgomery. This software was adapted with various enhancements to run on the VAXstation in support of this work.

The protocols for the use of experimental animals in this research were approved by the Duke University Institutional Animal Care and Use Committee, Registry Numbers A344-89-9R1 and A258-90-6. Applications of the EIS technology to human volunteers was approved by the Duke University Medical Center Institutional Review Board for Clinical Investigations, Protocol Number 310-89-4R4 (as amended May 1989).

Large measures of the experimental and analytic work were completed by two Duke University graduate-level students. Yi-Chang Wu, M.D., a Ph.D. candidate in the Department of Cell Biology, Division of Physiology, completed many of the *in vitro* studies of bubble formation in gelatin and agar preparations. He also conducted the studies of bubble formation and hemodynamic changes in rats decompressed to simulated altitudes. As the program progressed into consideration of factors other than bubble formation that could affect the impedance spectrum of tissue, indications emerged that Electrical Impedance Spectroscopy could also be used to track shifts of fluid between the extra- and intracellular compartments of monitored tissues. David C. Sasser, a Medical Student in the Duke University School of Medicine, undertook the validation of such indications.

Various aspects of program results have been presented at three different scientific meetings to date, and another presentation is pending. Two additional manuscripts providing further details of completed work are presently in preparation for publication. The texts of these presentations and drafts of the manuscripts are included as Appendices to this report.

<b>Accession For</b>	
NTIS GRA&I	<input checked="" type="checkbox"/>
DTIC TAB	<input type="checkbox"/>
Unannounced	<input type="checkbox"/>
Justification	
By	
Distribution/	
Availability Codes	
Dist	Avail and/or Special
A-1	

# TABLE OF CONTENTS

<u>Section</u>	<u>Page</u>
Identifying Information .....	1
Foreward .....	2
Table of Contents .....	3
1.0 Introduction .....	5
2.0 Electrical Impedance Spectroscopic (EIS) System .....	7
2.1 Evolution .....	7
2.2 Final Configuration .....	8
2.2.1 Hardware .....	8
2.2.2 System Software .....	9
2.2.2.1 Data Acquisition .....	9
2.2.2.2 Data Analysis .....	11
Impedance and Its Transforms	
Equivalent Circuit Models	
2.3 Performance Validation .....	13
3.0 EIS Bubble Detection In Vitro .....	15
3.1 Materials and Methods .....	15
3.2 Bubble Dielectric Signature .....	16
4.0 EIS Bubble Detection In Vivo .....	23
4.1 Hyperbaric Decompression; Goats .....	23
4.2 Methodological Specificity:	
Bubbles vs. Physiological Fluid Shifts .....	24
4.3 Methodological Enhancement: Concurrent	
Impedance Plethysmographic (IPG) Measures of	
Blood Flow and Hemodynamics .....	25
4.4 Hypobaric Decompression; Rats .....	26
4.4.1 Materials and Methods .....	27
4.4.1.1 Decompression Apparatus .....	27
4.4.1.2 Impedance Plethysmographic System .....	27
4.4.1.3 Experimental Protocol .....	28
4.4.1.4 Data Analysis .....	28
4.4.2 Results and Discussion .....	29
5.0 Summary and Conclusions .....	33
6.0 References .....	35
7.0 Figures .....	39

TABLE OF CONTENTS (Continued)Appendices

- A. Structural Dielectric Relaxation:  
Theory Pertinent to *In Vivo* Bubble Detection ..... 77
- B. Impedance Plethysmography ..... 85
- C. Presentations and Manuscripts
  - 1. Effects of Decompression-Induced Gas Bubbles on the Electrical Impedance Spectrum of Gelatine.
  - 2. Bioelectrical Impedance Indices of Decompression-Induced Bubble Formation and Hemodynamic Changes in Rats.
  - 3. Monitoring of Fluid Redistribution During Head-Down Tilt by Bioelectrical Impedance Spectroscopy.
  - 4. A Computer-Based Bioelectrical Impedance Spectroscopic System for Noninvasive Assessment of Compartmental Fluid Redistribution.
  - 5. Noninvasive Measurement of Changes in Segmental Fluid Compartmentalization and Hemodynamics.
  - 6. Monitoring of Segmental Intra- and Extracellular Volume Changes Using Electrical Impedance Spectroscopy.

## 1.0 INTRODUCTION

Personnel engaged in diving, compressed air work and high altitude aviation and space missions are at risk for developing decompression sickness (DCS) or "bends" as a result of excessively rapid and extensive reductions of their ambient atmospheric pressures. DCS is a serious hazard because its initial symptoms, which are most often experienced as dull persistent pain in and around body joints, can rapidly become incapacitating, while more severe cases involve visual field disturbances, other neurological disorders, syncope and death. There is a widespread consensus that the first etiologic event of DCS is the formation and growth of gas bubbles in tissues that become gas-supersaturated as a result of decompression. Common symptomatic manifestations of DCS are then thought to be caused by mechanical deformation of pain receptors as extravascular bubbles grow beyond a certain size, or by localized ischemia as bubbles either directly or indirectly occlude the circulation [11]. Following from these premises, it has long been recognized that the onset of DCS symptoms might be anticipated by monitoring certain DCS-susceptible tissues for bubble formation and growth before the bubbles attain size and/or profusion sufficient to cause symptoms. Several methods of *in vivo* bubble detection have been developed with this goal in mind [31], but with only limited success.

Ultrasonic Doppler techniques have been used extensively to obtain information about bubble presence and profusion in decompressed experimental animals and man [24,35,37,38]. Such methods are advantageously noninvasive, but are limited because only moving and, therefore, only intravascular bubbles can be detected. The method is most conveniently used to "image" the right heart via the precordium, where bubbles originating from any source in the body can be detected as they are recruited into the central venous circulation [37]. Because such bubbles usually fail to pass the pulmonary circulation, they are plainly not those that cause DCS symptoms at peripheral sites. Accordingly, correlations between bubble profusion indicated by these methods and DCS incidence are generally poor [7]. Additionally, the raw data provided by these methods is extremely difficult to quantify in any objective, rigorous way, which has confounded the development of any automatic, machine-implemented version of the method. The most common methodological implementation is by a trained operator who positions and focuses the transducer and, through monitoring of an aural rendition of the Doppler signal, reduces the result to a semiquantitative index of bubble profusion. In addition to the foregoing difficulties, field applications of this technique entail even more onerous demands in establishing and maintaining proper transducer placement and transcutaneous coupling of the ultrasonic field.

The field applicability of another initially promising ultrasonic technique, pulse-echo ultrasonic imaging [7,27], has proven even more difficult. Although capable of detecting stationary bubbles as small as 10  $\mu\text{m}$  in diameter, these methods suffer from difficulties similar to those plaguing Doppler ultrasonic methods: maintenance of transcutaneous coupling between transducer and tissue is critical and transducer placement must be precisely reproduced for each monitoring period.

The present program entailed development of a bubble detection method based on bioelectrical impedance that promises to overcome many of the difficulties presented by the above ultrasonic methods. Living tissue is a

heterogeneous ionic conductor of electric current that presents a resistance,  $R$ , or an impedance,  $Z$ , to the passage of direct or alternating current, respectively. This resistance or impedance depends on the physical dimensions and volume resistivity of the tissue. The latter is particularly sensitive to the presence and volume gas bubbles, which act as dielectric or nonconducting particles regardless of their anatomical locations or velocities. Early attempts to exploit these effects to detect bubbles in living tissue entailed measuring the impedance of tissue at single fixed frequencies [12-14,32]. For example, using a fixed excitation frequency of 2500 Hz to reduce the influence of electrode polarization and avoid tissue excitation that occurs at lower frequencies, Jossinet, et al. [14], measured muscular impedances in rats and human subjects during decompressions from hyperbaric exposures. Impedance increases from 3 to 30% were observed. An increase of about 11% was observed in the quadriceps muscles of a human subject before the subject developed bends in the monitored thigh. Such fixed frequency approaches, however, provide no information by which observed impedance changes can be unequivocally ascribed to bubble formation and growth *per se*: Contributions from artifacts such as changes in temperature cannot be ruled out.

These impedance approaches have been extended in the present work to allow examination of the effects of bubble formation and growth on the impedance **spectrum** of a material. The impedance,  $Z$ , consists of contributions from both electrically resistive and electrically reactive components of the monitored material. The magnitude of  $Z$  consequently varies with the frequency of the applied current in a fashion that is governed by dielectric relaxation phenomena at structural heterogeneities in the material. A theoretical analysis (Appendix A.) indicates that gas bubble formation and growth should effect the frequency dependence of the impedance, as well as the value of the impedance at a given fixed frequency. The principal objective of the present work was to obtain empirical verification of this indication and assess whether electrical impedance spectroscopy can be used to detect bubbles *in vivo* with greater sensitivity and specificity than attainable with conventional fixed frequency methods.

## 2.0 ELECTRICAL IMPEDANCE SPECTROSCOPIC SYSTEM

### 2.1 Evolution

An impedance spectrum of a test material is obtained from the voltages that are developed across the material in response to sinusoidal electric current excitation of known amplitude and phase at different frequencies [1]. In principle, such voltages can be measured at least two different ways; by Fourier-transforming the measured response to a broad band excitation signal or by measuring the voltage at each of a series of discrete excitation frequencies. Although the first method allows a spectrum to be measured very quickly, the latter is the method of choice for its accuracy and relative immunity to electrical noise. Adopting this swept frequency approach in the present program, impedance spectrum measurements were first undertaken using the system schematized in Figure 1. The material under test in the figure is a cylindrical sample of gelatine contained in the electrochemical cell that was developed for work described in Section 3.0.

The main system component was a Princeton Applied Research (PAR) Model 129A Two-Phase Vector Voltmeter/Lock-in Amplifier. The Model 129A was operated in differential mode to maximize common mode noise rejection. Measured resistance and reactance at a given frequency was displayed on calibrated digital panel meters connected to PAR analog outputs. A Krohn-Hite Model 5800 signal generator provided both the drive current at specific frequencies as well as a reference signal for the lock-in amplifier. Drive current to the material under test was conditioned by a constant current amplifier at about 0.1 ma (pk-pk). The signal generator output frequency was set manually and measured by a digital frequency counter (Fluke Model 8060A autoranging digital multimeter).

In order to measure an impedance spectrum, the 129A was first calibrated at a given frequency to give the correct value of a known resistance with zero reactance using a tetrapolar resistance circuit across system outputs and inputs. This was achieved by reciprocal adjustment of the signal generator output amplitude and the offset phase of the 129A phase detection circuitry. The 129A was then connected to the test sample. Resistances and reactances were measured and manually recorded at each of a series of frequencies covering the desired range as successively set by manually adjusting the signal generator.

This system was found to suffer from serious problems, some of which entailed obvious procedural inconveniences that would have become important only in real-time applications. Other problems, however, were more important and precluded use of the system in the applications required by this program. The latter are briefly reviewed here because their understanding was vital to the subsequent development of a more successful system configuration.

The most serious problem arose from the method by which the reference signal, against which the phase of the input signal was measured, was derived from the excitation circuitry. As shown in Figure 1, this reference signal was derived from the signal generator output, before the latter was fed to the constant current amplifier and in turn to the drive leads and electrodes on the material being tested. As a result, any reactive components in the drive



circuitry, including those in the current amplifier, cables and electrode/sample junctions themselves, affected the amplitude and phase of the transmitted current. While the constant current amplifier obviated any attenuations of drive current amplitude, it did not maintain the phase of the drive current. Because the phase of the signal between the pickup electrodes was measured with respect to the uncontaminated reference signal, measured reactances included unwanted phase-shift contributions from these drive circuit components. Most importantly, contributions of drive electrode impedance were included that were impossible to quantify. Other workers [16] have rectified this problem in similarly configured systems by deriving the reference signal from across a low-valued resistor placed in one of the drive cables. However, because of limiting 129A reference channel input signal-strength requirements, an additional amplifier would have been required in the present system to boost the signal into the reference input. It was concluded that measurement of the transmitted current was a better solution to this problem that would also more readily enable dynamic adjustment of the drive current as frequencies changed in each sweep.

## 2.2 Final Configuration

Following the above definition-phase work, a comprehensive Electrical Impedance Spectroscopic system was developed that obviated or overcame the problems and operational difficulties inherent in the initial approach.

### 2.2.1 Hardware

The system consisted of a Solartron 1260 Impedance/Gain-Phase Analyzer (Schlumberger Technologies, Farnborough, England) controlled via an IEEE-488 General Purpose Interface Bus (GPIB) by a Digital Equipment Corporation (DEC) VAXstation 3200 computer. The VAXstation end of the GPIB was a DEC IEQ11-A IEEE-488 Interface Bus option installed on the VAXstation backplane. The VAXstation was configured with 8 Mb RAM, a VR260 Monochrome Monitor, a RD54 159 Mb fixed disk drive, a 4-line DZQ11 Asynchronous Multiplexer for serial communications and a TK50 Tape Drive Subsystem for data loading and backup. A LaserWriter IINTX (Apple Computer, Inc.) was configured on one of the serial ports for hardcopy data and graphics output. The entire system, except the LaserWriter, was mounted in one full EIA standard cabinet rack on castors for portability in the laboratory.

The Analyzer contained an internal microprocessor that was programmed and controlled via the GPIB to effect swept frequency impedance measurements and upload the results to the VAXstation in real-time. A signal generator and current amplifier in the Analyzer provided the excitation signals which were passed through the material under test and terminated at a current input channel on the Analyzer. The amplitudes and phases of the transmitted currents were measured at this latter terminal. The voltage responses of up to two non-overlapping segments in the excitation path were measured across each of two independent differential voltage input channels.

Tetrapolar electrode configurations were used in all applications to minimize electrode impedance effects on measured voltages. All output and input leads connecting the Analyzer to the electrodes were made of RGU-174/U 50

Ohm shielded coaxial cable. Proper grounding of the shields was essential to minimize the influence of ground loops and stray capacitance. The shields of all leads were grounded to the Analyzer chassis through BNC panel connectors on the Analyzer. The shields of the leads were also brought to equal potential at a single point near the electrode ends of the leads.

## 2.2.2 System Software

Supporting system software was developed to program the Analyzer in real-time and control all aspects of Analyzer operation, data acquisition, data analysis and results output. The operating environment was VAX/VMS 4.7A and the software source code was written in VAX FORTRAN-77. Windowing functions and graphics displays were implemented using DEC VMS Workstation Graphics Software invoked through use of UIS Graphics Routines. The IEQ11-A IEEE-488 Interface Bus was accessed through a VAX/VMS IEX Driver that was purchased with the bus option. Driver functions were invoked using calls to both the VMS QIO (Queued I/O) System Service and a FORTRAN Simplified User Interface (SUI) supplied with the driver.

The analytic components of the software were bundled to run under a real-time data acquisition program or under a separate post-run data processing program as schematized in Figure 2. This organization enabled real-time data passed from the impedance spectrum acquisition program, or data files from earlier experiments, to be processed with identical output in either case. In the former mode, the analyses were automatically performed and the results displays were updated immediately after acquisition of each spectrum.

### 2.2.2.1 Data Acquisition

Operation of the Analyzer was effected through EISSYS, a menu-driven routine that accessed and exercised the most important internal functions and commands of the Analyzer. This routine fully configured the analyzer for spectrum acquisition using default parameters, or otherwise, as directed by the user. The first menu screen is illustrated in Figure 3 to show the range of settable sweep parameters available to the user.

The range of frequencies in each sweep, the number of separate frequencies at which measurements were made and the analyzer integration time specified for each measurement governed the time required to measure a given spectrum. Each of these settings could be modified from the start-up default values to tailor Analyzer operation to conform to experimental requirements for spectrum acquisition speed, accuracy and frequency resolution. Based on the number of points and the frequency range specified for each sweep, the Analyzer was set to select the actual frequencies according to a logarithmic distribution proceeding from the lowest to the highest frequency. With a fixed integration time for measurements at each frequency, the time required to acquire a single spectrum was about equal to the product of the number of points and the integration time. Thus, with a 1 sec integration time, a 50 point impedance spectrum spanning 10 to 150,000 Hz could be measured and uploaded to the VAXstation in about 65 sec, with a point-by-point reproducibility of better than 0.5% in both equivalent series resistance and reactance. Higher spectrum acquisition speeds could be attained by reducing

the frequency resolution or by adjusting the measurement parameters to optimize speed while compromising measurement precision.

One option to attain higher acquisition speeds entailed dynamic adjustment of the integration time to encompass a constant, user-specified number of cycles at each excitation frequency as each sweep progressed. With such departures from static integration times, measurements at each point in a sweep required less time down to a minimum of 0.01 sec as the frequency increased. With exercise of this option, the actual measurement after each frequency change was begun only after a default 0.2 sec delay to accommodate Analyzer and sample settling times.

As part of its battery of built-in functions for measuring the transmitted current, the Analyzer included a monitor that helped to ensure that the current or voltage actually passed through the sample under test remained within a given range of the intended value. Although this capability provided a valuable safety feature for *in vivo* applications and was useful in maintaining measurement accuracy under conditions where drive electrode impedances deteriorated during the course of an experiment, its use tended to slow Analyzer operation and lengthen spectrum acquisition times. Operation of this monitor could be overridden by the user.

Typical excitation currents were in the 0.1 to 5.0 milliamp range (@ 3.0 V max.). Because the transmitted current was always measured, the drive current could be dynamically adjusted during the course of any given frequency sweep in order to maximize signal-to-noise ratios and measurement accuracy. Exercise of this capability proved important in *in vivo* applications, where maximum safe drive currents decrease with decreasing frequency. As the measurement frequency increased during each sweep from about 2.5 kHz to 150 kHz, the drive current was automatically adjusted upward using the log-log relationship:

$$\ln(I) = m \cdot \ln(f) + b;$$

where  $I$  is the current at frequency  $f$ . Values of the parameters  $m$  and  $b$  were conservatively set according to data provided by Geddes and Baker [10] for the frequency dependence of the threshold for current sensation in the human thorax. A minimum current of 0.3 - 1.0 mA was used when this relationship gave smaller values and a limit of 5.0 mA was imposed at higher frequencies. The resultant current vs frequency profile was within the limits prescribed for patient auxiliary currents in the 1979 British Standards Institution, Specifications for Safety of Medical Electrical Equipment, Part 1. Specification for General Safety Requirements, Subclause 19.3.

After the Analyzer was parameterized for operation, the user was presented with the menu shown in Figure 4. Impedance spectra could be measured singly as directed by the user, or automatically throughout a prolonged period after the number of spectra to be measured and the time between successive sweep starts was specified. Alternatively, the user could call up another menu shown in Figure 5 to review and/or reset the data acquisition, data processing and results display modes. If the latter menu was called, the user was returned to the menu in Figure 4 after exercise of any option in the data processing menu. After acquisition of a given spectrum or series of timed spectra, the user was returned to the menu in Figure 4 to either continue or

quit Analyzer operation.

The current generator in the Analyzer was automatically shut down during Analyzer idle periods between sweeps. Additionally, the user could abort and idle the generator at any time during a sweep by clicking the mouse in a sweep abort window that was opened at the bottom of the VAXstation screen during spectrum acquisition periods. A hardware generator kill switch was also mounted adjacent to the VAXstation keyboard.

#### 2.2.2.2 Data Analysis

The data for each measurement consisted of the following seven floating point values:

frequency (Hz),	$f$ ;
a and b of the complex excitation current (amp),	$I^* = \bar{a} + bj$ ;
c and d of the complex voltage response (V), channel 1,	$V_1^* = c + dj$ ;
e and f of the complex voltage response (V), channel 2,	$V_2^* = e + fj$ ;

where  $j = \sqrt{-1}$ . These data were received from the Analyzer in ANSI/IEEE Standard 754 format. After conversion to internal VAX/VMS REAL form, analysis proceeded using FORTRAN intrinsic functions for complex arithmetic.

#### Impedance and Its Transforms

The complex impedance for each measurement on each channel was obtained from the relation:

$$Z^* = V^*/I^* = R + Xj, \quad (1)$$

where R and X are the equivalent series resistance and reactance, respectively. The impedance locus was obtained by plotting X vs R for  $Z^*$  at each frequency in the spectrum. The three other complex transforms are:

$$\text{Modulus, } M^* = Z^* \cdot j\omega ; \quad (2)$$

$$\text{Admittance, } Y^* = 1/Z^* ; \quad (3)$$

$$\text{Capacitance, } C^* = Y^*/j\omega ; \quad (4)$$

where  $\omega = 2\pi f$  is the angular frequency. As for the impedance, the respective locus for each of these transforms was obtained by plotting the imaginary part vs the real part for the value at each frequency. The four loci for each of the Analyzer channels were displayed in separate windows opened on the VAXstation screen.

#### Equivalent Circuit Models

The measured impedance spectrum of a given sample can be reproduced by one or more hard-wired "equivalent" electric circuits of appropriate design. The configuration of the equivalent circuit model, with the values of its component resistances and capacitances found by numerically fitting the model to the measured spectrum, provided a means of summarizing the measured spectrum in terms of a relatively few parameters. The simple equivalent circuit models used are schematized in Figures 6 and 7.

The complex impedance for the series circuit in Figure 6 is given as a function of frequency by

$$Z^* = R_s + \frac{R_p}{1 + j\omega\tau}, \text{ where } \tau = R_p C_p. \quad (5.a.)$$

Similarly, the complex admittance for the parallel circuit in Figure 7 is given by

$$Y^* = \frac{1}{Z^*} = \frac{1}{R_p} + \frac{1}{R_s} - \frac{1/R_s}{1 + j\omega\tau}, \text{ where } \tau = R_s C_s. \quad (5.b.)$$

The impedance locus of the series circuit (Figure 6) and the admittance locus of the parallel circuit (Figure 7) each form a semi-circle in the complex plane with center on the real axis. Impedance and admittance loci of biological materials are also usually semi-circular, but with centers that lie, respectively, above and below the real axis. The cause of this is not well understood but can be attributed to the presence in each of the model circuits of an infinitude of R-C elements with different time constants,  $\tau_i$ , distributed about a mean value of  $\tau$ . This behavior is modeled mathematically by raising  $j\omega\tau$  in each of the above equations to a power of  $(1-\alpha)$ :

$$Z^* = R_s + \frac{R_p}{1 + j\omega\tau^{(1-\alpha)}}, \quad 0 < \alpha < 1; \quad (6.a.)$$

for the series circuit in Figure 6 and Eq. (5.a.), and;

$$Y^* = \frac{1}{Z^*} = \frac{1}{R_p} + \frac{1}{R_s} - \frac{1/R_s}{1 + j\omega\tau^{(1-\alpha)}}, \quad \tau = R_s C_s; \quad (6.b.)$$

for the parallel circuit in Figure 7 and Eq. (5.b.). In either model, the quantity  $\alpha\pi/2$  is the angle between the real axis and a radius of the respective impedance or admittance locus passing through either of the two real axis intercepts. By definition,  $\alpha=0$  when the center of the locus lies on the real

axis. According to the significance of the  $\alpha$  value forwarded above, increasing values of  $\alpha$  from 0 towards unity indicate a widening of the distribution of time constants, with increasing standard deviation of the distribution about the mean at  $\tau^0$ .

These equivalent circuit models were fitted to measured spectra using a nonlinear least squares routine based on Marquardt's algorithm [20]. The impedance is a complex number while the algorithm operates on real numbers. The algorithm was consequently implemented using the norm of each observed impedance,  $|Z^*|$ , and that of the corresponding fitted impedance,  $|Z^*|$ . The algorithm adjusted the model parameters to minimize the sum of squares, SS,

$$SS = \sum_{i=1}^n (|Z_i^*| - |\hat{Z}_i^*|)^2, \quad (7)$$

over the  $n$  measured frequencies in the spectrum.

Fitted parameters from each spectrum were displayed vs time or acquisition sequence number in "strip chart" format in a separate window that was opened for each channel on the VAXstation screen. The values for each parameter were scaled so that deviations from the initial parameter value at time = 0 or sequence number = 1 were displayed on the ordinate in terms of the percent change in the parameter value. These displays afforded a means to track the equivalent circuit parameters of each monitored body segment as they changed throughout the course of an experiment.

Up to eleven separate windows; one for the system control menus and ten others showing different aspects of the spectroscopic results; were opened on the VAXstation screen during the course of runs in which both Analyzer channels were being used. In order to ensure that each display was presented at a convenient size, these were grouped and configured in layers so that no more than four displays were visible at any one time. A cursor-driven display manager was provided to automatically pop and push the window sets to bring any desired set into view.

### 2.3 Performance validation.

Determination of sample impedance using the measured amplitude and phase of the current actually passed through the sample [c.f., Eq. (1)] was an important feature of the system. This feature eliminated errors arising from the nonzero impedances of the current electrodes. As reviewed in Section 2.1, the latter errors emerge in other systems lacking this feature, even when constant current tetrapolar electrode circuitry is used, if the impedance is computed using a current value,  $I$ , with phase equated to that of a reference signal that is not passed through the drive electrodes and sample under test. Impedance spectra of hard-wired circuits measured using the present system were unchanged when current electrode impedance was modeled by placing parallel R-C legs in series with either or both of the current leads in the tetrapolar measurement configuration. Practically identical impedance spectra were obtained for the same monitored circuit with either of the two electrode/cabling configurations shown in Figure 8.

The ability of the system to quantitatively determine the electrical properties of hard-wired circuits of known components served to further validate system function and illustrate certain system capabilities. Using the same cabling as that used in various experimental applications, impedance spectra were accurately measured for certain hard-wired circuits to frequencies greater than 1 MHz. For example, the characteristic frequency,  $f^\circ$ , at which the reactance of the circuit schematized in Figure 6 should be minimal, is given by:

$$f^\circ = 1/2\pi\tau = 1/2\pi R_p C_p. \quad (8)$$

With parallel leg components,  $R_p = 100 \, \Omega$  and  $C_p = 0.0015 \, \mu\text{F}$ , this circuit should theoretically produce an impedance spectrum with minimum reactance at frequency equal to 1.06 MHz. Figure 9 gives the impedance spectrum and transforms of a circuit so wired, measured to a maximum frequency of 1.5 MHz.

With the sheet viewed in portrait orientation, the panels in the figure are: impedance plane; top left, admittance plane; top right, modulus plane; bottom left, and capacitance plane; bottom right.

Note that the spectrum exhibits a maximum at the characteristic frequency in the modulus domain. Table I gives the actual and calculated equivalent circuit parameters.

Table I. Known vs Measured Component Values for the Hard-wired Circuit in Figure 6.

	Actual	Fitted
$R_s \, (\Omega)$	0.0	0.01896
$R_p \, (\Omega)$	100.	98.9727
$C_p \, (\mu\text{F})$	0.0015	0.00152
$f^\circ \, (\text{MHz})$	1.06	1.058

The tabulated results show that the characteristic frequency was correctly resolved from the measured spectrum to within 0.1%, well within the  $\pm 10\%$  ratings of the individual circuit components. Results also show that the influence of stray capacitance in the instrumentation was minimal over our normal experimental frequency range, which rarely exceeded 150kHz.

The behavior of a hard-wired circuit configured as that shown in Figure 10.A illustrates the utility of different impedance transforms; in this case, the modulus; to illuminate essential features of more complex circuits. Figure 10.B shows the measured impedance spectrum and its transforms for such a circuit wired with components valued as given in Table II. (Figure 10.B is of the same format as Figure 9.) While the impedance equation for this circuit was not supported in our model fitting routine, each R-C leg had a

characteristic frequency given by Equation (8). These different characteristic frequencies are not discernable in the impedance domain but are clearly distinguished in the modulus domain where two separate maxima are correctly resolved, one at each characteristic frequency.

Table II. Known vs Measured Component Values  
for the Hard-wired Circuit in  
Figure 9.

	Actual		$f^\circ$ (theoretical)
$R_s$ ( $\Omega$ )	0.		
$R_{p1}$ ( $\Omega$ )	100.	]	1.06 MHz
$C_{p1}$ ( $\mu F$ )	0.0015		
$R_{p2}$ ( $\Omega$ )	1000.	]	106.0 kHz
$C_{p2}$ ( $\mu F$ )	0.0015		

### 3.0 EIS BUBBLE DETECTION In Vitro.

Initial experiments were designed to provide empirical support for the central hypothesis that gas bubbles in a liquid should affect the impedance spectrum of the liquid, and that such effects should manifest in changes of dielectric properties that, if observed in living tissue, could be unequivocally ascribed to bubble formation and growth rather than to other factors. The experiments were conducted using *in vitro* systems in which the appropriate physical-chemical factors could be most readily controlled.

#### 3.1 Materials and Methods

Gelatin and agar preparations were chosen as the liquid media because their transparency allows ready visual observation of bubble formation and growth while their viscosities keep any bubbles in place and tend to prevent separate bubbles from coalescing. Bubble formation and growth was induced by decompression of preparations that were initially free of macroscopic bubbles. All media were prepared by weight using Knox gelatine (U.S.P.) purchased from a local grocery or Bacto-Agar (Difco Laboratories; Detroit, MI). Small amounts (0.1 - 0.5% bw) of NaCl were included, when necessary, to reduce bulk resistivity. Various surface active agents in varying concentrations were included in most preparations to adsorb to the bubble surfaces.

Experimental design was constrained by the desire to use the gels with associated tetrapolar electrode circuitry in a configuration that would produce an experimental analog of the theoretically-simple cylindrical conductor between parallel endplate current electrodes. Because bubble trapping (and subsequent expansion by Boyle's law effects during decompression) is



unavoidable when working with gels *per se*, a gel cylinder is most readily contained in a tube which is loaded with the gel in a liquid (sol) state and allowed to solidify (gel) *in situ*. Such a cylinder is most conveniently loaded on the bench at atmospheric pressure. However, the cost of such convenience is that the dissolved gas concentration in the resultant gel is limited to that achieved in the sol immediately prior to its insertion into the cylinder. The gas-supersaturations achievable by subsequent decompression to drive bubble formation and growth are correspondingly limited.

The electrochemical cell schematized in Figure 11 was developed to contain the gelatine preparations, while allowing them to be decompressed to produce bubble formation and growth. A current electrode plate (316 stainless steel) was embedded in each of two plexiglass pistons, one at either end of a plexiglass cylinder (3.5 cm I.D., 39 cm length). One piston was movable to accommodate volume changes caused by bubble growth and resolution in the material between the electrodes. Two additional pickup electrodes rings (also 316 ss) were embedded in the body of the cylinder about midway between the current electrodes. These circumferential electrodes, with inner edges separated by 4.0 cm, defined a fixed volume of monitored material in each experiment.

The cell was assembled containing a given gelatine or agar preparation that had been warmed to sol-state and air-saturated at ambient barometric pressure. After the cell was cooled in an ice bath to gel the preparation, it was inserted into a transparent plexiglass chamber. The latter could be decompressed to any hypobaric pressure greater than about 1 mm-Hg at any desired rate up to explosive to induce bubble formation and growth. The chamber afforded ready visual observation of the cell and test material. Shielded wires connected to each of the electrodes were collected into a bundle, passed through the chamber closure at one end of the chamber and connected to the Impedance Analyzer. The excitation current was passed through the gel across the end-plate current electrodes. The relative amplitude and phase of the voltage developed in response to this excitation was measured across the pickup electrodes.

### 3.2 Bubble Dielectric Signature

Typical impedance loci from a gelatin preparation (gelatin, 4.0% bw; Na-lauryl sulfate, 1.0% bw) are shown in Figure 12. Locus A is from a spectrum measured for the bubble-free gel before decompression. Locus B is from a spectrum taken after the gel had been decompressed to produce a profusion of bubbles in the monitored gel section. Finally, locus C is from a spectrum taken after the gel had been recompressed, but before the bubbles had completely resolved. Each locus is built from 50 discrete measurements made at frequencies from 85 Hz to 2 kHz. Individual points are obscured in the figure by connecting straight lines. The loci fail to exhibit their actual semi-circular geometry only because the aspect ratio of the plot is not unity. The point for the lowest frequency impedance defines the right-most or highest resistance end of each locus. The point for the highest frequency impedance defines the left-most or lowest resistance end of each locus. Points from impedances at intermediate frequencies define the intervening locus regions. Thus, each locus shows how the resistance decreases monotonically with increasing frequency, while the reactance first decreases then increases.

Measured spectra were first analyzed using the equivalent series circuit in Figure 6. Values of the circuit components in this model are reflected directly in the impedance locus, so that variations in these values could be readily understood in graphical terms. For example, the series resistance,  $R_s$ , in this model corresponds to the limiting infinite frequency resistance,  $R_\infty$ , at the left-most real axis intercept of the impedance locus. The parallel resistance,  $R_p$ , corresponds to the span between this infinite frequency resistance and the dc resistance,  $R^0$ , at the right-most real axis intercept of the locus.

### Temperature Effects

Establishment of baseline or control behavior of the preparations required examination of the effects of temperature *per se*. In accord with known dielectric behavior of electrolytic solutions, the impedance of the preparations at given excitation frequencies decreased with increasing temperature. In the impedance domain, these decreases manifested as left-ward shifts of the entire spectrum along the real axis. Conversely, cooling of the preparations caused right-ward spectral shifts.

Figure 13 shows the effects of temperature on the equivalent series circuit parameters fitted to measured spectra of a 2.0% bw gelatine preparation containing 0.9% bw NaCl. Parameters shown from bottom to top are:  $R_s$ ,  $R_p$  and  $C_p$ . The values for each parameter are scaled such that a one tick-mark deviation from the centerline of each parameter, where the initial point is drawn, corresponds to a 4% change in parameter value.

Spectra 1 through 6 were taken as the preparation was cooling from a temperature of about 38°C to the room temperature of approximately 20°C. Increases in the equivalent series resistance,  $R_s$ , reflect cooling-induced right-ward shifts of the spectra along the real axis. These were accompanied by even greater increases in equivalent parallel resistance,  $R_p$ , while the equivalent parallel capacitance,  $C_p$ , tended to decrease. The gel cartridge was then refrigerated, lowering the gel temperature to 7°C. Spectra 7 through 11 were taken as the cartridge warmed toward room temperature. The equivalent circuit parameters changed in directions opposite those that accompanied cooling, with return toward the same room temperature values that had been reached during cooling. Failure to reach the latter values correctly indicated that the warming cycle was not followed to complete equilibrium at room temperature. Importantly, these changes, particularly the near-parallel changes in  $R_s$  and  $R_p$ , were typical of those caused by temperature change alone in all of the preparations studied.

Parenthetically, the effects of temperature illustrate how fixed frequency impedance measurements can provide only nonspecific information about the presence of bubbles. The complex admittance  $Y^*$  of a bubble suspension is given by Equation (8) in Appendix A. At low frequencies, this admittance reduces to the conductivity of the suspension:  $Y^* = G_1$ . If the bubbles are assumed to be nonconducting, spherical and homogeneously distributed, this expression becomes [Appendix A, Equations (17) and (18)]:

$$Y = \kappa^{\circ} = \kappa_1 \cdot \left( 1 - \frac{3\rho}{2} \right) ;$$

where  $\kappa_1$  is the conductivity of the medium in which the bubbles are dispersed and  $\rho = V_b/V_T$  is the ratio of the bubble volume to the overall volume. Substitution of  $\kappa_1 = 1/R^{\circ} = 1/Z^{\circ}$  and  $Z = 1/Y$  then yields, after some rearrangement [c.f., Refs. 13, 14]:

$$(Z - Z^{\circ})/Z^{\circ} = 3\rho/2, \quad (9)$$

where  $Z$  is the sample impedance after bubble formation and  $Z^{\circ}$  is the impedance of the medium within which the bubbles are dispersed. When this relationship is applied to quantify the extent of bubble formation in gas-supersaturated liquids,  $Z^{\circ}$  is taken as the impedance of the sample before bubble formation. In view of the above effects of temperature, it is clear that such applications can be valid only in the absence of changes in  $Z$  that occur incidentally to bubble formation and growth.

#### Pressure effects

In contrast to the effects of temperature, decompression *per se* did not cause measureable changes in the dielectric properties of the gel or agar preparations. Impedance spectral properties often showed slow changes that reflected underlying temperature reequilibration, but any spectral changes beyond such baseline drifts always coincided with the appearance, growth or resolution of bubbles; not with any decompression or recompression itself. Such behavior also indicated that thermal effects of decompression or recompression were negligible in the chamber and gel cartridge used for these experiments.

For example, Figure 14 is a time series of equivalent series circuit parameters for spectra obtained from a gelatine preparation (gelatine, 3.0% bw; detergent, 1.0% bw) that was decompressed to 360 mm-Hg and held at this pressure for a prolonged period with no bubble formation. Spectrum 1 was obtained before decompression and spectra 2 - 4 were taken over a 40 min period after decompression during which no bubbles formed. Note that no immediate differences are evident between spectra 1 and 2 that would be attributable to the decompression. Additionally, ensuing decreases in  $R_p$  were small and were paralleled by small decreases in  $R_s$  and increases in  $C_p$ . Reference to Figure 13 shows that this pattern indicates that the preparation was warming over this period, whereas any thermal effect of decompression would have entailed cooling of the gel.

#### Bubble Formation and Gel Composition

When decompression was followed by bubble formation and growth, changes in the impedance spectrum occurred that depended on the presence of surface active substances and that differed from those caused by temperature changes alone. The spectral changes observed in the presence of surface active substances are typified by those illustrated in Figure 12. Bubble formation in

such preparations caused a rightward shift of the locus along the real axis, a narrowing in the span between low and high frequency real-axis intercepts and an increase in the reactances. These changes reversed when the gel was recompressed and the bubbles resolved.

Because bubble formation entailed the introduction of new structural features in the gels, it was important to demonstrate that the impedance loci could be described by the same equivalent circuit model both before and after bubble formation. Analysis of residuals for the model fits indicated that the patterns for lack-of-fit were not changed by bubble formation and growth. Typical results of such analyses are shown in Figure 15. The residuals from two fits are shown; one to a spectrum of a bubble-free gel and the other to a spectrum of the same gel after it had been decompressed to produce a profusion of bubbles. No significant change in the residuals distribution vs frequency is evident. An important indication of these results is that bubble-induced effects on the impedance spectrum were fully "captured" by variations in the equivalent circuit parameter values. The latter consequently provide valid quantitative indices of bubble formation and growth in the preparations.

The importance of gel composition as governor of bubble effects on the impedance spectrum, as well as the absence of a decompression effect, is illustrated by the results of two experiments shown in Figures 16 and 17. Figure 16 gives the data for a gelatine preparation (2.0% bw) that included NaCl (0.5% bw) as the only added solute. Bubbles of diameter less than 1 mm formed in great profusion with decompression between spectra 2 and 3, but changes in equivalent circuit  $R_p$  and  $C_p$  were small. The corresponding small changes in series resistance,  $R_s$ , were within a range attributable to small temperature changes that probably occurred during the course of the experiment. In fact,  $R_s$  decreased slightly with bubble formation. In view of behavior prescribed by Equation (9),  $R_s$  increases arising from increasing  $\rho$  were too small to overcome either a thermal drift and/or other bubble-induced changes in medium resistance. Observed behavior consequently attested to the relatively small total volume of the bubbles, despite their large number: The bubbles were, for all practical purposes, dielectrically invisible.

Figure 17 shows results of a similar experiment, differing only in that the gelatine preparation included 0.5% bw ionic detergent instead of NaCl. The preparation was decompressed between spectra 2 and 3, again resulting in a high profusion of small bubbles (< 1 mm dia). In this case, however, bubble formation and growth occasioned a marked increase of  $C_p$  and a corresponding decrease of  $R_p$ . The relatively small increase of  $R_s$  was evidence again of the relatively small total volume of exsolved gas. Note that these bubble-induced changes differed qualitatively from those caused by temperature changes alone. The directions and opposition of the changes in  $C_p$  and  $R_p$  would have suggested that a sharp warming of the preparation had occurred, but the attendant decrease of  $R_s$  was not evident. In spectrum 11, taken immediately after recompression of the preparation to ambient pressure,  $C_p$  and  $R_p$  showed sharp changes in directions opposite those that accompanied decompression and bubble formation. Correspondingly,  $R_s$  decreased in reflection of compression and resolution of the bubble volume. These concerted changes in the equivalent circuit parameters were always among those observed when bubbles formed and resolved in preparations that contained some sort of surface active substance with no other micellar or emulsified dispersed phase.

Notably, the  $R_p$  and  $C_p$  parameters exhibited substantially greater sensitivity to bubble formation than the series  $R_s$ . This sensitivity is evident in the experiment of Figure 14 as well as in the experiment of Figure 17. After the 40 min period of no visible bubble formation in Figure 14, four small bubbles (<0.5mm dia) became visible and gradually increased in size during the ensuing 2 hr when spectra 5 through 9 were taken. Changes in  $R_p$  and  $C_p$  similar to the bubble-induced changes in Figure 17 are evident but are not accompanied by a definitive change in  $R_s$ . After recompression to atmospheric pressure, the gel was decompressed again to 90 mm-Hg before acquisition of spectrum 13. In the ensuing spectra (13 - 18), evidence of enhanced bubble formation and growth is more clear with the widening between  $C_p$  and  $R_p$  attended by slight increases of  $R_s$ .

Seemingly inordinate attenuation or outright disappearance of these bubble-induced effects was often observed with recompression, even though bubbles of substantial size and number remained. These observations indicated that the structural features of the liquid around the bubbles that give rise to the bubble dielectric signature could be disrupted with forced collapse of the bubbles. Experiments in which the impedance was monitored during the full course of post-recompression bubble resolution provided some evidence that these structural features could reform around the residual bubbles;  $C_p$  was observed to increase then decrease, with concomitant decreases and increases of  $R_p$ , before the bubbles completely resolved.

Other gelatine and agar preparations were studied that contained an insoluble phase dispersed through action of a nonionic emulsifier. Bubble-induced changes in the parallel parameters of the fitted equivalent circuit were attenuated compared to those observed in similar preparations that lacked the emulsified phase. This difference in behavior may reflect that any changes in the parallel parameters for the simple equivalent circuit presently modeled can manifest only when bubble formation gives rise to liquid structural properties that had been absent before formation of the bubbles. Preparations containing emulsified insoluble phase may already contain the structural features that are otherwise newly formed in conjunction with bubble formation and growth. Nevertheless, these observations provided further indication that the bubble dielectric signature is critically governed by liquid composition.

It is important to note that bubble formation in these preparations displaced gel from the monitored volume between the pickup electrodes. Because the aqueous gel with relatively high dielectric constant ( $\epsilon \approx 70$ ) was replaced by gas with a dielectric constant practically equal to 1, material displacement alone would have caused the overall capacitance of the remaining volume, which was unchanged by design, to decrease. Figure 18 shows the capacitance plane transforms of the impedance loci presented in Figure 12. Bubble-induced decreases of system capacitance are indeed evident in the leftward shift of the capacitance locus (B) that was obtained after decompression and bubble formation. Additionally, this leftward shift reversed with recompression and bubble resolution. Such behavior, in conformance with simple bubble-induced exclusion of conductive material from the monitored volume, was typically observed irrespective of gel composition. However, the shifts appeared to be greatly potentiated in preparations that contained surface active substances.

When the results were viewed in the context of dielectric relaxation theory, indications clearly emerged that bubble formation and growth caused

more than simple material exclusion in these preparations. If bubble formation caused no effect other than to exclude conductive material from the monitored volume, such theory indicates that parameters in the present equivalent circuit would have changed with increases in bubble volume as follows (Appendix A):

- a)  $\tau (= R_p \cdot C_p)$  would be unchanged;
- b)  $R^\circ$  would increase;
- c)  $R^\infty (= R_s)$  would increase, and;
- d)  $R^\circ - R^\infty (= R_p)$  would increase.

It follows from (a) and (d) that  $C_p$  would decrease in inverse proportion to increases of  $R_p$ . These theoretical predictions are summarized and compared to the observed changes in Table III.

Table III. Effects of Bubble Formation and Growth: Comparison of Simple Material-Exclusion Theory with Experiment

Z-Locus Property	Equivalent Series Circuit Parameter	Exclusion Theory	Observed
a)	$\tau (= R_p \cdot C_p)$	no change	no change
b) $R^\circ$		$\uparrow$	$\uparrow$ or $\downarrow$
c) $R^\infty$	$= R_s$	$\uparrow$	$\uparrow$ or $\downarrow$
d) $R^\circ - R^\infty$	$= R_p$	$\uparrow$	$\downarrow$
e)	$C_p$	$\downarrow \propto 1/R_p^*$	$\uparrow$

\* Follows from (a) and (d).

As indicated by comparison of the entries in the two right-most columns in Table III, the experimental results violated the predictions in several ways. While  $\tau$  tended to remain unchanged, the span of the impedance locus ( $R^\circ - R^\infty$ ) decreased with bubble formation and growth. Moreover, these decreases were more pronounced in gelatine with surfactants than in preparations that lacked them. Similarly, the equivalent circuit capacitance  $C_p$  changed negligibly with bubble formation in gelatine that lacked surfactants, but increased markedly with bubble formation in preparations that included surfactant. These contrasts between simple theory and observed results can only be explained in terms of gas bubble effects on the structure and/or composition of the liquid surrounding the bubbles: Other potential artificial effectors of measured dielectric properties had to prevail to a near equal extent in these experiments, regardless of the presence or absence of surface

active agents. Results indicated that such effects were strongly governed by solute adsorption at the bubble gas-liquid interfaces.

The above indication was confirmed and amplified in a more focused series of experiments that was intended to characterize the influence of surfactant concentration and bubble size and number density on bubble-induced changes in the impedance spectrum. In contrast to the above, however, it became convenient to analyze results of these and all following studies using the equivalent parallel circuit in Figure 7. For given changes in the impedance spectrum, parameters in this model vary differently from those in the equivalent series circuit. For example, data from the same experiment in which decompression produced a profusion of bubbles in a gel sample are shown in both panels of Figure 19. The top panel shows the time series of the parameters for the equivalent series circuit fitted to the measured spectra and the bottom panel shows the corresponding series of parameters for the equivalent parallel circuit fitted to the same spectra. While the capacitance  $C_s$  in the equivalent series circuit increases with bubble formation and growth, its analog  $C_p$  in the equivalent parallel circuit decreases. Similarly, the resistance  $R_s$  in the equivalent series circuit decreases with bubble formation and growth while its analog  $R_p$  in the equivalent parallel circuit increases. Both the series resistance  $R_s$  in the equivalent series circuit and the shunt resistance  $R_p$  in the equivalent parallel circuit increase with bubble formation and growth. Because the equivalent circuit parameters are used in the present context simply as quantitative indices without reference to particular structural features of the systems, either alternative circuit model can be used provided that these differences in their behaviors are kept in mind.

The influence of various concentrations of Na-lauryl sulfate surfactant is summarized in Figures 20-22. The time series of observed bubble-induced changes in the equivalent parallel circuit parameters are combined and averaged for all the preparations in each figure. The illustrated significances of the changes in each parameter with respect to the last pre-decompression value were determined using paired 2-tailed t-tests. Bubble formation in these preparations resulted in significant increases in  $R_p$  (Figure 20) and significant decreases in  $C_p$  (Figure 21). In contrast, while  $R_p$  tended to increase with bubble formation and growth (Figure 22), the increases were not significant. The latter result, indicating that  $R_p$  is a poor discriminator for bubble formation, assumed particular importance in view of later results outlined in Section 4.2.

The specific surfactant concentration dependences of the bubble-induced changes in  $R_p$  and  $C_p$  are shown in Figures 23 and 24, respectively. Bubble-induced changes in each of these parameters tended to increase with surfactant concentration from 0.1% to 1.0% bw.

The preceding results can only be considered in semi-quantitative terms because the bubble numbers and sizes in the different runs could not be controlled. Correlations of the dielectric signature with bubble size and number density were confounded by difficulties in producing preparations in which bubble formation occurred homogeneously and reproducibly from run to run. However, data were obtained that substantiated the dependence of the bubble dielectric signature on bubble volume and number density.

The total volume of bubbles formed after any given decompression was quantified by measuring the bubble-induced displacement of the movable piston in the gel cartridge. The bubble volume in the electrically monitored section of the cartridge was then estimated from the fraction of the total gel volume that this section contained, under the assumption that the measured overall bubble volume was uniformly distributed throughout the entire gel volume. The estimated resolution of these determinations was  $\pm 0.2$  ml.

Changes in the equivalent parallel circuit parameters *vs* bubble volume for several selected experiments are shown in Figures 25 - 28. In each of the figures,  $R_s$  increased with bubble volume in any given experiment while  $C_s$  decreased. However, in Figures 25 and 26, the increases in  $R_s$ , and the corresponding decreases in  $C_s$ , for given bubble volumes clearly increased with the number of bubbles. These results typify those indicating that bubble-induced spectral changes are governed by gas-liquid surface area. Importantly, simple bubble-induced material exclusion cannot account for such behavior. On the other hand, such behavior was not always observed. Bubble formation and growth in the experiments illustrated in Figures 27 and 28 caused changes in  $R_s$  and  $C_s$  that were dependent only on bubble volume and not on bubble number density.

#### 4.0 EIS BUBBLE DETECTION In Vivo.

With the essential features of a bubble dielectric signature defined from results of the *in vitro* experiments, the EIS technology was transitioned to *in vivo* applications in order to determine whether bubble-induced changes occur in the impedance spectra of living tissue and whether such changes are similar to those observed in the simpler gelatine and agar preparations.

##### 4.1 Hyperbaric Decompression; Goats

A series of experiments was undertaken to obtain concurrent EIS and Doppler indices of bubble formation in decompressed goats for comparison of the sensitivities of the two bubble detection methods. These experiments were attempted because Doppler ultrasonic measures of bubble presence and profusion in the central venous circulations of decompressed goats are readily obtained. Because of certain technical difficulties, however, results of these experiments were disappointing.

Each experiment involved a single goat which was transported in a cage the morning of the experiment from the Duke University DLAR (Division of Laboratory Animal Resources) research farm to F-Chamber of the F.G. Hall Hypo-Hyperbaric Center. Sites on the hindlimbs for placement of six noninvasive tetrapolar impedance electrodes (3M Corporation, Red Dot ECG Monitoring Electrodes; type Ag/AgCl) were prepared by clipping surface hair, scrubbing with soap and shaving with a disposable razor. Under a liberal BETADINE (Povidone-Iodine) wash, the skin at each site was lightly abraded using the abrasive pad supplied with each electrode. After the sites were dried, the electrodes were positioned and secured with BLENDERM tape, and then connected to shielded cables that penetrated via a through-hull connector from the EIS system located immediately outside the chamber. An area on the right precordium was similarly washed, cleared of surface hair and disinfected with



BETADINE wash for later noninvasive application of a transcutaneous Doppler ultrasonic transducer for ultrasonic detection of central venous bubbles.

All personnel then cleared the chamber and the goat was dived on a schedule adopted from the USN Standard Air Decompression Table for exceptional exposures. The dive profile consisted of a 60 f/min descent to a 20 min stage at 220 fsw (feet seawater), followed by 60 f/min decompressions with stops of 1, 3, 11 and 24 min duration at 40, 30, 20 and 10 fsw, respectively. Smith and Stayton (1978) previously showed that this dive profile produces profusions of central venous bubbles in goats soon after arrival at the 40 fsw stop and thereafter, with only moderate risk of DCS.

During the decompression, the goat was continually monitored for signs of Decompression Sickness and for bubbles in the electrically instrumented hindlimb using the EIS system. Monitoring for DCS signs was via closed-circuit television during the initial decompression from 220 to 40 fsw, when the goat was unaccompanied by any investigative personnel. Immediately upon reaching the 40 fsw stop, an investigator locked-in from an adjacent chamber to monitor the precordium for central venous bubbles at 5-10 min intervals using Doppler ultrasound. Subsequent monitoring for DCS signs was by direct observation.

At the conclusion of the experiment, all external instrumentation was removed and the goat was returned to the DLAR research farm.

A single goat completed a total of four dives on this protocol with a minimum of 6 days between successive dives. Doppler bubbles of grade 4 were observed during each of the decompressions with no observable signs of DCS. However, the EIS results were equivocal because impedance spectra of the hindlimb or any segment thereof could not be reliably measured. It was determined that the problem was related to some sort of anomaly in the current conduction path through the goat hindlimb, but despite attempting a variety of electrode placement schemes, the problem could not be solved. The experimental series was consequently abandoned.

#### 4.2 Methodological Specificity: Bubbles vs. Physiological Fluid Shifts

Concurrent with the above abortive experiments with goats, the EIS system was tested on human subjects to further establish its safety and illuminate whether processes in living tissue other than bubble formation might mimic bubble dielectric signatures. Impedance spectra of the left calf and thigh on each of four human subjects were taken at 5 min intervals during three successive periods: a) seated control (0.5 h); b) 6° Head-down tilt bed rest [HDT] (1.5 h), and; c) seated recovery (1 h). The equivalent parallel circuit schematized in Figure 7. (Eq. 6.b) was fit to each measured spectrum. "Strip chart" renditions of the resultant equivalent circuit parameters showing the time-courses of observed parametric changes are presented in Appendices C.3-C.5. As evident in the latter figures and summarized in Table IV, systematic, reproducible and reversible changes in the dielectric properties of the monitored body segments occurred in response to changes in orthostatic stress -- absent any decompression with risk of *in vivo* bubble formation. These results have important implications for uses of EIS in applications other than bubble detection. Although these are beyond the scope of this report, they are discussed in some detail in Appendices C.3 - C.6.

Table IV. Comparison of Fluid Shift-Induced and Bubble-Induced Equivalent Circuit Parameter Changes

Effector	Observed Change in Equivalent Parallel Circuit Parameter <sup>*</sup>			
	$R_p$	$R_s$	$C_s$	$\alpha$
Seated → HDT (calf & thigh)	↑	↓	↑	
HDT → Seated (calf & thigh)	↓	↑	↓	
Bubble Formation, Growth	↑(?)	↑	↓	
Bubble Resolution	↓(?)	↓	↑	

<sup>\*</sup> Equivalent parallel circuit in Figure 7, Eq. (6.b):  
 ↓ indicates decrease in parameter;  
 ↑ indicates increase in parameter.

More pertinently, the table also includes parametric changes for the same equivalent circuit that are characteristic of bubble formation and resolution in gelatine and agar preparations. Changing body position from seated to HDT produced impedance spectral changes in both the calf and thigh similar to those characteristic of bubble resolution in these preparations. Similarly, changing body position from HDT to seated produced spectral changes reminiscent of those characteristic of bubble formation and growth. The behavior of the  $R_p$  parameter emerged as the only means by which bubble-related effects could be distinguished from orthostatically-induced fluid shift effects.

As discussed in Section 3.2, the  $R_p$  parameter tends to increase with bubble formation and growth and decrease with bubble resolution. But because these changes were not statistically significant, this parameter is only a poor discriminator for bubble formation or resolution. The specificity of EIS bubble detection may therefore be compromised by its susceptibility to the influence of extraneous factors.

#### 4.3 Methodological Enhancement: Concurrent Impedance Plethysmographic Measures of Blood Flow and Hemodynamics

Questions about the specificity of EIS indices of bubble formation and growth *in vivo* motivated consideration of additional measurements that could be made with the same instrumentation that could potentiate the specificity of the EIS indices. Another potential means to anticipate DCS onset may be afforded by the detection of regional hemodynamic impairment that is thought to arise

from direct occlusion of the vasculature by intravascular bubbles or from vascular deformation by extravascular bubbles [2,4,11,26,34,43]. These hemodynamic effects are exacerbated by biophysical processes at the bubble-tissue interfaces, particularly if the bubbles are intravascular [26,34]. Almost immediately on appearance in tissue, gas bubbles adsorb proteins and other surface active materials from the vicinal liquid. As a result of the initially high surface tension of the bubble-tissue interfaces, the adsorbed proteins denature and become antigenic, activating the normal clotting mechanisms in blood. It has been proposed that the resulting rheologic impairment leads to ischemia and, in turn, to the symptoms and signs of DCS [11,43]. Even absent ischemia, however, rheologic impairment can adversely impact the perfusion-limited elimination of excess dissolved gas from a gas-supersaturated tissue. Such impairment serves only to increase the persistence of the local gas-supersaturated condition and increase the likelihood of bubble formation. Bubble formation and its rheological effects consequently become critical elements of a positive feed-back loop, the action of which can lead to development of DCS under conditions less severe than might be required if either or both elements acted only alone or independently. If such incidental rheological impairment remains subsymptomatic, its repetitive occurrence may cause cumulative tissue damage that can eventually culminate in longer-term neuropathology or aseptic necrosis of the juxta-articular regions of the long bones.

Decompressed dogs and sheep have been shown to develop disseminated intravascular coagulation after extremely severe decompressions, but such a systemic response was not evident after less severe decompressions [4]. In the latter cases, however, it is likely that coagulation, blood sludging and microcirculatory impairment occur in localized vascular beds without effect at the systemic level. This likelihood is supported indirectly by evidence in experimental animals and man that the susceptibility of complement activation by bubbles in different individuals, as determined using an *in vitro* assay, correlates with the DCS susceptibility of the individuals in a given decompression profile: Individuals with bubble-sensitive complement have higher DCS susceptibilities than individuals with bubble-insensitive complement [42]. The occurrence of localized vascular occlusion in DCS has been experimentally difficult to observe because methods sufficiently convenient for extensive application in the decompression environment have not been available to monitor decompression-induced changes in local hemodynamics. However, technology to achieve these ends was available in the present program.

Accordingly, the experimental objectives were expanded to include examination of the issue of whether the utility of EIS bubble detection might be enhanced by concurrent Impedance Plethysmographic measurements of segmental blood flow and hemodynamics.

#### 4.4 Hypobaric Decompression; Rats

The inability to obtain useful EIS data from goats forced the adoption of a different experimental model. Rats were chosen because of their ready availability and low cost and because earlier workers had established that useful Impedance Plethysmographic data could be obtained noninvasively from the rat tail [3].

#### 4.4.1 Materials and Methods

##### 4.4.1.1 Decompression Apparatus

The experimental apparatus is schematized in Figure 29. Rats were decompressed in a transparent plexiglass chamber that afforded ready visual observation of DCS signs. The chamber contained 36 gas-filled stainless steel cylinders to decrease the chamber working volume to 39 L. These also provided a thermal buffer to the temperature changes that were caused by chamber decompression and compression. The chamber was connected in parallel with a direct-drive rotary vane vacuum pump (Edwards High Vacuum, Crawley, England; Model EDM 2) and a 117 L vacuum accumulator that was fully evacuated prior to each run. The experimental chamber could be decompressed directly into the accumulator to achieve rapid decompression rates. The vacuum pump provided continuous evacuation of the chamber, allowing either air or 100%  $O_2$  to be vented into the chamber at measured rates to control chamber atmosphere. A vacuum regulator (Matheson Co., Model 3491) positioned between the vacuum pump and the experimental chamber admitted and controlled a second continuous flow of air to the pump as was required to maintain the vented chamber at the desired pressure. Chamber pressure was monitored using a Bourdon pressure gauge (Weksler Instruments) and was controlled to within  $\pm 5$  mmHg of the desired pressure throughout the course of each run. Chamber temperature was monitored using an in-chamber thermistor connected to an external tele-thermometer, and was found to vary by no more than  $\pm 1.0^\circ\text{C}$  throughout any run.

EIS and IPG measurements of the tail were made using a tetrapolar electrode configuration to minimize electrode impedance effects on measured voltages. Each of the four electrodes consisted of a copper plate rounded to accommodate the circumference of the tail. These were mounted in a flexible harness that facilitated electrode placement and immobilization on the tail. The distance between the inner edges of the drive electrodes was 4.45 cm. Two pickup electrodes, with inner edges separated by 1.45 cm, were centered between the drive electrodes.

##### 4.4.1.2 Impedance Plethysmographic (IPG) System

Impedance Plethysmographic monitoring of segmental blood flow and hemodynamics requires measuring the segmental impedance to an excitation current of fixed frequency at a rate high compared to the heart rate (Appendix B.). IPG monitoring in rats, with heart rates of about 250 bpm, consequently requires impedance sampling rates greater than about 200 Hz. Because hardware and firmware limitations prevented the achievement of such sampling rates using the Solartron Analyzer, a BioImpedance Analyzer (BoMed Medical Manufacturing, Ltd., Irvine, CA) was used to make the required measurements. The latter was a single channel instrument that operated using a 0.1 mA, 50 KHz excitation current and provided continuous analog output signals for the measured impedances. A Corbin Farnsworth Inc., Model LGDD Cardiac Monitor that also provided continuous analog output was used to measure a 3-lead EKG. Because the VAXstation lacked analog-to-digital (A/D) conversion capability and a programmable high resolution real-time clock, a Digital Equipment Corp. MINC

11/23 with these features was used to sample, A/D convert and store the BoMed and EKG outputs at a rate of 1000 Hz. At the end of a given sampling period, digitized data were transferred in binary form via the GPIB to the VAXstation for analysis and final storage. These processes were controlled at the VAXstation terminal through the operation of software modules written for this application. The VAXstation module effected communications and control of the MINC data acquisition front end through the GPIB. Its operation was coordinated and linked to the run-time EIS system, EISSYS. IPG data acquisition and uploading could be automatically invoked when the EIS system was idle simply by clicking the VAXstation mouse with the screen cursor positioned in a control window that was open on the VAXstation screen only during EIS-idle periods.

#### 4.4.1.3 Experimental Protocol

Thirty-nine runs were made, each using one adult male Sprague-Dawley rat (Charles River Breeding Lab). In each run, the rat was first anesthetized by intraperitoneal injection of Nembutal (50 mmg/Kg). The chest and abdominal regions were then shaved and electrodes were placed for a 3-lead EKG. After the tail was degreased with alcohol, the surfaces of the four electrodes in the tail harness were wetted with conductive paste and the harness was positioned on the tail and secured in place with adhesive tape. The rat was then placed inside the altitude chamber and the electrical connections to the chamber through-hull cable were completed.

After chamber closure, the rat was exposed to a pressure profile consisting of three consecutive 30-min stages: a) ground-level control; b) altitude, and; c) ground-level recovery. The altitude stage consisted of exposure to one of four different pressures: 1) ambient atmospheric pressure (no decompression); 2) 560 mmHg; 3) 360 mmHg, and; 4) 260 mmHg. The chamber was ventilated with air during the ground-level stages to prevent CO<sub>2</sub> accumulation. Commencing at 1 min before the altitude stage, the chamber was ventilated with 100% O<sub>2</sub> at 20L min<sup>-1</sup>. The chamber was then decompressed to the desired altitude within 30 s. Chamber ventilation with 100% O<sub>2</sub> was continued at 5L min<sup>-1</sup> throughout the ensuing altitude stage to prevent hypoxia.

The impedance pulse waveform and EKG were recorded for 2-4 sec periods at 6 min intervals throughout the entire pressure profile. Immediately after each of these periods, the external cable connections were switched and the impedance spectrum of the tail was measured. The impedance pulse waveform and EKG were also measured immediately before descent to ground-level. The rat was monitored continuously for observable DCS signs. DCS was judged to have occurred with exhibition of respiratory distress, convulsions or death.

#### 4.4.1.4 Data Analysis

Measured electrical impedance spectra of the tail were analyzed using the equivalent parallel circuit model in Figure 7 as detailed in Section 2.2.2.2. The nomenclature for the circuit parameter values was changed so that  $R_1 = R_s$ ,  $C_m = C_s$  and  $R_e = R_p$ .

The impedance plethysmographic and EKG data were first smoothed using an

11-point moving quadratic convolute. Figure 30 shows a typical 1 sec epoch of smoothed impedance plethysmographic data from a rat tail. The upper trace is the impedance pulse waveform, which reflects the pulsatile volume changes in the monitored segment that were caused by the passage of blood from each cardiac pulse. The middle trace is the time derivative of the pulse waveform, and the bottom trace is the EKG, in which only the QRS complexes were of interest. These waveforms and the EKG were then analyzed on a pulse-by-pulse basis to obtain heart rate, tail blood flow and other hemodynamic indices. This was accomplished using an interactive software package that provided a graphic user-data interface through which the user selected and specified certain landmarks in each pulse waveform by positioning and clicking a mouse-driven cursor. After specification of the required landmarks in each pulse, the desired parameters were automatically calculated from the times, differential resistances and basal resistances at the landmarks as outlined in Appendix B. Finally, the value of each parameter at each elapsed time was taken as its mean over 6 pulses selected from the 2-4 sec epoch recorded at that time.

The value of each EIS and IPG parameter at each point throughout the run for a given rat was first normalized with respect to the first value of the parameter obtained in the run, and then expressed as a percentage of that first value. The time series of the parameteric data for all of the subjects were then separated into two groups; DCS and no-DCS; regardless of the decompression profile. The mean percent changes for every parameter obtained at the different elapsed times were compared between the two outcome groups using repeated measures ANOVA.

#### 4.4.2 Results and Discussion

The outcomes of the runs are summarized in Table V. Respiratory distress, presenting as tachypnea or labored, long inspirations followed by transient apnea, was the earliest and most common sign of DCS. The mean onset time of DCS was 6 min, ranging from 1 to 13 min.

TABLE V. Experimental Outcomes: Rat Decompressions

-- DCS Incidence --			
Profile	# DCS <sup>a</sup>	# No-DCS	Total
$\Delta P = 0$ mm-Hg	-	10	10
$\Delta P = 200$ mm-Hg	-	8	8
$\Delta P = 400$ mm-Hg	8 <sup>b</sup>	2	10
$\Delta P = 500$ mm-Hg	11 <sup>b</sup>	-	11
Total	19	20	39

<sup>a</sup> Obvious respiratory distress

<sup>b</sup> Respiratory distress proceeded to convulsions in 2 rats and to death in 3 others.

Figure 31 summarizes the EIS equivalent circuit parameter changes that were observed in the DCS group rats throughout the runs. Grouped mean percent parameter values from each of the successive impedance spectra in the runs are drawn in "strip chart" form with the means arranged on the ordinate versus the corresponding run sequence numbers on the abscissa. The mean onset time for DCS is indicated by the arrow on the abscissa. While at altitude, both of the resistance parameters,  $R_e$  and  $R_i$ , increased, while the capacitance  $C_m$  decreased. Note that these changes commenced before the mean onset of DCS and that, with the exception of the changes in the  $R_e$  parameter, they were reversed by recompression. This pattern is strikingly similar to that observed with decompression-induced bubble formation in certain gelatin preparations.

The upper illustration in Figure 32 typifies the effect of decompression and bubble formation on the  $R_i$  parameter in gelatin. The format is similar to that of Figure 31. Progressive increases in  $R_i$  were associated with bubble formation and growth. The lower illustration in the figure shows the grouped mean results from the DCS group rats in this study. Rats with DCS clearly exhibited changes in this parameter that were similar to those exhibited with bubble formation in gelatin.

These changes in  $R_i$  were different from those observed in the no-DCS group. Figure 33 shows the mean percent changes in the  $R_i$  parameter for the DCS group compared to those for the no-DCS group. There was no significant difference in this parameter between the two groups before decompression, but it increased in the DCS group to values significantly larger than those in the no-DCS group after decompression. Importantly, the changes emerged as significant before the mean onset of DCS. Thus, the no-DCS group failed to exhibit this element of the bubble dielectric signature that was evident in the DCS group.

Results shown in Figure 34 illustrate that a similar correspondence between bubble formation in gelatin and DCS in rats occurred for the capacitance parameter. The upper panel shows the effect of decompression and bubble formation on the capacitance parameter of gelatin. Bubble formation and growth caused the capacitance to decrease. As shown in the lower panel, this parameter also decreased in the rat tail with decompression and DCS. Recompression prevented further decreases in this parameter, but did not cause it to increase to its pre-decompression value.

As with the  $R_i$  parameter, these changes in the equivalent capacitance were also different from those observed in the no-DCS group. Figure 35 shows the time course of the changes in the  $C_m$  parameter in both groups. Again, there was no significant difference between the two groups before decompression, but the capacitance parameter decreased in the DCS group to values significantly lower than those in the no-DCS group after decompression. The no-DCS group consequently also failed to exhibit this second element of the bubble dielectric signature that was evident in the DCS group. -

The  $R_e$  parameter (Figure 36) tended to increase during the altitude stage regardless of DCS outcome and did not significantly differ between the DCS and no-DCS groups at any point during the runs.

Summarizing to this point, then, a bubble dielectric signature, indicating the presence of bubbles, was observed in the tails of decompressed rats that developed DCS. Such a signature was not observed in rats that did not develop DCS. The IPG results provided additional amplification of these EIS bubble detection results.

Figure 37 shows the time courses of changes in the calculated tail blood flows in the DCS and no-DCS groups. In the DCS group, tail blood flow showed a large decrease immediately on decompression and continued to decrease more slowly thereafter. The maximum mean percent decrease in blood flow was  $32 \pm 6\%$ . These blood flow decreases were reversed by recompression. In contrast, tail blood flow either remained unchanged or increased in the no-DCS group during the altitude stages. Importantly, the blood flow in the DCS group tended to start recovering in the middle of the decompression stage. This finding suggests that a vascular autoregulatory reflex was evoked to prevent further hemodynamic impairment caused by bubbles' mechanical obstruction.

As shown in Figure 38, the heart rate in both groups increased immediately after decompression. In the DCS group, however, the heart rate then soon began a decrease that continued throughout the remaining period at altitude, finally reaching a mean value  $21 \pm 7\%$  lower than that preceding decompression. This decrease was reversed by recompression. Note that the decreased tail blood flow preceded the onset of DCS, but bradycardia occurred only after DCS appeared.

Segmental arterial filling during systole precedes and is more rapid than venous runoff during diastole. Thus, as shown in Figure 39, each impedance pulse can be resolved into two portions: a period of excess arterial filling ( $T_i$ ) defined as that period of the pulse preceding the dicrotic notch, and a period of excess venous outflow ( $T_o$ ) defined as the period of the pulse following the dicrotic notch. The time courses of changes in the excess venous outflow time between the DCS and no-DCS groups are shown in Figure 40.



After decompression, the period of excess outflow increased throughout the decompression stage in the DCS group, but remained unchanged in the no-DCS group. The results strongly indicated that venous outflow was seriously obstructed in the DCS group but not in the no-DCS group. In contrast, there was no significant difference in the excess arterial inflow time between the DCS and no-DCS groups (Figure 41). Thus, decompression-induced intrasegmental hemodynamic changes were confined to the venous circulation, as would be expected if bubbles occurred primarily in the venous circulation.

Decompression effects on the systemic arterial circulation are evident in changes in the pulse transit time, which is a measure of the time interval between the QRS complex of the EKG and the beginning point of the ensuing segmental impedance pulse. The pulse transit time increases when the arterial vascular compliance between the heart and the monitored segment increases. Figure 42 illustrates that the pulse transit time during the altitude stage increased significantly in the DCS group but decreased only insignificantly in the no-DCS group. Results consequently indicate that systemic arterial compliance was increased. Coupled with the observed decreases in heart rate and tail blood flow, this result is consistent with a decreased systemic arterial volume arising from decreased venous return and cardiac output.

The observed temporal relationships between the various events illuminated by these measurements offers some insight into the pathophysiological mechanism of DCS. Decreases in peripheral blood flow concurrent with the appearance of a bubble dielectric signature occurred before DCS onset. This finding is consistent with the hypothesis that peripheral circulatory impairment occurs in asymptomatic decompressions and that DCS occurs only as such impairment becomes more severe. Bradycardia occurred only after DCS onset. With further impairment, central cardiovascular function is then affected.

## 5.0 SUMMARY and CONCLUSIONS

A computer-driven Electrical Impedance Spectroscopic (EIS) system suitable for use in both *in vitro* and *in vivo* applications was developed and successfully used in a series of *in vitro* model system studies to show that gas bubble formation and growth can cause detectable changes in the impedance spectra of liquids depending on their composition. The presence of surface active agents was found to be the most important governor of these changes. This result supported the original hypothesis that bubble-induced impedance spectral changes ought to occur and arise not from the presence of bubbles *per se*, but from effects of the bubbles on the composition and structure of the liquid in the immediate vicinities of the gas-liquid interfaces. Semi-quantitative characterization of these changes enabled the essential features of a bubble "dielectric signature" to be defined as they varied with bubble number density and size in given preparations. These features were embodied in the fashion by which the impedance spectrum changed during the course of bubble formation, growth and resolution: No bubble-induced spectral features were observed that would enable detection of bubble presence or profusion on the basis of only a single spectrum. It followed from the dependence of this signature on the liquid composition that any "calibration" of the signature would be sample specific and not generally applicable to computations of bubble numbers and sizes from measured data for nonspecific liquids or tissues.

A series of experiments was undertaken but failed to obtain concurrent EIS and Doppler ultrasonic indices of bubble formation in decompressed goats for comparison of the sensitivities of the two methods. This occurred due to technical difficulties that were encountered in establishing a proper EIS excitation current path through the goat hindlimb, not from problems intrinsic to the method. Impedance spectra of select body segments of human volunteers were successfully obtained under various experimental conditions, demonstrating the safety of Electrical Impedance Spectroscopy in application to human subjects. Orthostatically-induced shifts of fluid in the absence of any decompression and bubble formation were found to mimic the most important features of the bubble-induced effects observed in *in vitro* preparations. Evidence was obtained indicating that these orthostatically-induced spectral changes were caused by fluid shifts between the intra- and extracellular compartments of the monitored tissues, illustrating that EIS may have important applications in contexts other than bubble detection.

Questions about the specificity of EIS bubble detection that emerged from the above results were addressed in a series of experiments in which rats were decompressed to simulated altitudes. Measured EIS indices of bubble formation and growth were augmented by Impedance Plethysmographic measures of secondary bubble effects on blood flow and various hemodynamic parameters. Bubble dielectric signatures similar to those characterized in certain gelatine and agar preparations that contained surface active additives were observed in the tails of decompressed rats that developed DCS, but not in rats that failed to develop DCS. Hemodynamic changes obtained by concurrent Impedance Plethysmographic monitoring paralleled the EIS results: Blood flow and hemodynamic changes in the tails of rats that developed DCS were different from and/or more severe than those observed in rats that failed to develop DCS.

In conclusion, the pre-symptomatic course of DCS includes bubble

formation, growth of the bubbles to pain-inducing threshold size and/or the development of impaired circulation from either direct mechanical or secondary hematological effects of the bubbles. EIS monitoring of select body segments for decompression-induced bubble formation and growth with concurrent IPG monitoring for hemodynamic changes was shown able to track the course of these putative etiologic processes of DCS in decompressed rats both before and after the processes proceeded to development of DCS signs. By necessity, however, these exposures were severe and it remains to be determined whether these techniques are sufficiently sensitive to provide noninvasive, premonitory and objective indices of DCS in decompressed man.

6.0 REFERENCES

1. Ackmann, J.J. and Seitz, M.A. Methods of complex impedance measurements in biologic tissue. CRC Critical Reviews in Biomedical Engineering. 11: 281-311, 1984.
2. Barnard, E.E.P., J.M. Hanson, M.A. Rowton-Lee, A.G. Morgan, A. Polak and D.R. Tidy. Post-decompression shock due to extravasation of plasma. Brit. Med. J., 2:154-155, 1966.
3. Berry, J.J., L.D. Montgomery, and B.A. Williams. Thermoregulatory responses of rats to varying environmental temperatures. Aviat. Space Environ. Med. 55:546-549, 1984.
4. Bove, A.A., J.M. Hallenbeck, and D.H. Elliott. Circulatory responses to venous air embolism and decompression sickness in dogs. Undersea Biomed. Res., 1(3):207-220, 1974.
5. Cole, K.S. Electric impedance of suspensions of spheres. J. Gen. Physiol. 12:29-36, 1929.
6. Cole, K.S. and R.H. Cole. Dispersion and absorption in dielectrics. I. Alternating current characteristics. J. Chem. Phys. 9:341-351 (1941).
7. Daniels, S. Ultrasonic monitoring of decompression procedures. Phil. Trans. R. Soc. Lond. B304:153-175 (1984).
8. Fox, F.E. and K.F. Herzfeld. Gas bubbles with organic skins as cavitation nuclei. J. Acoust. Soc. Amer. 26:984-989 (1959).
9. Fricke, H. and H.J. Curtis. The dielectric properties of water-dielectric interphases. J. Phys. Chem. 41:729-745 (1937).
10. Geddes LA, Baker LE. Hazards in the use of low frequencies for the measurement of physiological events by impedance. Med. & Biol. Engng., 7:289-96, 1969.
11. Hallenbeck, J.M. and J.C. Andersen. Pathogenesis of decompression sickness. In: The Physiology and Medicine of Diving and Compressed Air Work. 3rd. ed. (Bennett, P.B., and D.H. Elliott, Eds.) Best Publishing Co., San Pedro, CA. 1982.
12. Hills, B.A. Concepts of inert gas exchange in tissues during decompresssion. In: Underwater Physiology. Vol. IV. (C.J. Lambertsen, Ed.) Academic Press, New York, pp. 115-122 (1971).
13. Jossinet, J., Gardette, B., Fourcade, C. and Matheron, P. An application for bubble detection in living tissue under decompression. Advances in Bioelectrical Impedance Measurements (Technic-Laboratory-Clinic). Second Comptes Rendus International Congress of Bioelectrical Impedance, Lyon, June 16-19, pp. 148-150 (1976).
14. Jossinet, J., Fourcade, C., and Gardette, B. An application of bioelectrical impedance for the detection of tissular bubbles in the diver:

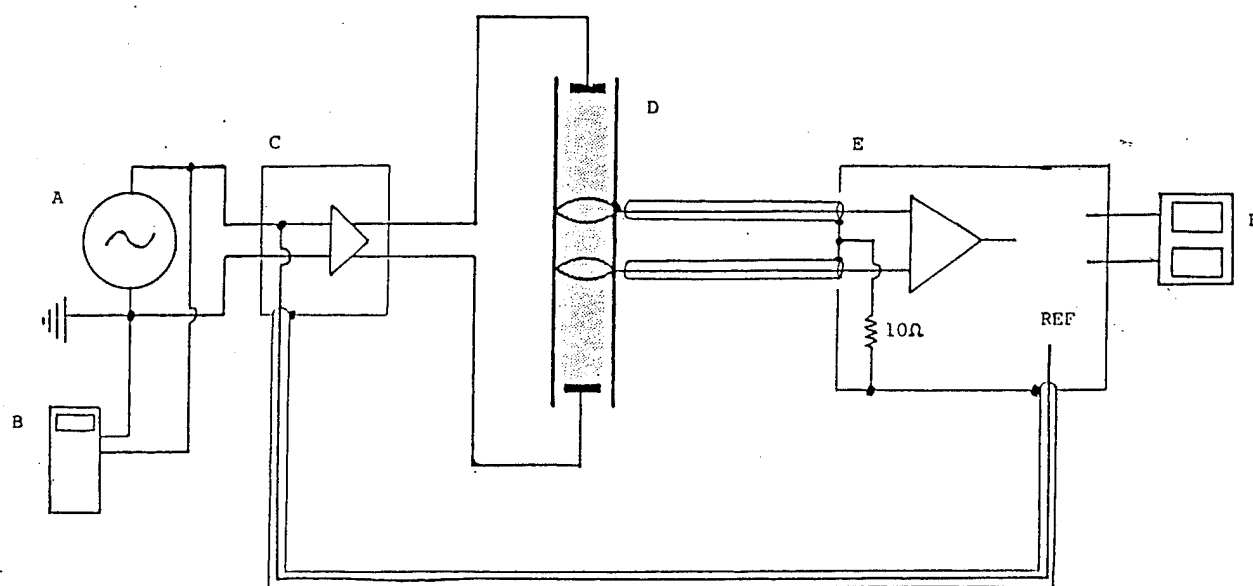
- Preliminary results. *Med. & Biol. Eng. & Comput.*, 19:419-425 (1981).
15. Kabesheva TA, Kopanov SV, Panferova NY, Zavadovskiy AF. Vascular mechanisms of adaptation to antiorthostatic position. *Kosmich. Biol. Aviak. Med.*, 19(2):35-9, 1985.
  16. Kanai, H., Katsuyuki, S. and Haeno, M. Electrical measurement of fluid distribution in human legs: Estimation of extra- and intracellular fluid volume. *J. Microwave Power*. 18:233-243 (1983).
  17. Kubicek, W.G., J.R. Karnegis, R.P. Patterson, D.A. Witose and R.H. Mattson. Development and evaluation of an impedance cardiac output system. *Aerosp. Med.* 37:1208-1212, 1966.
  18. Lofgren, B. The electrical impedance of a complex tissue and its relation to changes in volume and fluid distribution. *Acta Physiol. Scand.* 23, Suppl. 81, 51 pp. (1951).
  19. Maksimov DG, Domracheva MV. Changes in central and peripheral hemodynamics during prolonged antiorthostatic hypokinesia as weightlessness models. *Kosmich. Biol. Aviak. Med.*, 5:52-7, 1976.
  20. Marquardt, D.W. An algorithm for least-squares estimation of nonlinear parameters. *J. Soc. Indust. Appl. Math.* 11: 431-441, 1963.
  21. Maxwell, J.C. A Treatise on Electricity and Magnetism. Vol. I. 3rd ED. Dover Publications, Inc., New York (1954).
  22. Mohapatra, S.N. "Non-Invasive Cardiovascular Monitoring By Electrical Impedance Technique". Pitman Med. Ltd., 1981.
  23. Montgomery LD, Hanish HM, Marker RA. An impedance device for study of multisegmental hemodynamic changes during orthostatic stress. *Aviat. Space Environ. Med.*, 60:116-22, 1989.
  24. Nishi, R.Y. Problem areas in the ultrasonic detection of decompression bubbles. Workshop of early diagnosis of DCS, the 12th Undersea Med. Society Workshop. Toronto. pp.50-68, 1977.
  25. Nyboer, J. Electrical Impedance Plethysmography. Springfield, MA, Charles C. Thomas, 1970.
  26. Philp, R.B. A review of blood changes associated with compression-decompression: relationship to decompression sickness. *Undersea Biomed. Res.*, 1:117-150, 1974.
  27. Rubissow, G.J. and R.S. Mackay. Decompression study and control using ultrasonics. *Aerosp. Med.* 45:473-478, 1974.
  28. Schwan, H.P. Electrical properties of tissue and cell suspensions. In: *Advances in Biological and Medical Physics*. Vol V. (J.H. Lawrence and C.A. Tobias, Eds.) Academic Press, New York, pp. 147-224 (1957).
  29. Schwan, H.P. Alternating current spectroscopy of biological substances.

- Proc. I.R.E., 10:1845-1855 (1959).
30. Schwan, H.P. Alternating current electrode polarization. *Biophysik*. 3: 181-201 (1966).
  31. Shilling, C.W. and M.F. Werts. Physical Methods of Bubble Detection in Blood and Tissues. An Annotated Bibliography with Preliminary Analysis. Undersea Biomedical society Report No. UMS 7-30-77-A. Bethesda MD. 85 pp. 1977.
  32. Shurubura, A.A., Petrash, V.V., Voinov, V.A., and Danilov, E.N. An impedance method of measuring the volume of gas bubbles formed in blood during a fall in atmospheric pressure. *Dokl. Biol. Sci. (Engl. Trans., Dokl. Akad. Nauk. SSSR Ser. Biol.)* 227(1-6):155-158 (1976).
  33. Smith, K.H. and M.P. Spencer. Doppler indices of decompression sickness: their evaluation and use. *Aerosp. Med.* 41:1396-1400, 1970. —
  34. Smith, K.H., P.J. Stegall, L.A. Harker, and T.W. Huang. Hemostatic function changes in the pathogenesis of decompression sickness. *Undersea Biomed. Res.* 1974; 1(1):A21.
  35. Smith, K.H. and L. Stayton. Hyperbaric Decompression by Means of Bubble Detection. Final Report ONR Contract No. N00014 69-C-042. Virginia Mason Research Center, Seattle WA, 1978.
  36. Smyth, C.P. Dielectric Behavior and Structure: Dielectric Constant and Loss, Dipole Moment and Molecular Structure. McGraw-Hill, New York (1955).
  37. Spencer, M.P. and H.F. Clarke. Precordial monitoring of pulmonary gas embolism and decompression bubbles. *Aerosp. Med.* 43: 762-767, 1972.
  38. Spencer, M.P. D.C. Johnson and S.D. Campbell. Safe decompression with the Doppler ultrasonic bubble detector. In: Lambertsen, C.J., Ed. *Underwater Physiology V*. Baltimore: Publication Press, 1976.
  39. Strandness DE, Sumner DS. **Hemodynamics for Surgeons**. New York: Grune and Stratton, pp. 187-96, 1975.
  40. Strauss, R.H. Bubble formation in gelatin: Implications for prevention of decompression sickness. *Undersea Biomed. Res.*, 1:169-179 (1974).
  41. Usochev VV, Shinkarevskaya IP. Functional changes in systemic and regional (intracranial) circulation accompanying low acceleration. *Kosmich. Biol. Aviak. Med.*, 19(1):59-64, 1973.
  42. Ward, C.A., P.K. Weathersby, D. McCullough and W.D. Fraser. Identification of individuals susceptible to decompression sickness. In: 9th International Symposium on Underwater and Hyperbaric Physiology. UHMS, Bethesda, MD. pp. 239-247. 1987.
  43. Wells, C.H., T.P. Bond, M.M. Guest, and C.C. Barnhart. Rheologic impairment of the microcirculation during decompression sickness. *Microvascular Res.*, 3:162-169, 1971.

44. Yarullin KK, Krupina TN, Vasil'yeva TD, Buyvolova NN. Changes in cerebral, pulmonary, and peripheral blood circulation. Kosmich. Biol. Aviak. Med., 6(4):33-9, 1972.
45. Yount, D.E. and R.H. Strauss. Bubble formation in gelatin: A model for decompression sickness. J. Appl. Phys. 47: 5081-5089 (1976).
46. Yount, D.E., T.D. Kunkle, J.S. D'Arrigo, F.W. Ingle, C.M. Yeung and E.L. Beckman. Stabilization of gas cavitation nuclei by surface active compounds. Aviat. Space and Environ. Med. 48; 185-191 (1977).
47. Yount, D.E., C.M. Yeung and F.W. Ingle. Determination of the radii of gas cavitation nuclei by filtering gelatin. J. Acoust. Soc. Amer. 65: 1440-1450 (1979).

7.0 FIGURES

Figure 1:



- A) Signal Generator
- B) Digital Multimeter-Frequency Counter
- C) Constant Current Amplifier
- D) Electrochemical Cell, Gel Cartridge
- E) PAR Model 129A Vector Voltmeter/Lock-In Amplifier
- F) Digital Panel Meters



Figure 2:

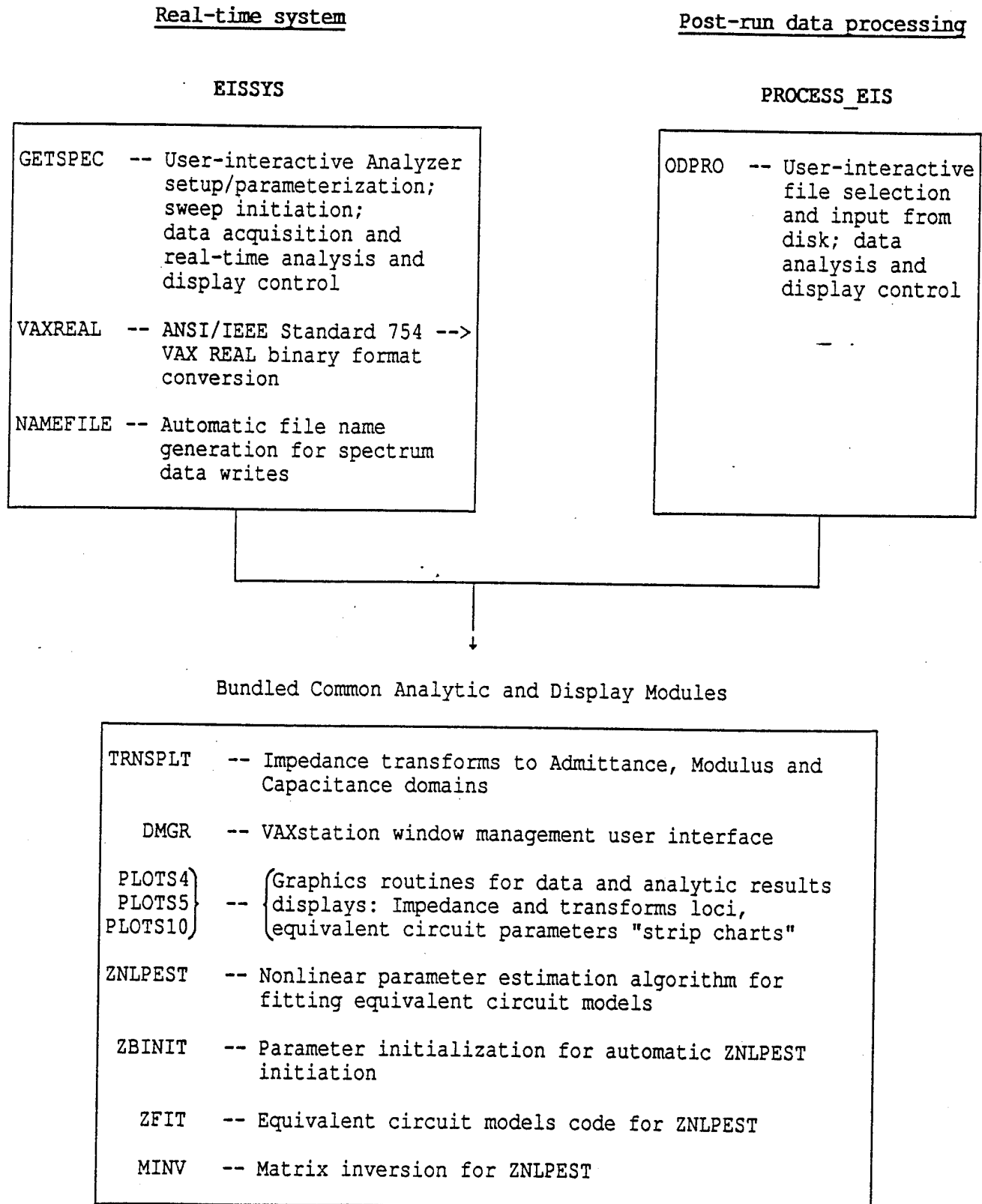


Figure 3:

```

      Electric Impedance Spectroscopic System
    1260 Analyzer and Data Acquisition Control Program
      EIS_SYS
    -----

SCHLUMBERGER TECHNOLOGIES,1260 IMPEDANCE ANALYZER,0,0: ONLINE IN REMOTE MODE.

SWEEP PARAMETERS AND RESET OPTIONS:

  0 - CONTINUE, USING PRESENT SETTINGS:
  1 - Minimum frequency in sweep = 2.500E+03 Hz;
  2 - Maximum frequency in sweep = 1.500E+05 Hz;
  3 - Number of points in sweep = 50;
  4 - Integration time: STATIC, = 1.000E+00 sec;
  5 - Current MONITOR: ON;
  6 - Drive Current: STATIC; Amplitude = .0005 amps (rms);
  7 - NULL facility: OFF;
  9 - EXIT without FRA RESET.

ENTER "0" OR PARAMETER NUMBER TO RESET -->

```

Figure 4:

```

FRA SETUP COMPLETE.

READY TO MEASURE IMPEDANCE SPECTRUM.
OPTIONS:
  0 - CONTINUE;
  1 - Review/Reset SWEEP PARAMETERS;
  2 - Review/Reset DATA OUTPUT and ANALYSIS Settings;
  3 - Set/Commence AUTO-CYCLE Periodic Sweeps;
  4 - STOP

DESIRED OPTION = ?

```

Figure 5:

Data Disposition Settings and RESET Options:

- 0 - CONTINUE
- 1 - ANALYZER CHANNELS PROCESSED; ..... 1 and 2
- 2 - AUTO-WRITE EIS Data to Files; ..... ON
- 3 - AUTO-FIT Equivalent Circuit Model; ..... ON Model 1
- 4 - Fitted EC Parameters presented vs: ELAPSED TIME
- 5 - Record-by-Record Analytic Results WRITES: OFF
- 6 - CLEAR DISPLAYS for RESTART with Next Run.

ENTER "0" OR OPTION NUMBER TO RESET -->

Figure 6:

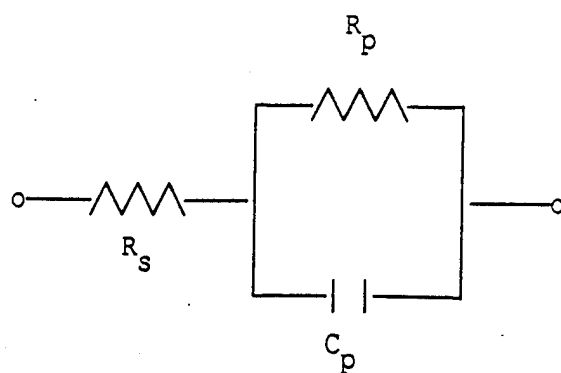
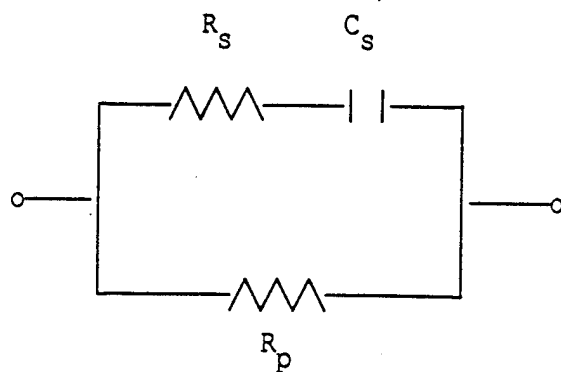


Figure 7:



Note:  $R_p \equiv R_e$   
 $R_s \equiv R_i$   
 $C_s \equiv C_m$

Figure 8:

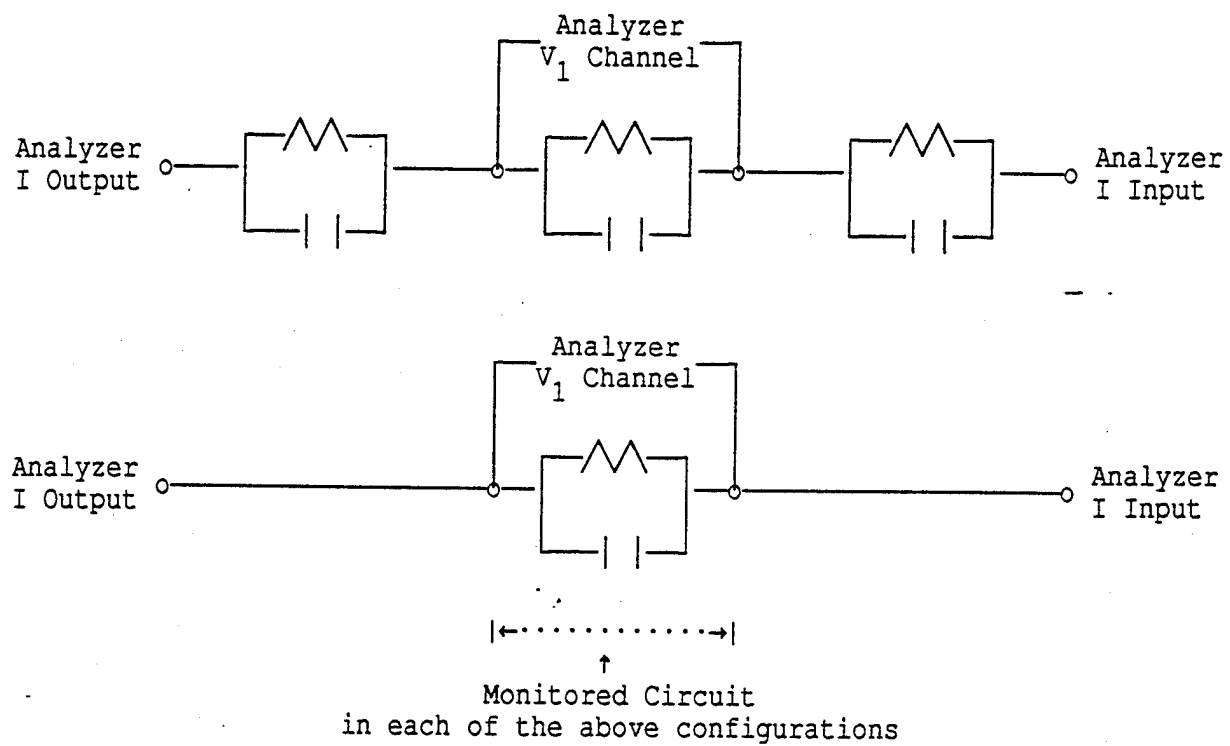


Figure 9:

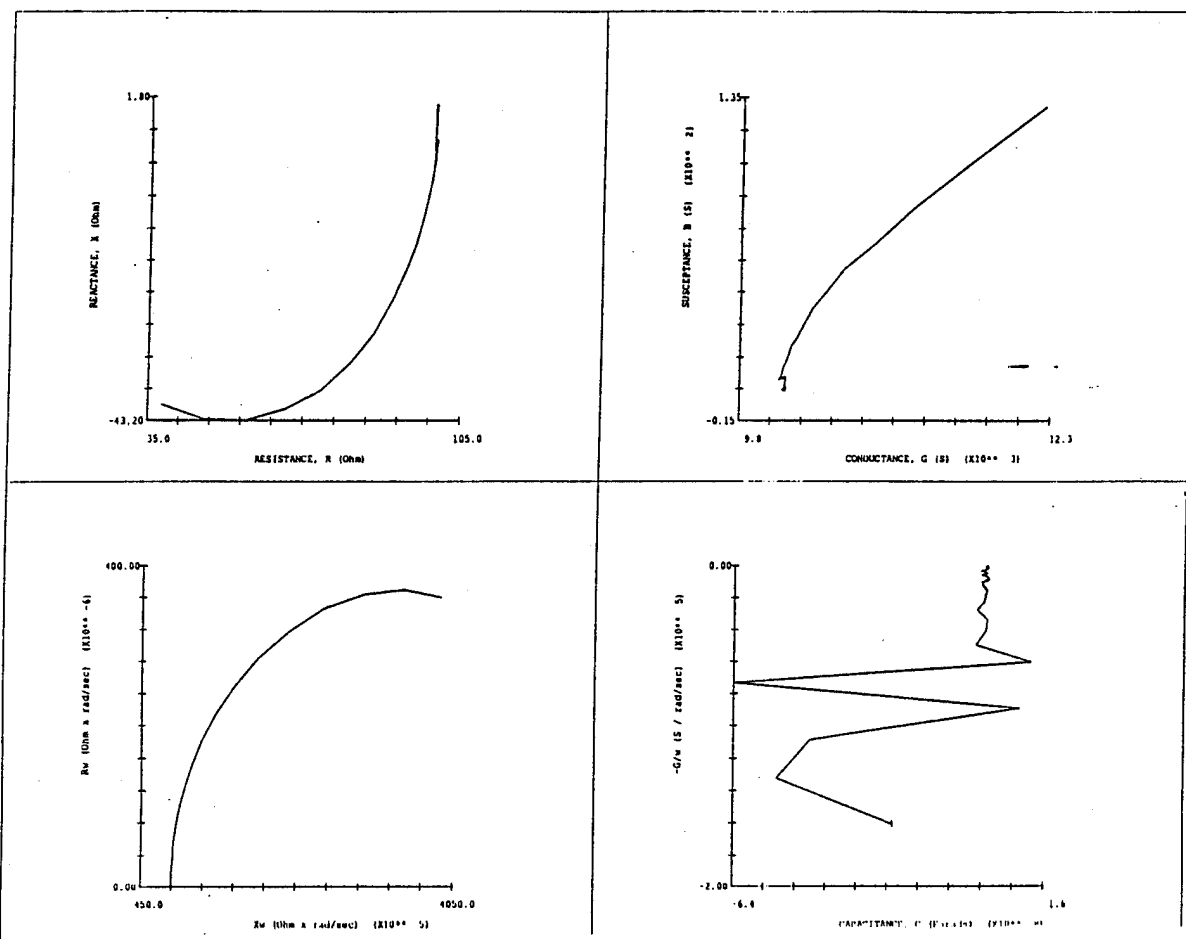


Figure 10:

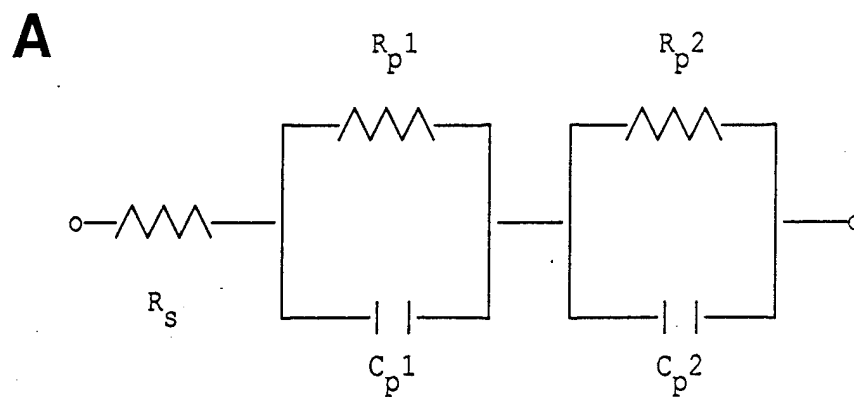
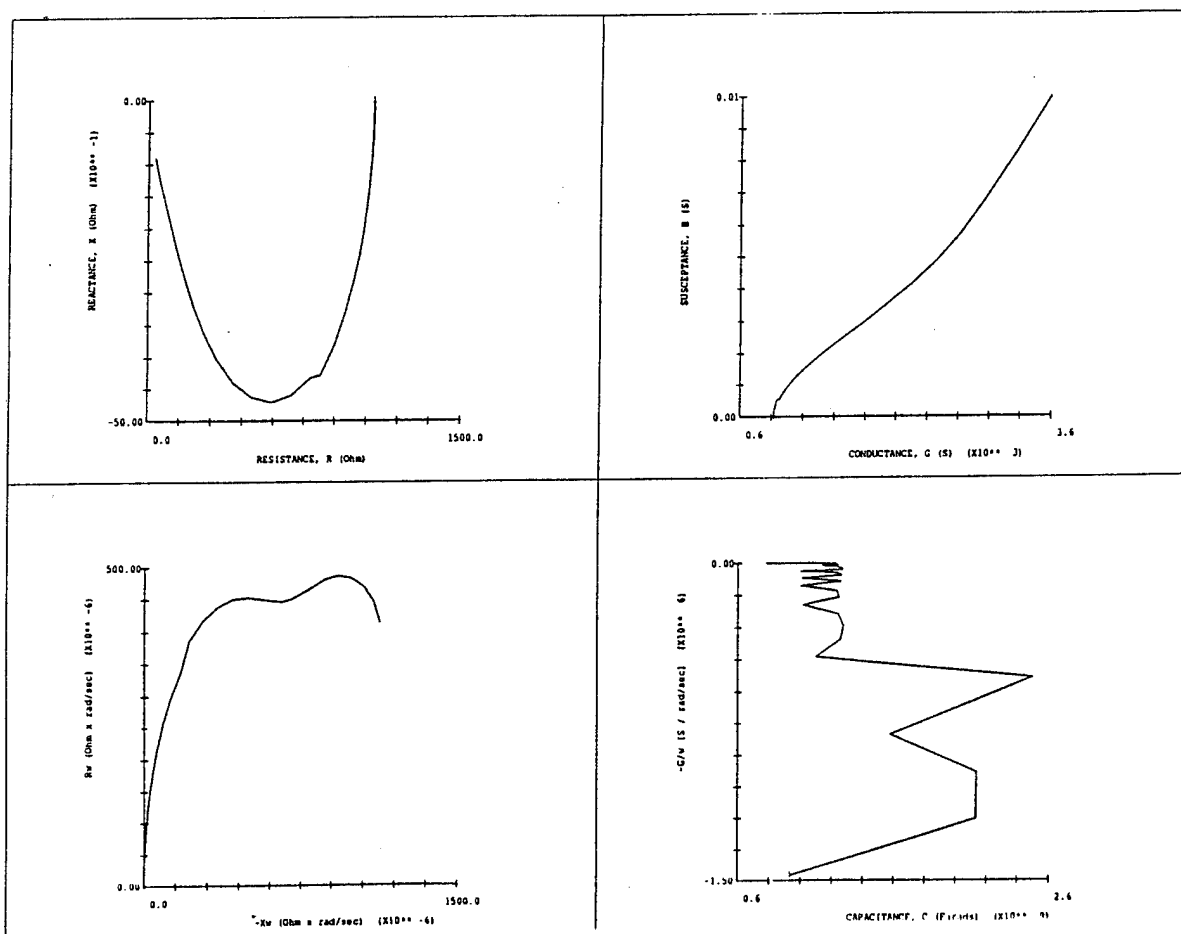
**B**

Figure 11:

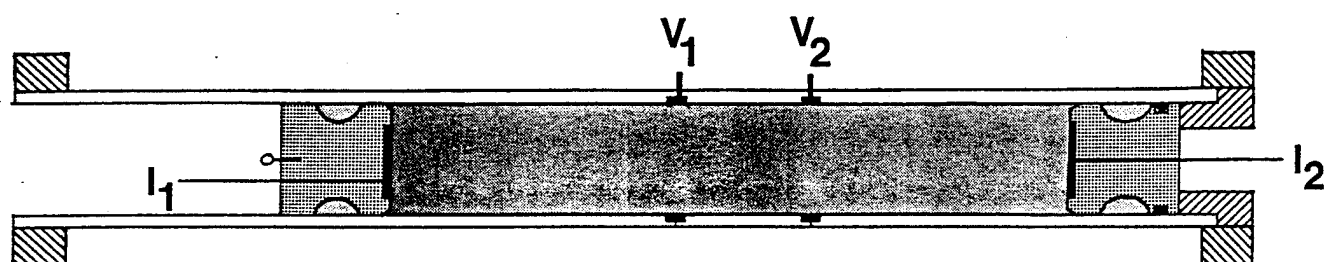




Figure 12:

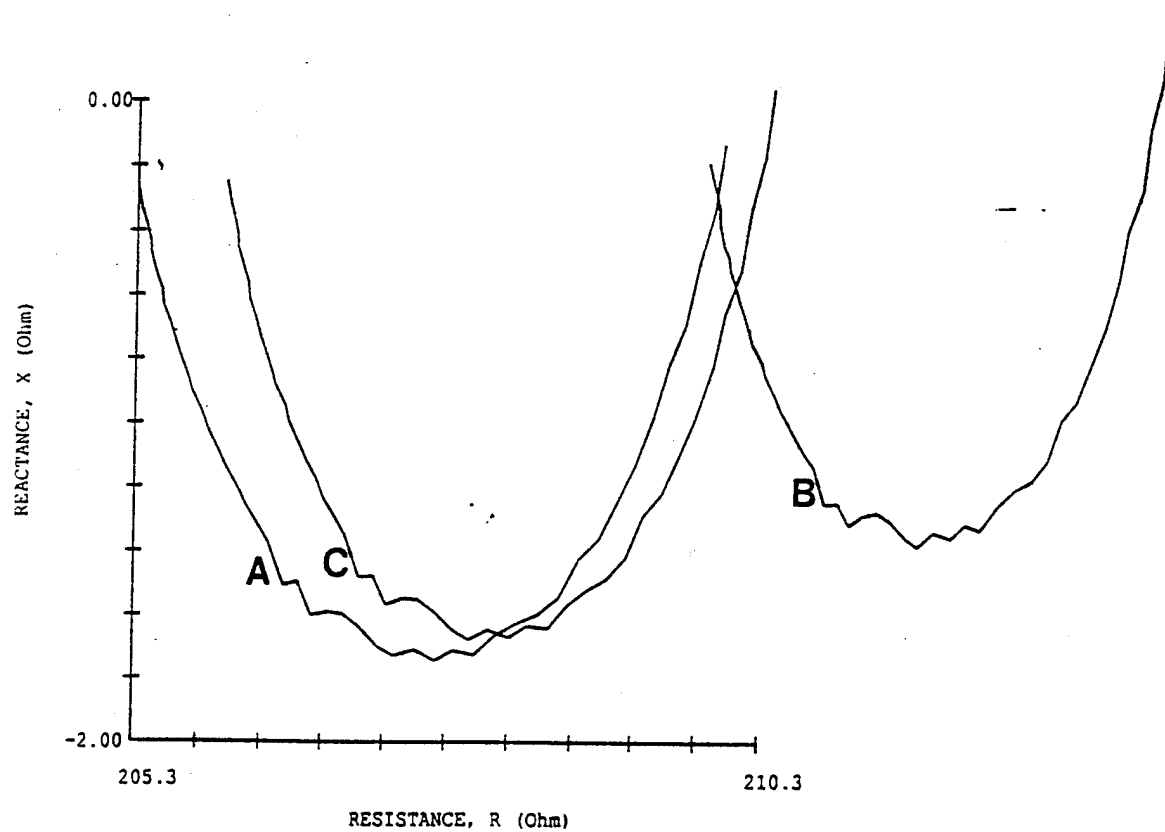


Figure 13:

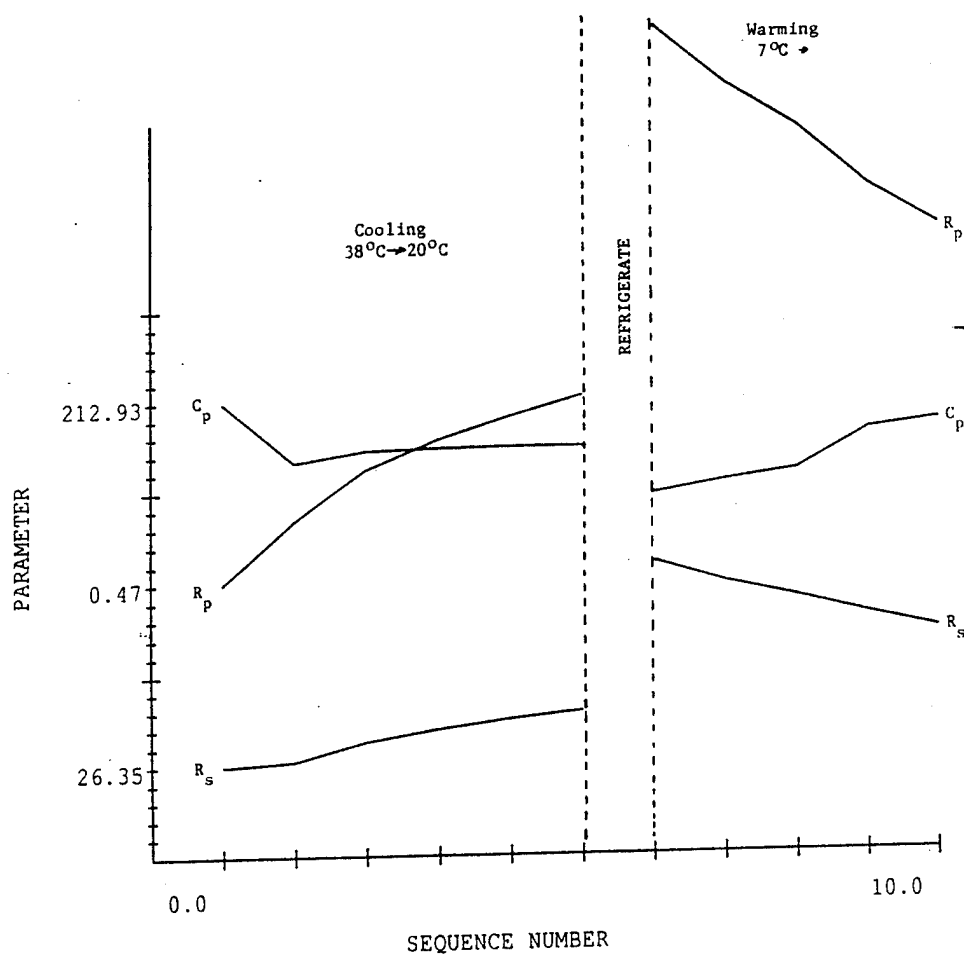


Figure 14:

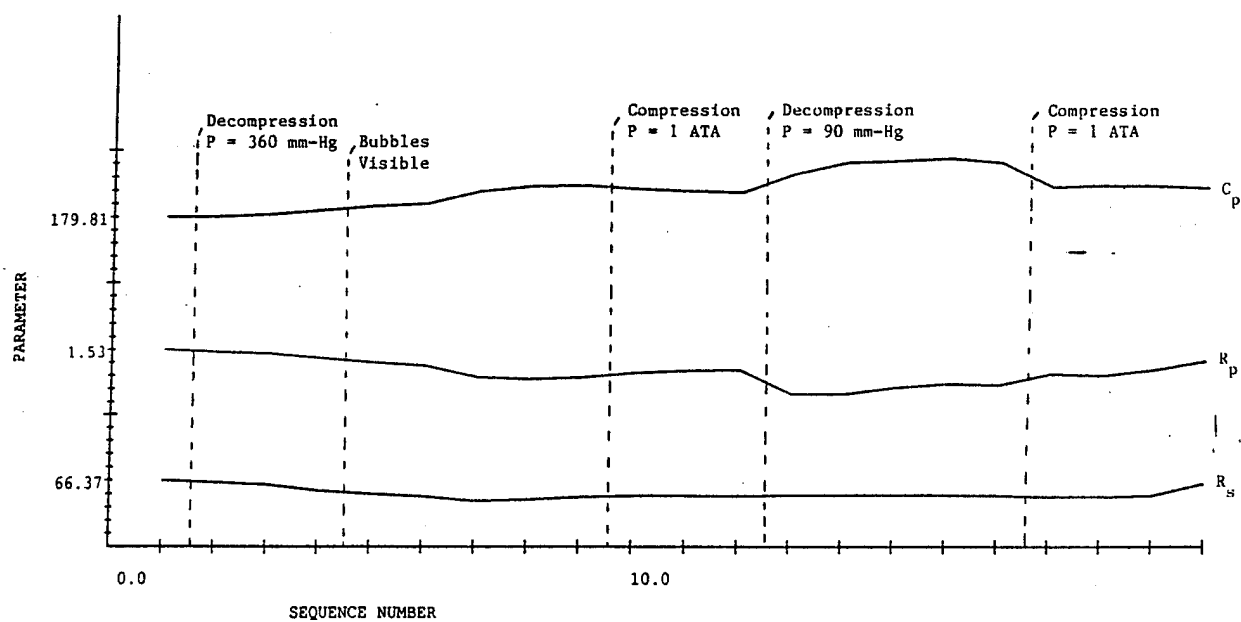


Figure 15:

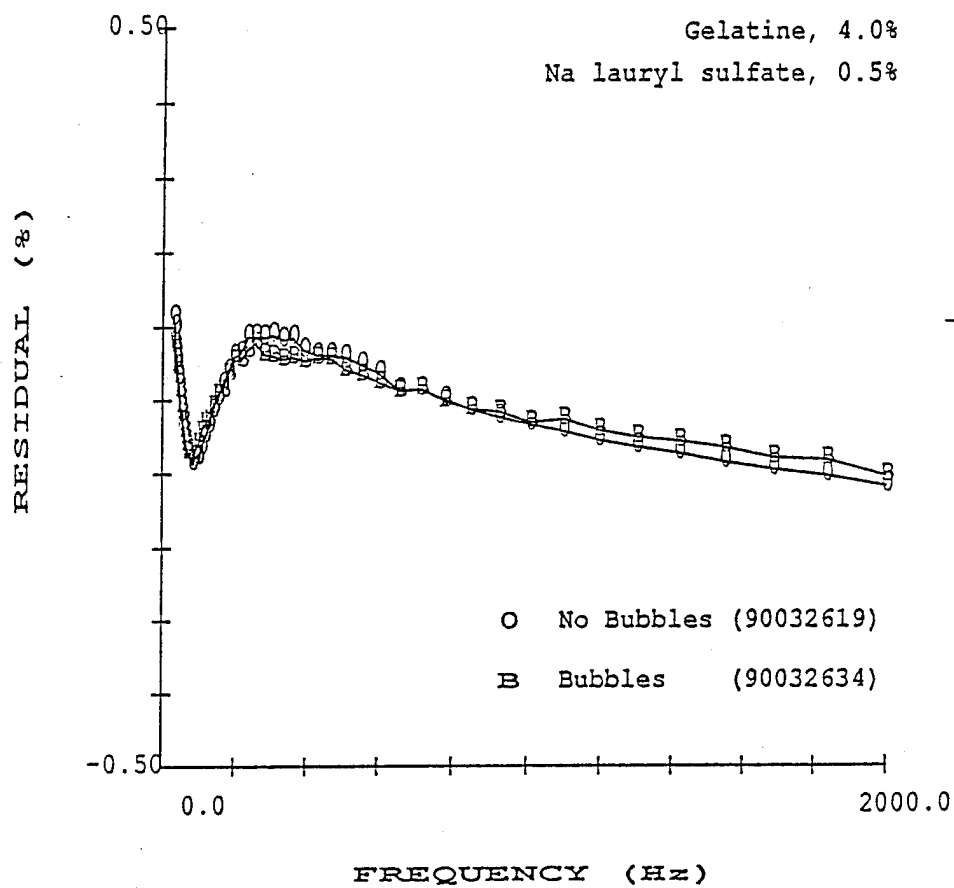


Figure 16:

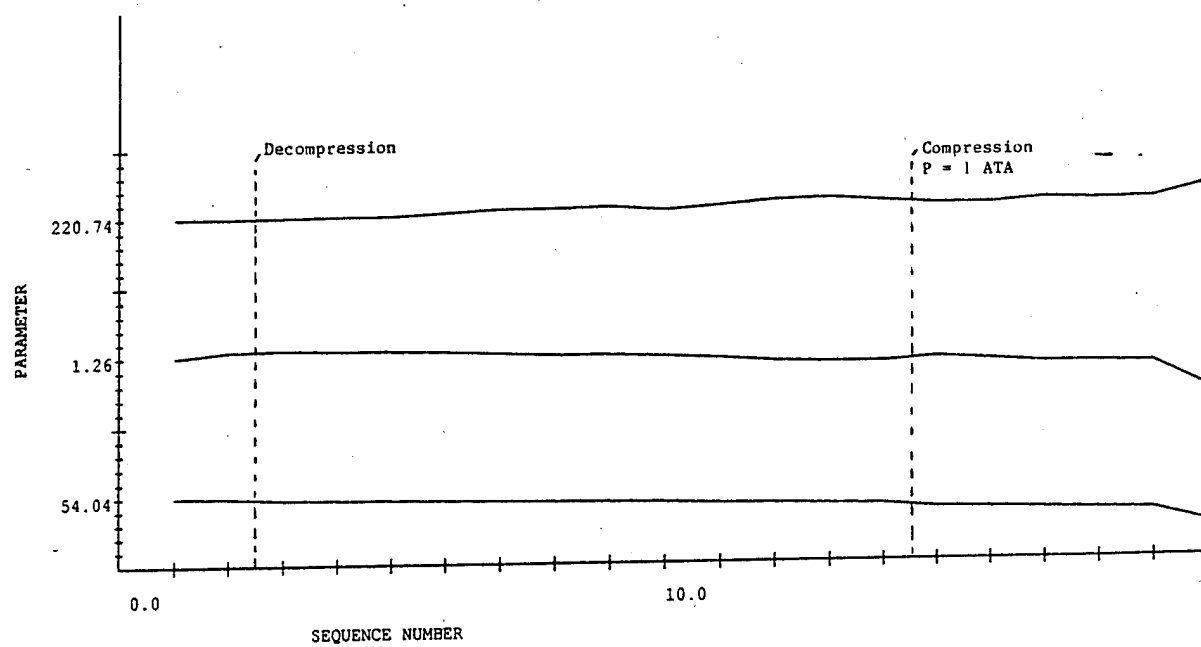


Figure 17:

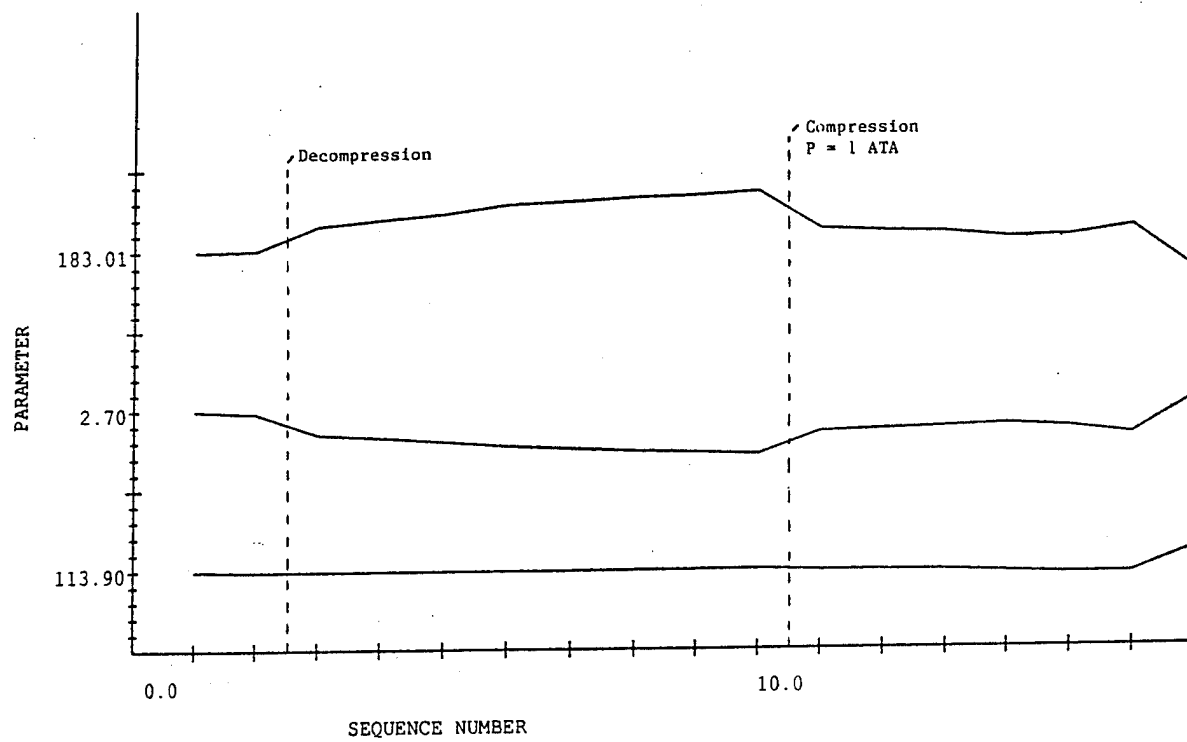


Figure 18:

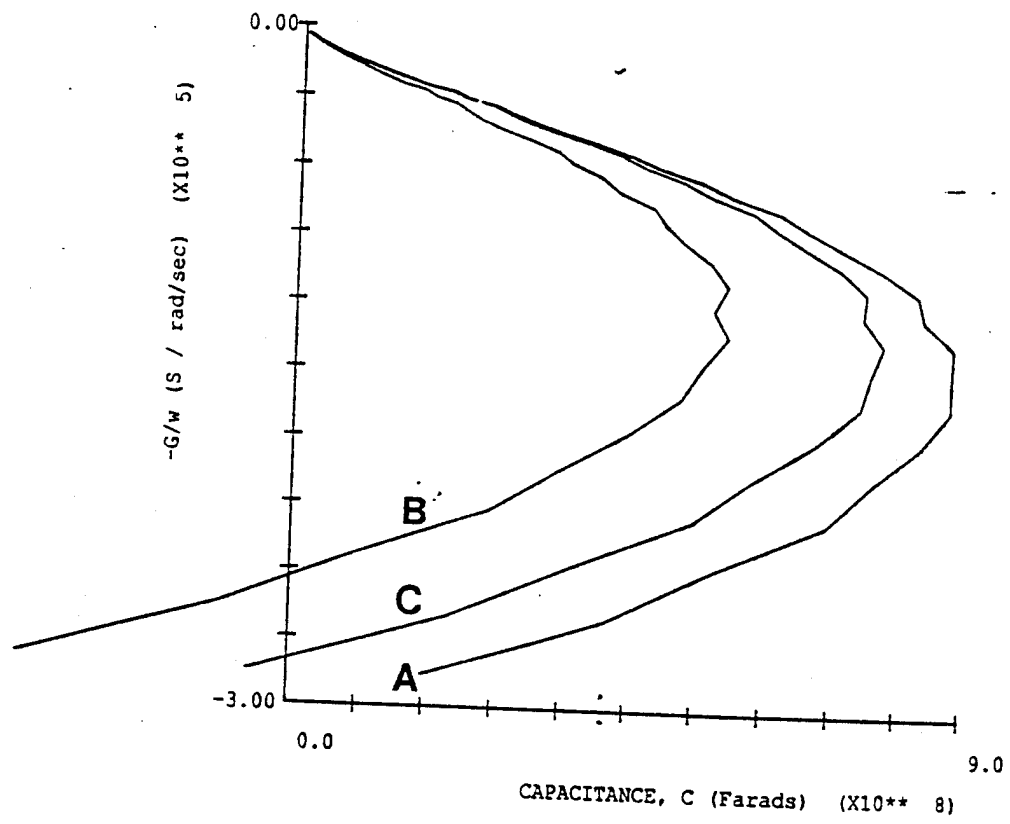


Figure 19:

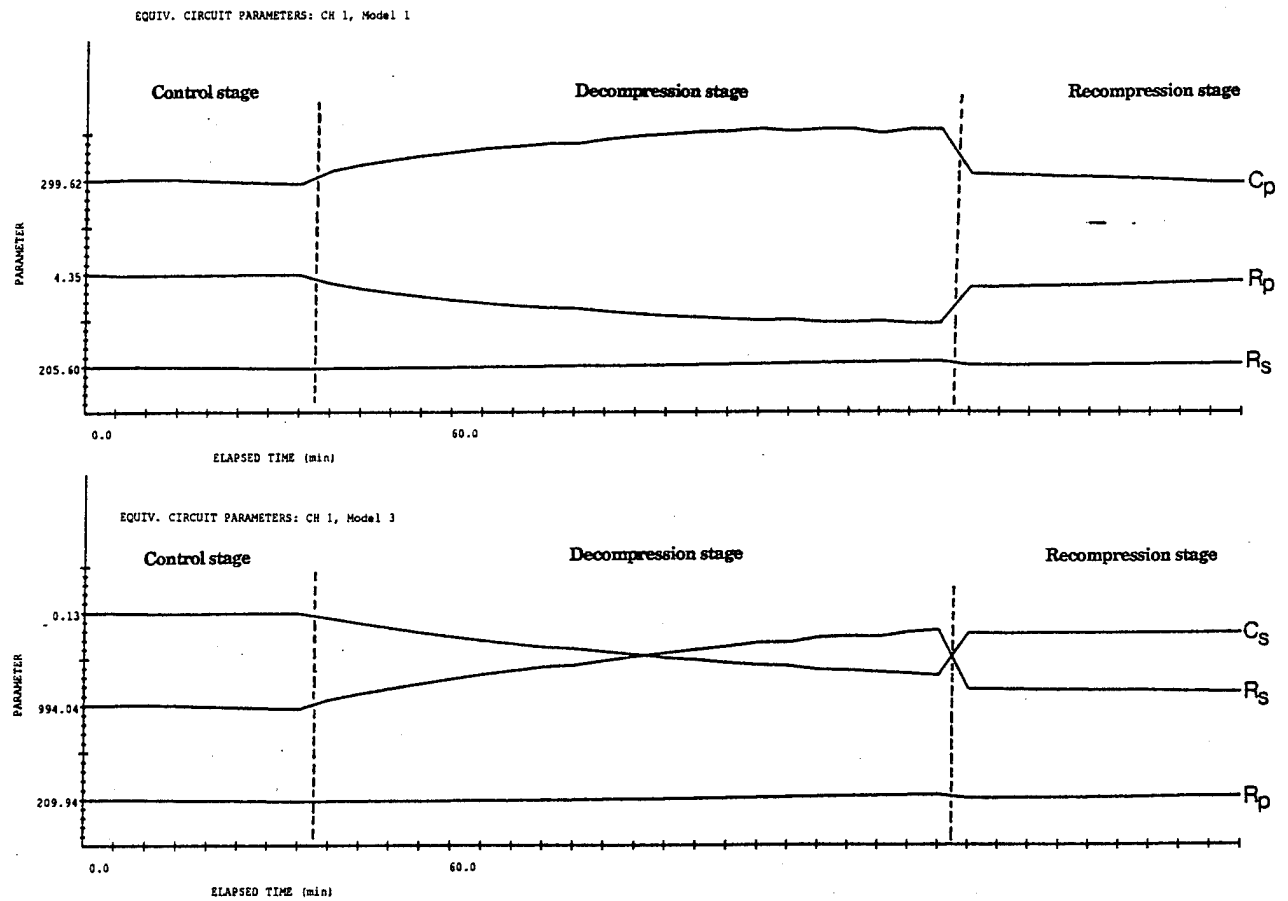




Figure 20:

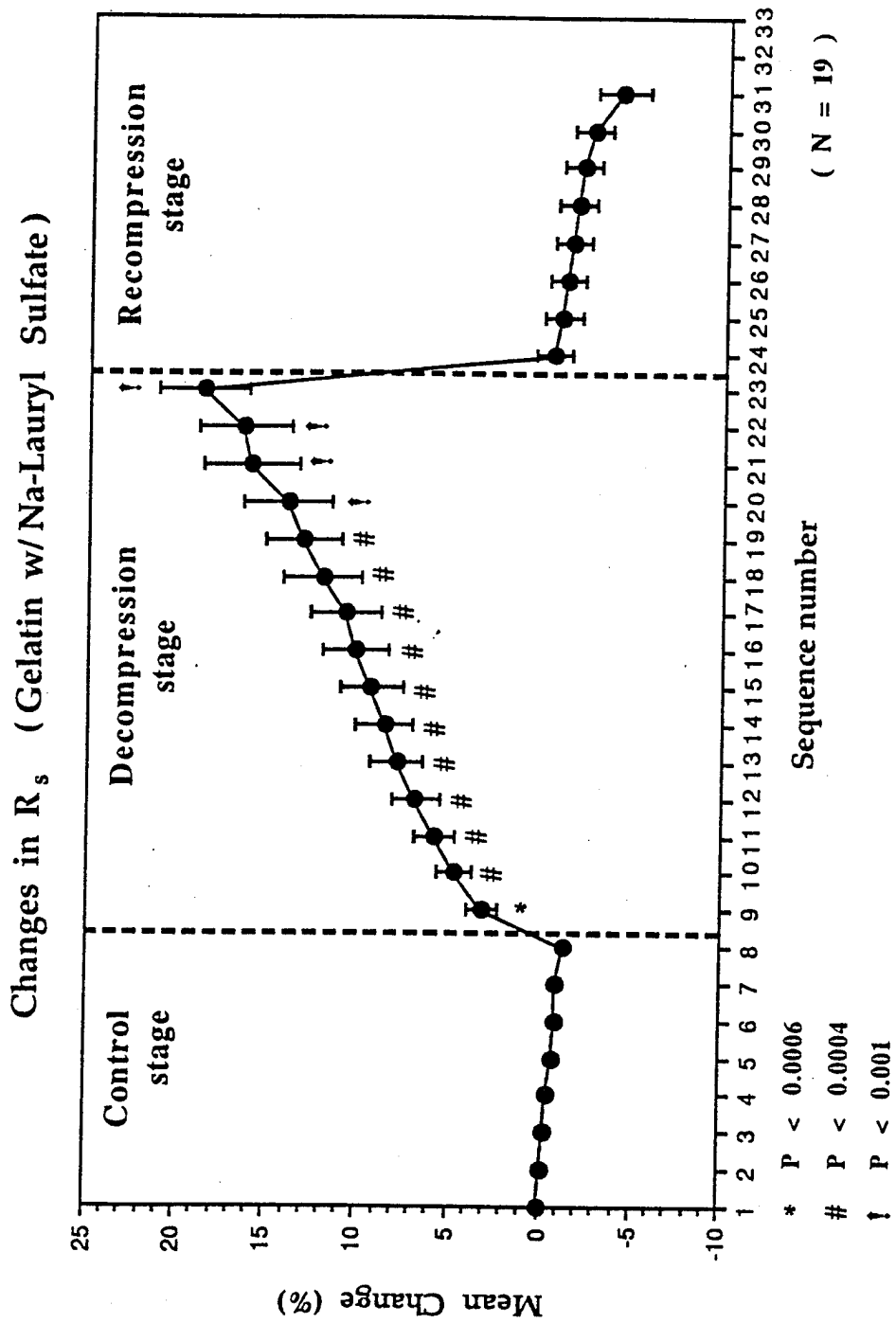


Figure 21:

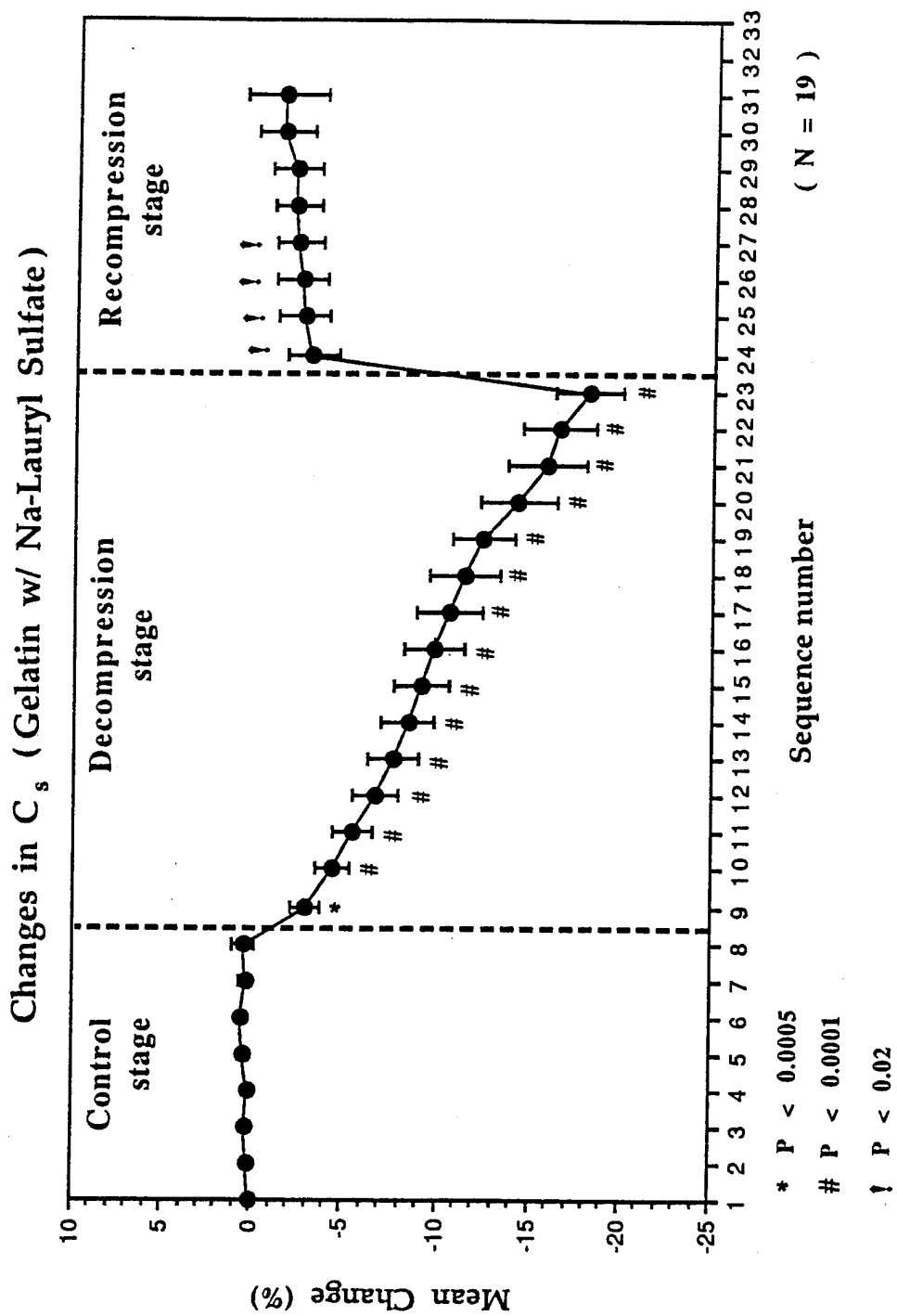


Figure 22:

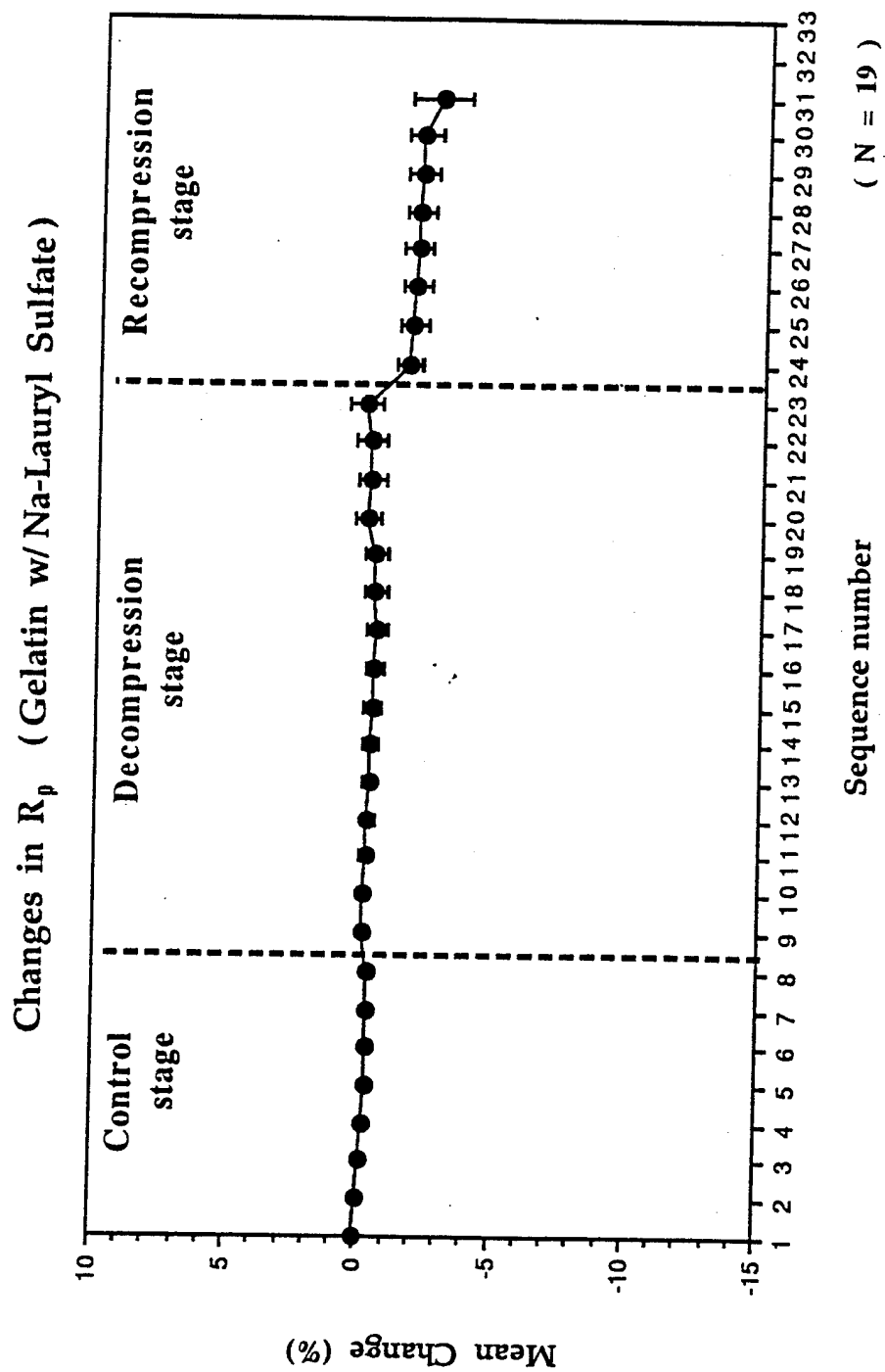


Figure 23:

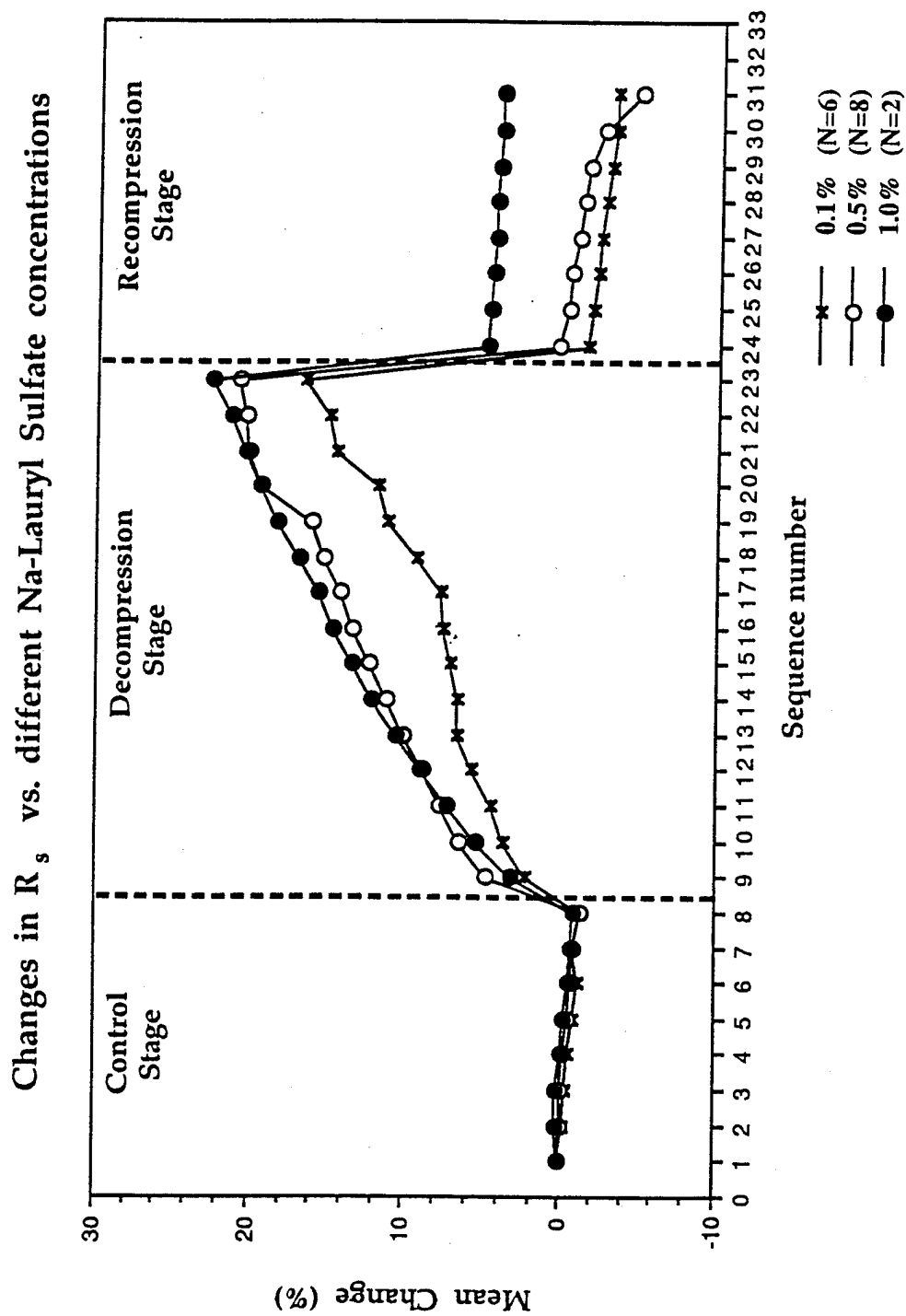


Figure 24:

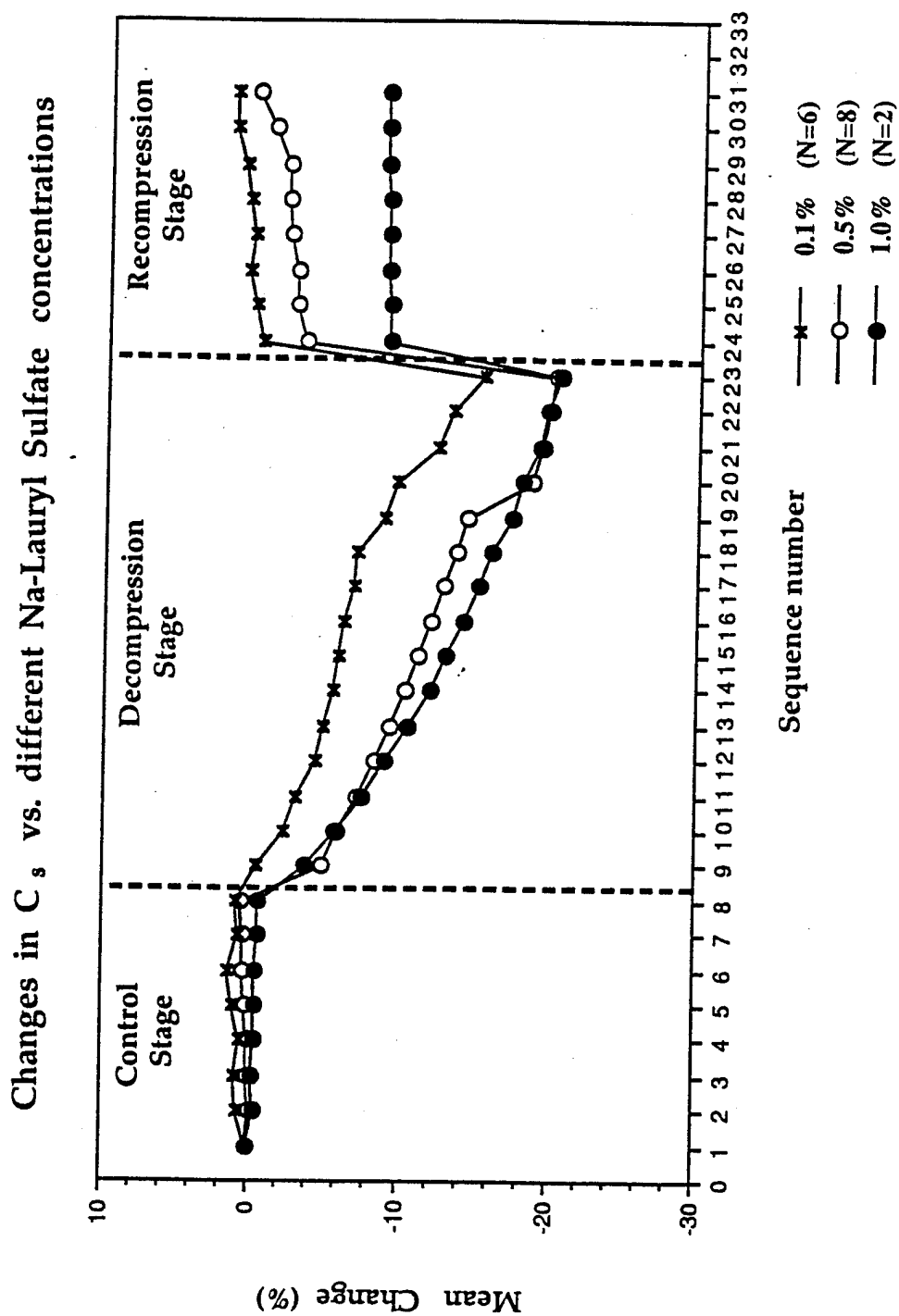


Figure 25:

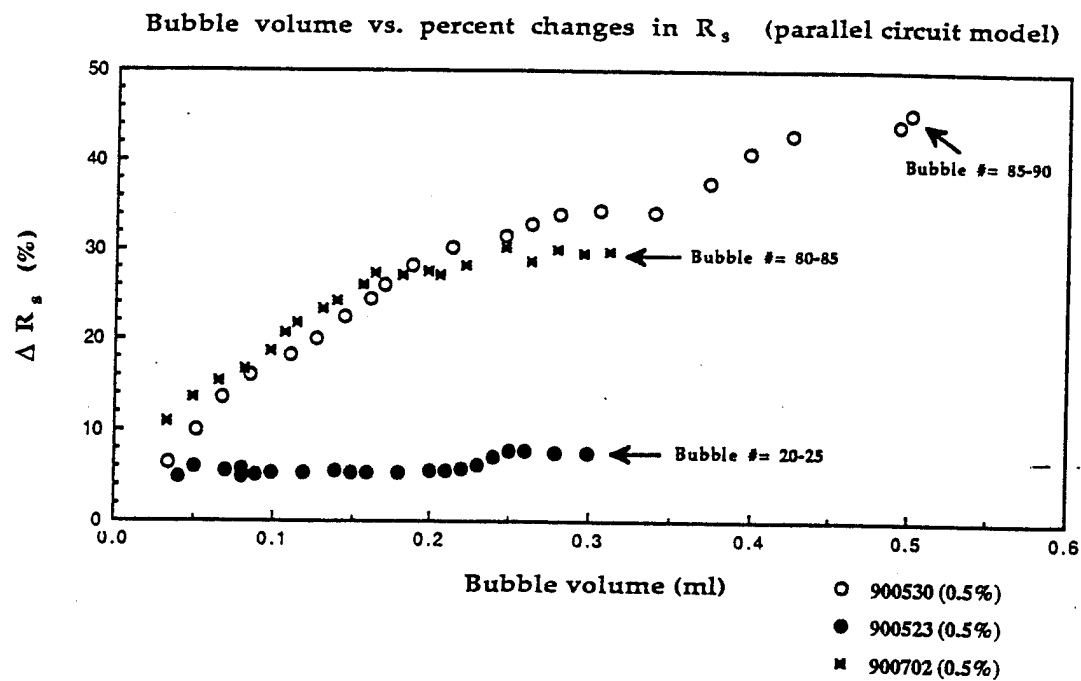


Figure 26:

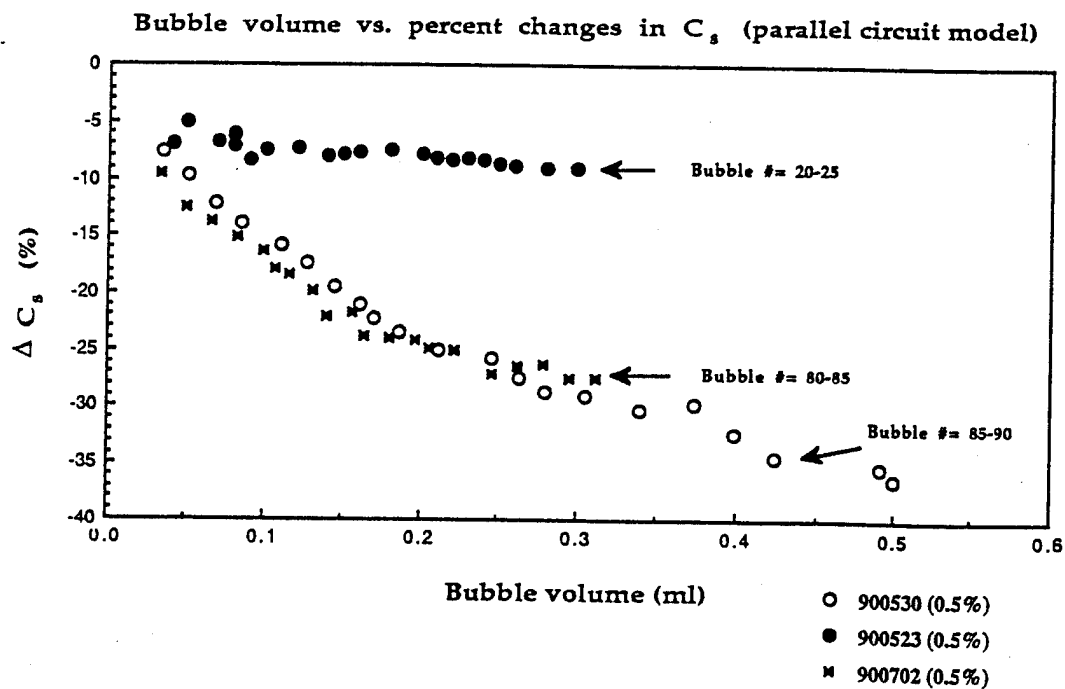


Figure 27:

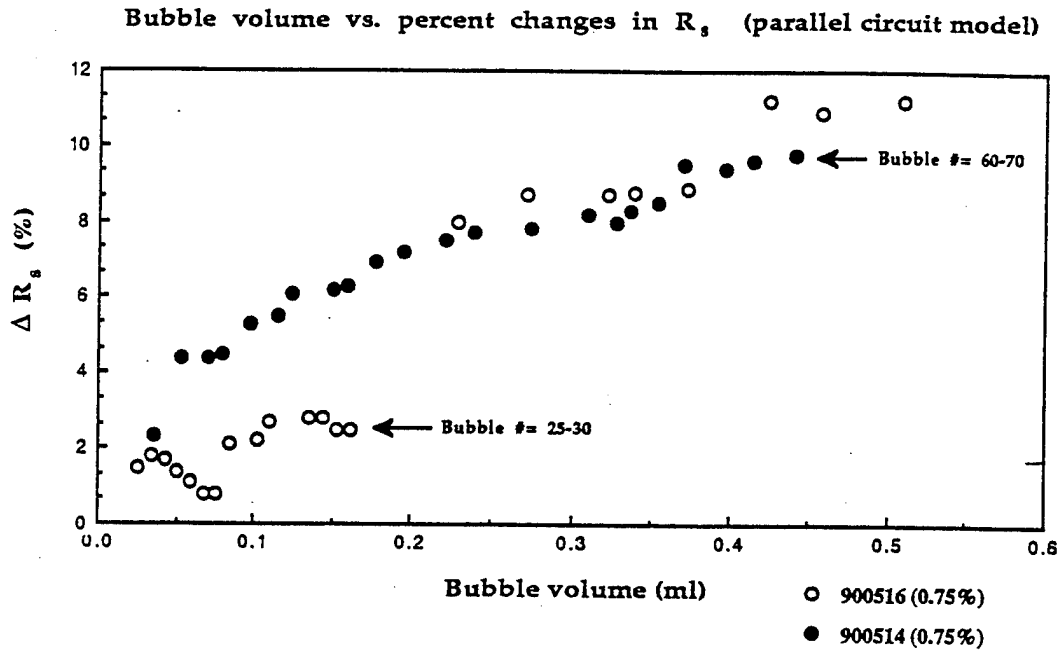


Figure 28:

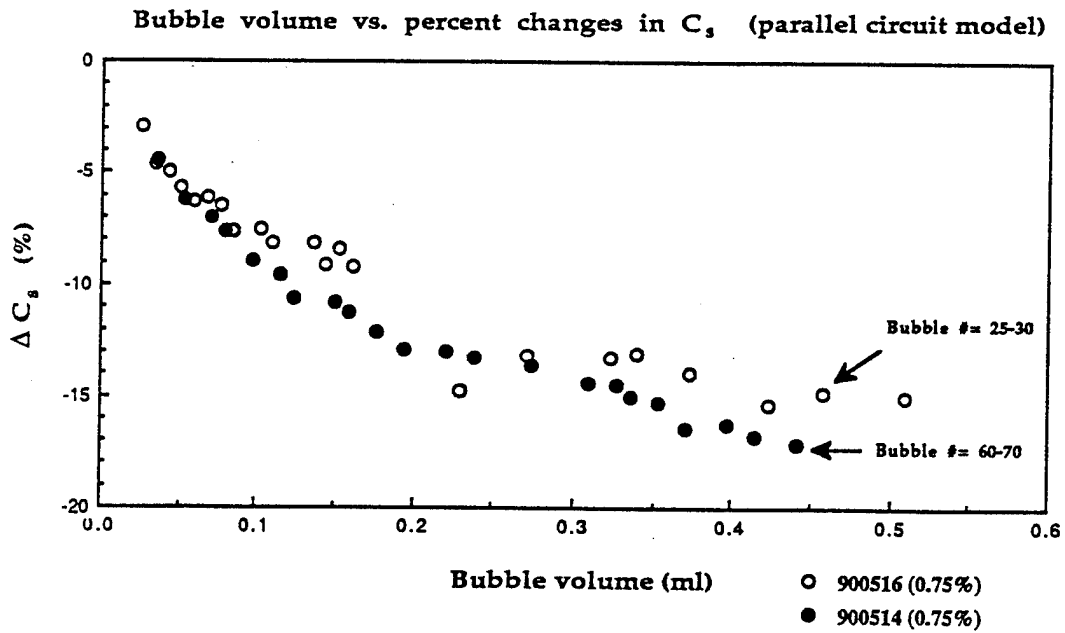
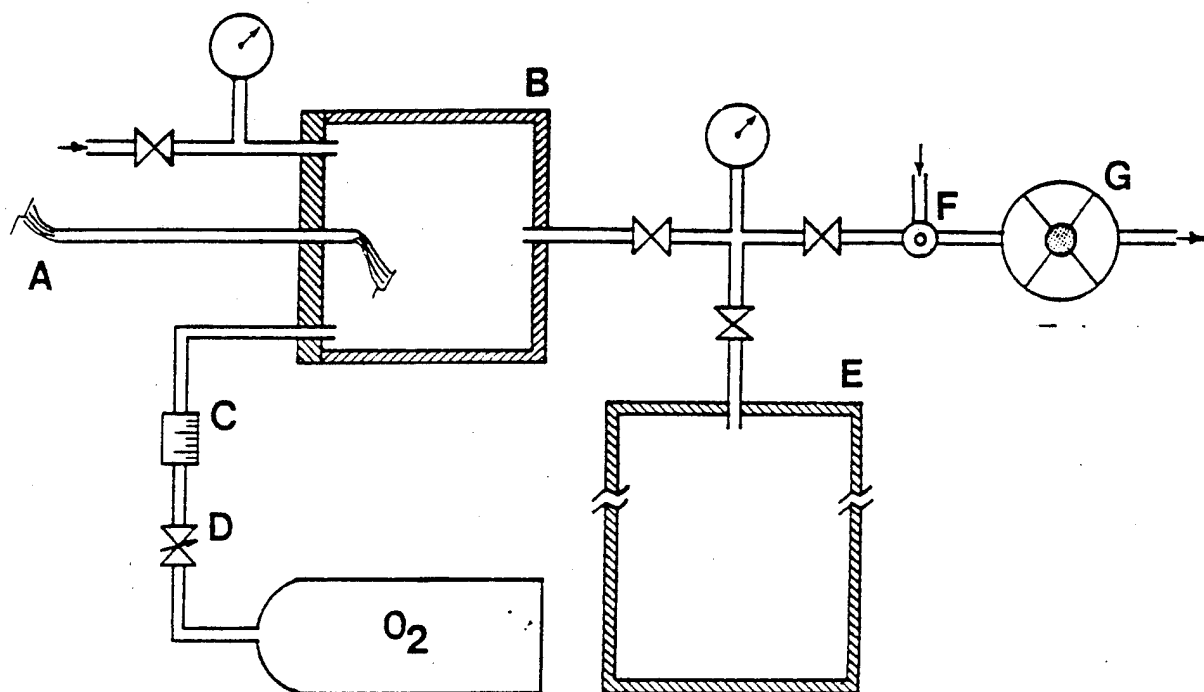


Figure 29:



- A) Cable Bundle
- B) Experimental Chamber
- C)  $O_2$  Flowmeter
- D)  $O_2$  Regulating Valve

- E) Vacuum Accumulator
- F) Vacuum Regulator
- G) Vacuum Pump



Figure 30:

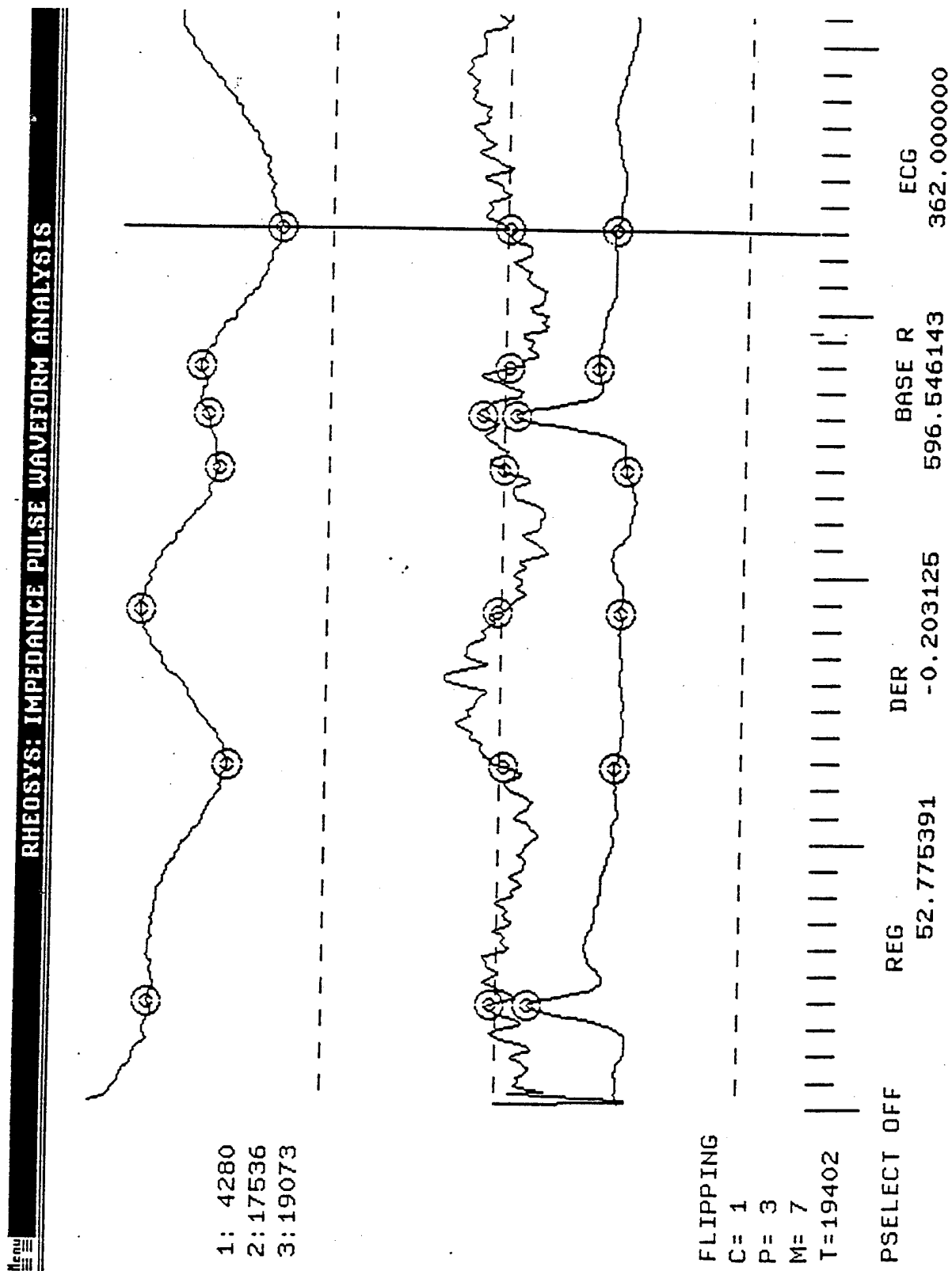


Figure 31:

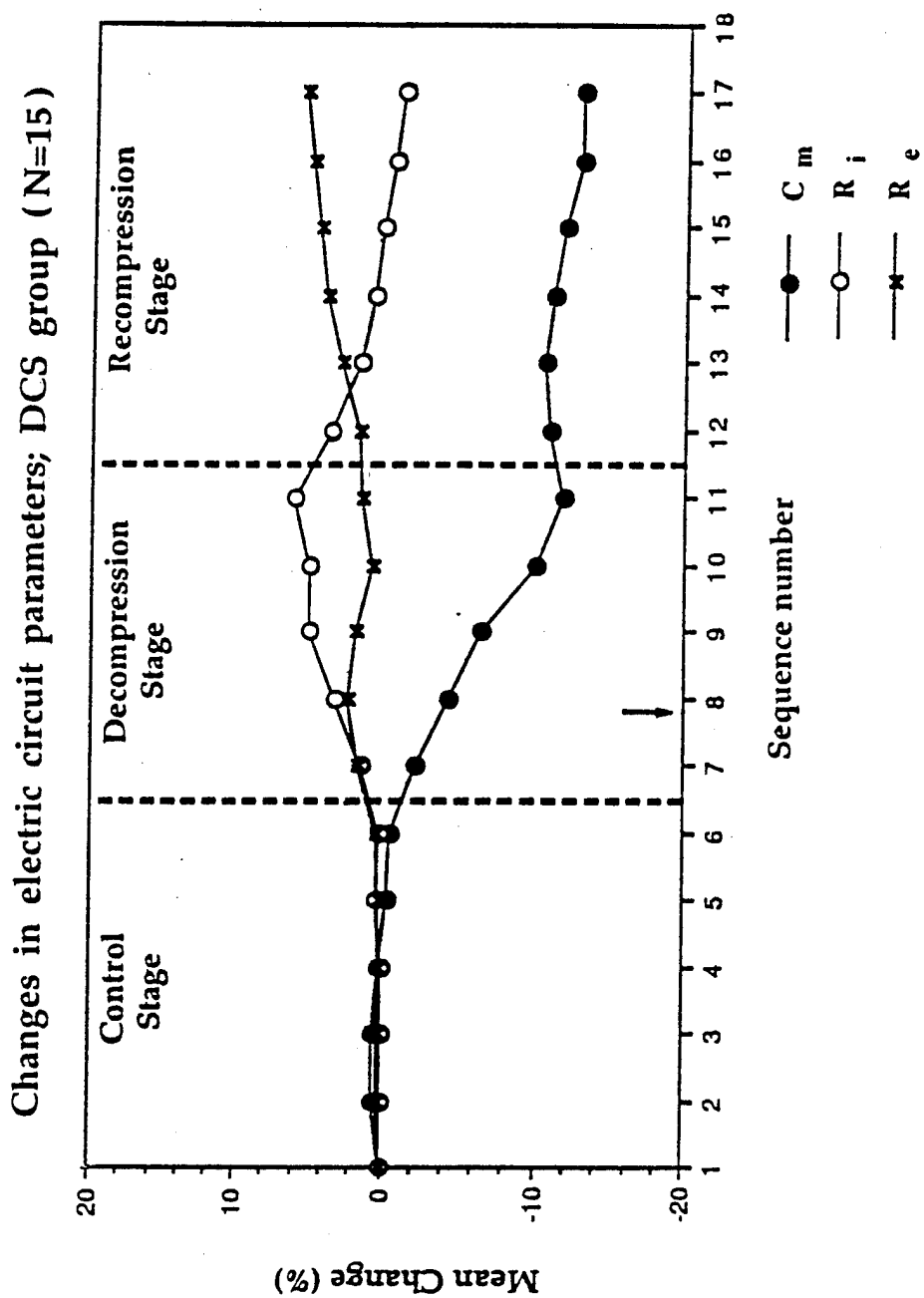


Figure 32:

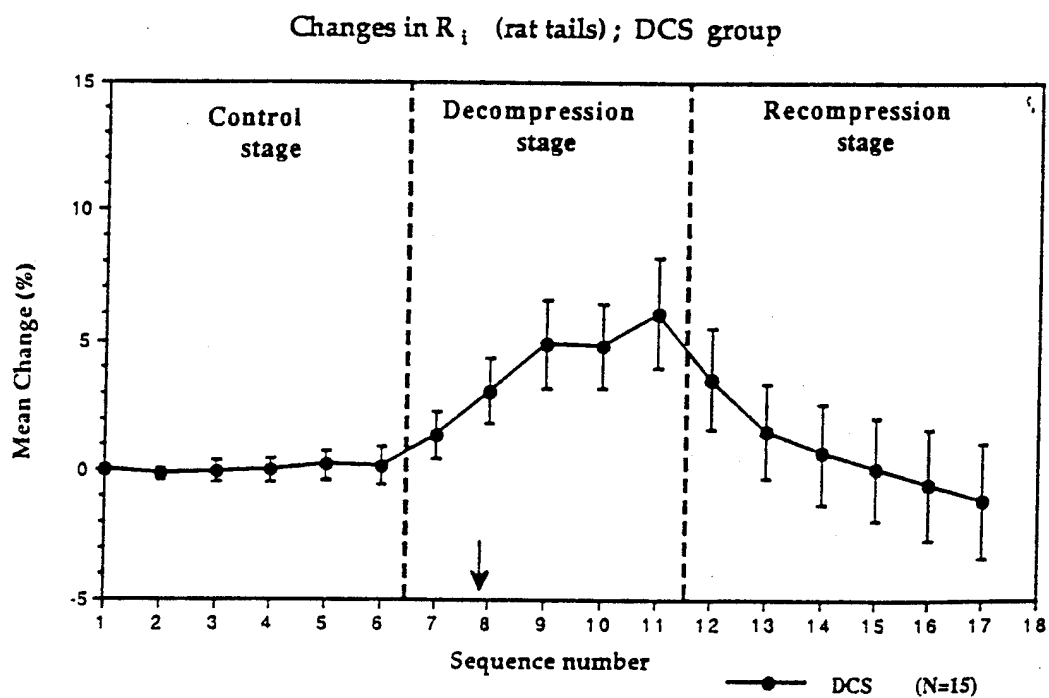
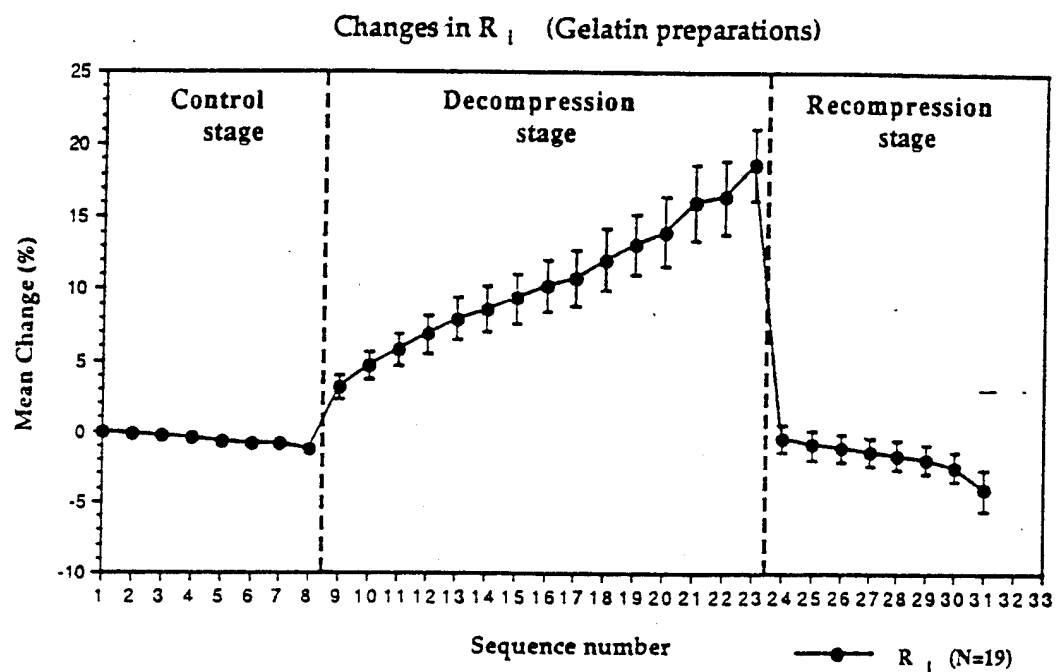


Figure 33:

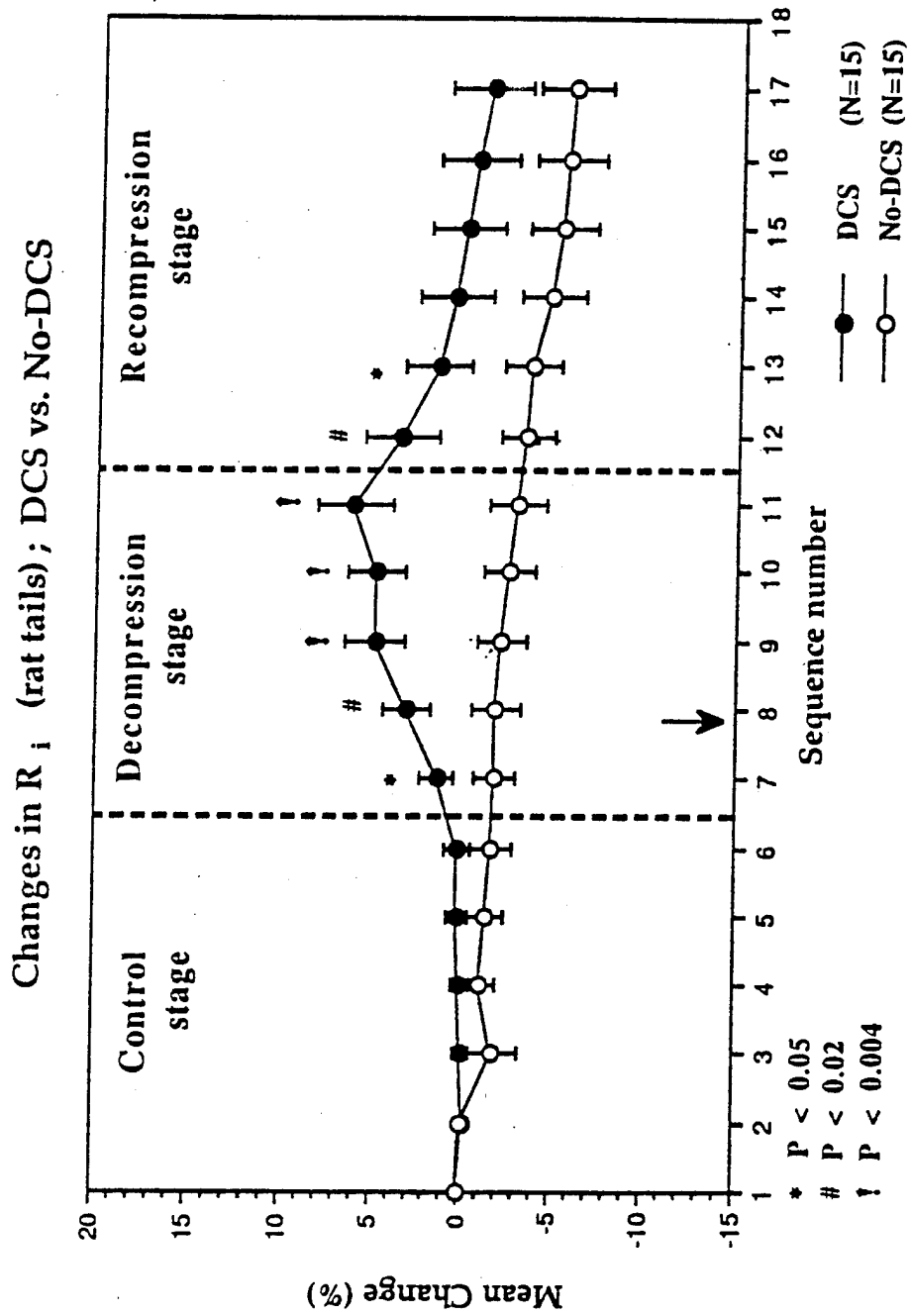


Figure 34:

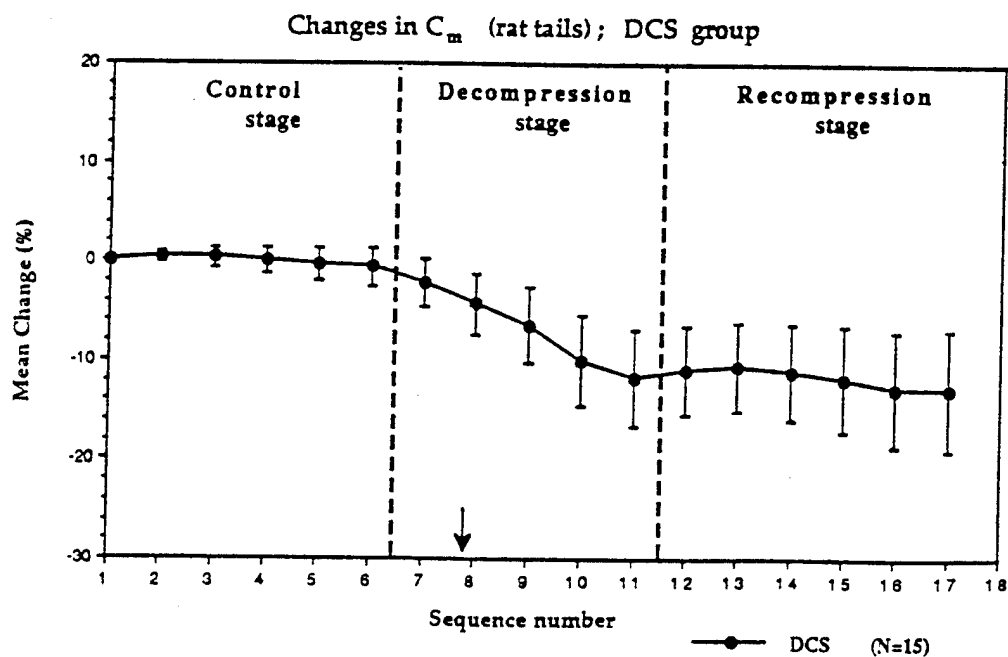
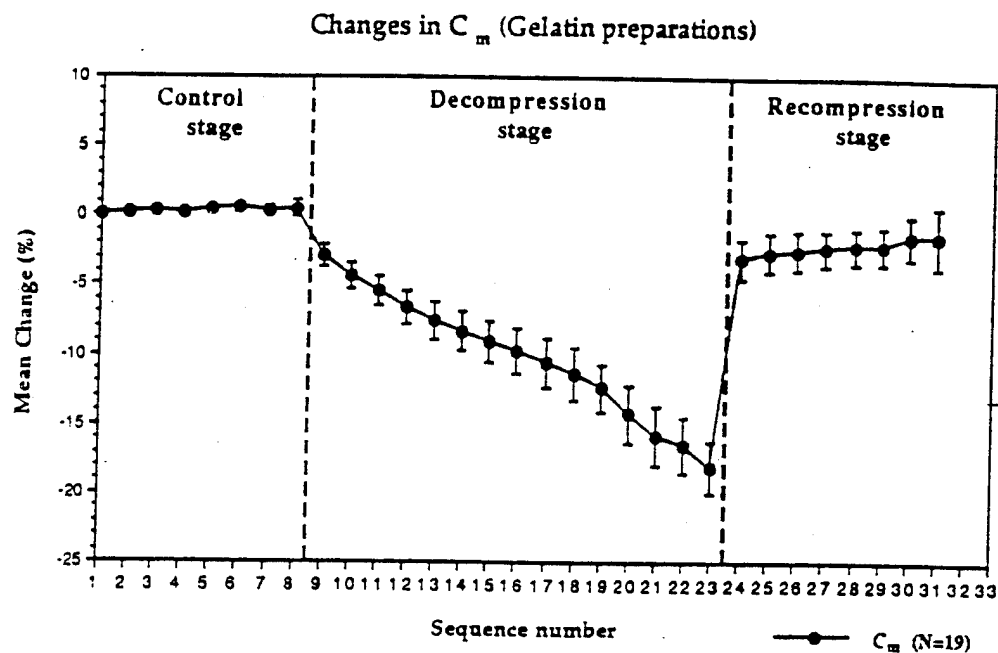


Figure 35:

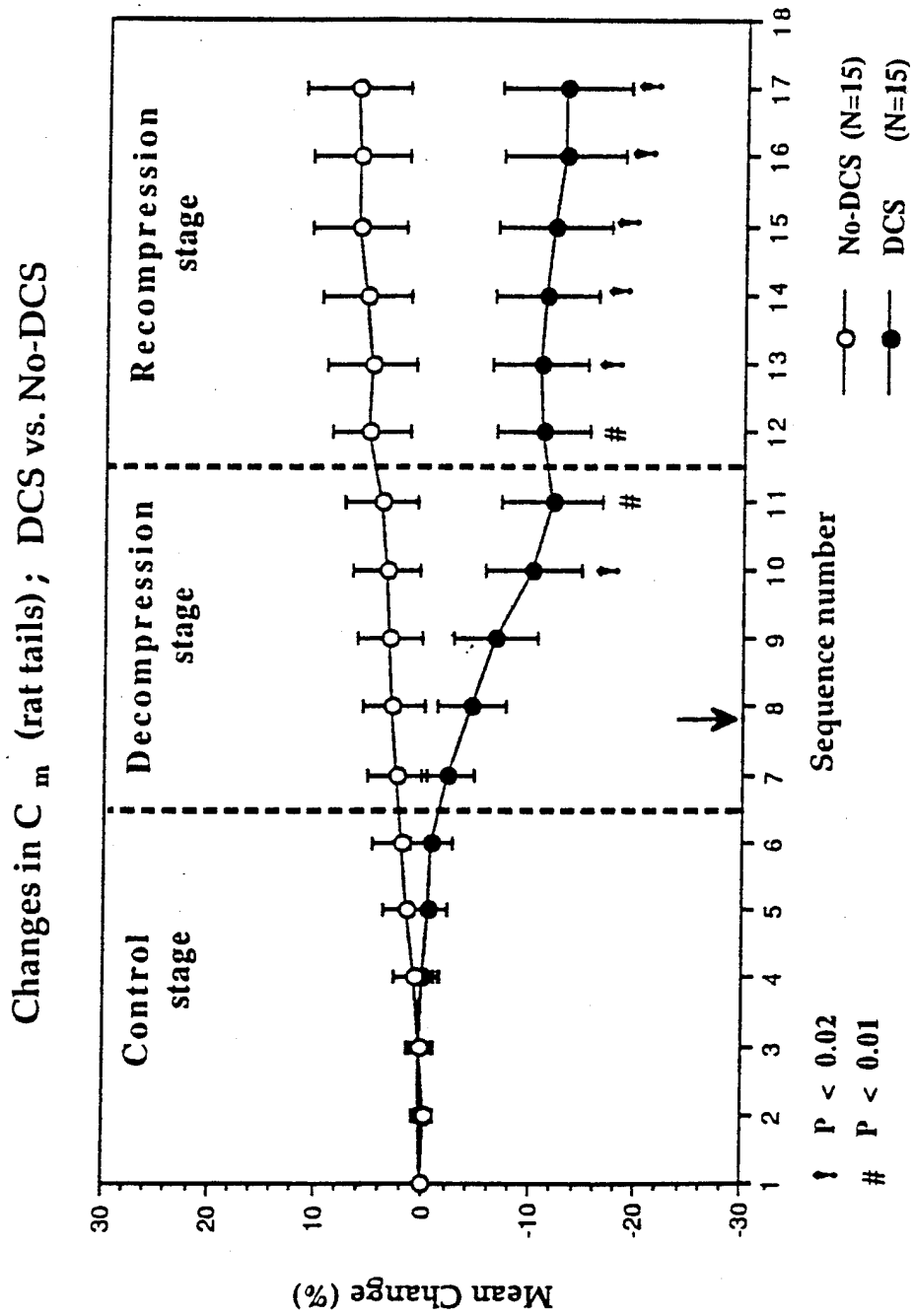


Figure 36:

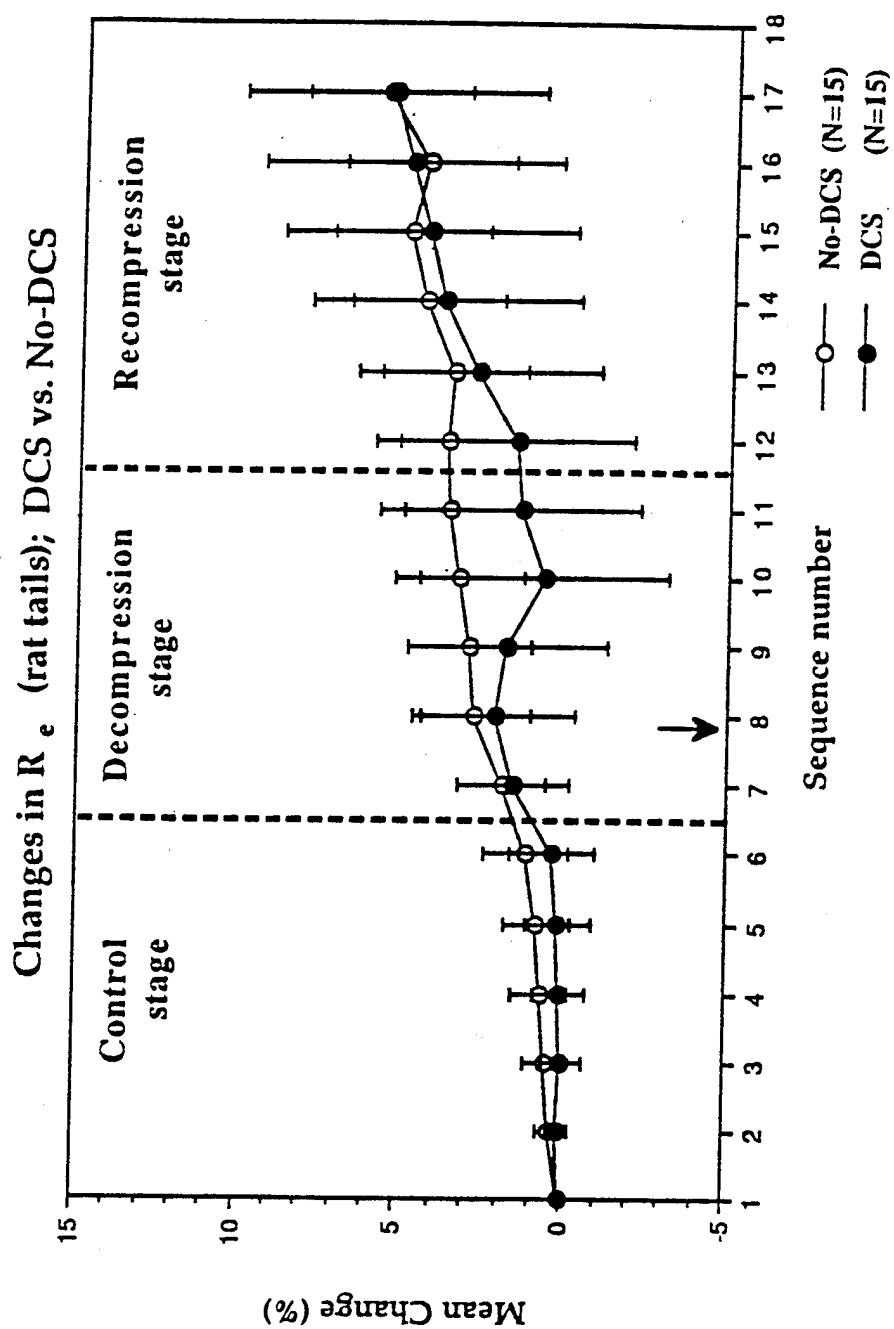


Figure 37:

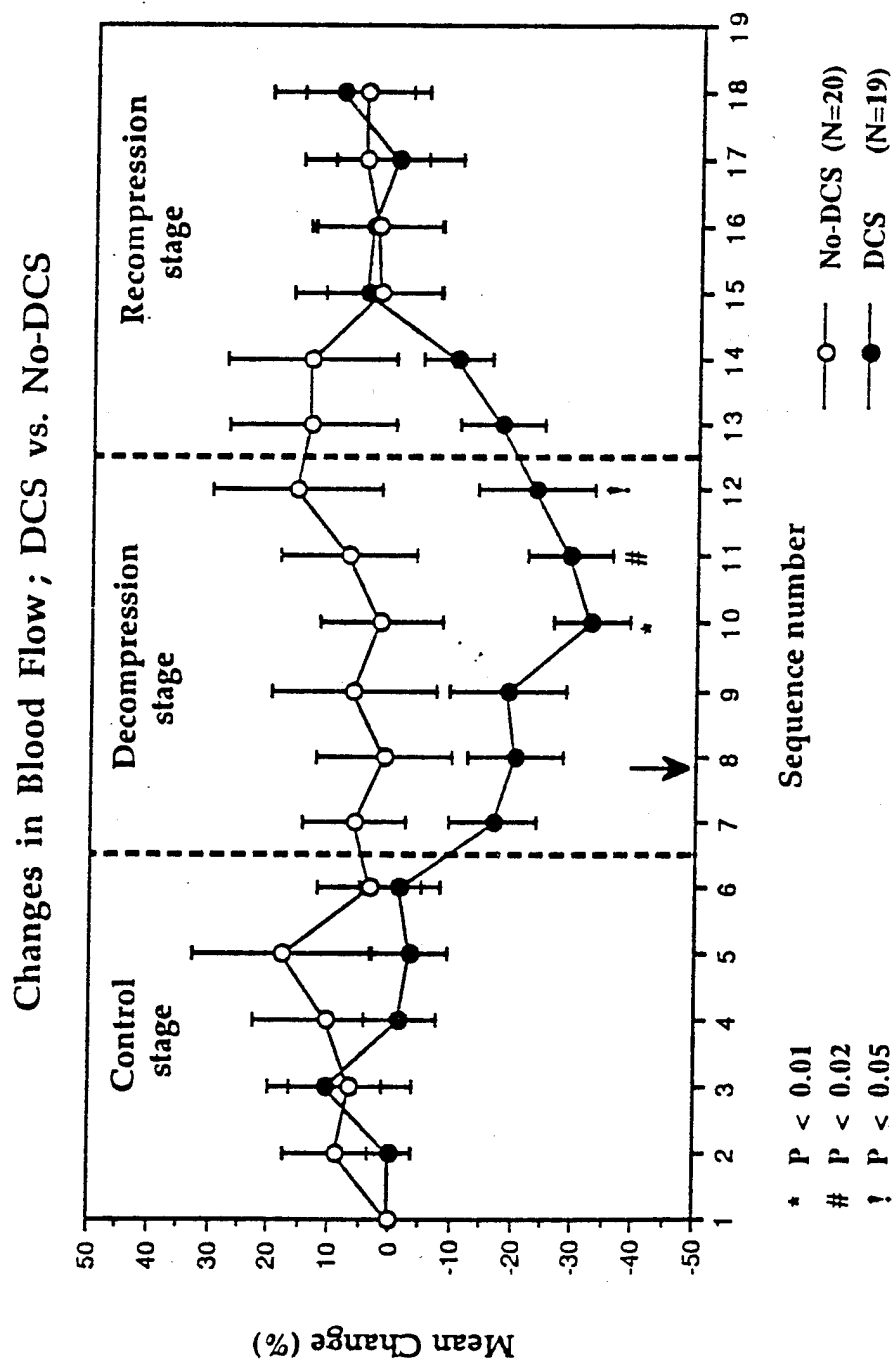




Figure 38:

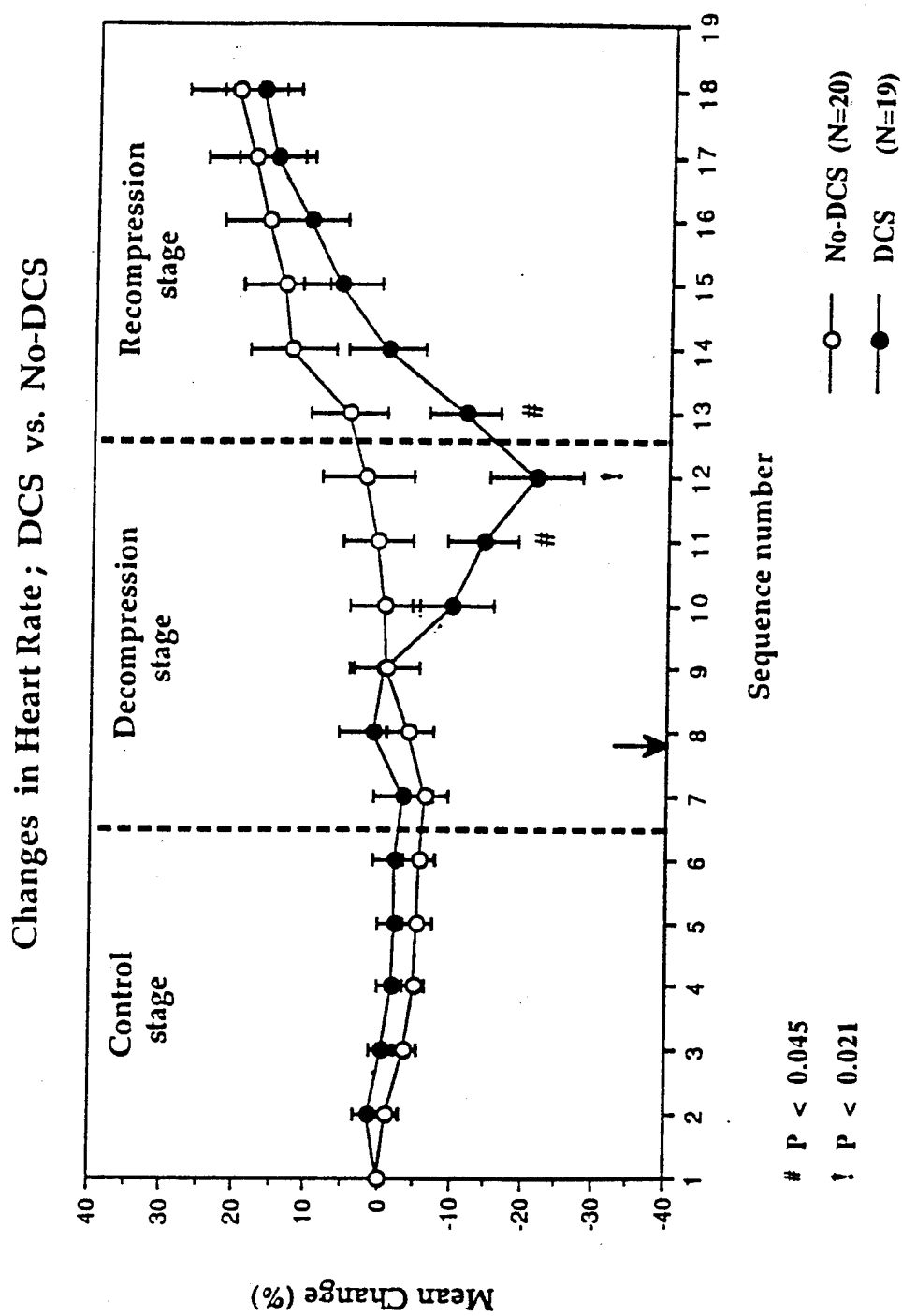


Figure 39:

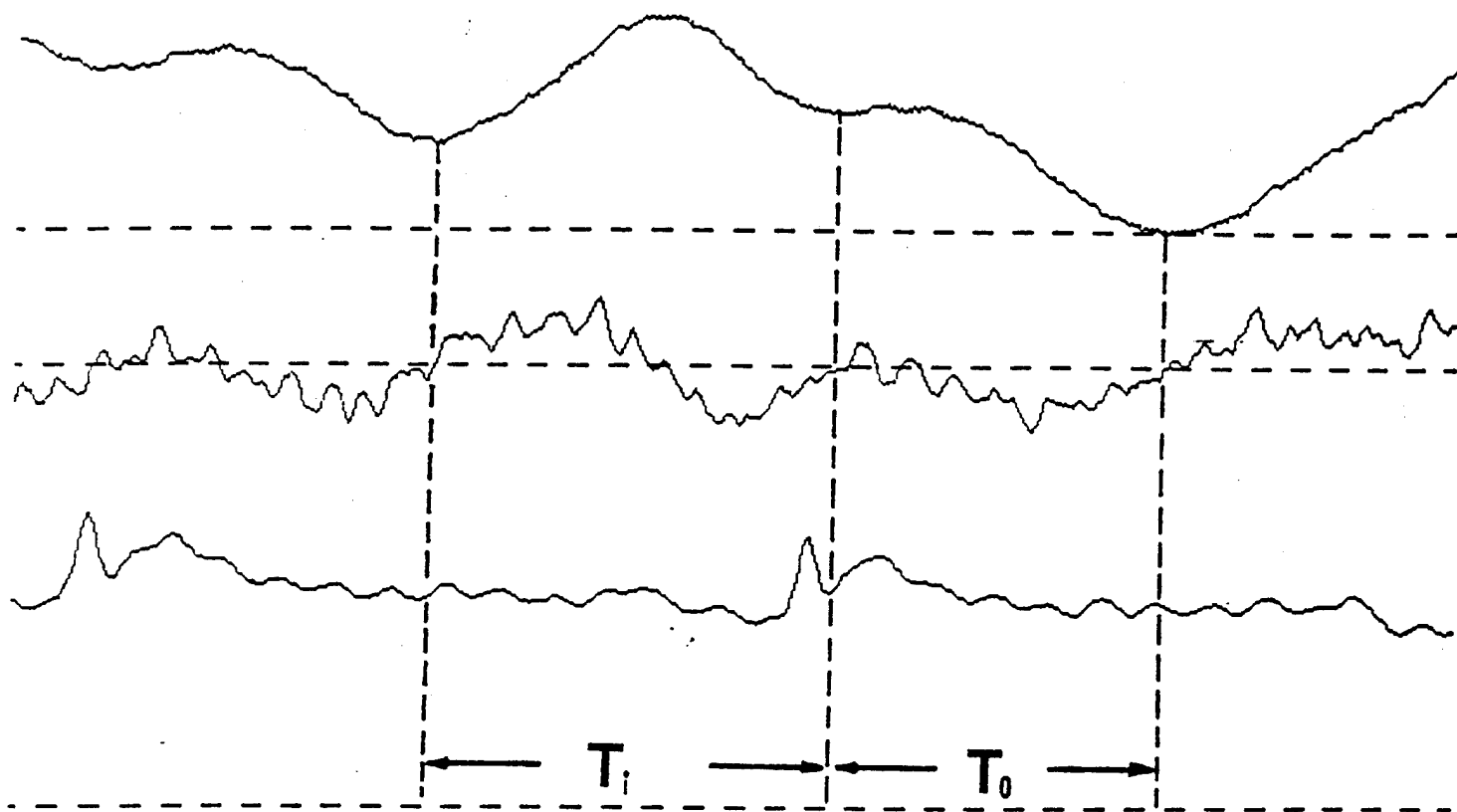


Figure 40:

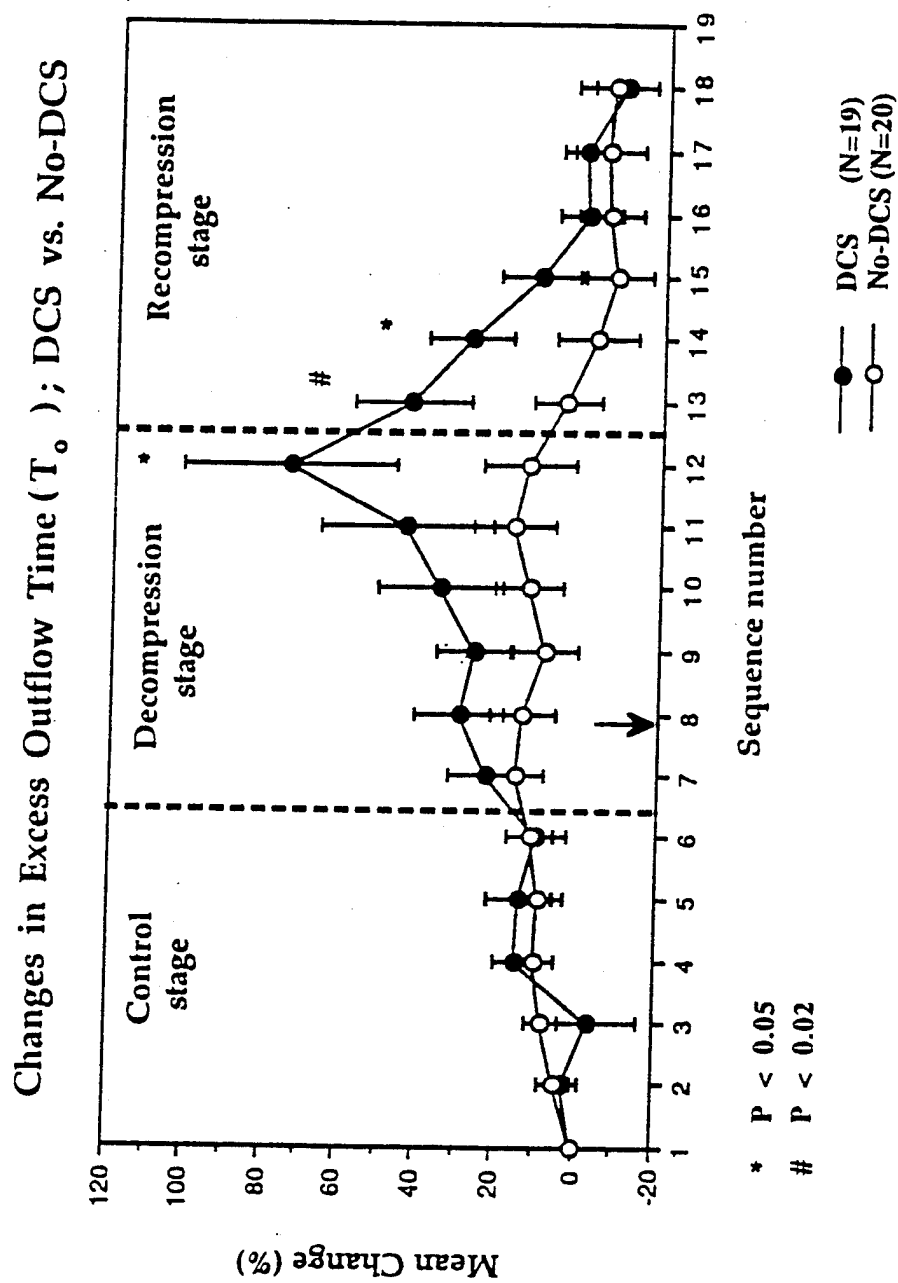


Figure 41:

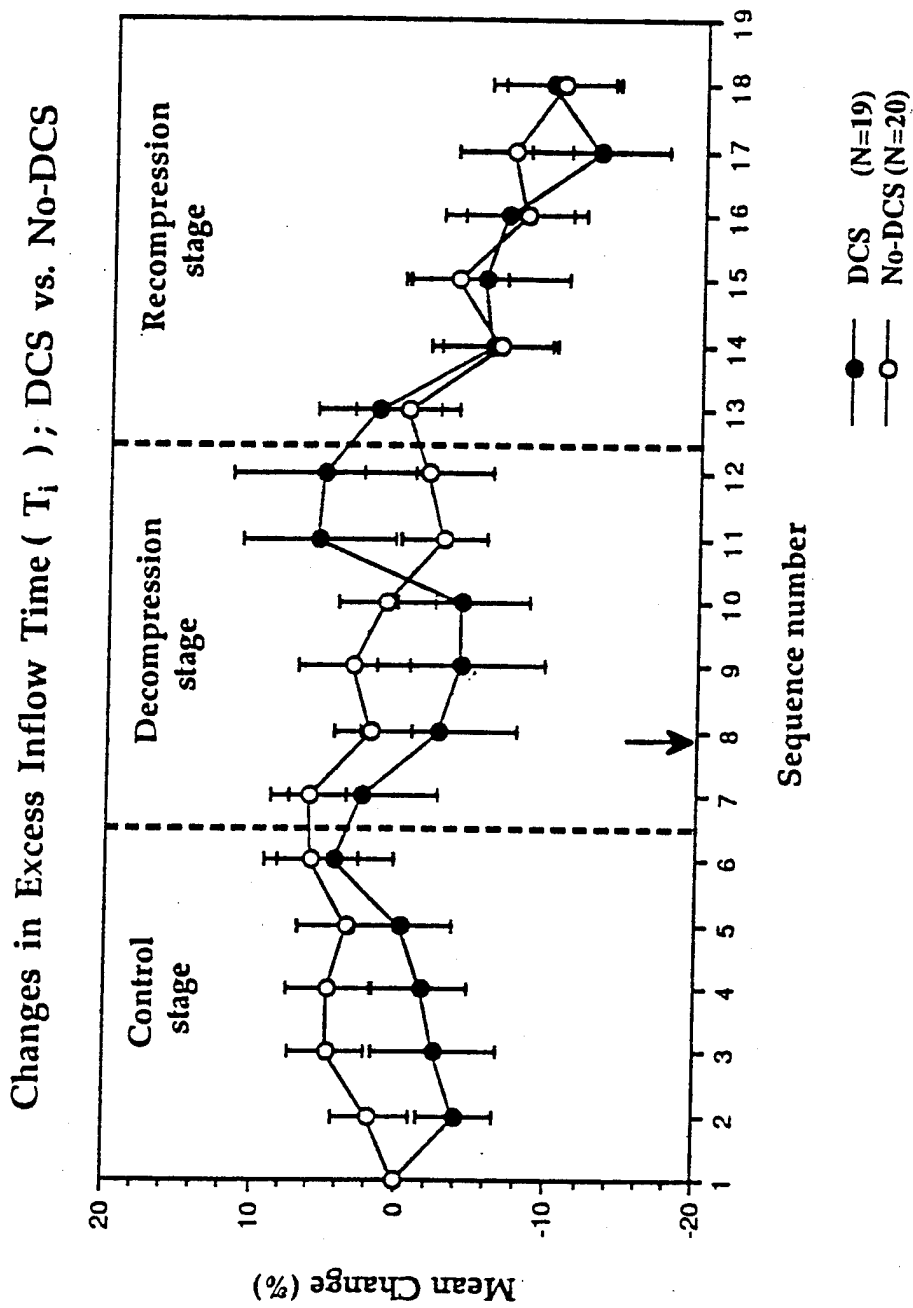
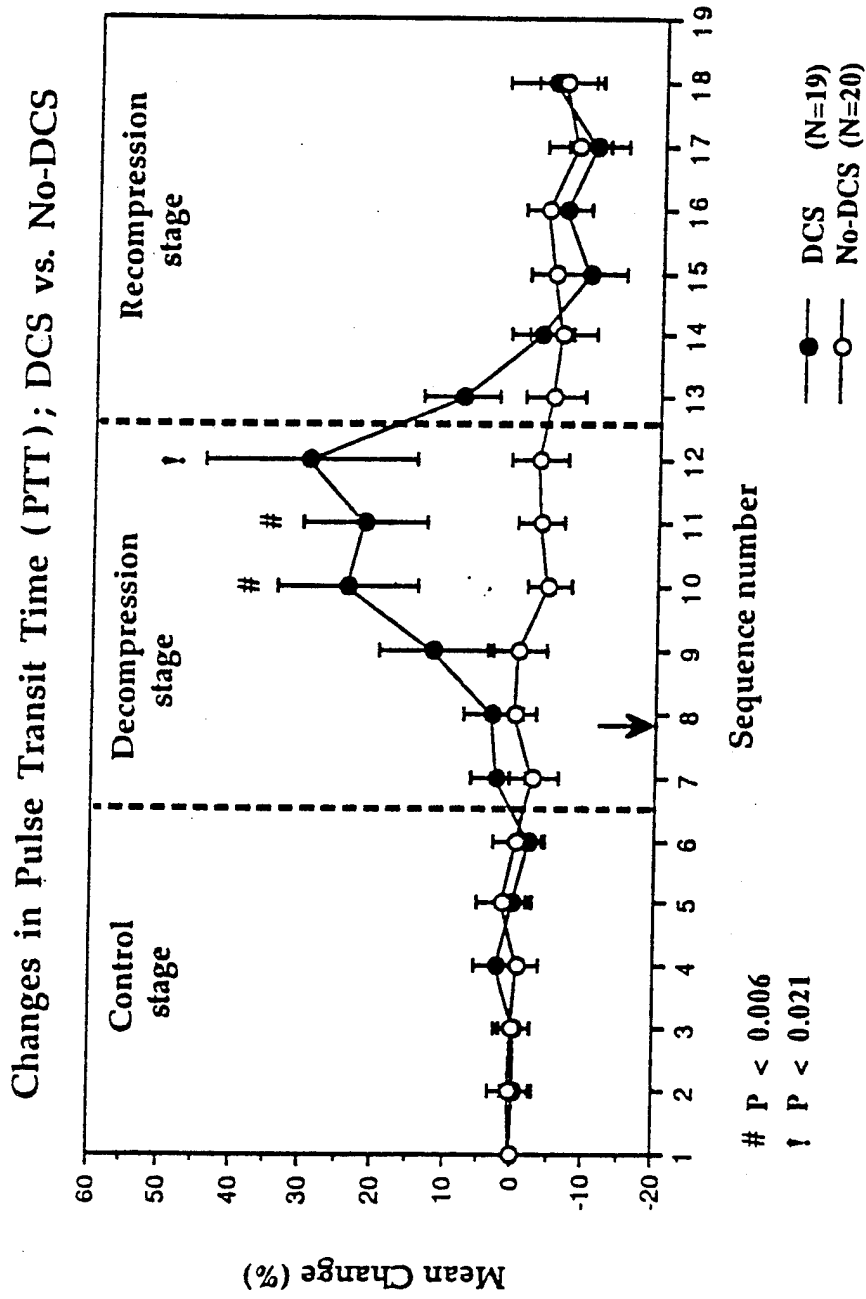


Figure 42:



## Appendix A.

Structural Dielectric Relaxation:  
Theory Pertinent to In Vivo Bubble Detection

In the following, only the "passive" electrical properties of tissues that obtain at low current intensities where Ohm's Law holds are considered. Under this restriction, the responses of different polarizing elements to different step function potential changes are additive. The limiting current intensity above which this linearity fails (the rheobase) is frequency dependent and in the range of 1 ma/cm<sup>2</sup> for tissue. It is also assumed that in vivo bubble formation affects electrical properties of tissue principally through perturbations of the structural heterogeneity of tissue. Consequently, only those aspects of dielectric relaxation that arise from structural heterogeneity of the medium are considered.

Consider application of a step function potential gradient,  $\bar{E}$ , to a specimen of heterogeneous material which is initially in a completely uncharged state. The dielectric displacement,  $D$ , defined as the charge per unit electrode area [also equal to the product of the dielectric constant,  $\epsilon$ , and the field strength,  $E$  ( $D = \epsilon E$ )], is at first constant throughout the material because charges have yet to penetrate into it. In comparison, the current density,  $J$ , defined by the product of the conductivity,  $\kappa$ , and the field strength ( $J = \kappa E = \kappa D / \epsilon$ ), must vary across boundaries between regions in the material with different  $\kappa / \epsilon$  values. Thus, with the onset of current flux into the material, charges must accumulate at these boundaries until  $J$  is again constant and  $D$  varies according to regional  $\epsilon$  values. The time required for these charge accumulations to occur is the cause of structural dielectric relaxation.

If the material is configured as a cylinder of length  $d$  between two parallel end-plate electrodes of area  $A$ , the dielectric constant and conductivity are related to the conductance,  $G$ , and capacitance,  $C$ , of the material by:

$$G = \kappa A / d \quad \text{and} \quad C = \epsilon A / (4\pi d), \quad (1)$$

where  $C$  is in electrostatic units. Because conversion of  $C$  to farads requires multiplication by  $1/(9 \cdot 10^{11})$ , it is convenient to define a factor,  $\epsilon_r = 1/(4\pi \cdot 9 \cdot 10^{11})$  and rewrite the above expression for  $C$  in farads:

$$C = \epsilon \epsilon_r A / d.$$

In the simplest case, the noninstantaneous contribution to the total polarization is an exponential function of the time,  $t$ , following imposition of the step function potential:

$$D(t) = E\epsilon^\infty + E(\epsilon^\circ - \epsilon^\infty) [1 - \exp(-t/\tau)], \quad (2)$$

where  $\epsilon^\circ$  and  $\epsilon^\infty$  are defined as indicated in Figure 1. The product  $\epsilon^\infty E$  gives the instantaneous polarization of the material, while  $\epsilon^\circ E$  gives the extent of polarization after a time long compared to the time constant  $\tau$  of the relaxation. If the current is sinusoidal and of frequency with period  $2\pi f$

comparable to  $\tau$ , the dielectric relaxation causes the dielectric displacement and the applied field to be out of phase. In order to examine the frequency dependence of this behavior, a complex dielectric constant is defined:

$$\epsilon^* = \epsilon' - \epsilon''j, \quad (3)$$

where  $j = \sqrt{-1}$  and the imaginary part of  $\epsilon^*$ ,  $\epsilon''$ , is related to the conductivity by;

$$\kappa = \epsilon'' \epsilon_r \omega, \quad (4)$$

where  $\omega = 2\pi f$  is the angular frequency. Under the assumption of linearity noted above, the complex dielectric constant for the system is given by [36]:

$$\epsilon^* = \epsilon^\infty + (\epsilon^0 - \epsilon^\infty) / (1 + j\omega\tau), \quad (5)$$

for which the real part is

$$\epsilon' = \epsilon^\infty + (\epsilon^0 - \epsilon^\infty) / (1 + (\omega\tau)^2), \quad (6.a)$$

and the imaginary part is

$$\epsilon'' = (\omega\tau) (\epsilon^0 - \epsilon^\infty) / (1 + (\omega\tau)^2). \quad (6.b)$$

Using equation (4) for the conductivity  $\kappa$ , equation (6.b) becomes:

$$\kappa = \omega^2 \tau [\epsilon_r (\epsilon^0 - \epsilon^\infty)] / (1 + (\omega\tau)^2).$$

At very high frequencies, 1 can be neglected with respect to  $(\omega\tau)^2$  in the denominator, so that

$$\kappa^\infty \tau = \epsilon_r (\epsilon^0 - \epsilon^\infty),$$

which, upon substitution into the preceding equation for  $\kappa$ , yields:

$$\kappa = \kappa^\infty (\omega\tau)^2 / (1 + (\omega\tau)^2).$$

Finally, a term  $\kappa^0$  is added to account for dielectric losses unrelated to the assumed transient electrical behavior of the material:

$$\kappa = \kappa^0 + (\kappa^\infty - \kappa^0) (\omega\tau)^2 / (1 + (\omega\tau)^2). \quad (6.c)$$

The frequency dependence of  $\epsilon$  and  $\kappa$  given by equations (6.a) and (6.c), respectively, is shown in Figure 2. Dielectric relaxation causes the dielectric constant to decrease to  $\epsilon^\infty$  and the conductivity to increase to  $\kappa^\infty$  as the frequency of the applied field increases. Note that at the characteristic frequency of the dispersion,  $f^0 = 1/(2\pi\tau)$ ;

$$\epsilon = (\epsilon^0 + \epsilon^\infty) / 2 \quad \text{and} \quad \kappa = (\kappa^0 + \kappa^\infty) / 2.$$

Substitution of the equations in (1) into equations (6.a) and (6.c) yields:

$$C = C_1 + C_2 / (1 + (\omega\tau)^2)$$

and

$$G = G_1 + G_2 (\omega\tau)^2 / (1 + (\omega\tau)^2), \quad (7)$$

where;  $C_1 = \epsilon^\infty$  and  $C_1 + C_2 = \epsilon^0$

$$G_1 = \kappa^0 \quad \text{and} \quad G_1 + G_2 = \kappa^\infty.$$

The complex admittance,  $Y^*$ , of the material is given by;

$$\begin{aligned} Y^* &= G + C\omega j, \\ &= G_1 + \frac{G_2 (\omega\tau)^2}{1 + (\omega\tau)^2} + \left\{ C_1 + \frac{C_2}{1 + (\omega\tau)^2} \right\} \omega j \\ &= G_1 + G_2 - \frac{G_2}{1 + (\omega\tau)^2} + \left\{ C_1 + \frac{C_2}{1 + (\omega\tau)^2} \right\} \omega j \end{aligned} \quad (8)$$

and the complex impedance,  $Z^*$ , by;

$$Z^* = 1/Y^* = 1/G + j/\omega C = R + Xj, \quad (9)$$

where  $R=1/G$  is the resistance and  $X=1/(\omega C)$  is the reactance. Note that at low frequencies the admittance is a pure conductance equal to  $G_1$ . If  $C_1=0$ , the admittance is again a pure conductance,  $G_1+G_2$ , at very high frequencies.

Each of the complex quantities,  $\epsilon^*$ ,  $Y^*$  and  $Z^*$  describes a vector in the complex plane with corresponding magnitude and direction. The complex impedance  $Z^*$ , for example, is completely described by its coordinates in the complex plane ( $R, X$ ) or by its magnitude and phase angle,  $\theta$ , which gives the direction of  $Z^*$  with respect to the positive real axis. Thus, in the latter case, the magnitude or modulus  $|Z|$  of  $Z$  is

$$|Z| = \sqrt{R^2 + X^2} \quad (10)$$

and the phase angle is

$$\theta = \arctan (X/R). \quad (11)$$

Either  $|Z|$  and  $\theta$  or  $R$  and  $X$  are quantities that can be empirically determined by measuring the voltage developed across the material in response to sinusoidal current excitation. Thus,  $\theta$  is the angular phase displacement between the measured voltage and the transmitted current. Importantly, equations (6)-(11) show how the dielectric relaxation described by equation (5) manifests in measurable electrical properties. These equations consequently provide the vehicle by which properties of the dispersion can be determined from the measured frequency dependence of the admittance or impedance of the material.

Dielectric relaxation in cell suspensions and in both in vitro and in vivo tissue preparations has been extensively studied at frequencies from 10 Hz to greater than 30,000 MHz. Dispersion phenomena in these materials are found



to be considerably more complex than that described above for a hypothetical single time constant system. For example, the curve shown in Figure 3 gives the frequency dependence of the dielectric constant of muscle tissue. This curve, which is typical of biological material, shows the presence of three separate dispersions, denoted by  $\alpha$ ,  $\beta$  and  $\gamma$  (cf. Figure 2). Each dispersion corresponds to a different relaxation mechanism, two of which prevail by virtue of the intrinsic structural heterogeneity of tissue and are important in the present context. The first, giving rise to the  $\alpha$ -dispersion in the audio-frequency range, entails dielectric relaxation of the ionic atmospheres surrounding tissue cells. The second, giving rise to the  $\beta$ -dispersion in the 10-100 kHz frequency range, entails capacitative current fluxes across cell membranes.

A more detailed review of the  $\alpha$  and  $\beta$  dispersions and underlying relaxation mechanisms in normal tissue is beyond the scope of this report. However, certain theoretical treatments that have been formulated to understand these dispersions [28,29] are of particular interest. These treatments give quantitative accounts of the dielectric dispersion(s) in homogeneous suspensions of the following:

A) spherical dielectric particles;

Maxwell [21] showed that the conductivity  $\kappa$  of such a suspension is given by;

$$\frac{\kappa - \kappa_1}{\kappa + 2\kappa_1} = p \left\{ \frac{\kappa_2 - \kappa_1}{\kappa_2 + 2\kappa_1} \right\},$$

where  $\kappa_1$  and  $\kappa_2$  are the conductivities of the suspending and suspended phases, respectively, and  $p$  is the volume fraction of the suspended phase. Solving the above for  $\kappa$ ;

$$\kappa = \kappa_1 \left\{ \frac{2(1-p)\kappa_1 + (1+2p)\kappa_2}{(2+p)\kappa_1 + (1-p)\kappa_2} \right\}. \quad (12)$$

The complex admittances,  $y^* = \kappa_1 + \epsilon_1 \epsilon_r \omega j$  and  $y^* = \kappa_2 + \epsilon_2 \epsilon_r \omega j$ , can be substituted for  $\kappa_1$  and  $\kappa_2$  in equation (12) to obtain an expression for the complex admittance,  $Y^*$ , of the suspension. It follows that the parameters in the dispersion equations (6) are given by;

$$\tau = \epsilon_r \left\{ \frac{\epsilon_2 + 2\epsilon_1}{\kappa_2 + 2\kappa_1} \right\}; \quad \epsilon^\circ = \epsilon^\infty + 9p \left\{ \frac{(\epsilon_2 \kappa_1 + \epsilon_1 \kappa_2)^2}{(\epsilon_2 + 2\epsilon_1)(\kappa_2 + 2\kappa_1)^2} \right\};$$

$$\kappa^\circ = \kappa_1 \left\{ 1 + 3p \frac{\kappa_2 - \kappa_1}{\kappa_2 + 2\kappa_1} \right\}; \quad \epsilon^\infty = \epsilon_1 \left\{ 1 + 3p \frac{\epsilon_2 - \epsilon_1}{\epsilon_2 + 2\epsilon_1} \right\};$$

$$\kappa^{\infty} = \kappa^0 + \left\{ \frac{\epsilon_r (\epsilon^0 - \epsilon^{\infty})}{\tau} \right\}. \quad (13)$$

Significantly, the dispersion is characterized by a single time constant that is a function of only intrinsic electrical properties of the suspending and suspended phases. Being independent of particle size, the same dispersion is produced by a homogeneous suspension of identically sized particles as by a suspension with a distribution of particle sizes, provided the respective  $p$  values for the suspensions are the same.

- B) spherical dielectric particles, each surrounded by a concentric shell with dielectric properties different from those of the particles or suspending medium;

Maxwell [21] showed that the conductivity of each sphere with its shell can be characterized by an equivalent homogeneous sphere conductance,  $\hat{\kappa}_2$ ;

$$\hat{\kappa}_2 = \kappa_3 \left\{ \frac{2(\kappa_3 + \kappa_2)(R+d)^3 - 2(\kappa_3 - \kappa_2)R^3}{(2\kappa_3 + \kappa_2)(R+d)^3 + (\kappa_3 - \kappa_2)R^3} \right\}, \quad (14)$$

where  $d$  is the thickness of the shell surrounding each sphere of radius  $R$ ,  $\kappa_3$  is the conductivity of the shell and  $\kappa_2$  is as defined above. If  $d$  is small, powers of  $d$  higher than 1 can be neglected and Equation (14) reduces to:

$$\hat{\kappa}_2 = \frac{\kappa_2 + d\kappa_3[2+(\kappa_2/\kappa_3)]/R}{1 + d[2+(\kappa_2/\kappa_3)]/R}.$$

Finally, if  $d$  is small compared to  $R$ :

$$\hat{\kappa}_2 = \kappa_2 + (d\kappa_3/R)[2+(\kappa_2/\kappa_3)]. \quad (15)$$

Substitution of  $\hat{\kappa}_2$  for  $\kappa_2$  in equation (12) yields the expression for the conductivity of the suspension. As in (A), the complex admittance  $Y^*$  of the suspension is given by substitution of the appropriate complex admittances for the conductivities. The complex admittance of the shell itself is given generally by:

$$Y^* = (\kappa_{3,N} + \kappa_{3,P})/d + (\epsilon_{3,N} + \epsilon_{3,P})\epsilon_r \omega j/d,$$

where subscripts  $N$  and  $P$  refer to the conductivities and dielectric constants of the shell in directions normal and parallel to the plane of the shell, respectively. Thus, the complex admittance of the adsorbent layer must generally include terms for both radial and tangential conduction, but the latter are assumed negligible here. The parametric equations for  $\tau$ ,  $\kappa^0$  and  $\kappa^{\infty}$  then reduce to the following if the adsorbent layer is assumed poorly conducting and the internal and external media are purely resistive:

$$\begin{aligned}
\tau &= RC_3 \left\{ \frac{\kappa_2 + 2\kappa_1}{2\kappa_2\kappa_1 + RG_3(\kappa_2 + 2\kappa_1)} \right\} \\
\kappa^0 &= \kappa_1 \left\{ 1 - (3p/2) \frac{2\kappa_1\kappa_2 + 2RG_3(\kappa_1 - \kappa_2)}{2\kappa_1\kappa_2 + RG_3(2\kappa_1 + \kappa_2)} \right\} \\
\kappa^\infty &= \kappa_1 \left\{ 1 + 3p \frac{\kappa_2 + \kappa_1}{\kappa_2 + 2\kappa_1} \right\}
\end{aligned} \tag{16}$$

Bubble-Induced Dielectric Dispersions. Although conceived principally to understand dielectric dispersion in cell suspensions and tissues per se, the above equations are equally as applicable to gas bubbles as to cells suspended in a liquid medium. After simplification by substitution of  $\kappa_2=0$  and  $\epsilon_2=1$ , values characteristic of a suspended gas phase, these equations indicate that gas bubbles in tissue will produce dielectric dispersions of their own, notwithstanding any other impact they may also have on the dispersions which are characteristic of bubble-free tissue.

In the hypothetical case where gas bubbles in a tissue are spherical and homogeneously distributed and the influences of any adsorbed proteins, etc., at the gas-liquid interfaces are neglected, the dispersion equations (6) - (9) are applicable with parameters as given in (A) above. With substitution of  $\epsilon_2 = 1$  and  $\kappa_2 = 0$ , the parametric equations in (13) reduce to:

$$\begin{aligned}
\tau &= \epsilon_r \left\{ \frac{1+2\epsilon_1}{2\kappa_1} \right\} ; & \epsilon^0 &= \epsilon^\infty + 9p \left\{ \frac{1}{4(1+2\epsilon_1)} \right\} ; \\
\kappa^0 &= \kappa_1 \left\{ 1 - \frac{3p}{2} \right\} ; & \epsilon^\infty &= \epsilon_1 \left\{ 1 + 3p \frac{1-\epsilon_1}{(1+2\epsilon_1)} \right\} ; \\
\kappa^\infty &= \kappa^0 + \left\{ \frac{\epsilon_r(\epsilon^0 - \epsilon^\infty)}{\tau} \right\} = \kappa_1 \left\{ 1 - \frac{3p}{2} \cdot \left\{ 1 - \frac{3}{(1+2\epsilon_1)^2} \right\} \right\}.
\end{aligned} \tag{17}$$

Properties of the bubble-induced dispersion will qualitatively resemble those discussed above for heterogeneous media in general, and will exhibit additional dependence on the relative volumes of the bubbles. Thus, with increasing bubble volume,  $p$ , characteristics of the dispersion will change as follows:

- a)  $\tau$ , and hence the characteristic frequency  $f^0$ , being independent of  $p$ , will remain unchanged;

- b)  $\kappa^\circ$  will decrease;
- c) because  $3/(1+2\epsilon_1)^2 < 1$ ,  $\kappa^\infty$  will also decrease, and;
- d) by inspection,  $\kappa^\circ$  will decrease more rapidly than  $\kappa^\infty$ . Hence, the span of the impedance locus given by the difference between the limiting low and high frequency resistances,  $R^\circ - R^\infty = 1/\kappa^\circ - 1/\kappa^\infty$ , will increase.

The location of the bubble-induced dispersion in the frequency domain will be dependent only on intrinsic electrical properties of the suspended gas phase and the surrounding medium.

Complete descriptions of the dielectric properties of bubbles in physiological systems require consideration of gas-liquid interfacial properties. Gas bubbles rapidly adsorb chemical constituents from the surrounding liquid phase, and for all practical purposes, never exist free of such adsorbents in tissue [8,45-47]. Gas-liquid interfaces in physiological liquids consequently carry a capacitive double layer, by virtue of the boundary between the regions of different  $\epsilon/\kappa$  values in the adsorbent layer, that is in turn surrounded by a dipolar atmosphere. These interfacial features can theoretically cause dielectric dispersions that fall into three categories to which the model in (B) is applicable for homogeneous suspensions of spherical bubbles:

Bubble-Induced Dispersion Due to the Presence Per Se of an Adsorbed Macromolecular Layer. The first category consists of dielectric properties of an adsorbent layer which occur irrespective of its intrinsic structure. The applicable dispersion equations are obtained as outlined in (B). Substitution of  $\kappa_2=0$  into the parametric expressions in (16) yields:

$$\begin{aligned}\tau &= C_3/G_3 \\ \kappa^\circ &= \kappa_1(1-3p/2) \\ \kappa^\infty &= \kappa_1(1+3p/2)\end{aligned}\tag{18}$$

To the extent that the resistive and capacitive properties of adsorbed layers around different bubbles are the same, the bubble-induced dispersion attributable to adsorbed macromolecules will occur about a single characteristic frequency and increase in magnitude in proportion with both  $p$  and  $R$  (the latter because  $p$  increases with  $R$  when the number of bubbles remains constant).

The adsorbent layer may be assumed to have a conductance similar to those of other biomembranes;  $G=0.1$  to  $1.0$  mho/cm<sup>2</sup>; and, due to its smaller thickness, a capacitance about twice those of biomembranes;  $C=2$  to  $20$   $\mu$ f/cm<sup>2</sup>. Time constants calculated from these parameters correspond to characteristic frequencies in the range of  $0.8$  to  $80$  kHz. The magnitude of the dispersion will also be high. The conductivity  $\kappa$  will increase by a factor of about  $6p$  over the two decade range of frequencies spanning  $f^\circ$ .

Bubble-Induced Dispersion Due to the Intrinsic Structure of an Adsorbed Macromolecular Layer. Schwan [28] has shown that the dispersion arising from

the intrinsic structure of a biomembrane must be characterized by a single time constant corresponding to a characteristic frequency in the range of 10 Hz to 1 kHz. However, a dielectric dispersion in this frequency range is not always observed in biological preparations which contain intact membranes [28]. Thus, the expected dispersion may occur at frequencies too low to be measured and/or may be too small to be resolved. Dispersions caused by the intrinsic structure of adsorbed macromolecular layers on bubbles are expected to be similarly elusive.

Bubble-Induced Dispersion Arising from the Presence of A Diffuse Double Layer or "Ionic Atmosphere" Surrounding the Exterior of the Adsorbent Layer. The mechanism by which ion atmospheres may contribute to the overall dielectric behavior of bubbles is different from those underlying the dispersions discussed above. The relaxation arises from an applied field-induced displacement of the polarizable atmosphere from its normally symmetric distribution around each bubble. The displacement causes the appearance of an induced dipole moment which characterizes the polarization. The theory of the dispersion arising from this polarization is developed in a fashion analogous to that for the dispersion arising from a concentric shell or adsorbent layer. The polarization is simply simulated by stipulating the existence of yet another shell or "surface layer" with appropriately defined properties around the sphere. Because of the relatively unique nature of these properties, however, the dielectric behavior of a surface layer diverges from that discussed above for the adsorbent layer. Surface polarization typically exhibits an impedance whose phase angle is constant and whose magnitude is a power function of the frequency. Cole and Cole [6] have shown that the overall dispersion is described by an expression identical to that given in equation (5), but where  $(j\omega\tau)$  in the denominator is raised to a power of  $(1-a)$ , where  $a$  is valued between zero and unity. Thus, the dispersion simulates that which is obtained in a system with a distribution of time constants arising from a series of different polarizing elements each with frequency independent properties.

Fricke and Curtis [9] studied surface conductance in a variety of colloidal and aqueous suspensions of nonconducting particles. The magnitudes of the dispersions in these systems varied approximately as a negative power of the frequency, inversely with the particle size and roughly in proportion to the fractional volume of the suspended phase. Schwan [21] compiled other empirical results to examine the particle R dependence of the characteristic frequency about which the dispersion occurs. The characteristic frequency was found to decrease to frequencies too low to be safely applied in *in vivo* applications with increasing R up to only about 1.5  $\mu\text{m}$ .

## Appendix B.

## Physical Basis of Electrical Impedance Plethysmography

When the impedance of any given body segment is monitored at a fixed excitation frequency over time periods short with respect to the cardiac cycle, a pulsatile impedance waveform is observed superimposed on the baseline impedance governed by longer-term average segmental geometry and composition. These pulsatile impedance waveforms arise from volume changes caused by the pulsing of blood through the monitored body segment with each cardiac cycle. The systolic and diastolic phases of the segmental cardiac pulse partially resolve as distinct features in the impedance waveform because segmental arterial filling during systole precedes and is more rapid than venous runoff during diastole. Because blood is more conductive than tissue, the impedance of the segment decreases when a pulse of blood enters the segment and increases when the pulse flows out of the segment. Such waveforms consequently provide information from which segmental blood flow and other hemodynamic parameters can be computed [22,25]. The following provides an outline of the biophysical basis for such computations.

The passive electrical properties of tissue are governed by ionic conduction mechanisms that follow classical electrical laws in which geometry plays a principal role. Tissues permit ionic electrical current to pass in three dimensions distributed along continuous isopotential field lines that are influenced by volume changes within the tissue under study. The resistance to this current flux is directly related to the length and specific resistivity of the conductor and inversely related to the conductor cross-sectional area:

$$R = \frac{\rho L}{A}, \quad (1)$$

where:

$\rho$  = specific electrical resistivity of a unit volume ( $1 \text{ cm}^3$ ) of the sample material in ohm-centimeters

$L$  = length of the sample in centimeters

$A$  = cross-sectional area of the sample in square centimeters.

If the sample is assumed to be cylindrical,  $V = A \cdot L$ , and Eq. (1) becomes:

$$R = \frac{\rho L^2}{V}. \quad (2)$$

At the end of diastole, when a given body segment contains a minimum amount of blood, Eq. (2) is rearranged to give the baseline segmental volume,  $V_0$ , in terms of the baseline segmental resistance,  $R_0$ :

$$V_0 = \frac{\rho L^2}{R_0}, \quad (3)$$

where, the specific resistivity,  $\rho$ , is conditioned by properties of the entire volume of monitored tissue. As an added volume of blood,  $V_b$ , is pumped into the segment during systole, the segmental resistance,  $R_m$ , decreases from baseline by an amount  $\Delta R = R_o - R_m$ . The tissue is then considered to consist of two parallel conduction paths; one through the added blood with resistance  $R_b$ , and the other through the baseline tissue volume with resistance  $R_o$ . The measured segmental resistance is consequently the mutual resistance,  $R_m$ , of these two conduction paths, given by the parallel combination of  $R_b$  and  $R_o$ :

$$R_m = \frac{R_o \cdot R_b}{R_o + R_b}, \quad (4)$$

If the added volume of blood is assumed to accumulate in a uniform cylinder with resistivity equal to that of blood,  $\rho_b$ , Eq. (3) can be applied and substituted into Eq. (4) to give:

$$R_m = \frac{R_o \cdot \rho_b \cdot L^2}{V_b R_o + \rho_b L^2}. \quad (5)$$

The typical value of  $\rho_b$  is 150 ohm-cm. Solving Eq. (5) for  $V_b$ :

$$V_b = \frac{\rho_b L^2}{R_m} - \frac{\rho_b L^2}{R_o}. \quad (6)$$

The relationship between the change in segmental volume and the change in segmental resistance is given by differentiating Eq. (6):

$$\frac{\delta V_b}{\delta R_m} = \frac{-\rho_b L^2}{R_m^2}. \quad (7)$$

Most impedance plethysmographs provide a positive deflection for decreasing  $R_m$ , enabling the negative sign in Eq. (7) to be dropped. Noting that  $R_o = R_m$ , the differential is approximated;  $\Delta V_b / \Delta R = \delta V_b / \delta R_m$ ; and substituted to yield:

$$\Delta V_b = \frac{\rho_b \cdot L^2 \cdot \Delta R}{R_o^2}. \quad (8)$$

Eq. (8) provides the basis for impedance plethysmography, giving the pulsatile volume (the volume pumped into the segment during each cardiac cycle) in terms of the electrical characteristics of the segment. The total segmental blood flow, BF, is given by multiplying the pulsatile volume by the heart rate, Hr:

$$BF = \Delta V_b \cdot Hr = \frac{\rho_b \cdot L^2 \cdot \Delta R \cdot Hr}{R_o^2}. \quad (9)$$

The pulsatile impedance waveform for any given body segment is neither a simple step function nor composed wholly of features arising from arterial blood inflow. Practical application of Eq. (9) consequently requires:

- a) resolution of features in the measured impedance waveform that are attributable to arterial inflow from those attributable to venous outflow, and;
- b) approximation of the integral of the time-differential of the measured instantaneous resistance changes,  $R_o - R_m$ , that are attributable to arterial inflow.

The simplest and most common method used to meet these requirements is to assume that segmental arterial inflow occurs in "on/off" fashion, that the arterial inflow "plug" manifests completely in the portion of the impedance waveform preceding the dicrotic notch, and that the single-valued resistance amplitude of this inflow plug,  $R_o - R_m$ , is given by using the value of  $R_m$  where a linear projection of the maximum systolic upslope of measured instantaneous  $R_m$  values intersects the end of systole. According to this "forward projection" method, Eq. (9) is applied as [17]:

$$BF = \Delta V_b \cdot Hr = \frac{\rho_b \cdot L^2 \cdot (\delta R / \delta t)_{\max} \cdot T_s \cdot Hr}{R_o^2}, \quad (10)$$

where the systolic time,  $T_s$ , is the duration of that portion of the impedance pulse which begins at the first rise from baseline and ends at the subsequent local minimum that defines the dicrotic notch. Nyboer [25] proposed an alternative "back-projection" method resulting in the following analog of Eq. (10):

$$BF = \Delta V_b \cdot Hr = \frac{\rho_b \cdot L^2 \cdot (\Delta R)_{\max} \cdot Hr}{R_o^2}. \quad (11)$$

Indices of segmental vascular elasticity and tone are obtained as follows from other features of the pulsatile resistance waveforms [39,41,44]:

- 1) Rheographic index (RI) -- A measure of the relative level of pulsatile blood filling of a given body segment as determined from the maximum amplitude of the systolic portion of the impedance pulse;
- 2) Dicrotic amplitude (B) -- Height of the pulsatile waveform at the dicrotic notch;
- 3) Diastolic amplitude (C) -- Amplitude of the waveform peak after the dicrotic notch;
- 4) Dicrotic index (DCI) -- The ratio,  $B/RI$ , of the amplitude of the pulsatile waveform at the height of the dicrotic notch to the maximum pulse amplitude, which reflects primarily the tone of the arterioles;
- 5) Diastolic index (DSI) -- A measure of venular tone determined from the



ratio,  $C/RI$ ;

- 6) Anacrotic duration (D) -- Duration of anacrotic phase of each pulsatile wave, s, determined as the period from the start of a waveform pulse to the time of the dicrotic notch;
- 7) Pulse duration (T) -- Duration of the total pulsatile waveform cycle, s, determined as the period between the starts of two successive pulse waves;
- 8) Anacrotic index (AI) -- The ratio,  $D/T$ , of the duration of the anacrotic phase of the pulse wave to the duration of the entire cardiac cycle, used to assess the elasticity and tone of the vessels with large and intermediate lumens (The anacrotic index is inversely related to vascular contractility);
- 9) Total area (ST) -- Total area under the pulsatile waveform between the starts of two successive waveform pulses;
- 10) Systolic area (SS) -- Area under the systolic portion of the pulsatile waveform from the start of the pulse to the time of the dicrotic notch;
- 11) Diastolic area (SD) -- Area under the diastolic portion of the pulsatile waveform from time of the dicrotic notch to the end of the pulse;
- 12) Pulse transit time (PTT) -- The time interval between the onset of the ECG QRS complex and the onset of the IPG pulse waveform;
- 13) Systolic inflow angle (IA) -- Average angle of the systolic upslope between attainment of 10 and 90% maximum, providing an index that is inversely related to arterial contractility or cardiac force of contraction;
- 14) Systolic rise time (RT) -- Duration of the period of the systolic upslope between attainment of 10 and 90% maximum, providing another index inversely related to arterial contractility.

Finally, the segmental base resistance,  $R_o$ , may be monitored to determine the relative degree of blood pooling taking place in the body segment [23]. Baseline resistance values for a given segment are substituted into Eq. (3) to calculate the segment's baseline "electric" volume at specific times during an experimental protocol. As with pulsatile volume change calculations, but over much longer time frames, differences in various "electric" volumes can then be used to estimate the corresponding segmental volume changes attributable to changes in baseline blood volume.

A tetrapolar electrical impedance system is used in experimental settings to measure the required resistances. The typical system introduces a high-frequency, low-current signal into an outer set of circumferential strip or spot electrodes designated as I1 and I2. An inner set of electrodes, designated E1 and E2, define the length of the monitored segment and are the points across which the segmental electrical conductivity is measured. A three-lead electrocardiogram is measured using a separate monitor to enable determination of heart rate and pulse transit times. Thus, in addition to the

ECG, the following measures are sampled and recorded for each monitored segment at a rate high compared to the heart rate (e.g., 200 Hz):

$R$  = Instantaneous resistance, the time course of which defines the baseline and pulsatile segmental resistances;

$\Delta R/s$  = Instantaneous first derivative of the resistance over the sampling interval, s

The data for each cardiac cycle are then analyzed at the end of a several-heartbeat data acquisition period to obtain the quantitative values of baseline volumes (ml for total tissue volume or ml/100 ml of body tissue for blood volume), segmental blood flow (ml/minute or ml/100 ml of body tissue/minute) and other hemodynamic parameters.

## APPENDIX C.1

EFFECTS OF DECOMPRESSION-INDUCED GAS BUBBLES ON  
THE ELECTRICAL IMPEDANCE SPECTRUM OF GELATINE

W.A. Gerth<sup>\*</sup>, Y.C. Wu<sup>\*</sup>, L.D. Montgomery<sup>+</sup>

<sup>\*</sup>F.G. Hall Hypo/Hyperbaric Center  
Box 3823, Duke University Medical Center  
Durham, North Carolina 27710 USA  
Ph. (919) 684-5902

<sup>+</sup>LDM Associates  
1764 Emory Street  
San Jose, California 95126 USA  
Ph. (408) 293-7447

Presented at the  
1990 Joint Meeting on Diving and Hyperbaric Medicine  
August 12-17, 1990  
The Okura Hotel, Amsterdam THE NETHERLANDS

Indicate below the numbers and topics of sessions in which your abstract might be programed (see list of suggested topics.)

1st Choice: # ...2... Title Decompression Sickness

2nd Choice: # ..... Title .....

PRESENTATION PREFERENCE (scientific sessions only)

Preferred choice (CHECK ONE ONLY)

☒ Slide presentation

☐ Poster presentation

☐ Either

Do not fold this sheet.  
Use cardboard backing  
when mailing.

## 1990 JOINT MEETING ON DIVING AND HYPERBARIC MEDICINE

EFFECTS OF DECOMPRESSION-INDUCED GAS BUBBLES ON THE ELECTRICAL IMPEDANCE SPECTRUM OF GELATINE. W.A. Gerth,<sup>1</sup> Y.C. Wu<sup>1</sup> and L.D. Montgomery.<sup>2</sup>

<sup>1</sup>Duke University Hyperbaric Center, Durham, NC 27710, USA and

<sup>2</sup>LDM Associates, San Jose, CA 95126, USA.

Increases in the resistance or impedance of decompressed liquids and tissues to electric currents of various fixed frequencies have been used as indices of bubble formation and growth. These indices have been of limited utility because they are also affected by many factors other than bubble formation. These approaches have been extended, using Electrical Impedance Spectroscopy, to determine if more specific information is embodied in bubble-induced changes in the frequency dependence of the impedance. A computer-controlled impedance analyzer was used to periodically measure the impedance spectra of gelatine preparations in which bubble formation and growth was induced by hypobaric decompression. Each spectrum consisted of complex impedances measured at each of a series of discreet current frequencies ranging from 85 Hz to 10 kHz. In some preparations, depending on the presence of surface active additives, bubble formation was accompanied by a distinctive set of changes in dielectric properties that were reversible with recompression and bubble resolution. This set included changes in the shapes and positions of the impedance locus and its transforms and changes in the values of parameters obtained from least-squares fits of simple equivalent circuit models. Most elements of this dielectric response were greatly attenuated or absent in preparations lacking surface active agents, indicating that the dielectric effects of bubbles are conditioned by bubble effects on the structure and composition of the vicinal liquid. Continued development of this approach promises to provide a specific, noninvasive and quantitative means to detect bubble formation and resolution in man. (Supported by USN Contract N00014-87-C-0166)

Name and mailing address of presenting author:

Wayne A. Gerth, Ph.D.

Duke University Hyperbaric Center, Box 3823

Durham, NC Zip 27710

Telephone No.: Area Code 919 # 684-5902

**IMPORTANT:** Your abstract will appear in the Program/Abstract book exactly as you submit it.

Read all instructions before you type abstract. Also see sample abstracts and typing instructions on reverse side.

The original ribbon copy of this abstract form (for reproduction by photo-offset) must be submitted together with, where possible, 10 photocopies.

**SEE REVERSE FOR ABSTRACT DEADLINES  
AND MAILING INSTRUCTIONS**

## INTRODUCTION

## SLIDE 0. TITLE

Liquids and living tissues are heterogeneous ionic conductors of electric current that present a resistance,  $R$ , to the passage of direct current and an impedance,  $Z$ , to the passage of alternating current. This resistance or impedance depends on the the physical dimensions and volume resistivity of the material. The latter resistivity is particularly sensitive to the presence and volume gas bubbles, which act as dielectric or nonconducting particles regardless of their locations or velocities. Early attempts to exploit these effects to detect bubbles in living tissue entailed measuring the impedance of tissue at single fixed frequencies. Unfortunately, such fixed frequency approaches provide no information by which observed impedance changes can be unequivocally ascribed to bubble formation and growth per se: Contributions from artifacts such as changes in temperature or cutaneous impedance at the sensing electrodes cannot be ruled out. However, considering that bubbles introduce new structural heterogenieties into the materials in which they form and grow, more bubble-specific information ought to be embodied in bubble-induced changes in the frequency dependence of the impedance; i.e., in the impedance spectrum of a material.

## SLIDE 1. Ohm's Law; Direct current.

In accord with Ohm's law, a certain voltage  $V$  is developed across any given conductor in response to passage of a direct current of amplitude  $I$ : The ratio of  $V$  to  $I$  gives the resistance,  $R$ . Significantly, this equilibrium voltage is not achieved immediately on initial application of current to a structurally heterogeneous conductor.

SLIDE 2.  $V$  response to step function application of  $I$ .

This figure provides an idealized illustration of what occurs in such cases. The left panel shows an applied step function excitation potential, with voltage on the ordinate and time on the abscissa. The corresponding voltage response of the material is shown on the right. Only a partial polarization occurs immediately on application of current: The remainder of the response occurs exponentially over time as charge accumulates at boundaries between different structural features in the material. This time dependence of the polarization is called dielectric relaxation. When the applied current alternates sinusoidally at some nonzero frequency, dielectric relaxation causes the voltage response to be phase shifted and attenuated with respect to the applied current by amounts that depend on the frequency.

## SLIDE 3. Ohm's law; Alternating current.

These phenomena are considered quantitatively using a general form of Ohm's law, where the voltage response is decomposed into real and imaginary components of a complex number. The real component gives the fraction of the response which is in-phase with the applied current. The imaginary component gives the remaining fraction which is  $90^\circ$  out-of-phase with the

current. This complex voltage is divided by the current to give the complex impedance  $Z$ . The real part of  $Z$  is the resistance  $R$  and the imaginary part is the reactance  $X$ . In tissue, where any inductive properties manifest only at extremely low excitation frequencies, the reactance is in turn a function of the capacitance  $C$  as indicated. As a result of dielectric relaxation phenomena, the resistance, reactance and overall impedance of a heterogeneous conductor vary with the frequency of the applied current. This variation is in turn governed by the types, extents and geometries of the structural heterogeneities in the material. Thus, gas bubble formation and growth must effect the frequency dependence of the impedance, as well as the value of the impedance at any particular frequency.

The purpose of the present study was to use Electrical Impedance Spectroscopy to verify that gas bubble formation and growth manifests a unique "dielectric signature" in the impedance spectrum of the host material. Gelatine preparations containing various types and concentrations of surface-active agents were studied. Bubble formation and growth was induced by hypobaric decompression.

#### MATERIALS AND METHODS

##### SLIDE 4. EIS System photograph

The Electrical Impedance Spectroscopic system shown in this photograph was developed to measure the impedance spectra. The system consisted of a Schlumberger Technologies, Solartron 1260 Impedance/Gain-Phase Analyzer controlled via an IEEE-488 interface by a Digital Equipment Corporation VAXstation 3200 computer.

Each impedance spectrum was obtained by measuring the voltage developed across a gel sample in response to sinusoidal electric current excitation at each of a series of discrete frequencies from 85 to 10 kHz. A signal generator and current amplifier in the 1260 provided the excitation signal which was passed through the sample and terminated at a current input channel on the 1260, where the amplitude and phase of the current actually passed through the sample was measured. System software written for this work configured the analyzer for spectrum acquisition, setting values for all analyzer functions, including the excitation voltage and current and the frequencies to be swept. The software also handled all other aspects of Analyzer function, data acquisition and data processing.

##### SLIDE 5. Gel Cartridge Schematic

The electrochemical cell schematized here was developed to contain the gelatine preparations, while allowing them to be decompressed to produce bubble formation and growth. A current electrode plate (316 stainless steel) was embedded in each of two plexiglass pistons, one at either end of a plexiglass cylinder (3.5 cm I.D., 39 cm length). One piston was movable to accommodate volume changes caused by bubble growth and resolution in the material between the electrodes. Two additional pickup electrodes rings (also 316 ss) were embedded in the body of the

cylinder about midway between the current electrodes. These circumferential electrodes, with inner edges separated by 4 cm, defined a fixed volume of monitored material in each experiment.

The cell was assembled containing a given gelatine preparation that had been warmed to sol-state and air-saturated at ambient barometric pressure. After the cell was cooled in an ice bath to gel the preparation, it was inserted into a transparent plexiglass chamber. The latter could be decompressed to any hypobaric pressure greater than about 1 mm-Hg at any desired rate up to explosive to induce bubble formation and growth. The chamber afforded ready visual observation of the cell and test material. Shielded wires connected to each of the electrodes were collected into a bundle, passed through the chamber closure at one end of the chamber and connected to the Impedance Analyzer. The excitation current was passed through the gel across the end-plate current electrodes. The relative amplitude and phase of the voltage developed in response to this excitation was measured across the pickup electrodes.

Each impedance spectrum consisted of a series of discrete impedances measured at each of the separate frequencies in a given sweep.

#### SLIDE 6. Impedance locus of Bubble-Free Gelatine.

An impedance spectrum is visualized as a locus of points in the impedance domain by plotting the reactance, or imaginary part of the impedance vs the resistance or real part of the impedance at each frequency in the spectrum. A measured impedance locus of a gelatine preparation at ambient atmospheric pressure is shown as typically obtained here. The locus is built from 50 discrete measurements at frequencies from 85 Hz to 2 kHz. Individual points are obscured in the figure because they are connected by straight lines. The point from the lowest frequency impedance defines the right-most or highest resistance end of the locus. The point from the highest frequency impedance defines the left-most or lowest resistance end of the locus. Points from impedances at intermediate frequencies define the intervening locus region. Thus, the locus shows how the resistance decreases with increasing frequency. Similarly, the locus shows how the reactance first decreases from zero at infinitely low frequency, then increases towards zero at infinitely high frequency.

In principle, this or any other impedance spectrum can be reproduced by an electric circuit of appropriately configured resistive and capacitive components. When described in terms of such an equivalent circuit, the spectrum is fully characterized by only a few discrete parameters that give values of the circuit resistances and capacitances.

#### SLIDE 7. Equivalent Circuit Schematic

The simple equivalent circuit model shown in this figure was used to describe the measured spectra. The complex impedance for the circuit is given analytically in terms of the circuit parameters by the equation at the bottom of the figure. This equation was fitted to each spectrum using an iterative nonlinear least squares routine based on Marquardt's algorithm.



## SLIDE 8. Nonlinear Least-squares Implementation

As shown in this figure, the algorithm was implemented using the norm of each observed impedance and that of the corresponding fitted impedance. The algorithm adjusted the model parameters to minimize the sum of squares, SS, for the impedances at the  $n$  different frequencies in each spectrum.

## RESULTS

Decompression without bubble formation caused no discernable change in the impedance spectrum of any preparation. In preparations containing surface active additives, bubble formation was accompanied by a distinctive set of changes in dielectric properties that were reversible with recompression and bubble resolution.

## SLIDE 9. Impedance Loci: Decompression/Bubble formation/Recompression SERIES; Na lauryl sulfate (0.5%)

The changes typically observed are evident in this figure. Different spectra taken at 5 min intervals throughout the course of an experiment are all drawn in a single plot. The cluster of similarly-shaped spectra at the right of the figure was taken before the preparation was decompressed. Successive spectra are displaced left-wards, reflecting dielectric changes caused by continued warming of the gel after having been cooled prior to insertion into the cartridge. The next cluster to the left was obtained after decompression had produced a profusion of bubbles in the preparation. The spectra are seen to be displaced towards more positive reactances and become narrower in span between low and high frequency resistances. Note that the resistances decreased rather increased, reflecting continued warming of the gel, the effects of which overrode any resistance-increasing influence of bubble growth.

Bubble-induced changes in the shapes and positions of the impedance loci and their transforms were also evident in changes in the values of the fitted equivalent circuit parameters.

## SLIDE 10. Fitted Equivalent Circuit Parameters: SERIES

This figure gives a graphic rendition of the parameter values obtained from the spectral series shown in the previous slide. Each parameter is shown vs. elapsed time in "strip chart" format, with the ordinate scaled such that the major ticks above and below each value at  $t=0$  represent + and - 20% deviation, respectively, from that value.  $R_s$  and  $R_p$  are in Ohms and  $C_s$  is in micro-farads.

Parameter values remained relatively stable until bubbles formed after decompression at an elapsed time of 47 min. The equivalent  $R_p$  was decreased and the equivalent  $C_p$  was increased in the next spectrum taken at time 50 min. These parameters continued to change throughout the ensuing period at reduced pressure in reflection of continued bubble growth. The failure of the series resistance  $R_s$  to increase was a

consequence of the relatively small overall bubble volume. After recompression of the sample to ambient barometric pressure at 120 min, the parameters returned to their pre-decompression values.

Analysis of residuals for the model fits indicate that the patterns for lack-of-fit were not changed by bubble formation and growth.

SLIDE 11. Residuals Analysis for Lack-of-Fit: NO Bubbles/Bubbles

Typifying the results of such analyses, the residuals for two fits are shown in this figure; one to a spectrum of a bubble-free gel and the other to a spectrum of the same gel after it had been decompressed to produce a profusion of bubbles. No significant change in the residuals distribution vs frequency is evident. An important indication of this result is that bubble-induced changes in the impedance spectrum are fully "captured" by changes in the equivalent circuit parameter values. The latter consequently provide valid quantitative indices of bubble formation and growth in the preparations.

It is important to note that bubble formation in these preparations displaces gel from the monitored volume between the pickup electrodes: The aqueous gel, which has a relatively high dielectric constant of about 70, is replaced by gas, which has a dielectric constant practically equal to 1. Material displacement alone must consequently cause the overall capacitance of the monitored volume, which is unchanged by design of the cartridge, to decrease.

SLIDE 12. Capacitance Transform Plots: Bubble Effects

Capacitance transforms of three impedance spectra from the preceding experimental series are shown here. Again, individual points are from impedances measured at each of the different frequencies. Curve B, obtained after decompression and bubble formation, is clearly displaced to lower capacitances to the left of curve A, which was taken immediately before decompression. Curve C illustrates that this leftward shift reverses with recompression and bubble resolution. Thus, as was typically observed, system capacitance changes were in proper accord with expectations based on bubble-induced exclusion of conductive material from the monitored volume.

When the results are viewed in the context of dielectric relaxation theory, however, other indications emerge that bubble formation and growth cause more than simple material exclusion.

SLIDE 13. Table 1.

If bubble formation had no effect other than to exclude conductive material from the monitored volume, theory indicates that the impedance locus properties and corresponding equivalent circuit parameters would change with increases in bubble volume as indicated in the third column of this table. Experimental violations of these theoretical prescriptions are clear by comparison to entries in the right-most column.

While  $\tau$  remained unchanged as predicted, the span of the impedance locus ( $R^0-R^\infty$ ) did not increase, but decreased with bubble formation and growth. Similarly, the equivalent circuit capacitance  $C_p$  increased, sometimes markedly, with bubble formation and growth, opposite the predicted behavior. These contrasts between simple theory and observed results can only be explained in terms of gas bubble effects on the structure and/or composition of the liquid surrounding the bubbles. Despite any gel displacement, the conductive material remaining after bubble formation contains regions with sharper gradients in dielectric constant and conductivity than the bubble-free gel.

This indication was further strengthened by observed influences of liquid composition and bubble number density on most elements of bubble dielectric effects. Simple exclusion theory accommodates no such dependence.

#### SLIDE 14. Equivalent $R_p$ vs Bubble Volume

This figure shows values of the  $R_p$  parameter as functions of bubble volume from different experiments with similar gelatine preparations.  $R_p$  clearly varies systematically with bubble volume in any given preparation. Recall, however, that  $R_p$  should increase with bubble volume according to simple exclusion, while it clearly decreased with bubble volume in these experiments. Moreover, these decreases were larger in the preparation in which more bubbles formed. Deviations of observation from theory were consequently larger with larger bubble number densities. Because gas-liquid interfacial area increases with bubble number density, the indication is strong that these deviations arise from solute adsorption at the bubble gas-liquid interfaces.

### CONCLUSIONS

#### SLIDE 15. Conclusions

In conclusion, bubble formation in gelatine effects the frequency dependence of the impedance in a fashion that cannot be explained by material exclusion alone. The dependence of these effects on liquid composition and on the bubble number density indicates that the effects arise from influences of the bubbles on liquid structure and composition in the vicinity of the bubble gas-liquid interfaces. These effects are emerging as essential features of a bubble "dielectric signature", the detection of which in vivo promises to provide a specific, noninvasive and quantitative means to detect bubble formation and resolution in decompressed animals and man.

### ACKNOWLEDGEMENT

This work was supported by USN Contract N00014-87-C-0166.

EFFECTS OF DECOMPRESSION-INDUCED GAS BUBBLES ON  
THE ELECTRICAL IMPEDANCE SPECTRUM OF GELATINE

W.A. Gerth<sup>\*</sup>, Y.C. Wu<sup>\*</sup>, L.D. Montgomery<sup>+</sup>

<sup>\*</sup>F.G. Hall Hypo/Hyperbaric Center  
Duke University Medical Center  
Durham, North Carolina USA

<sup>+</sup>LDM Associates  
San Jose, California USA

OHM'S LAW; Direct Current

$R = V/I$  ;       $R$  = Resistance (Ohms)

$V$  = Voltage (Volts)

$I$  = Current (Amperes)

SLIDE 2.

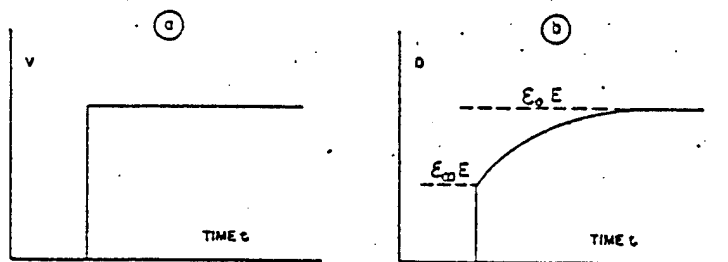


FIG. 2. A step function potential (a) applied to some dielectric sample will cause a time-dependence of polarization (b) if relaxation processes take place in the sample.

OHM'S LAW: Alternating current

$$Z^* = V^*/I ; \quad \text{complex voltage, } V^* = a + bj$$

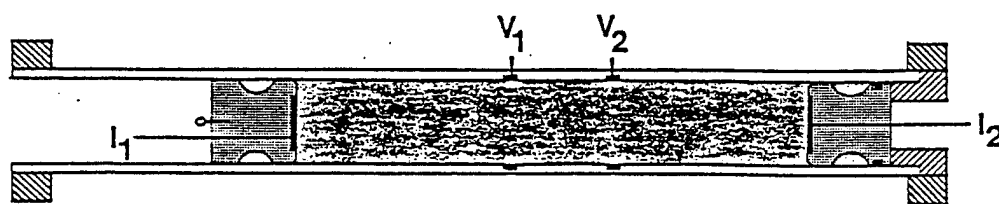
$$j = \sqrt{-1}$$

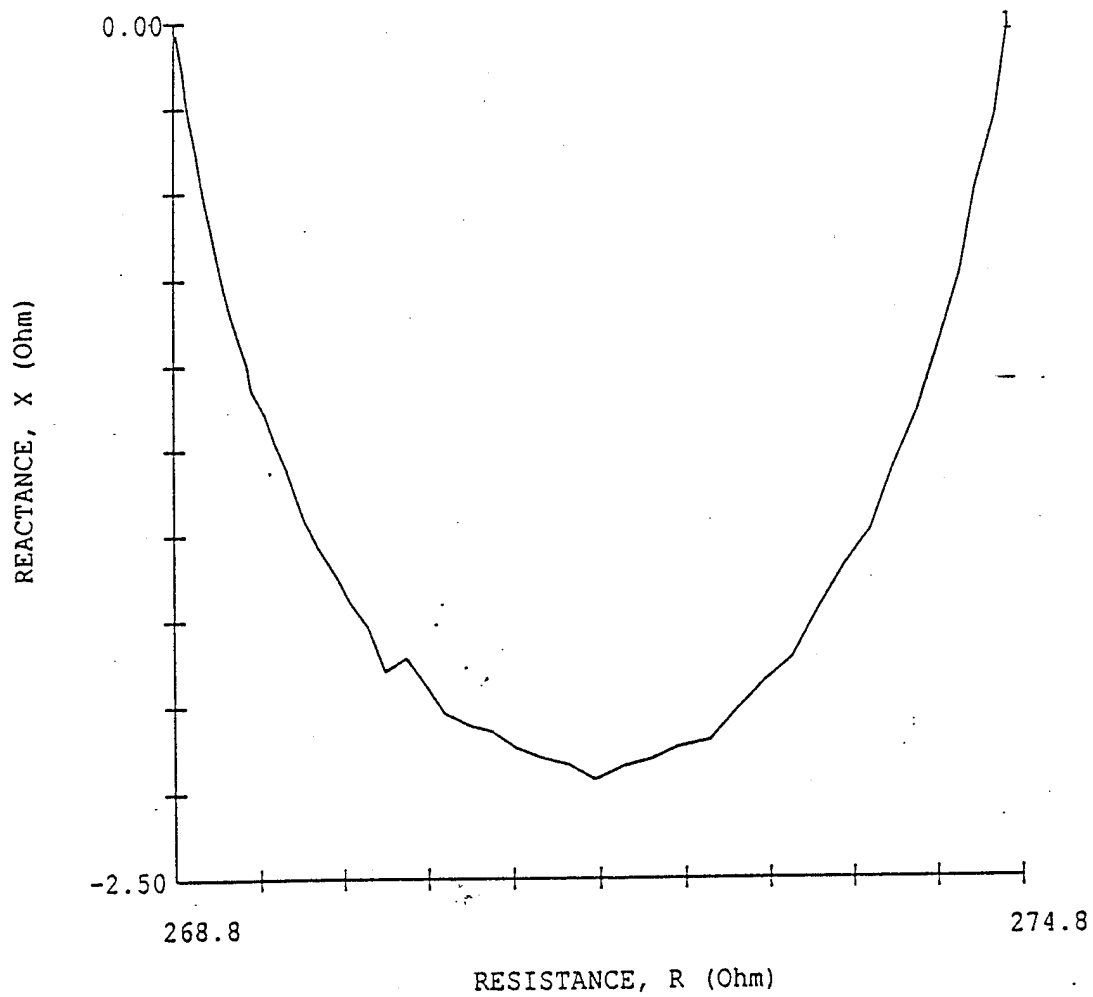
$$Z^* = R + Xj ; \quad \text{reactance, } X = -1/C\omega$$

$$\text{angular frequency, } \omega = 2\pi f$$

EIS SYSTEM PHOTOGRAPH

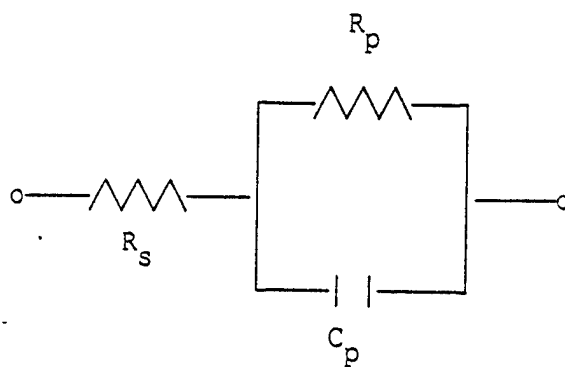
SLIDE 5.







EQUIVALENT CIRCUIT MODEL



$$Z^* = R_s + \frac{R_p}{1 + j\omega\tau} ; \quad j = \sqrt{-1}$$
$$\omega = 2\pi f$$
$$\tau = R_p \cdot C_p$$

### NONLINEAR LEAST SQUARES IMPLEMENTATION

Equivalent circuit parameters are adjusted to minimize SS:

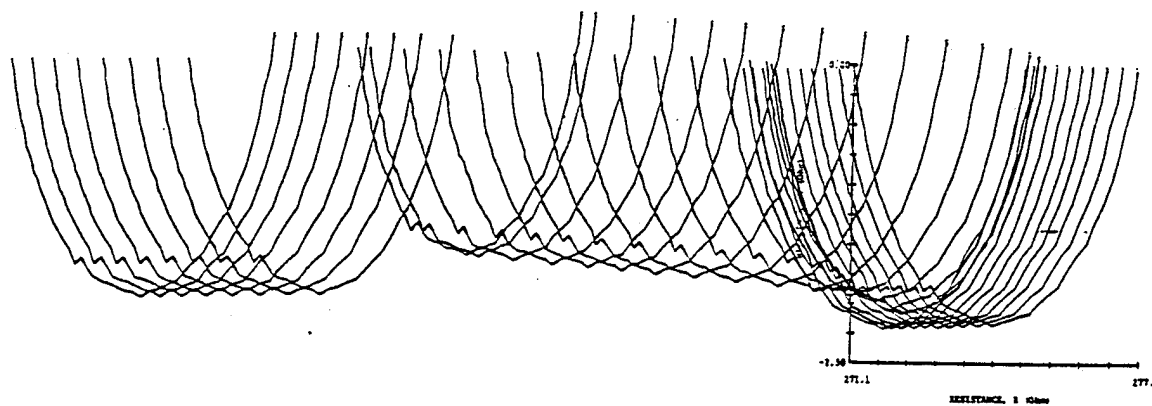
$$SS = \sum_{i=1}^n (|Z_i^*| - |\hat{Z}_i^*|)^2 ;$$

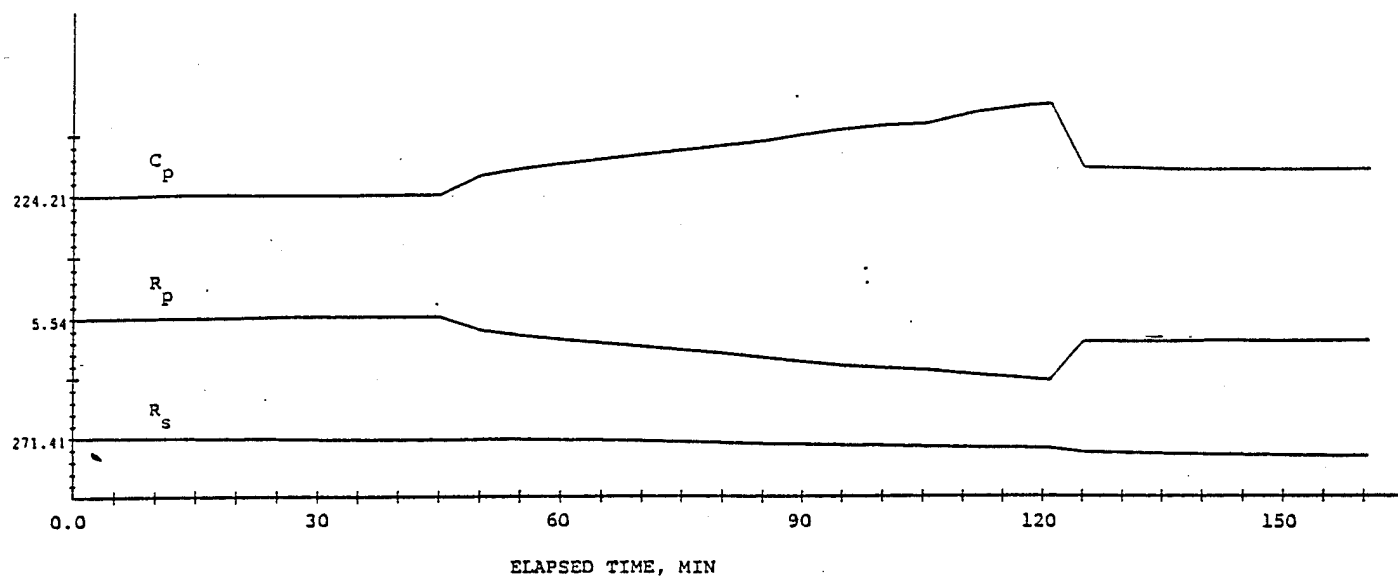
SS = Sum-of-Squares;

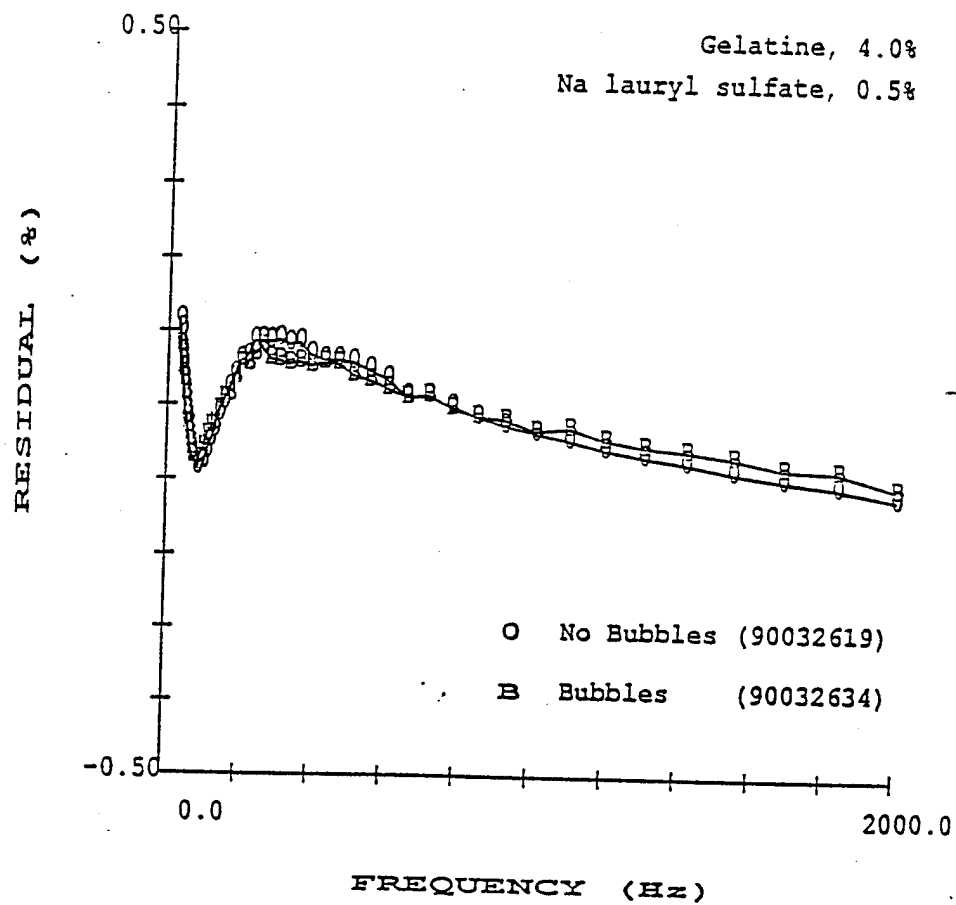
n = Number of frequencies in spectrum;

$|Z_i^*| = \sqrt{R^2 + X^2}$  = Norm of measured complex impedance at point i;

$|\hat{Z}_i^*|$  = Norm of fitted complex impedance at point i.







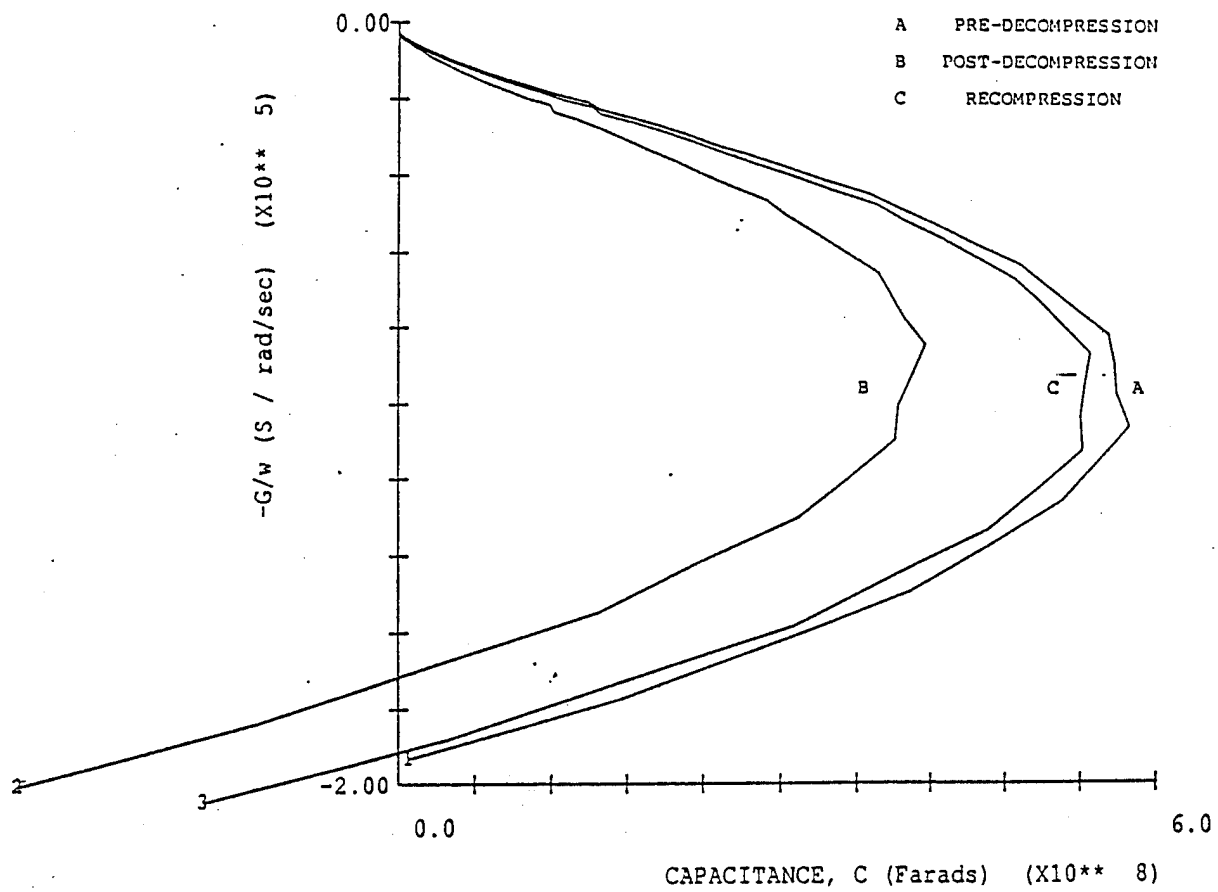
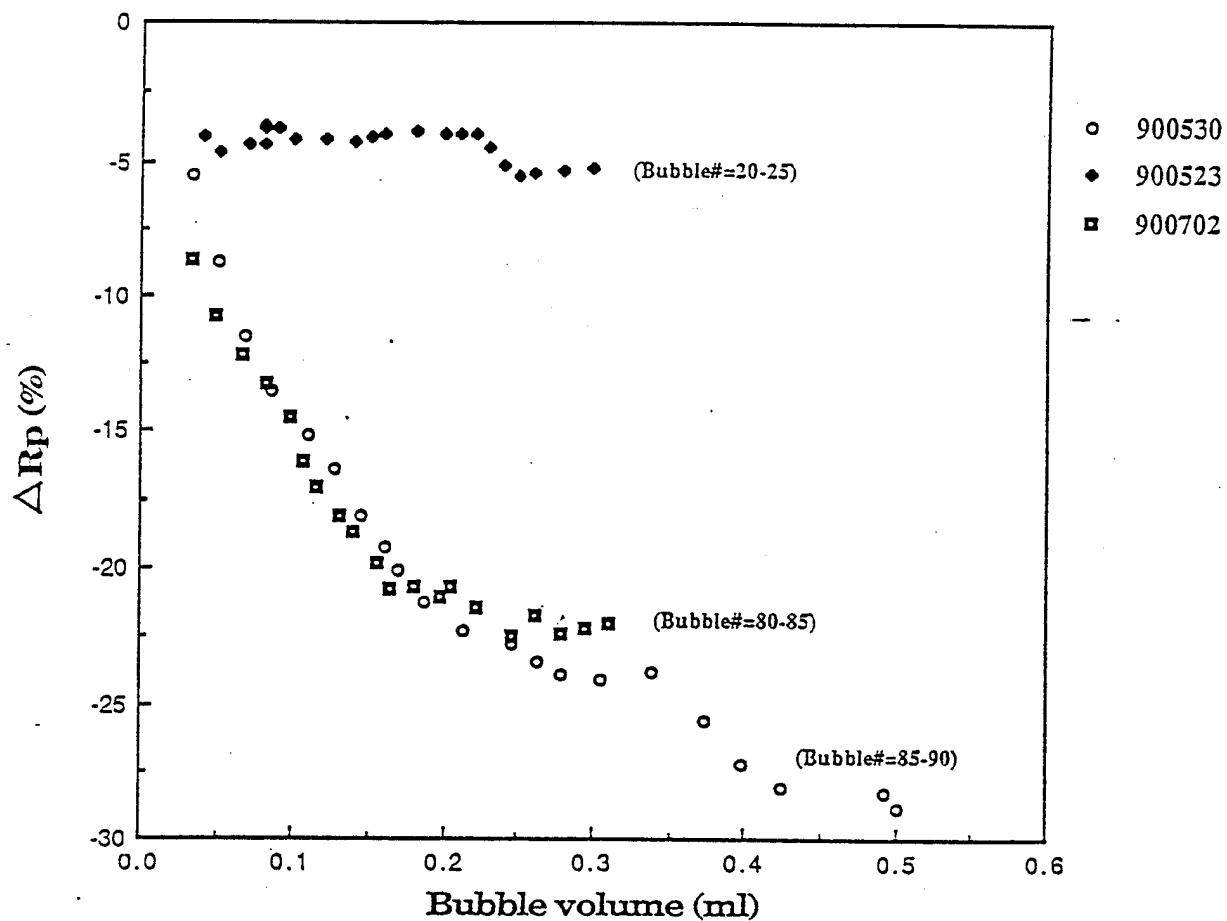


Table 1. Effects of Bubble Formation and Growth: Comparison of Simple Material-Exclusion Theory with Experiment

Z-Locus Property	Equivalent Circuit Parameter	Exclusion Theory	Observed
a)	$\tau (= R_p \cdot C_p)$	no change	<u>no</u> change
b) $R^\circ$		$\uparrow$	$\uparrow$ or $\downarrow$
c) $R^\infty$ =	$R_s$	$\uparrow$	$\uparrow$ or $\downarrow$
d) $R^\circ - R^\infty$ =	$R_p$	$\uparrow$	$\downarrow$
e)	$C_p$	$\downarrow \propto 1/R_p^*$	$\uparrow$

\* Follows from (a) and (d).

Bubble volume vs. percentage changes in Rp  
parameter (M-1); 4.0% gelatine; 0.5%  
Na lauryl sulfate; 95.5% tap water





### CONCLUSIONS

- Bubble formation in gelatine effects the frequency dependence of the impedance in a fashion that cannot be explained by material exclusion alone;
- the dependence of these effects on liquid composition and on the bubble number density indicates that the effects arise from influences of the bubbles on liquid structure and composition in the vicinity of the gas-liquid interfaces;
- Continued development of this approach promises to provide a specific, noninvasive and quantitative means to detect bubble formation and resolution in man.

## APPENDIX C.2

BIOELECTRICAL IMPEDANCE INDICES OF DECOMPRESSION-INDUCED  
BUBBLE FORMATION AND HEMODYNAMIC CHANGES IN RATS

Yi-Chang Wu<sup>1</sup>, Wayne A. Gerth<sup>1</sup>, and Leslie D. Montgomery<sup>2</sup>

<sup>1</sup>F.G. Hall Hypo-Hyperbaric Center  
Duke University Medical Center  
Box 3823  
Durham, NC 27710 USA

<sup>2</sup>LDM Associates  
1764 Emory Street  
San Jose, CA 95126 USA

Prepared for presentation at the  
1991 Annual Scientific Meeting of the  
Undersea and Hyperbaric Medical Society  
June 19-23, 1991  
San Diego Princess Hotel, San Diego, CA

Indicate below the numbers and topics of sessions in which your abstract might be programed (see list of suggested topics.)

1st Choice: # ..... Title ..Decompression Sickness  
2nd Choice: # ..... Title .....

Do not fold this sheet.  
Use cardboard backing  
when mailing.

PRESENTATION PREFERENCE (scientific sessions only)  
Preferred choice (CHECK ONE ONLY)

☒ Slide presentation ☐ Poster presentation  
☐ Either

1991 UNDERSEA AND HYPERBARIC MEDICAL SOCIETY  
ANNUAL SCIENTIFIC MEETING ABSTRACT FORM

BIOELECTRICAL IMPEDANCE INDICES OF DECOMPRESSION-INDUCED BUBBLE FORMATION AND HEMODYNAMIC CHANGES IN RATS. Yi-Chang Wu<sup>1</sup>, Wayne A. Gerth<sup>1</sup> and Leslie D. Montgomery<sup>2</sup>.

<sup>1</sup>Duke University Medical Center, Durham, NC 27710, USA and

<sup>2</sup>IDM Associates, San Jose, CA 95126, USA.

Noninvasive Electrical Impedance Spectroscopy (EIS) and Impedance Plethysmography (IPG) were used to monitor bubble formation and hemodynamic changes in the tails of anesthetized male albino rats rapidly decompressed from atmospheric pressure to simulated altitudes. Each experiment consisted of three successive 30 min stages: a) ambient pressure; b) ambient pressure, 8,200 ft altitude or 26,400 ft altitude, and; c) ambient pressure. The altitude chamber was ventilated with 100% O<sub>2</sub> during the second stage to prevent hypoxia. Using tetrapolar electrodes placed on the tail prior to run start, an electrical impedance spectrum followed by 2 sec of continuous IPG data were obtained at 6-min intervals throughout each run. A parallel equivalent circuit model representing the electrical properties of the monitored segment was fitted to each spectrum to obtain resistance ( $R_e$ ,  $R_i$ ) and capacitance ( $C_m$ ) parameters that have previously been shown to exhibit characteristic changes with the formation and growth of bubbles in gelatine. A 3-lead ECG and the IPG pulse waveforms were analyzed to obtain heart rate, blood flow, segmental base resistance, and pulse transit time. Decompression Sickness (DCS) was judged to have occurred with the exhibition of respiratory distress, convulsion and/or death. In rats that developed DCS (n=10), bubble dielectric signatures were observed in the form of increased  $R_e$  and  $R_i$  and decreased  $C_m$  parameters. Such signatures were absent in rats that were not decompressed (n=7) or were greatly attenuated in rats that failed to develop DCS at altitude (n=6): both  $R_e$  and  $C_m$  usually increased, while  $R_i$  decreased. Hemodynamic changes followed a similar pattern, exhibiting greater changes in rats exposed to greater decompressions. DCS was accompanied by decreases in tail blood flow and decreases in heart rate. Vascular compliance, indicated by the pulse transit time, and segmental base resistance increased. In the absence of DCS, heart rate and tail blood flow changed insignificantly or increased, while vascular compliance and base resistance remained unchanged or decreased. Results suggest that comprehensive EIS and IPG monitoring of select body segments may provide premonitory indices of DCS in decompressed animals and man.

Name and mailing address of presenting author:

Yi-Chang Wu, MD.  
.....  
F.G. Hall Hypo-Hyperbaric Center  
.....  
Duke University Medical Center  
.....  
Durham, North Carolina ..... Zip 27710 .....  
Telephone No.: Area Code (919) # 684-5902

IMPORTANT: Your abstract will appear in the Program/  
Abstract book exactly as you submit it.

Read all instructions before you type abstract. Also see sample  
abstracts and typing instructions on reverse side.

The original ribbon copy of this abstract form (for reproduction by  
photo-offset) must be submitted together with, where possible, 10  
photocopies.

SEE REVERSE FOR ABSTRACT DEADLINES  
AND MAILING INSTRUCTIONS

## INTRODUCTION

-----> Slide 1: Title

It is well-accepted that Decompression Sickness, or DCS, is caused by the formation and growth of gas bubbles in the body. Among the ensuing etiological events, such bubbles are thought to cause regional hemodynamic impairment by either direct or indirect occlusion of the vasculature. Early detection of bubble formation and growth and its consequent bubble-induced circulatory impairment could provide premonitory indices of DCS onset and further illuminate essential features of DCS pathophysiology.

In the present study, non-invasive electrical impedance spectroscopy (EIS) and impedance plethysmography (IPG) were used to detect bubble formation and monitor the attendant hemodynamic changes in rats decompressed from atmospheric pressure to simulated altitudes.

## MATERIALS AND METHODS

39 male Sprague-Dawley rats were studied. The tail was chosen for monitoring because of its ease of access and because its large amounts of connective and fascial tissue were thought to render it especially vulnerable to decompression-induced bubble formation.

-----> Slide 2: System Schematic

The experimental apparatus is schematized in this slide. The experimental chamber was made of transparent plexiglass which afforded ready visual observation of the rat for DCS signs. The chamber was connected in parallel with a vacuum pump and vacuum accumulator that was fully evacuated before each run. The experimental chamber was decompressed into the accumulator to achieve rapid decompression rates. The vacuum pump provided continuous evacuation of the chamber, allowing either air or 100% O<sub>2</sub> to be vented into the chamber at measured rates to control chamber atmosphere. A through-hull was provided for a bundle of shielded cables to make the required connections between electrodes on the rat and the EIS and IPG systems.

-----> Slide 3: System Photograph: EIS, IPG and VAXStation

EIS system: Electrical impedance spectra were measured using a system that consisted of a Schlumberger 1260 Impedance/Gain-phase Analyzer controlled via a IEEE-488 Interface by a VAXStation 3200 computer. The analyzer obtained an impedance spectrum of the tail by measuring the impedance at each of a series of discrete frequencies from 100 Hz to 150,000 Hz.

IPG system: A BoMed BioImpedance Analyzer (BoMed Medical Manufacturing, Ltd.) was used to measure the impedance plethysmographic data from which heart rate and various hemodynamic parameters were calculated. The instrument operated with a 0.1 mA excitation current at a frequency of 50 KHz.

-----> Slide 4: Electrode Placement Schematic

In each run, a rat was anesthetized with an intraperitoneal injection of Nembutal (50 mg/Kg). The anterior surface of the chest and abdomen was then shaved for placement of electrodes for a 3-lead EKG. The EIS and IPG systems shared another tetrapolar electrode set on the tail. These electrodes were copper and were fixed in a flexible harness that was readily placed and immobilized on the tail by wrapping with adhesive tape. The rat was then placed inside the altitude chamber and the electrical connections to the chamber through-hull cable were completed.

-----> Slide 5: Decompression Profile

After chamber closure, the rat was exposed to one of four different decompression profiles consisting of three successive 30 min stages: 1) ground-level control; 2) altitude, and; 3) ground-level recovery. The different profiles were distinguished by the altitude stage pressure: a)  $\Delta P=0$  mmHg (no decompression), b)  $\Delta P=200$  mmHg, c)  $\Delta P=400$  mmHg, and; d)  $\Delta P=500$  mmHg.

During the ground level stages, the chamber was ventilated with room air to prevent  $CO_2$  accumulation. Decompressions to the target altitudes were effected within 30 sec. During the altitude stages, the chamber was ventilated with 100% oxygen to prevent hypoxia. Chamber temperature was monitored using an in-chamber thermistor connected to an external tele-thermometer, and was found to vary by no more than  $\pm 1.0^\circ C$  throughout any run.

The impedance pulse waveform and EKG were recorded for 2-4 sec periods at 6 min intervals throughout the entire pressure profile. Immediately after each of these periods, the external cable connections were switched and the impedance spectrum of the tail was measured. The impedance pulse waveform and EKG were also measured immediately before descent to ground-level. The rat was monitored continuously for observable DCS signs. Decompression sickness was judged to have occurred with the exhibition of respiratory distress, convulsions, and/or death.

-----> Slide 6: EIS Data Analysis; Impedance locus,  
Equivalent circuit model

The upper figure is a typical impedance spectrum of a rat tail. The spectrum is illustrated as a locus of points generated by plotting the reactance of the impedance at each frequency vs its corresponding resistance. The middle schematic is the electric equivalent circuit model which was fitted to each measured impedance spectrum. The model describes each spectrum in terms of three adjustable parameters:  $R_e$ ,  $R_i$  resistances, and  $C_m$  capacitance.

-----> Slide 7: IPG Data Analysis

This is a typical impedance plethysmographic recording from a rat. The upper trace is the impedance pulse waveform, which reflects the pulsatile volume changes in the monitored segment that were caused by the passage of blood from each cardiac pulse. The middle trace is the time derivative of the pulse waveform, and the bottom trace is the EKG. The heart rate and

various hemodynamic parameters were calculated on a pulse-by-pulse basis from the times and resistances at each of 7 landmarks that were manually selected for each pulse.

The values of each EIS and IPG parameter throughout the run for a given rat were normalized with respect to the first value of the parameter obtained in the run, and expressed as a percentage of that first value. The data were then separated into two groups; DCS and no-DCS; regardless of the decompression profile. The mean percent changes for every parameter obtained at the different elapsed times were compared between the two outcome groups using repeated measures ANOVA.

## RESULTS

-----> Slide 8: Experimental Outcomes; DCS Incidence and Signs

The outcomes of the runs are summarized in this table. Respiratory distress, presenting as tachypnea or labored, long inspirations followed by transient apnea, was the earliest and most common sign of DCS. The mean onset time of DCS was 6 min, ranging from 1 to 13 min.

-----> Slide 9: Equivalent Circuit Parameters Strip Chart; DCS Group Means

This figure summarizes the EIS equivalent circuit parameter changes that were observed in the DCS group rats throughout the runs. Grouped mean percent parameter values from each of the successive impedance spectra in the runs are drawn in "strip chart" form with the means arranged on the ordinate versus the corresponding run sequence numbers on the abscissa. The mean onset time for DCS is indicated by the arrow on the abscissa. While at altitude, both of the resistance parameters,  $R_e$  and  $R_i$ , increased, while the capacitance  $C_m$  decreased. Note that these changes commenced before the mean onset of DCS and that, with the exception of the changes in the  $R_e$  parameter, they were reversed by recompression. This pattern is strikingly similar to that observed with decompression-induced bubble formation in certain gelatin preparations.

-----> Slide 10: Changes in  $R_i$ ; Gelatin w/bubbles vs Rats w/DCS

The upper figure in this slide typifies the effect of decompression and bubble formation on the  $R_i$  parameter in gelatin. The format is similar to that of the previous slide. Progressive increases in  $R_i$  were associated with bubble formation and growth. The lower figure shows the grouped mean results from the DCS group in this study. Rats with DCS clearly exhibited changes in this parameter that were similar to those exhibited with bubble formation in gelatin.

-----> Slide 11: Changes in  $R_i$ ; DCS group vs No-DCS group

These changes were different from those observed in the no-DCS group. Grouped mean percent changes in the  $R_i$  parameter for the DCS group are compared to those of the no-DCS group in this slide. There was no significant difference in this parameter between the two groups before decompression, but it increased in the DCS group to values significantly

larger than those in the no-DCS group after decompression. Importantly, the changes emerged as significant before the mean onset of DCS. Thus, the no-DCS group failed to exhibit this element of the bubble dielectric signature that was evident in the DCS group.

-----> Slide 12: Changes in  $C_m$ ; Gelatin w/bubbles vs Rats w/DCS

A similar correspondence between bubble formation in gelatin and DCS in rats occurred for the capacitance parameter. The upper figure shows the effect of decompression and bubble formation on the capacitance parameter of gelatin. Bubble formation and growth caused the capacitance to decrease. As shown in the lower figure, this parameter also decreased in the rat tail with decompression and DCS. Recompression prevented further decreases in this parameter, but did not cause it to increase to its pre-decompression value.

-----> Slide 13: Changes in  $C_m$ ; DCS group vs No-DCS group

As with the  $R_i$  parameter, these changes in the capacitance were also different from those observed in the no-DCS group. This slide shows the time course of the changes in the  $C_m$  parameter in both groups. Again, there was no significant difference between the two groups before decompression, but the capacitance parameter decreased in the DCS group to values significantly lower than those in the no-DCS group after decompression. The no-DCS group consequently also failed to exhibit this second element of the bubble dielectric signature that was evident in the DCS group.

-----> Slide 14 [optional]; Changes in  $R_e$ ; DCS vs no-DCS

The  $R_e$  parameter tended to increase during the decompression stage regardless of DCS outcome and did not significantly differ between the DCS and no-DCS groups at any point during the runs.

Summarizing to this point, then, a bubble dielectric signature, indicating the presence of bubbles, was observed in the tails of decompressed rats that developed DCS. Such a signature was not observed in rats that did not develop DCS.

The IPG results provided additional amplification of these EIS bubble detection results.

-----> Slide 15: Blood Flow; DCS vs no-DCS

This figure shows the time courses of changes in the calculated blood flows in the DCS and no-DCS groups. In the DCS group, tail blood flow showed a large decrease immediately on decompression and continued to decrease more slowly thereafter. The maximum mean percent decrease in blood flow was  $32 \pm 6\%$ . These blood flow decreases were reversed by recompression. In contrast, tail blood flow either remained unchanged or increased in the no-DCS group during the altitude stages. Importantly, the blood flow in the DCS group tended to start recovering in the middle of the decompression stage. This finding may indicate that a vascular autoregulatory reflex was evoked to prevent further hemodynamic impairment caused by bubbles' mechanical obstruction.



-----> Slide 16: Heart Rate; DCS vs no-DCS

The heart rate in both groups increased immediately after decompression. In the DCS group, however, the heart rate then soon began a decrease that continued throughout the remaining period at altitude, finally reaching a mean value  $21 \pm 7\%$  lower than that preceding decompression. This decrease was reversed by recompression. Note that the decreased tail blood flow preceded the onset of DCS, but bradycardia occurred only after DCS appeared.

-----> Slide 17: Pulse waveform;  
Excess Inflow and Outflow Times ( $T_i$  and  $T_o$ )

Segmental arterial filling during systole precedes and is more rapid than venous runoff during diastole. Thus, each impedance pulse can be resolved into two portions: a period of excess arterial filling ( $T_i$ ) defined as that period of the pulse preceding the diastolic notch, and a period of excess venous outflow ( $T_o$ ) defined as the period of the pulse following the diastolic notch.

-----> Slide 18: Changes in  $T_o$ ; DCS vs no-DCS

After decompression, the period of excess outflow increased throughout the decompression stage in the DCS group, but remained unchanged in the no-DCS group. The results strongly indicated that venous outflow was seriously obstructed in the DCS group but not in the no-DCS group.

-----> Slide 19: Changes in  $T_i$ ; DCS vs no-DCS

In contrast, there was no significant difference in the arterial inflow time between the DCS and no-DCS groups. Thus, decompression-induced intrasegmental hemodynamic changes were confined to the venous circulation, as would be expected if bubbles occur primarily in the venous circulation.

-----> Slide 20: Changes in Pulse Transit Time (PTT); DCS vs no-DCS

Decompression effects on the systemic arterial circulation are evident in changes in the pulse transit time, which is a measure of the time interval between the QRS complex of the EKG and the beginning point of the ensuing segmental impedance pulse. The pulse transit time increases when the arterial vascular compliance between the heart and the monitored segment increases.

This figure illustrates that the pulse transit time during the altitude stage increased significantly in the DCS group but decreased only insignificantly in the no-DCS group. Results consequently indicate that systemic arterial compliance was increased. Coupled with the observed decreases in heart rate and tail blood flow, this result is consistent with a decreased systemic arterial volume arising from decreased venous return and cardiac output.

## CONCLUSIONS

-----> Slide 21: Conclusions

Bubble dielectric signatures obtained by Electrical Impedance Spectroscopic monitoring were observed in the tails of decompressed rats that developed DCS but not in rats that failed to develop DCS.

Hemodynamic changes obtained by concurrent Impedance Plethysmographic monitoring paralleled the EIS results: Blood flow and hemodynamic changes in rats that developed DCS were different from and/or more severe than those observed in rats that failed to develop DCS.

The observed temporal relationships between the various events illuminated by these measurements offers some insight into the pathophysiological mechanism of DCS. Decreases in peripheral blood flow concurrent with the appearance of a bubble dielectric signature occurred before DCS onset. This finding is consistent with the hypothesis that peripheral circulatory impairment occurs in asymptomatic decompressions and that DCS occurs only as such impairment becomes more severe. Bradycardia occurred only after DCS onset. With further impairment, central cardiovascular function is then affected.

Real-time EIS monitoring of select body segments for decompression-induced bubble formation and growth with concurrent IPG monitoring for hemodynamic changes promises to provide noninvasive, premonitory and objective indices of DCS in decompressed animals and man.

## ACKNOWLEDGEMENT

Development of the Electrical Impedance Spectroscopic System used in this work was supported by USN contract N00014-87-C-0166.

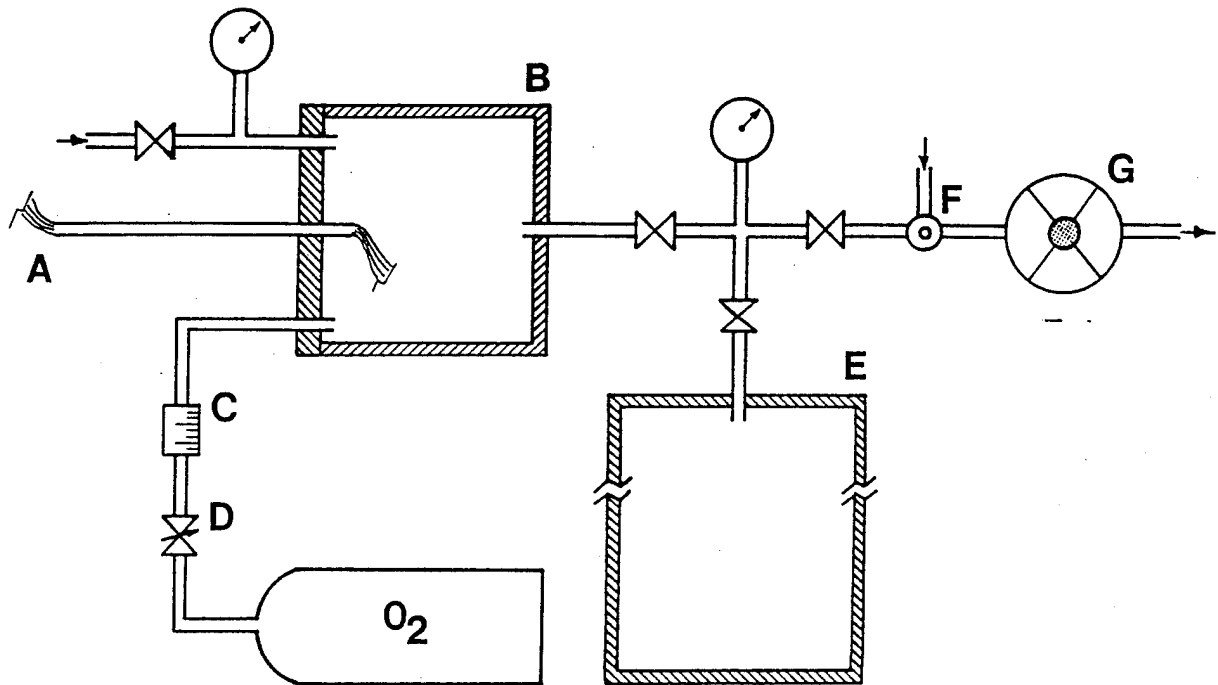
SLIDE 1:

Bioelectrical Impedance Indices of Decompression-Induced  
Bubble Formation and Hemodynamic Changes in Rats

Yi-Chang Wu<sup>1</sup>, Wayne A. Gerth<sup>1</sup>, and Leslie D. Montgomery<sup>2</sup>

<sup>1</sup>F.G. Hall Hypo-Hyperbaric Center  
Duke University Medical Center  
Durham, NC

<sup>2</sup>LDM Associates  
San Jose, CA

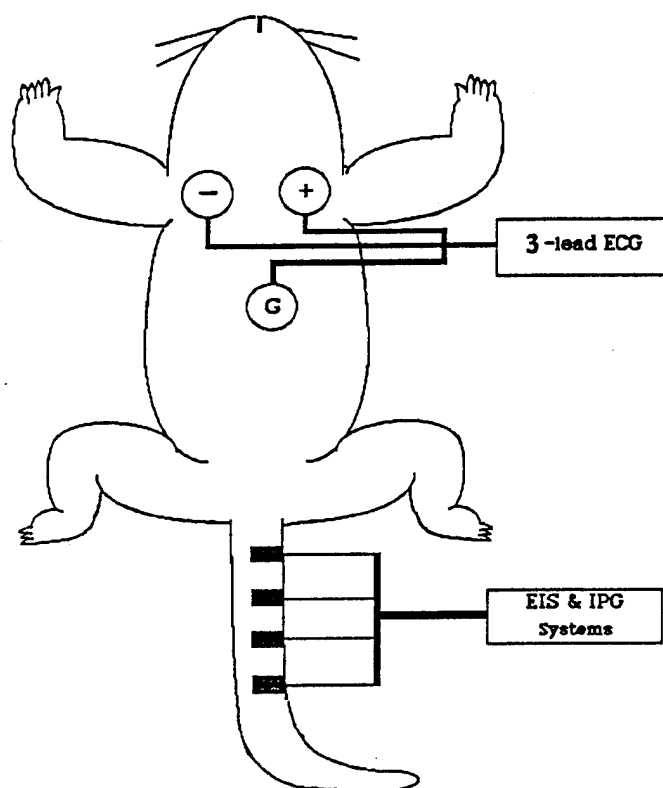
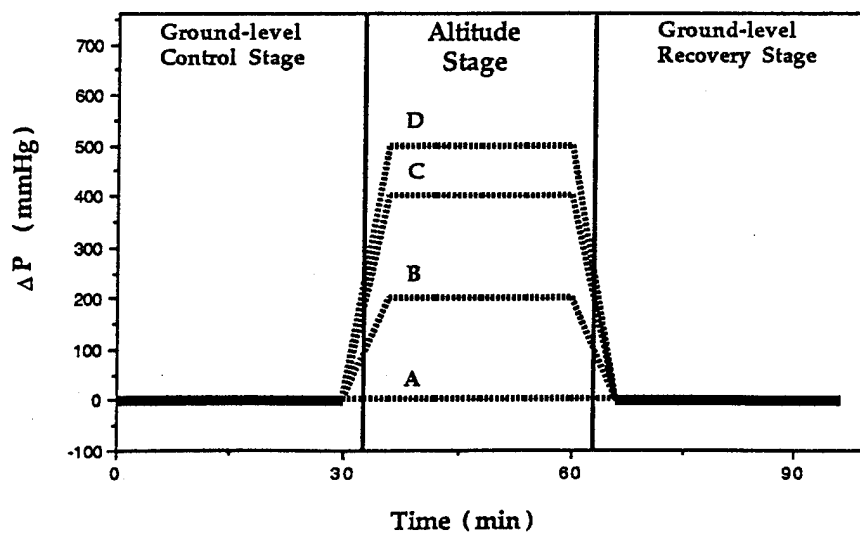
SLIDE 2:

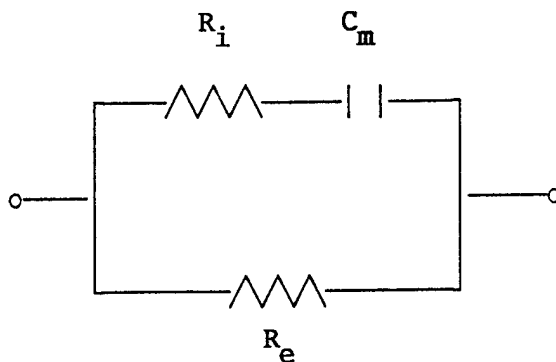
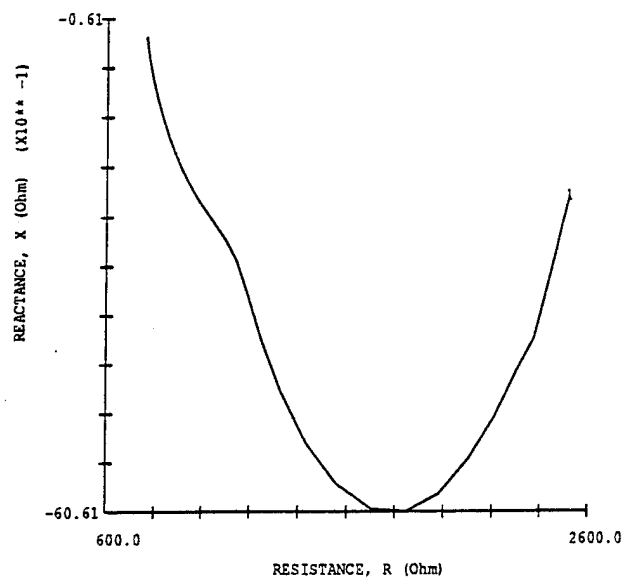
- A) Cable Bundle
- B) Experimental Chamber
- C) O<sub>2</sub> Flowmeter
- D) O<sub>2</sub> Regulating Valve

- E) Vacuum Accumulator
- F) Vacuum Regulator
- G) Vacuum Pump

SLIDE 3:

EIS/IPG System Photograph

SLIDE 4:**Electrode Placements**SLIDE 5:**Decompression Profiles**

SLIDE 6:

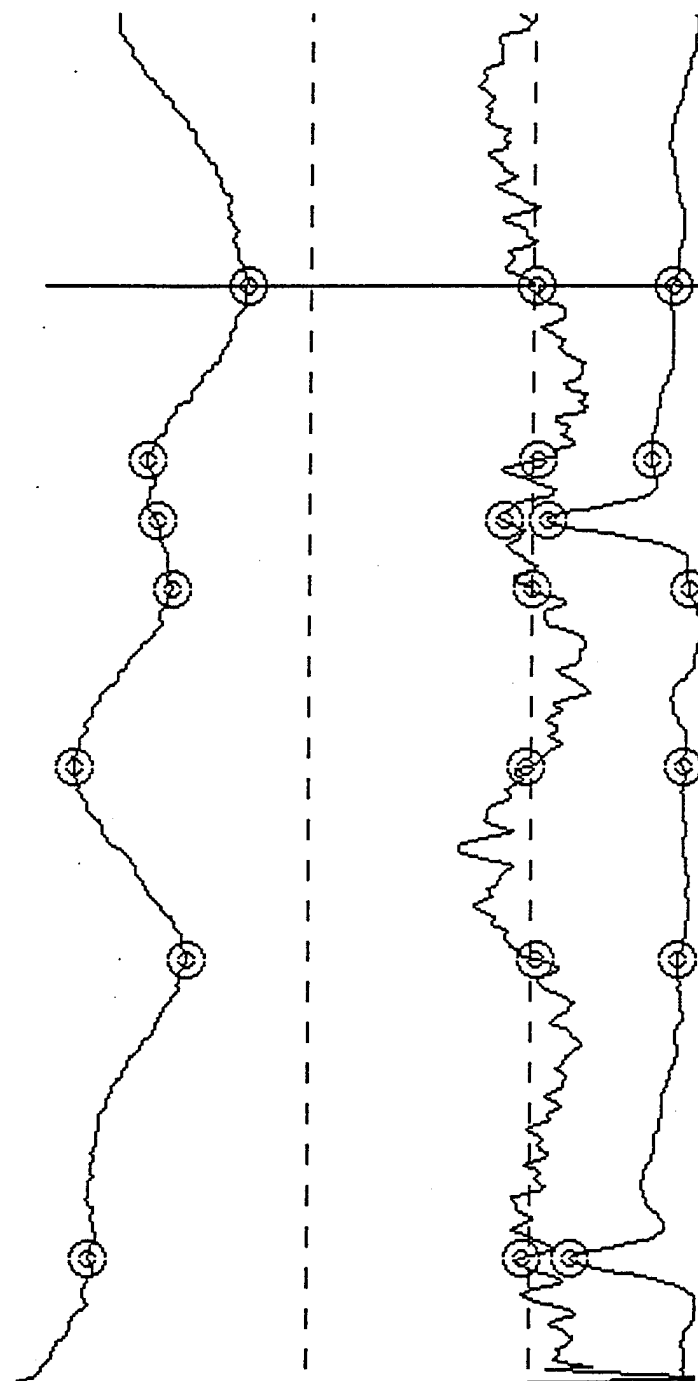
The frequency dependence of the admittance of this circuit is given by

$$Y^* = \frac{1}{Z^*} = \frac{1}{R_e} + \frac{1}{R_i} - \frac{1/R_i}{1 + j\omega\tau^\alpha(1-\alpha)},$$

where;  $0 < \alpha < 1$ .

SLIDE 7:

## RHEOSYS: IMPEDANCE PULSE WAVEFORM ANALYSIS



1: 4280  
2: 17536  
3: 19073

FLIPPING

C= 1

P= 3

M= 7

T=19402

PSELECT OFF

REG

52.775391

DER

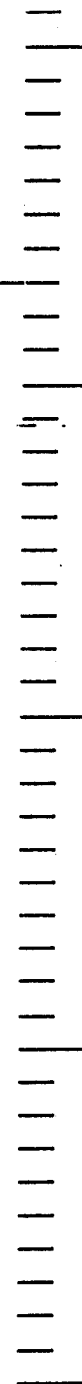
-0.203125

BASE R

596.546143

ECG

362.000000





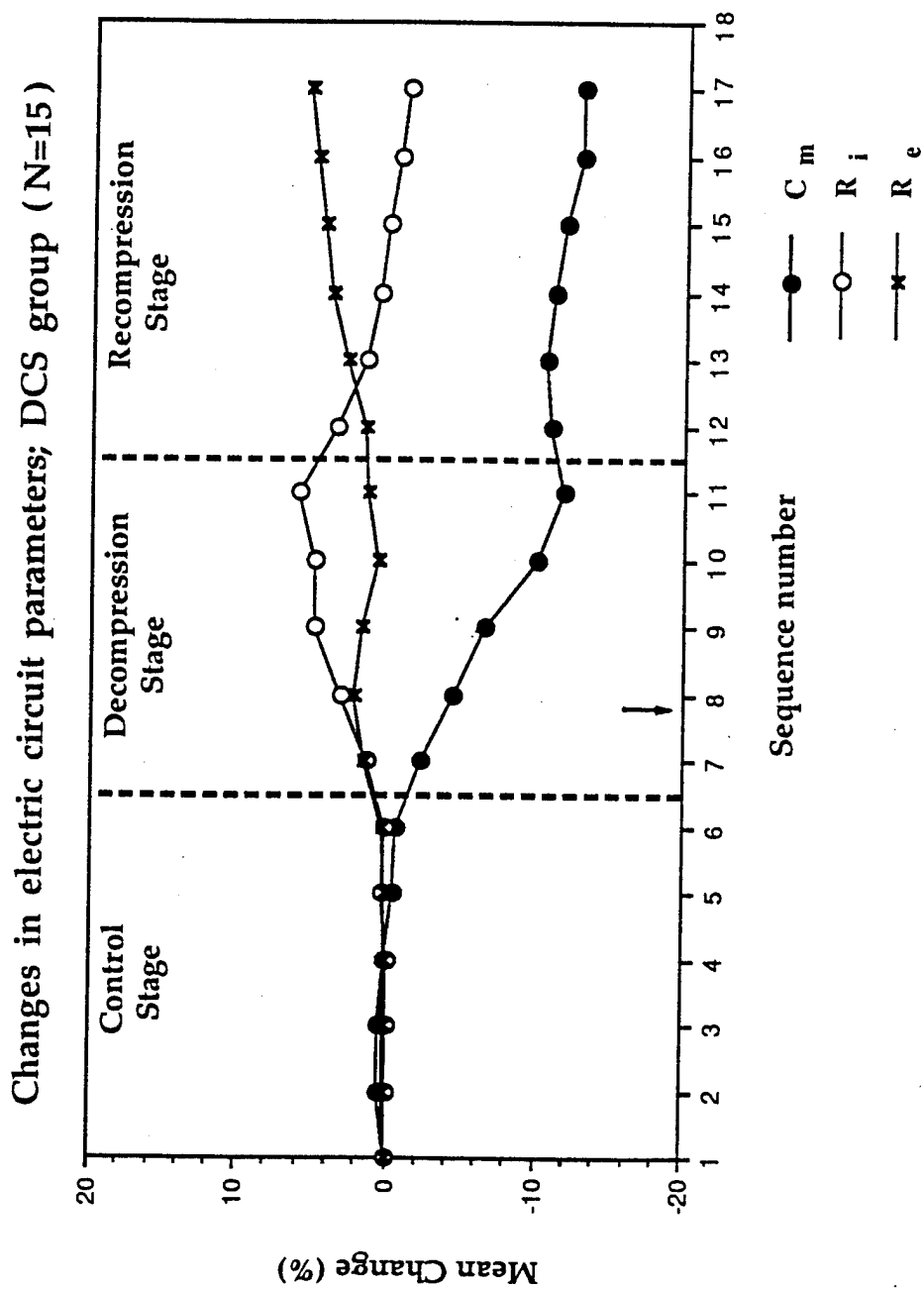
SLIDE 8:TABLE 1. Experimental Outcomes

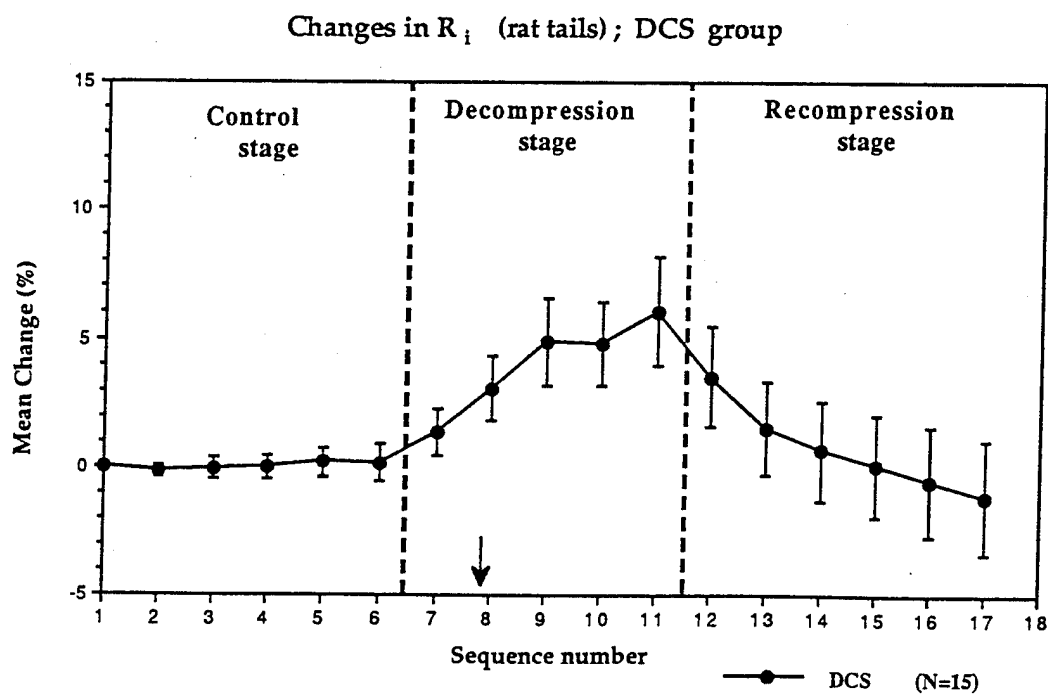
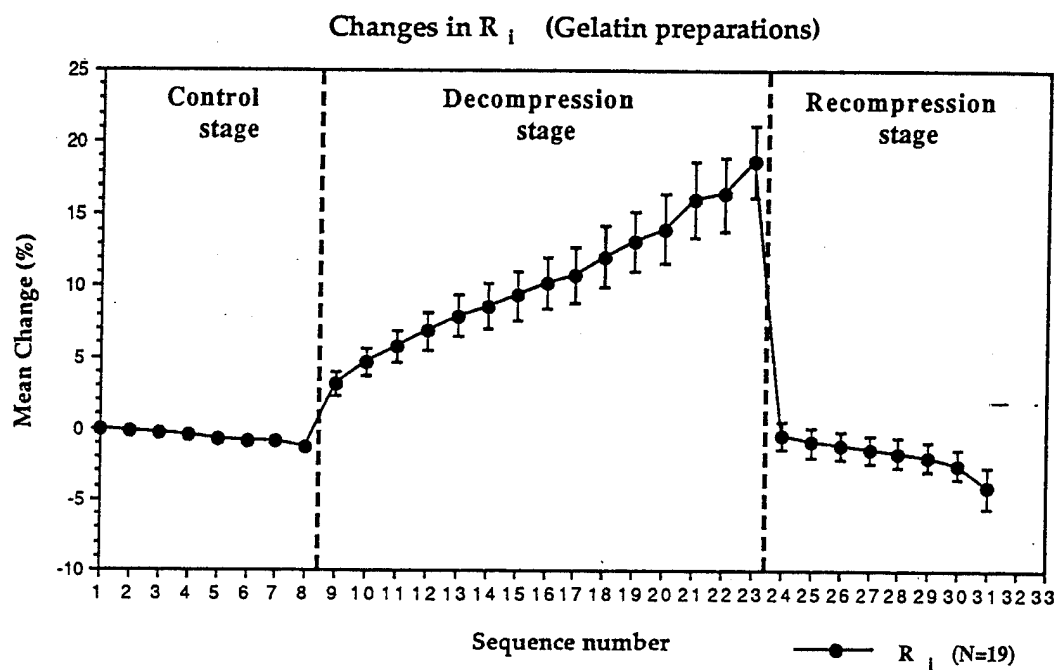
-- DCS Incidence --			
Profile	# DCS <sup>a</sup>	# No-DCS	Total
$\Delta P = 0$ mm-Hg	-	10	10
$\Delta P = 200$ mm-Hg	-	8	8
$\Delta P = 400$ mm-Hg	8	2	10
$\Delta P = 500$ mm-Hg	11 <sup>b</sup>	-	11
Total	19	20	39

<sup>a</sup> Obvious respiratory distress

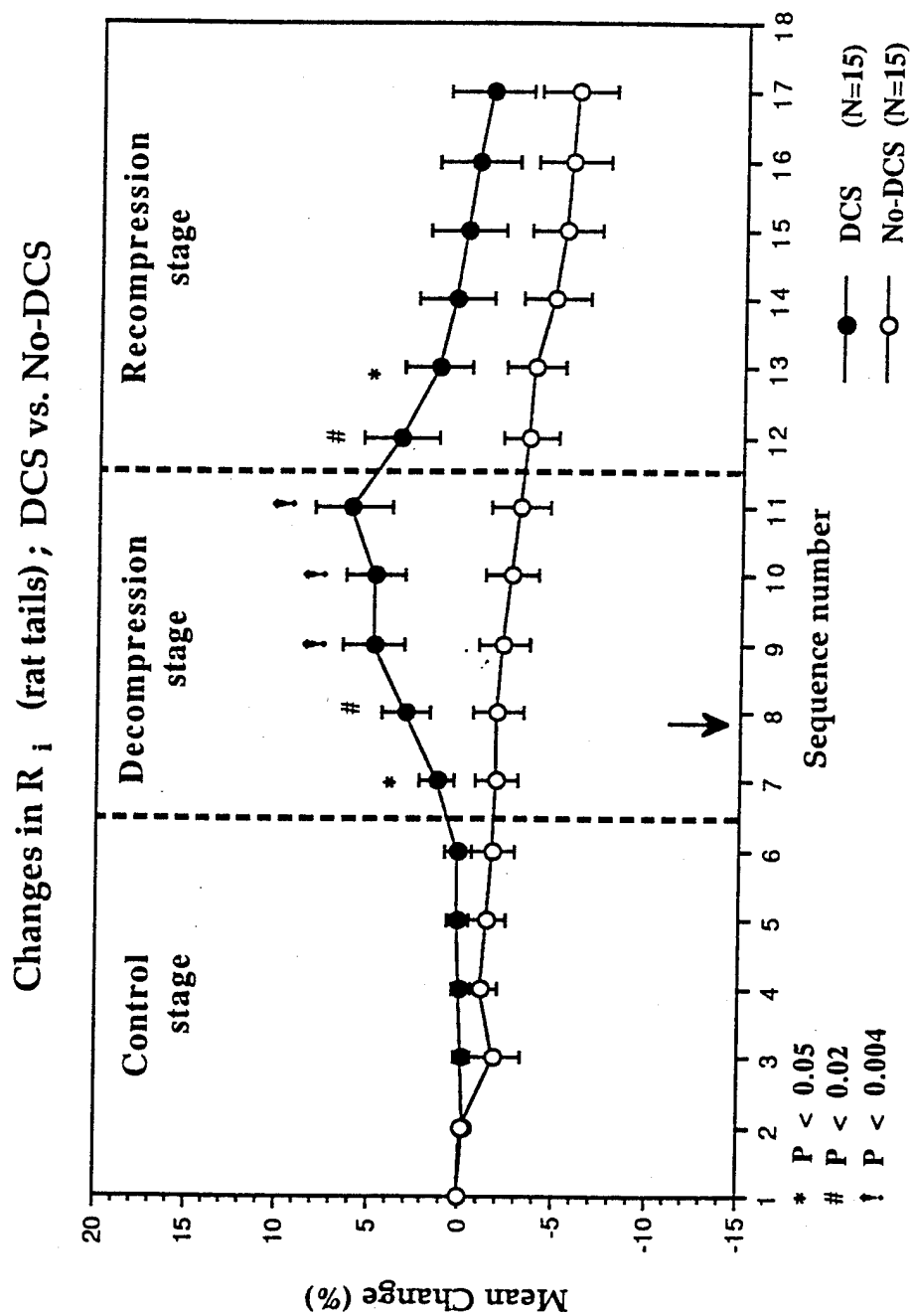
<sup>b</sup> Respiratory distress proceeded to convulsions in 2 rats and to death in 3 others.

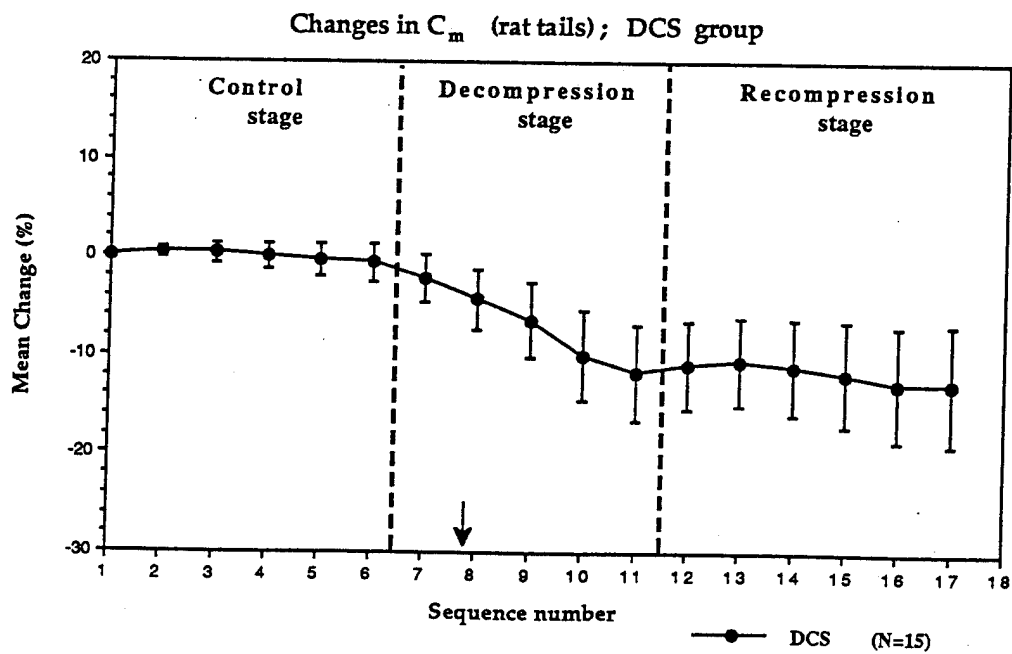
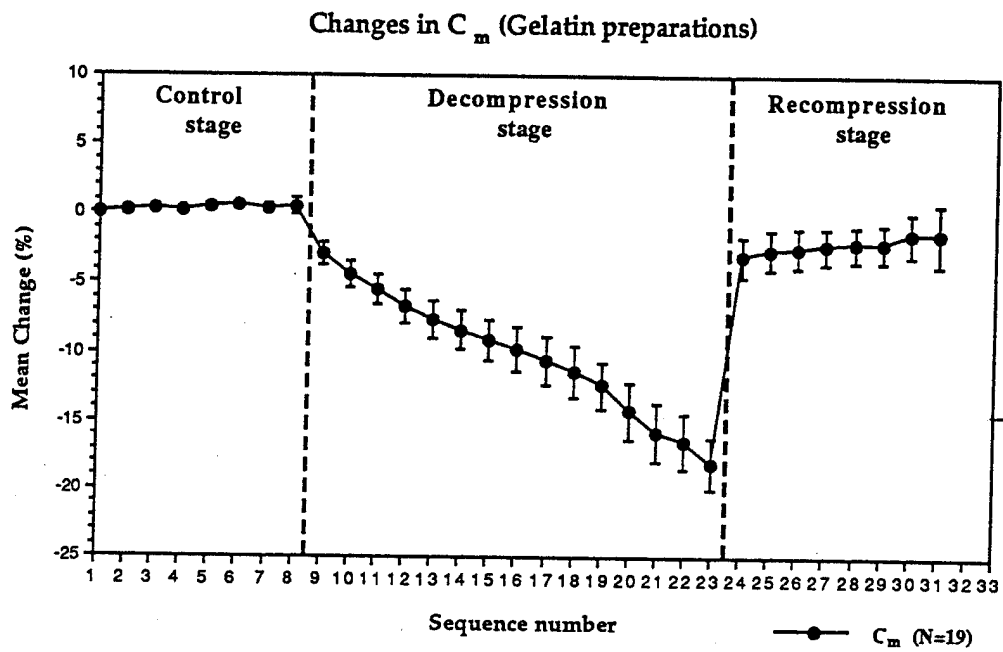
SLIDE 9:



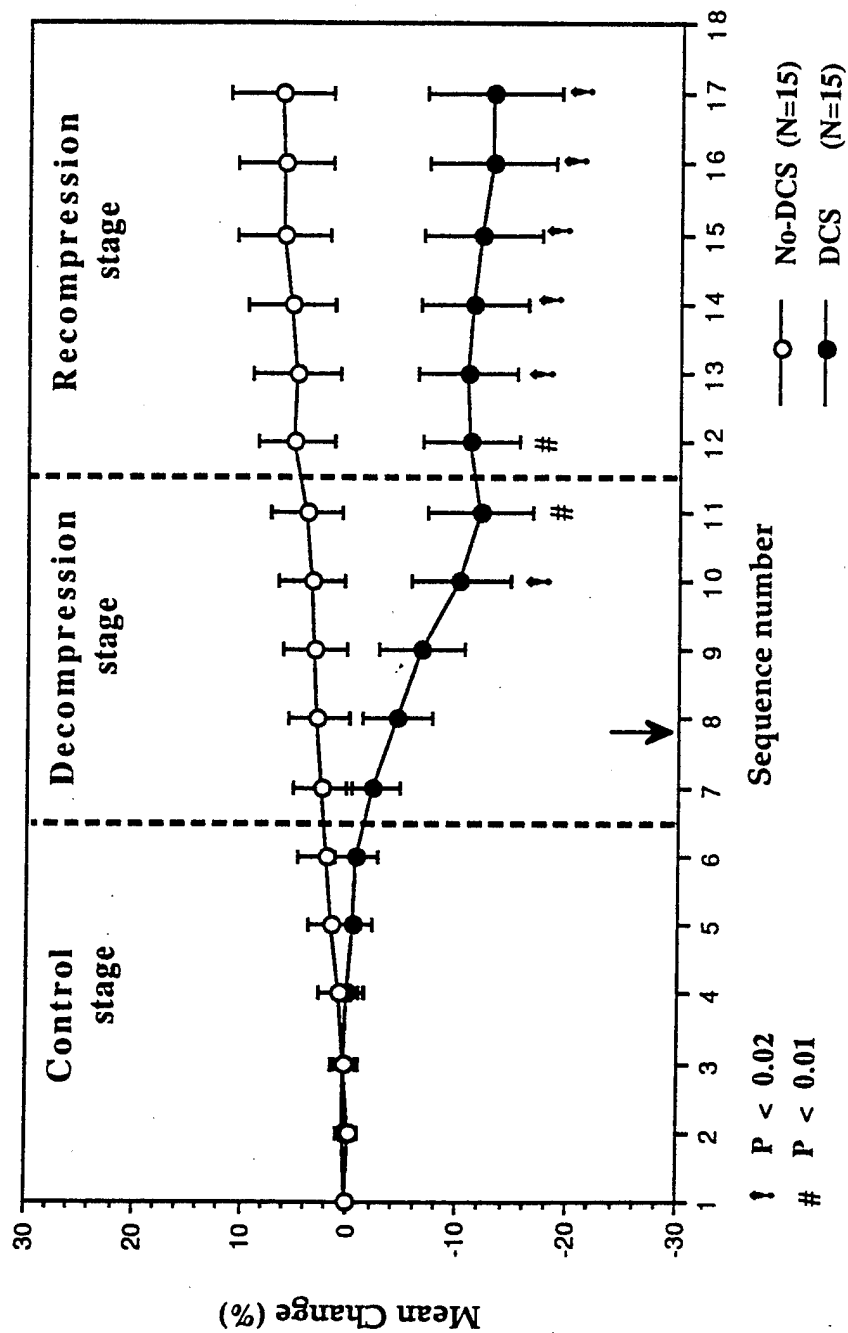
SLIDE 10:

SLIDE 11:

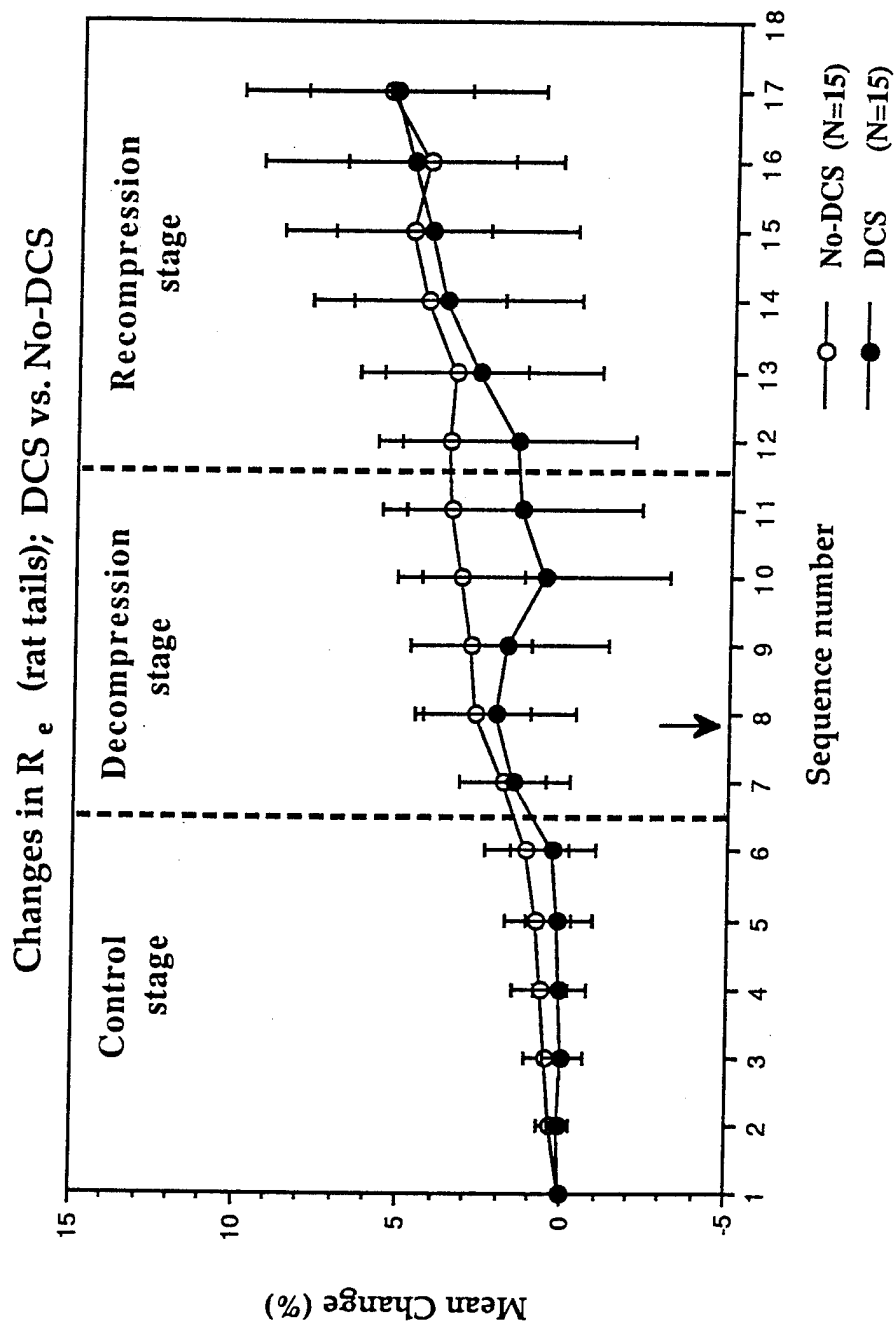


SLIDE 12:

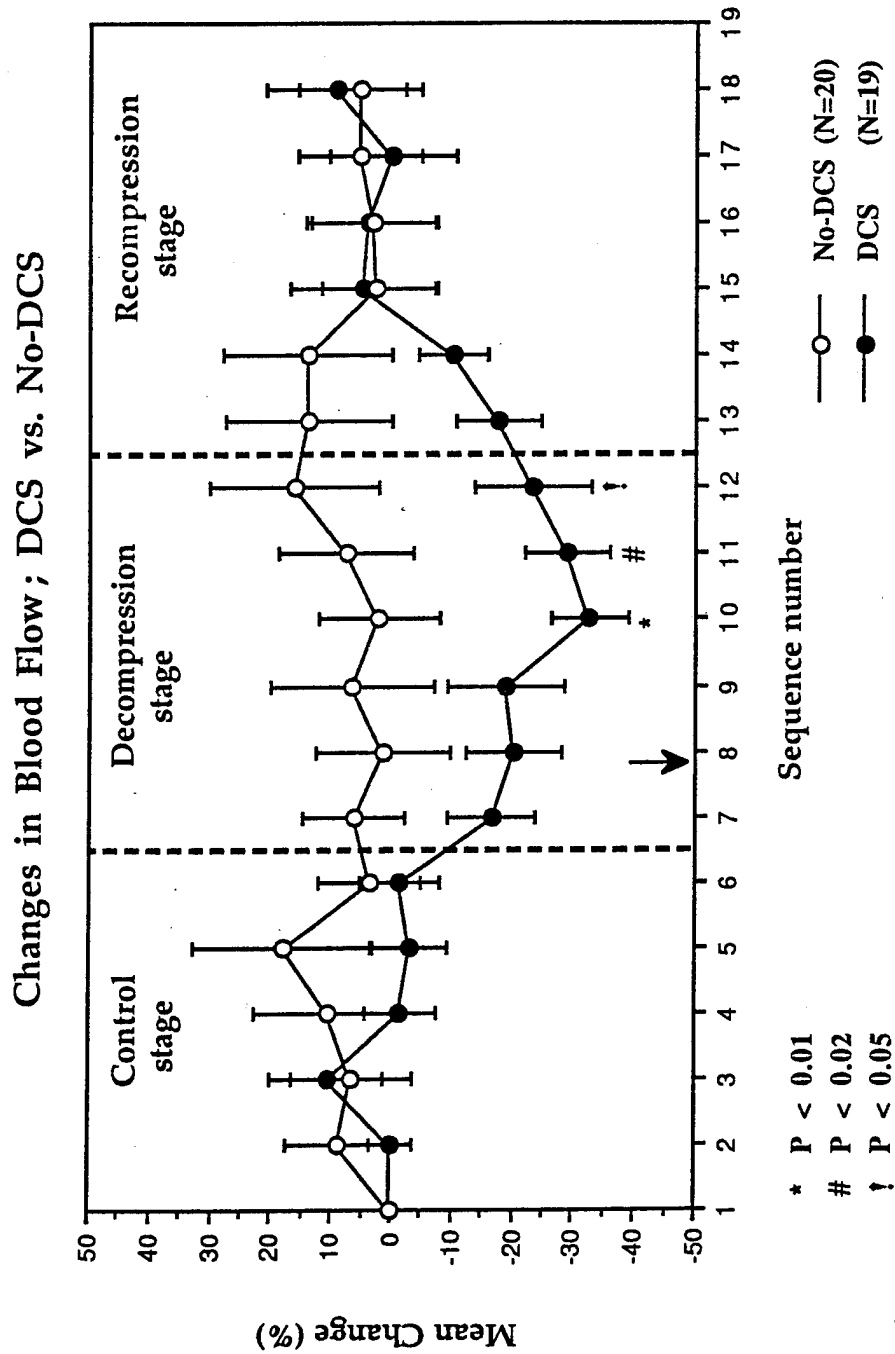
SLIDE 13:

Changes in  $C_m$  (rat tails); DCS vs. No-DCS

SLIDE 14:

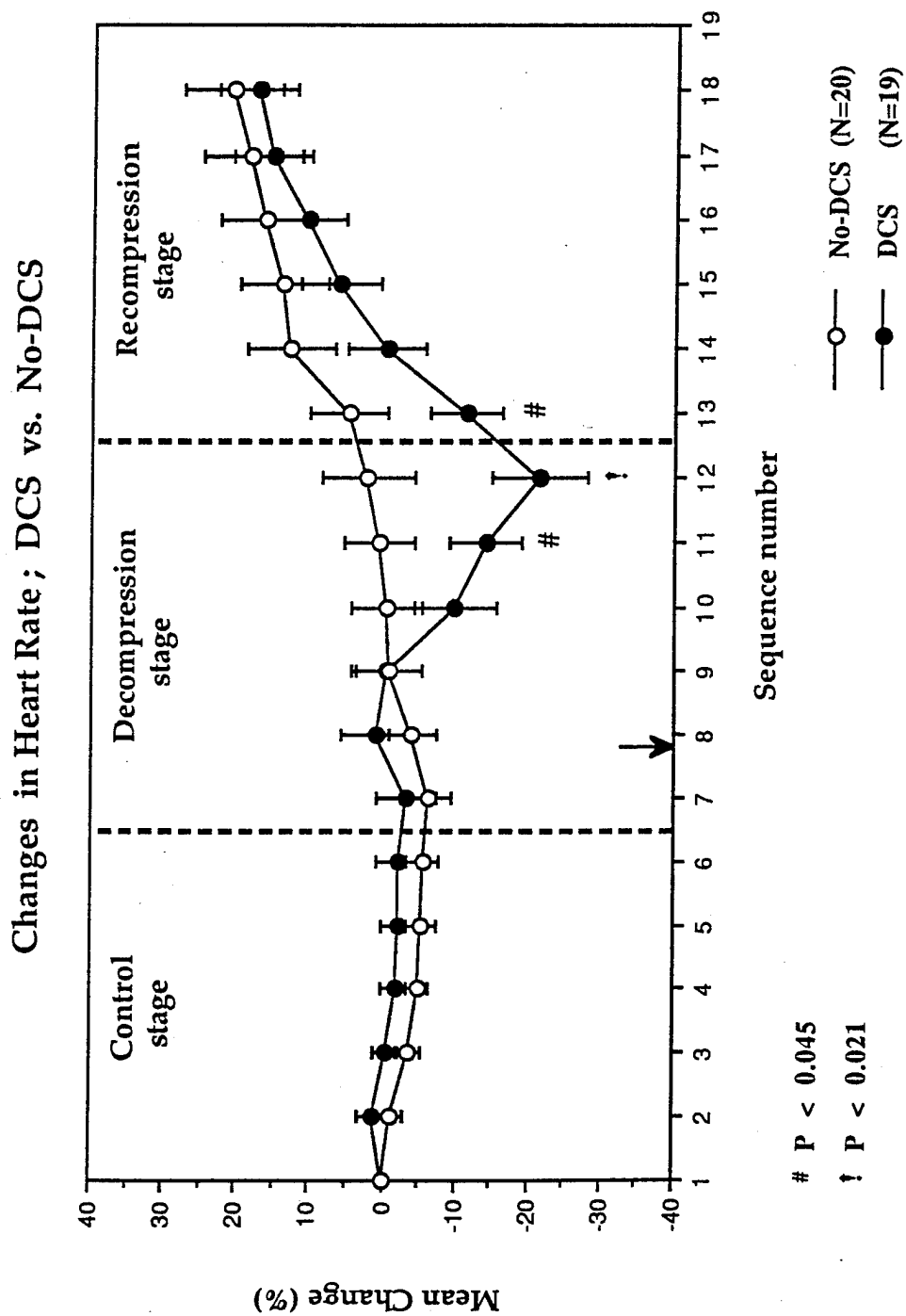


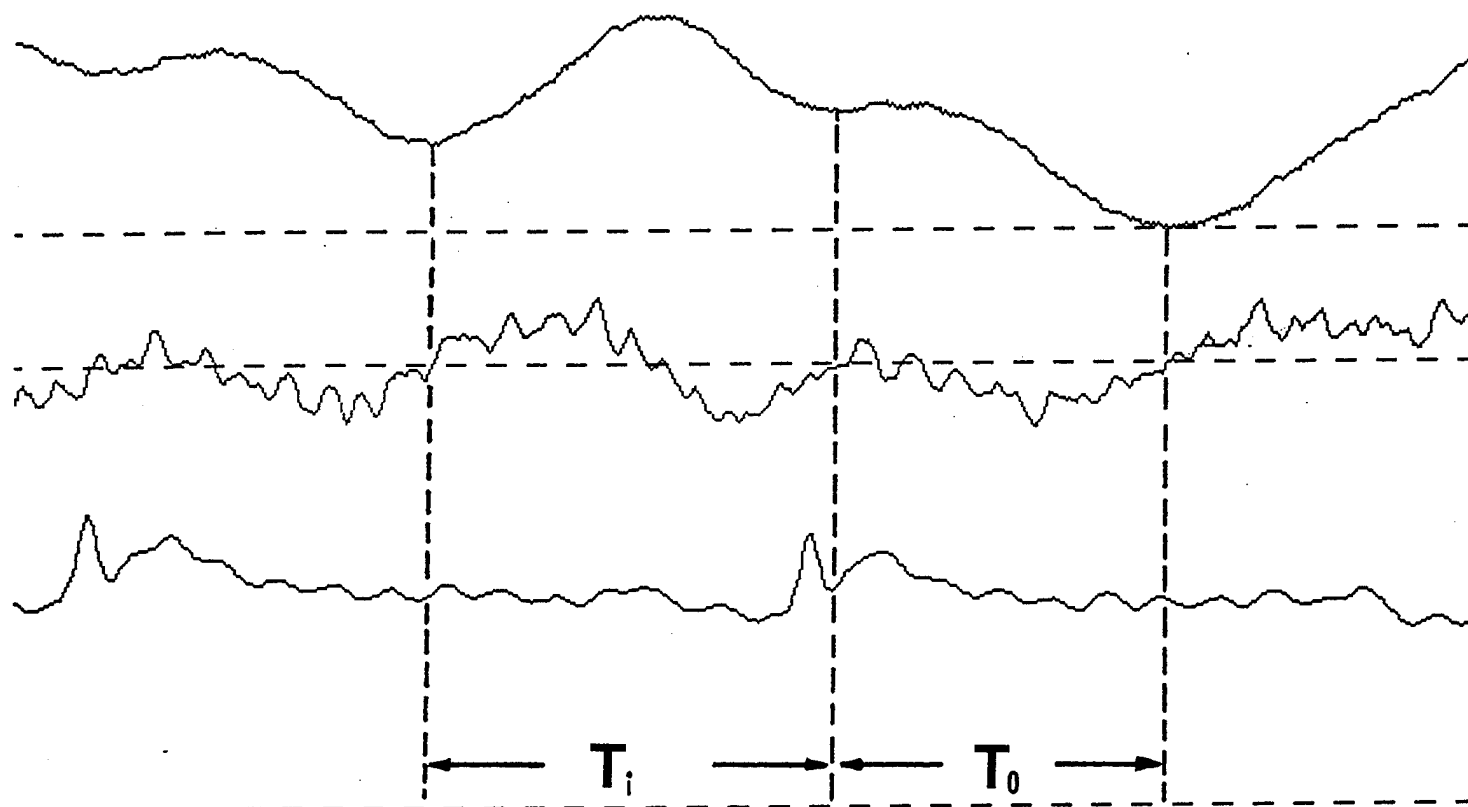
SLIDE 15:



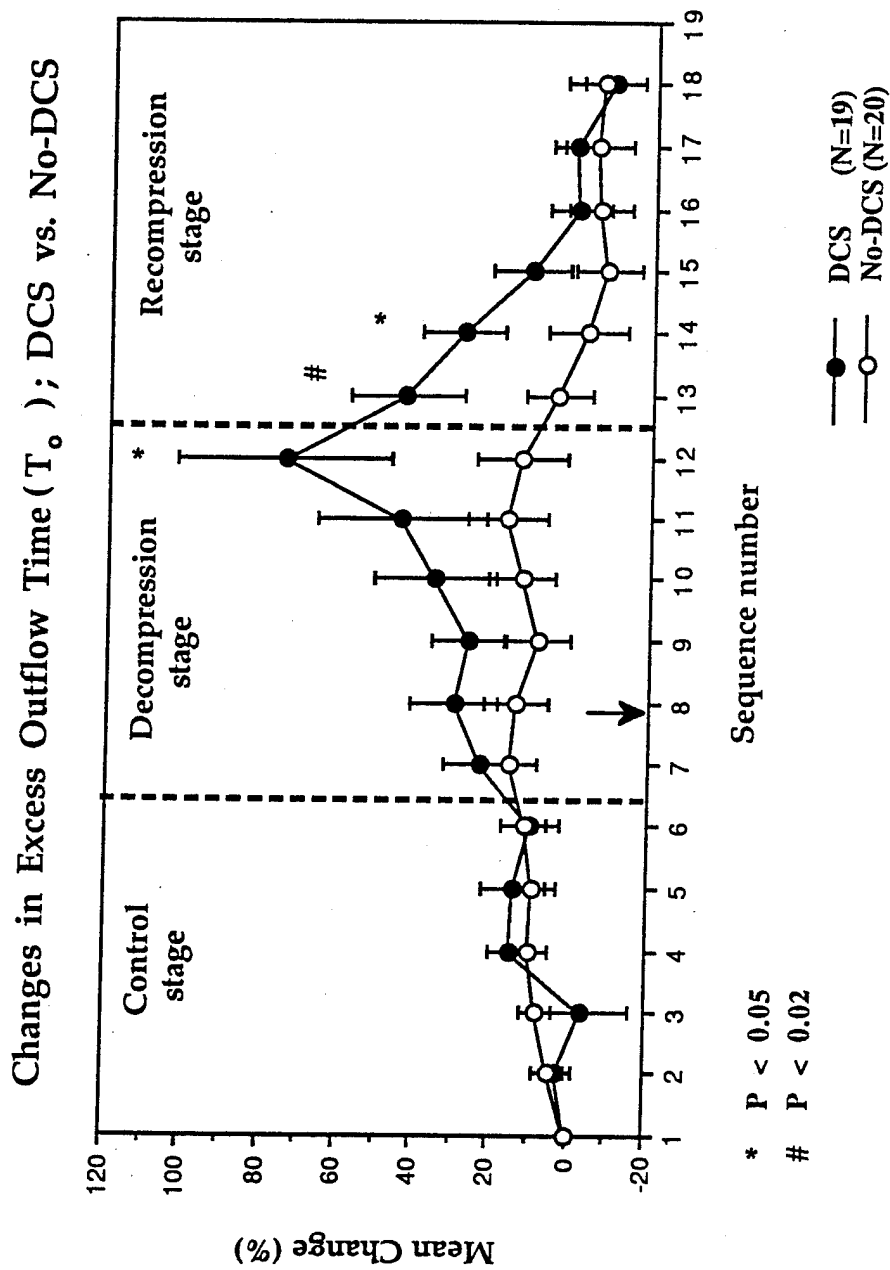


SLIDE 16:

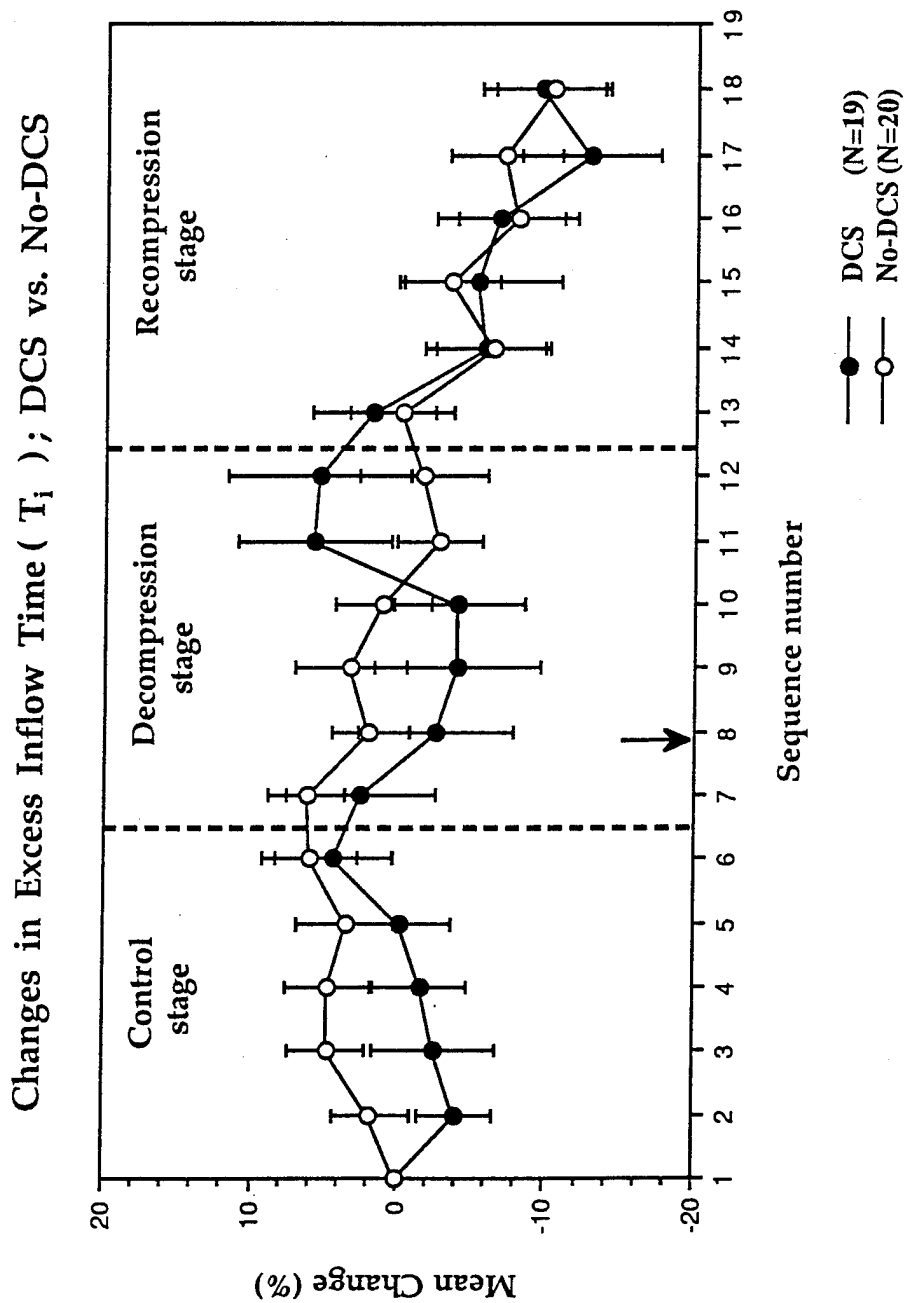


SLIDE 17:

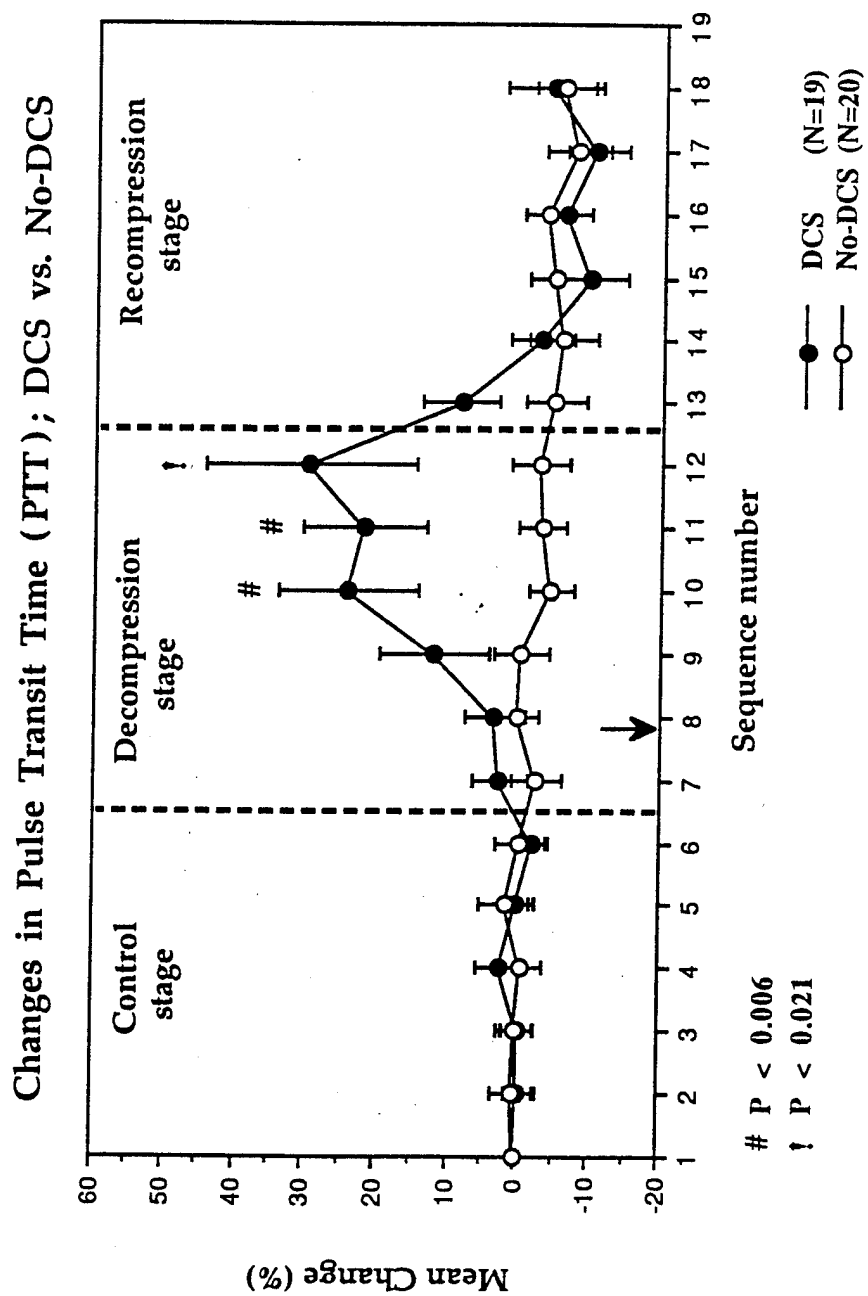
SLIDE 18:



SLIDE 19:



SLIDE 20:



SLIDE 21:CONCLUSIONS:

- Bubble dielectric signatures obtained by Electrical Impedance Spectroscopic (EIS) monitoring were observed in the tails of decompressed rats that developed DCS but not in rats that failed to develop DCS.
- Impedance Plethysmographic results paralleled the EIS results: Blood flow and hemodynamic changes in rats that developed DCS were different from and/or more severe than those observed in rats that failed to develop DCS.
- The appearance of bubble dielectric signatures and peripheral circulatory impairment tended to precede DCS onset.
- Real-time EIS monitoring of select body segments for decompression-induced bubble formation and growth with concurrent IPG monitoring for hemodynamic changes may provide noninvasive, premonitory and objective indices of DCS onset in decompressed animals and man.

### APPENDIX C.3

MONITORING OF FLUID REDISTRIBUTION DURING HEAD-DOWN TILT BY  
BIOELECTRICAL IMPEDANCE SPECTROSCOPY

Wayne A. Gerth, Ph.D.<sup>1,2</sup>  
Leslie D. Montgomery, Ph.D.<sup>3</sup>  
Yi-Chang Wu, M.D.<sup>1</sup>

Presented at the  
25<sup>th</sup> Annual Meeting and Exposition of the  
Association for the Advancement of Medical Instrumentation  
May 5-9, 1990; Anaheim, CA.

<sup>1</sup> Department of Cell Biology, Division of Physiology and  
F.G. Hall Hyperbaric/Hypobaric Center  
Duke University Medical Center  
Durham, NC 27710

<sup>2</sup> Department of Anesthesiology  
Duke University Medical Center  
Durham, NC 27710

<sup>3</sup> LDM Associates  
1764 Emory St.  
San Jose, CA 95126



# Proceedings



## AAMI 25<sup>th</sup> Annual Meeting & Exposition

*It's our Anniversary and we're throwing a party!*

May 5-9, 1990  
Anaheim, California

Association for the Advancement of Medical Instrumentation

Gerth  
TPMII  
Bioimpedance Techniques in Aerospace Research  
(L. Montgomery)

MONITORING OF FLUID REDISTRIBUTION DURING HEAD-DOWN TILT BY  
BIOELECTRICAL IMPEDANCE SPECTROSCOPY. W.A. Gerth, Ph.D.<sup>1</sup>,  
L.D. Montgomery, Ph.D.<sup>2</sup>, Y.C. Wu, M.D.<sup>1</sup>, F.G. Hall  
Hypo/Hyperbaric Center, Duke University Medical Center,  
Durham, NC 27710; <sup>2</sup>LDM Associates, San Jose, CA 95119.

INTRODUCTION: Bioimpedance methods using fixed frequency stimulation have been widely used to measure changes in the volume and hemodynamic status of body segments of human subjects under various conditions of body position and orthostatic stress. Electrical Impedance Spectroscopy (EIS) is an extension of these methods that is being developed to examine accompanying changes in the distribution of fluids between the intra- and extra-cellular compartments of the monitored body segments.

METHODS: After being fitted with noninvasive ECG electrodes to measure left calf and thigh segmental impedances, each of four human volunteers was successively placed in a normal seated rest position for 30 min, in a supine 6° head-down tilt (HDT) position for 90 min, and again in the seated rest position for 60 min. At 5 min intervals, a computer-controlled impedance analyzer was used to measure the complex impedances of the monitored segments at each of a series of discreet frequencies from 3 to 150 kHz. A simple equivalent circuit model representing idealized conductance paths through each segment was fit to each measured impedance spectrum using nonlinear least squares. Results provided estimates of the segmental-average intracellular resistance ( $R_i$ ), extracellular resistance ( $R_e$ ) and membrane capacitance ( $C_m$ ) as they varied throughout each run. RESULTS: Results for all subjects exhibited a similar pattern. During the initial seated phase, calf dielectric properties changed in ways indicative of blood pooling in the leg.  $R_e$  and  $C_m$  exhibited small but progressive decreases while  $R_i$  increased. Thigh  $R_e$  tended to remain stable or increase in evidence of slight fluid loss. During the ensuing HDT period, initial large increases in both calf and thigh  $R_e$  reflected the exsanguination of capacitance vessels, while smaller increases in these parameters continuing throughout HDT indicated interstitial fluid loss. Progressive increases in calf  $C_m$  accompanied by decreases of calf  $R_i$  during HDT in some subjects suggest that the average intracellular volume increased. Changes observed during HDT reversed during the subsequent seated recovery period. CONCLUSIONS: Both intra- and extra-cellular fluid compartments of the leg undergo dynamic changes during HDT. EIS affords a noninvasive means to illuminate the kinetics of these changes and promises to be a valuable tool for tracking similar events in various clinical contexts. (Supported by USN Contract N00014-87-C-0166)

Wayne A. Gerth, Ph.D.; Box 3823; Duke University Medical Center; Durham, NC 27710.

Published by  
Association for the Advancement of Medical Instrumentation  
3330 Washington Blvd., Suite 400  
Arlington, Virginia 22201

© 1990 by the Association for the Advancement of Medical Instrumentation

All Rights Reserved  
Printed in the United States of America  
ISBN 0-910275-96-3

## INTRODUCTION

## SLIDE 0. TITLE.

Redistributions of body fluids between different body segments, and between the intra- and extracellular compartments within these segments, are of particular interest as physiological indices of orthostatic stress. Such redistributions are also important features of physiological responses and adaptations to space weightlessness and of shock and other clinical disorders. Bioelectrical impedance spectroscopy, coupled with computer-aided equivalent circuit analysis, promises to provide a noninvasive means to track such changes with both anatomic and temporal resolution unattainable by more conventional methods, and under conditions in which the latter cannot be used.

## SLIDE 1. Ohm's Law; Direct current.

Tissues are ionic conductors of electric current. In accord with Ohm's law, a certain voltage  $V$  is developed across any given tissue in response to passage of a direct current of amplitude  $I$ , and the ratio of  $V$  to  $I$  gives the resistance,  $R$ . On initial application of the current, however, this equilibrium voltage is not achieved immediately.

SLIDE 2.  $V$  response to step function application of  $I$ .

This slide provides an idealized illustration of the polarization or voltage response of a tissue subjected to a step function application of current. The left figure shows the applied step function excitation potential, with voltage on the ordinate and time on the abscissa. The corresponding voltage response of the tissue is shown on the right. After an immediate but only partial polarization, the remainder of the response occurs exponentially over time as charge accumulates at boundaries between structural heterogeneities in the tissue. This time dependence of the polarization is called **dielectric relaxation**. When the applied current alternates sinusoidally at some nonzero frequency, dielectric relaxation causes the voltage response to be phase

shifted and attenuated with respect to the applied current by amounts that depend on the frequency.

SLIDE 3. Ohm's law; Alternating current.

These phenomena are considered quantitatively using a general form of Ohm's law, where the voltage response is decomposed into real and imaginary components of a complex number. The real component gives the fraction of the response which is in-phase with the applied current and the imaginary component gives the remaining fraction which is  $90^\circ$  out-of-phase with the current. This complex voltage is divided by the current to give the complex impedance  $Z^*$ . The real part of  $Z^*$  is the resistance  $R$  and the imaginary part is the reactance  $X$ . In tissue, where any inductive properties manifest only at extremely low excitation frequencies, the reactance is in turn a function of the capacitance  $C$  as indicated. As a result of dielectric relaxation phenomena, the resistance, reactance and overall impedance of tissue vary with the frequency of the applied current.

In the 1 - 150 kHz range, the frequency dependent variations of tissular impedance arise principally from the capacitive reactances of cell membranes.

SLIDE 4. Idealized tissular low-frequency current path;  
extracellular.

At low frequencies, high cell membrane reactances prohibit current flux through cells, so that tissular impedance is governed by properties of the extracellular fluid.

SLIDE 5. Idealized tissular high-frequency current paths;  
parallel intra- and extracellular.

At high frequencies, membrane reactance is negligible, so that current passes through both the extra- and intracellular spaces. Tissular impedance is then governed by the combined properties of the two compartments. Time series of tissue impedances measured as a function of frequency consequently embody tissue structural information that can illuminate changes in the relative

distributions of fluid between the tissular intra- and extracellular compartments.

We have developed an Electrical Impedance Spectroscopic, or EIS, system that measures the in vivo dielectric properties of tissue and, through analysis of these properties, provides real-time assessment of compartmental fluid redistribution in response to environmental or physiological stress.

## **MATERIALS**

### **System Overview**

The EIS system consists of a Schlumberger Technologies, Solartron 1260 Impedance/Gain-Phase Analyzer controlled via an IEEE-488 interface by a Digital Equipment Corporation VAXstation 3200 computer. The entire system, excepting a laserprinter for hardcopy data and graphics output, is mounted in one full EIA standard cabinet rack on castors for portability in the laboratory.

An impedance spectrum of a body segment is obtained by measuring the voltage developed across the segment in response to sinusoidal electric current excitation at each of a series of discrete frequencies from 3 to 150 kHz. A signal generator and current amplifier in the 1260 provides the excitation signal which is passed through the segment and terminated at a current input channel on the 1260. The amplitude and phase of the current actually passed through the segment is measured at this latter terminal. Electric response of up to two segments in the excitation current path is measured across independent differential voltage input channels. Noninvasive ECG electrodes are used in tetrapolar configuration to minimize interference of electrode impedance. System software configures the analyzer for spectrum acquisition, setting values for all analyzer functions, including the excitation voltage and current and the frequencies to be swept. The analyzer is operated in differential mode on each of its two channels with the shields for all output and input leads floated from ground at the analyzer chassis. Shields of all leads are also brought to equal potential at a single point near the monitoring ends of the leads.

SLIDE 6. Threshold for current sensation in human thorax.

Bioimpedance plethysmographic instruments using fixed frequency excitation typically operate at frequencies in excess of 50 kHz. Impedance spectroscopy, however, requires measurement of impedances at lower frequencies where, in living tissue, stimulation of muscle and nerve becomes a problem, even at the 1-4 mA currents commonly used in impedance plethysmography.

The bottom line in this figure, taken from a paper by Geddes and Baker, shows the threshold for sensation of sinusoidal current in the human thorax as a function of frequency from 10 Hz to 100 kHz. Subjects begin to feel applied currents of rms values above this line at a given frequency, while lower currents are imperceptible. Clearly, maximum safe drive currents decrease with decreasing frequency. Thus, safety considerations motivate use of the lowest acceptable excitation currents in spectroscopic work and, indeed, ultimately determine the lowest frequencies at which impedances can be safely measured. However, signal strength and measurement accuracy is compromised as the excitation current decreases, motivating use of higher currents. To resolve this conflict between safety and accuracy, and enable measurements at lower frequencies, the excitation current in our EIS system is increased as a function of frequency from about 0.3 mA to a maximum of 5.0 mA (3.0 V max.). As the measurement frequency increases during each sweep from about 2.5 kHz to 150 kHz, the drive current is adjusted upward using a log-log relationship that approximates the near linear portion of this lowest sensation threshold curve in the figure. A minimum current of 0.3 - 1.0 mA is used when this relationship gives smaller values and a limit of 5.0 mA is imposed at higher frequencies.

Measurement results are passed from the analyzer to the computer for immediate processing and storage on disk or magnetic tape.

### Data Analysis

Each impedance spectrum consists of a series of discrete impedances measured at each of the separate frequencies in the sweep.

## SLIDE 7. Impedance locus of human calf.

The spectrum can be visualized graphically in the impedance domain by plotting the reactance, or imaginary part of the impedance vs the resistance or real part of the impedance at each frequency in the spectrum. Such a representation is called an **impedance locus**. A measured impedance locus of a human calf is shown here. The locus is built from 50 discrete measurements at frequencies from 3 to 150 kHz. Individual points are obscured because they are connected by straight lines in the figure. The point from the lowest frequency impedance defines the right-most or highest resistance end of the locus. The point from the highest frequency impedance defines the left-most or lowest resistance end of the locus. Points from impedances at intermediate frequencies define the intervening locus region. Thus, the locus shows how the resistance decreases with increasing frequency. Similarly, the locus shows how the reactance first decreases from zero at infinitely low frequency, then increases towards zero at infinitely high frequency.

Note that the span of the ordinate values is 6 ohms, while the span of the abscissa is 20 ohms. The resultant nonunitary aspect ratio of the plot distorts the shape of the locus, which is actually semi-circular, and makes it appear parabolic.

Immediately after acquisition of each spectrum, the spectrum is analyzed and interpreted according to a simple lumped-parameter equivalent circuit model which represents idealized conductance paths through the monitored body segment.

## SLIDE 8. Equivalent circuit model.

The circuit model, shown in this figure, models the segment as a uniform isotropic bidomain conductor. That is, current through the segment is considered able to pass through two parallel conductance paths; one through an extracellular compartment having average resistance  $R_e$ , and the other through an intracellular compartment having average resistance  $R_i$  and capacitance  $C_m$ . The value of  $R_i$  is governed by both membrane and cytoplasmic

properties, while  $C_m$  is governed principally by membrane properties.

The complex admittance for this circuit is given analytically in terms of the complex impedance and the circuit parameters by the equation at the bottom of the figure. The  $(1-\alpha)$  exponent in the denominator of the rightmost term is included to account for tissue heterogeneity. Increasing values of  $\alpha$  from 0 towards unity indicate increasing heterogeneity.

#### SLIDE 9. Nonlinear least squares implementation.

The circuit equation is fitted to the spectrum using an iterative nonlinear least squares routine based on Marquardt's algorithm. The algorithm is implemented using the norm of each observed impedance and that of the corresponding fitted impedance. The algorithm adjusts the model parameters to minimize the sum of squares, SS, for the impedances at the  $n$  different frequencies in each spectrum.

### METHODS

System performance was evaluated on a small human subject population during short-term simulations of space weightlessness using 6° head-down tilt.

#### SLIDE 10. Experimental Protocol.

After providing informed consent, each of four male human volunteers was fitted with ECG electrodes for bioimpedance monitoring of the left calf and thigh. Effects of body position on the dielectric properties of the monitored segments were then characterized at 5 min intervals during three successive periods during which the subject was in the normal seated rest position (30 min), in a supine, 6° head-down tilt (HDT) position (90 min), and again in the seated rest position (60 min). Each impedance spectrum required about 70 s to acquire and consisted of measurements taken at 50 discrete frequencies distributed logarithmically from 3 to 150 kHz.



## RESULTS and DISCUSSION

SLIDE 11. Typical impedance loci of the calf  
at the end of each test period.

Impedance loci exhibited systematic changes in response to changed orthostatic stress that were consistent among all the subjects. This figure illustrates impedance loci of the calf of one subject at the end of each of the three periods in the test protocol. Typifying the results in all subjects, the locus widened and shifted towards higher resistance and more negative reactance values at the end of the HDT period. At the end of the post-tilt recovery period, the locus resembled that obtained at the end of the pre-tilt period.

SLIDE 12. Typical impedance loci of the thigh  
at the end of each test period.

Impedance loci of the same subject's thigh are shown here, as obtained in parallel with those of the calf shown previously. Changes in the shape and position of the locus throughout the test protocol are similar to those for the calf.

SLIDE 13. Fitted equivalent circuit parameters; typical subject.

Reflecting the systematic changes in the impedance loci, fitted equivalent circuit parameters also changed systematically throughout the test protocol. Results are typified by those shown in this figure for the calf (TOP) and thigh (BOTTOM) of one subject. Each parameter is shown vs. elapsed time in "strip chart" format, with the ordinate scaled such that the major ticks above and below the first value shown at  $t=0$  represent + and - 20% deviation, respectively, from that value.  $R_e$  and  $R_i$  are in Ohms,  $C_m$  is in micro-farads and  $\alpha$  is dimensionless.

Rapid changes in the extracellular resistance  $R_e$  following each change in body position correspond to the emptying or filling of segmental capacitance vessels, while the slower, more progressive changes in this parameter during maintenance of the different body positions probably reflect

fluid movement out of or into the segmental interstitial space. Thus, the observed decreases in the calf shunt or extracellular resistance,  $R_e$ , with assumption and maintenance of the seated position reflect the pooling of blood and other fluid in this segment. In contrast, thigh  $R_e$  increased somewhat in this subject, indicating fluid loss from this segment that was less evident or absent in other subjects during this period.

The time courses of the segmental  $R_e$  and  $R_i$  changes during HDT followed somewhat different patterns in the two segments, reflecting the different levels of segmental orthostatic stress. On initial assumption of the HDT position, both of these parameters showed large rapid changes in both segments. However, the tendency for these parameters to continue changing throughout the remaining period of HDT was more pronounced in the calf than in the thigh. This pattern suggests that interstitial fluid loss in the thigh during maintenance of the HDT position was not as great as in the calf.

Changes in the intracellular resistance  $R_i$  and membrane capacitance  $C_m$  illuminate changes in the volumes and ionic concentrations of the segmental intracellular spaces. The decreases in calf intracellular resistance  $R_i$  that accompanied assumption and maintenance of the HDT position indicate that the average volume and/or the electrolyte concentration of the intracellular space increased. The former interpretation is supported by the observed coincident increases of calf membrane capacitance. Increases in this parameter are plausibly interpreted to arise from decreases in the segmental average cell membrane thickness, such as would accompany increases in average cell volume. Thus, results indicate that cells in the calf swell when the body is under anti-orthostatic stress. This indication is in accord with evidence reported by other workers that calf interstitial osmotic pressure decreases during HDT. Similar but attenuated indications obtained for the compartmental responses in the thigh.

Changes observed during HDT reversed during the subsequent seated recovery period in all subjects.

SLIDE 14. Fitted equivalent circuit parameters; Grouped MEANS

Grouped mean values of the fitted equivalent circuit parameters at the

various elapsed times in the protocol are shown in this slide for the four subjects studied. Again, data for the calf are shown in the top figure and data for the thigh in the bottom figure. Although somewhat noisier, results generally show the trends that were clearly evident in the data for the single subject just shown. At the end of the HDT period, mean calf  $R_e$  values had increased 35%, mean calf  $R_i$  values had decreased 24% and mean calf  $C_m$  values had increased 33% from their values at the end of the pre-tilt period. Parametric changes in the thigh were similar but attenuated. Mean thigh  $R_e$  increased 26%, mean thigh  $R_i$  decreased 14% and mean thigh  $C_m$  increased 12% over the same interval.

It is important to note that the large increases in segmental extracellular resistance during HDT were significantly compensated by corresponding decreases in segmental intracellular resistance. The results can be reduced to segmental mutual resistances that are comparable to the overall segmental resistance that would have been obtained had a conventional fixed frequency impedance plethysmographic method been used. From the end of the pre-tilt seated period to the end of the HDT period, such reduced mutual impedances increased by only 16% in the calf and 9% in the thigh. The latter are comparable to the corresponding segmental volume decreases reported by other workers in similar studies. The present application of EIS technology thus augments these earlier results by suggesting that the HDT-induced volume losses in the lower extremities come from the extracellular rather than the intracellular space.

## CONCLUSIONS

### SLIDE 15. CONCLUSIONS.

Results show that impedance spectra of the human calf and thigh undergo systematic and dynamic changes in response to changes in orthostatic stress. The changes are reversible and can be related to the redistribution of fluid between segmental intracellular and extracellular fluid compartments by lumped-parameter equivalent circuit analysis. These redistributions differ between the two segments in each subject in accord with the orthostatic dependence of the segments. EIS promises to provide a noninvasive means to

quantify the kinetics of fluid shifts and compartmental fluid redistribution on a segmental level under conditions where high temporal resolution is desired.

#### ACKNOWLEDGEMENT

This research was supported by a contract from the U.S. Navy Bureau of Medicine, Contract No. N00014-87-C-0166.

SLIDE 0:MONITORING OF FLUID REDISTRIBUTION DURING HEAD-DOWN TILT BY  
BIOELECTRICAL IMPEDANCE SPECTROSCOPY

Wayne A. Gerth, Ph.D.  
Leslie D. Montgomery, Ph.D.  
Yi-Chang Wu, M.D.

Duke University Medical Center  
Durham, NC

and

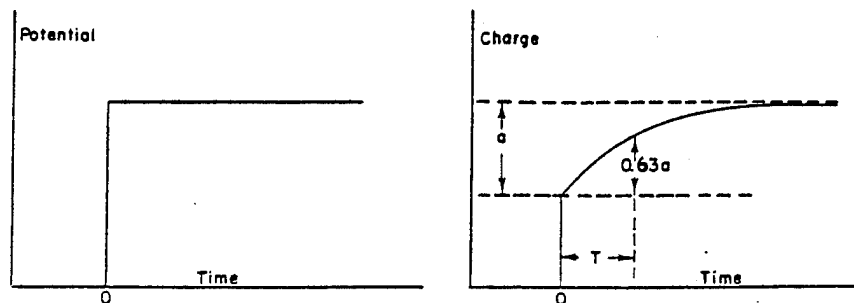
LDM Associates  
San Jose, CA

SLIDE 1:OHM'S LAW; Direct Current

$R = V/I$  ;      R = Resistance (Ohms)

V = Voltage (Volts)

I = Current (Amperes)

SLIDE 2:SLIDE 3:OHM'S LAW: Alternating current

$$Z^* = V^*/I ; \quad \text{complex voltage, } V^* = a + bj$$

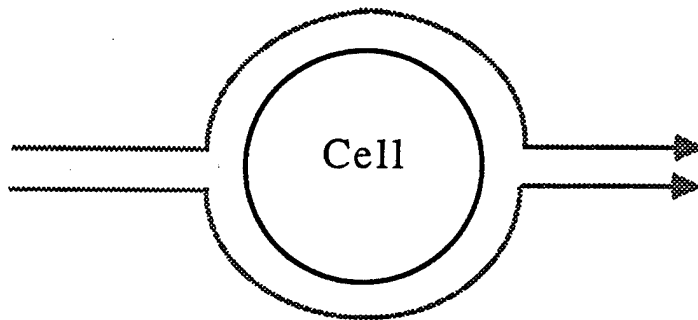
$$j = \sqrt{-1}$$

$$Z^* = R + Xj ; \quad \text{reactance, } X = -1/C\omega$$

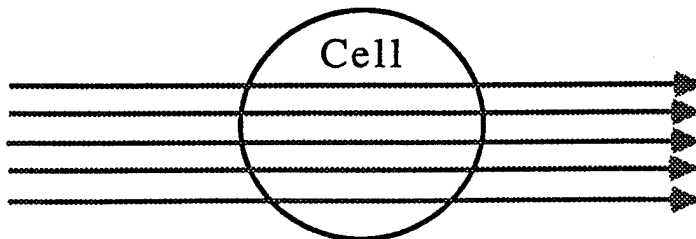
$$\text{angular frequency, } \omega = 2\pi f$$

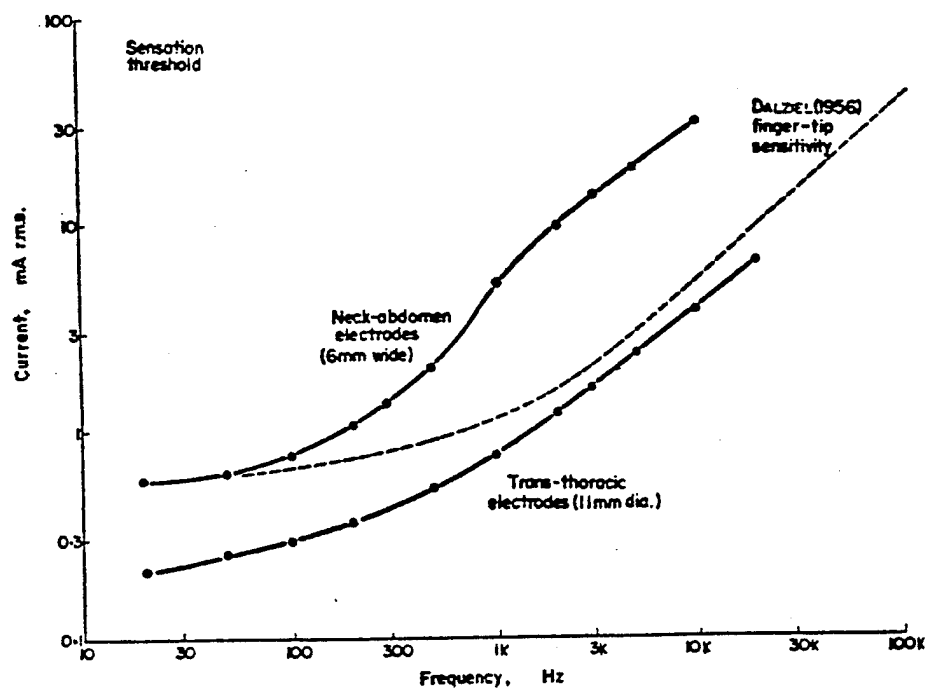
SLIDE 4:

Current Paths; Low Frequencies

SLIDE 5:

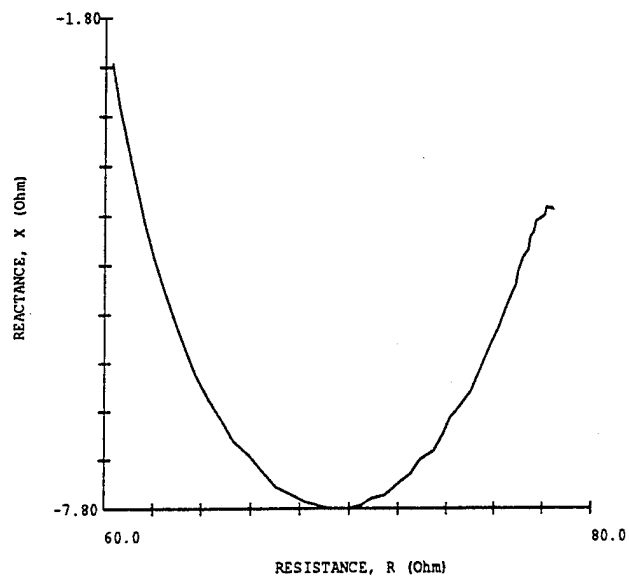
Current Paths; High Frequencies

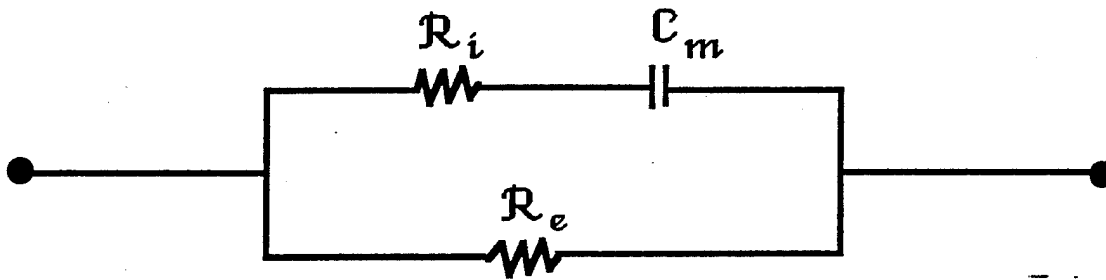


SLIDE 6:

Threshold of sensation as a function of frequency for sinusoidal alternating current.



SLIDE 7:

SLIDE 8:

Equivalent Circuit Model

$$Y^* = 1/Z^* = 1/R_e + 1/R_i - \frac{1/R_i}{1 + j\omega\tau^{\circ(1-\alpha)}}$$

$$Z^* = R + jX$$

$$\tau^{\circ} = R_i \cdot C_m$$

$$0 < \alpha < 1$$

SLIDE 9:NONLINEAR LEAST SQUARES IMPLEMENTATION

Equivalent circuit parameters are adjusted to minimize SS:

$$SS = \sum_{i=1}^n \{ |Z_i^*| - |z_i^*| \}^2 ;$$

SS = Sum-of-Squares;

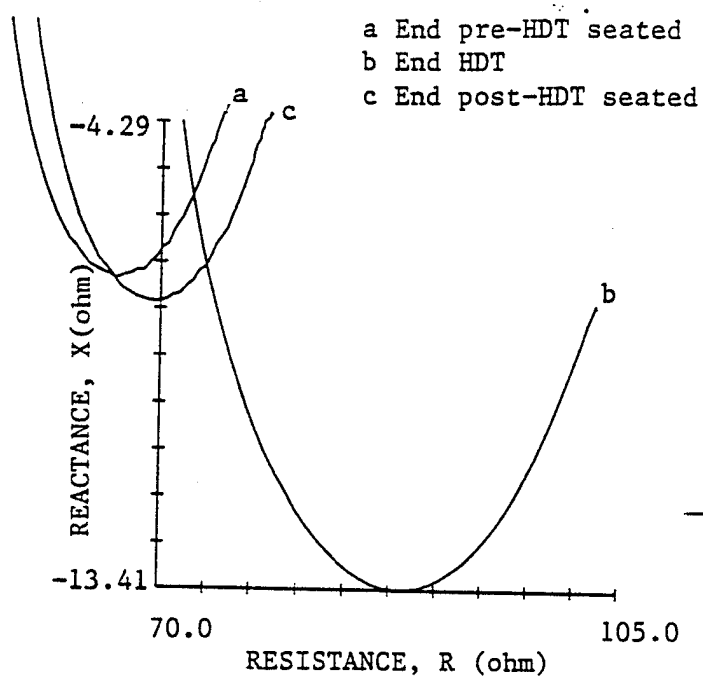
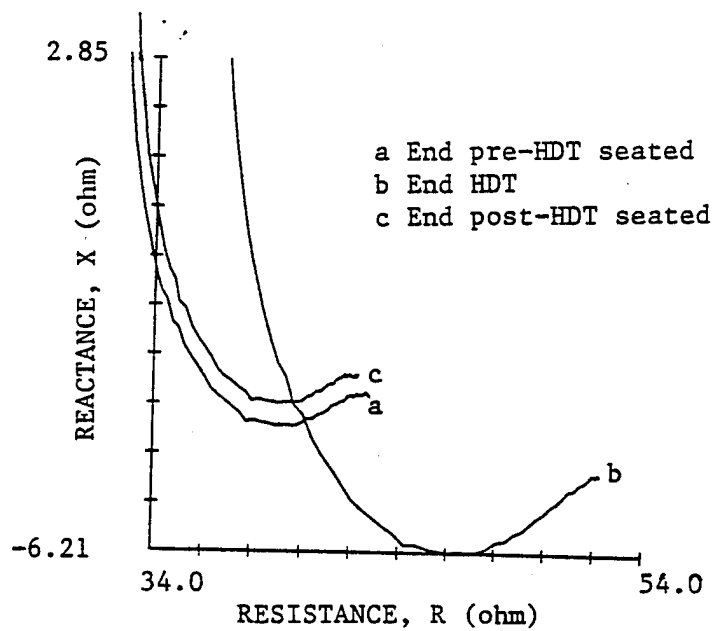
n = Number of frequencies in spectrum;

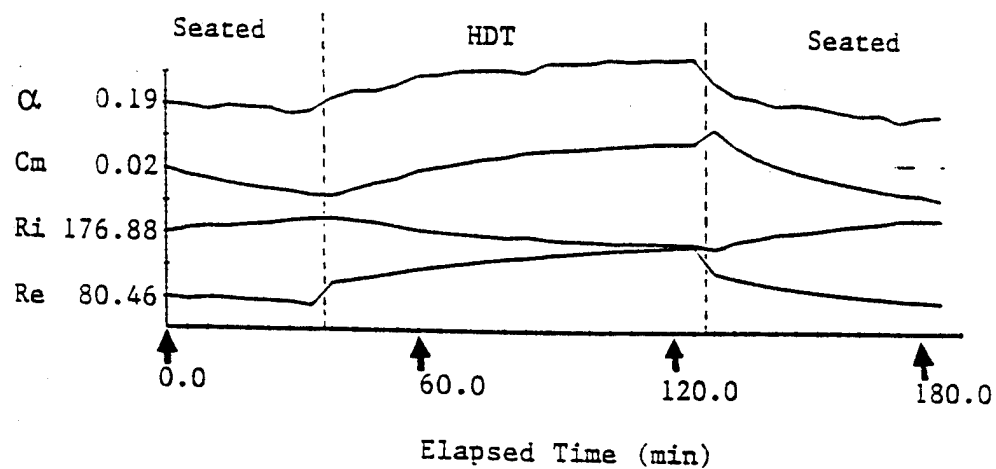
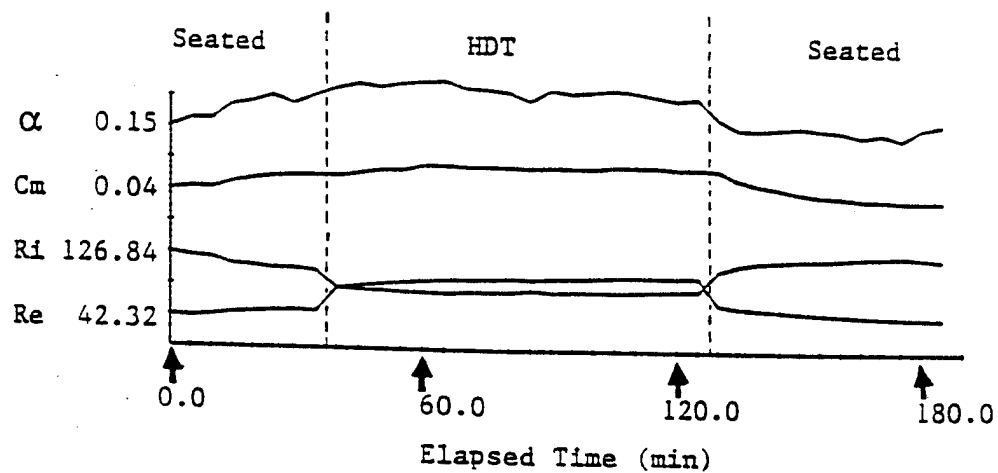
$|Z_i^*| = \sqrt{R^2 + X^2}$  = Norm of measured complex impedance at point i;

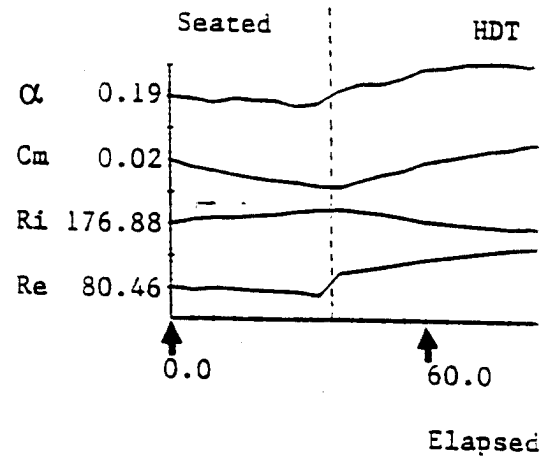
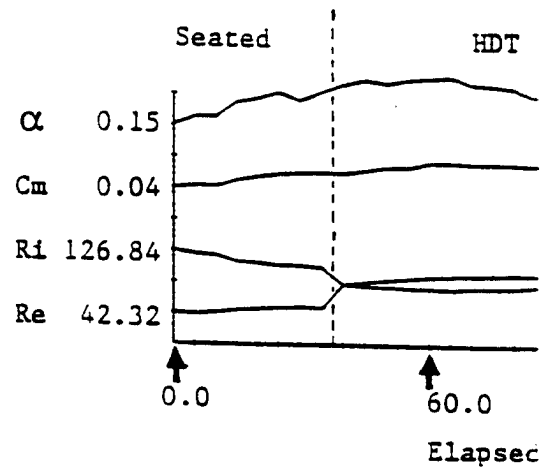
$|z_i^*|$  = Norm of fitted complex impedance at point i.

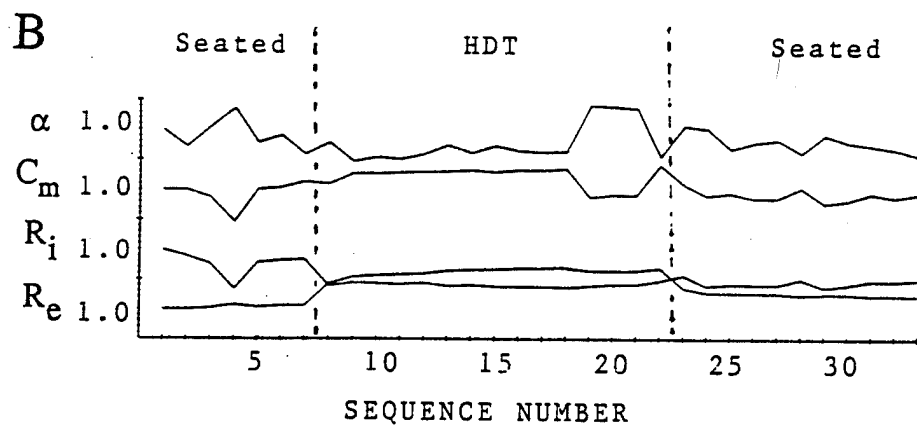
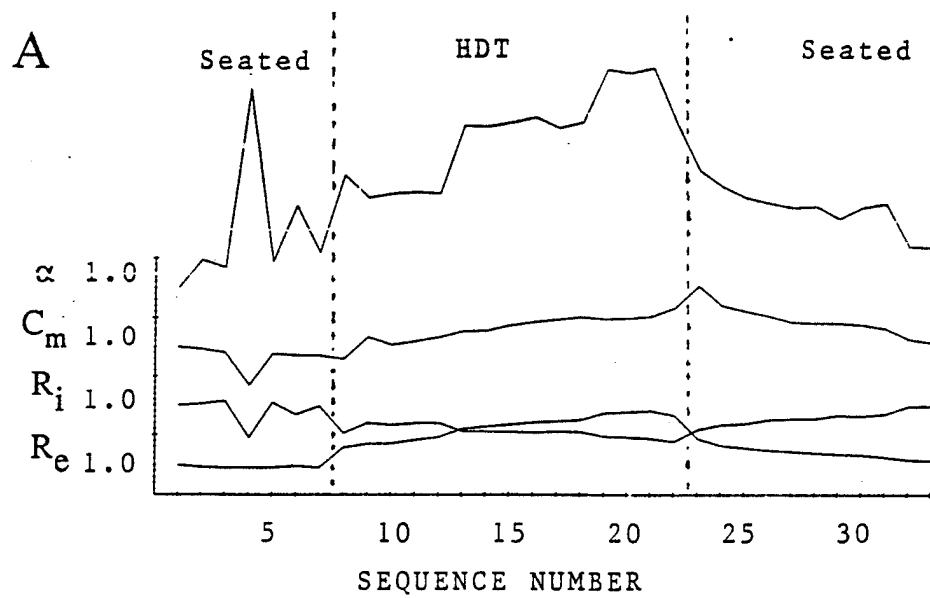
SLIDE 10:EXPERIMENTAL PROTOCOL

- Noninvasive ECG electrodes (3-M, Red Dot) placed for impedance monitoring of left calf and thigh;
- Impedance spectra taken at 5 min intervals during the following successive periods with the subject:
  - 1) seated, 30 min;
  - 2) supine, 6° head-down tilt, 90 min;
  - 3) seated, 60 min.

SLIDE 11:**A**SLIDE 12:**B**

SLIDE 13:**A****B**

SLIDE 13:**A****B**

SLIDE 14:

SLIDE 15:CONCLUSIONS

- Impedance spectra of the human calf and thigh change systematically with changes in orthostatic stress;
- Lumped-parameter equivalent circuit analysis allows these changes to be related to changes in extra- and intracellular fluid distribution within the monitored body segments;
- EIS promises to provide a noninvasive means to monitor fluid shifts between and within monitored body segments with a high level of temporal resolution.



#### APPENDIX C.4

Proceedings  
**Third Annual IEEE Symposium on  
COMPUTER-BASED MEDICAL SYSTEMS**

June 3-6, 1990  
University of North Carolina at Chapel Hill

Sponsored by  
IEEE Computer Society  
IEEE Engineering in Medicine and Biology Society  
IEEE Eastern North Carolina Section

In cooperation with  
University of North Carolina  
North Carolina State University  
Duke University  
Research Triangle Institute

With contributions by  
MCNC  
North Carolina Biotechnology Center



IEEE Computer Society Press  
Los Alamitos, California

Washington • Brussels • Tokyo

A COMPUTER-BASED BIOELECTRICAL IMPEDANCE SPECTROSCOPIC SYSTEM FOR  
NONINVASIVE ASSESSMENT OF COMPARTMENTAL FLUID REDISTRIBUTION.

W.A. GERTH,<sup>1</sup> L.D. MONTGOMERY<sup>2</sup> and Y.C. WU<sup>1</sup>

<sup>1</sup>F.G. Hall Hypo/Hyperbaric Center  
Box 3823  
Duke University Medical Center  
Durham, NC 27710

<sup>2</sup>LDM Associates  
1764 Emory Street  
San Jose, CA 95119

ABSTRACT

Bioimpedance methods using fixed frequency stimulation have been widely used to measure volume changes and hemodynamic parameters in body segments of human subjects under various conditions of body position and orthostatic stress. An Electrical Impedance Spectroscopic (EIS) system has been developed to allow extension of these studies to include examination of the redistribution of fluids between the intracellular and extracellular compartments of the monitored body segments. Evaluated in studies of the human calf and thigh during 90 min of 6° or 10° head-down bedrest, the system promises to enable tracking of segmental and compartmental fluid redistribution in response to various environmental and physiological stresses with both temporal and anatomic resolution greater than attainable by other methods.

INTRODUCTION

Redistributions of body fluids between different body segments, and between the intra- and extra-cellular compartments within these segments, are of particular interest as physiological indices of orthostatic stress, responses and adaptations to space weightlessness and the severity of shock and other clinical disorders. Bioelectrical impedance spectroscopy, coupled with computer-aided equivalent circuit analysis, promises to provide a noninvasive means to track such changes with both anatomic and temporal resolution unattainable by more conventional methods and under conditions in which the latter cannot be used.

Tissues are ionic conductors of electric current which, by virtue of their structural heterogeneity, exhibit dielectric relaxation phenomena that give rise to frequency dependent variations of the impedance to such conduction [1]. In the 1 - 150 kHz range, the resultant dielectric dispersions arise principally from the capacitive reactances of cell membranes. At low frequencies in this range, high cell membrane reactances prohibit current flux through cells, so that

tissular impedance is governed by properties of the extracellular fluid. At high frequencies, membrane reactance is negligible, allowing current to pass through both the extra- and intracellular spaces. Tissular impedance is then governed by the combined properties of the two compartments. Time series of tissue impedances measured as a function of frequency consequently embody tissue structural information that can illuminate changes in the relative distributions of fluid between the tissular intra- and extracellular compartments [1,2].

We have developed an Electrical Impedance Spectroscopic (EIS) system that measures the in vivo dielectric properties of tissue and, through analysis of these properties, provides real-time assessment of compartmental fluid redistribution in response to environmental or physiological stress.

## MATERIALS

### System Overview

The EIS system consists of a Schlumberger Solartron 1260 Impedance/Gain-Phase Analyzer controlled via an IEEE-488 interface by a Digital Equipment Corporation VAXstation 3200 computer. The entire system, excepting a laserprinter for hardcopy data and graphics output, is mounted in one full EIA standard cabinet rack on castors for portability in the laboratory.

An impedance spectrum of a body segment is obtained by measuring the voltage developed across the segment in response to sinusoidal electric current excitation at each of a series of discrete frequencies from 3 to 150 kHz. A signal generator and current amplifier in the 1260 provides the excitation signal which is passed through the segment and terminated at a current input channel on the 1260. The amplitude and phase of the current actually passed through the segment is measured at this latter terminal. Electric response of up to two segments in the excitation current path is measured across independent differential voltage input channels. Noninvasive ECG electrodes (3M, Ag/AgCl Red Dot) are used in tetrapolar configuration to minimize interference of electrode impedance. System software configures the analyzer for spectrum acquisition, setting appropriate values for a variety of analyzer functions, including the excitation voltage and current and the frequencies to be swept. The analyzer is operated in differential mode on each of its two channels with the shields for all output and input leads floated from ground at the analyzer chassis. Shields of all leads are also brought to equal potential at a single point near the monitoring ends of the leads.

The excitation current is either kept fixed at about 0.5 mA or increased as a function of frequency from about 0.3 mA to a maximum of 5.0 mA (3.0 V max.). The latter procedure maximizes signal-to-noise ratios and measurement accuracy in animal or human applications where

maximum safe drive currents decrease with decreasing frequency. As the measurement frequency increases during each sweep from about 2.5 kHz to 150 kHz, the drive current is adjusted upward using the log-log relationship:  $\ln I = m \ln f + b$ ; where  $I$  is the current at frequency  $f$ . Values of the parameters  $m$  and  $b$  are conservatively set according to data provided by Geddes and Baker [3] for the frequency dependence of the threshold for current sensation in the human thorax. A minimum current of 0.3 - 1.0 mA is used when this relationship gives smaller values and a limit of 5.0 mA is imposed at higher frequencies.

Measurement results are passed from the analyzer to the computer for immediate processing and storage on disk or magnetic tape.

#### Data Analysis

The data for each measurement consists of the following seven floating point values:

frequency (Hz),  $f$ ;  
 $a$  and  $b$  of the complex excitation current (amp),  $I^* = a + bj$ ;  
 $c$  and  $d$  of the complex voltage response (V), channel 1,  $V_1^* = c + dj$ ;  
 $e$  and  $f$  of the complex voltage response (V), channel 2,  $V_2^* = e + fj$ ;

where  $j = \sqrt{-1}$ . The complex impedance for each measurement on each channel is given by

$$Z^* = V^*/I^* = R + Xj, \quad (1)$$

where  $R$  and  $X$  are the equivalent series resistance and reactance, respectively. The three other complex transforms of the impedance are:

$$\text{Modulus, } M^* = Z^* \cdot j\omega; \quad (2)$$

$$\text{Admittance, } Y^* = 1/Z^*; \quad (3)$$

$$\text{Capacitance, } C^* = Y^*/j\omega; \quad (4)$$

where  $\omega = 2\pi f$  is the angular frequency. The locus of the impedance and each of its transforms is obtained by plotting the imaginary part vs the real part for the value at each frequency in the spectrum.

Immediately after acquisition of each impedance spectrum, simple lumped-parameter equivalent circuit models representing idealized conductance paths through the segment are fitted to the spectrum using a nonlinear least squares routine based on Marquardt's algorithm [4]. Present results are based on the equivalent circuit shown in Figure 1. Values of each circuit parameter can be examined as fitted to measured data, as in present work, or normalized with respect to the average segmental cross-sectional area and pickup electrode separation to give resistivities and capacities per unit volume of monitored tissue.

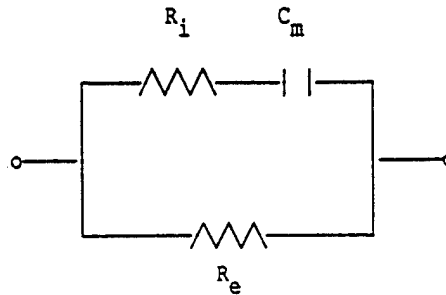


Figure 1. Equivalent circuit used in present work, representing an idealized tissue with an extracellular compartment having average resistance  $R_e$ , and an intracellular compartment having average resistance  $R_i$  and average capacitance  $C_m$ . The value of  $R_i$  is governed by both membrane and cytoplasmic properties, while  $C_m$  is governed principally by membrane properties.

The complex admittance for this circuit is given by

$$Y^* = \frac{1}{Z^*} = \frac{1}{R_e} + \frac{1}{R_i} - \frac{1/R_i}{1 + j\omega\tau^\circ(1-\alpha)} \quad (5)$$

where  $\tau^\circ$  is the time constant given by  $\tau^\circ = R_i C_m$ , and the quantity  $\alpha\pi/2$  is the angle between the real axis and a radius of the admittance locus passing through either of its two real axis intercepts. The  $(1-\alpha)$  exponent in eq. (5) is included to account for the typical failure of tissular impedance loci to be centered on the real axis. This behavior is consistent with the presence in tissue of a practical infinitude of R-C elements each with different time constants with values distributed about a mean at  $\tau^\circ$  [1,2,5]. By definition,  $\alpha=0$  when the center of the locus lies on the real axis. Increasing values of  $\alpha$  from 0 towards unity indicate a widening of the distribution of time constants, with increasing standard deviation of the distribution about  $\tau^\circ$ .

Marquardt's algorithm is implemented using the norm of each observed impedance,  $|Z^*|$ , and that of the corresponding fitted impedance,  $|\hat{Z}^*|$ . The algorithm adjusts the model parameters to minimize the sum of squares, SS,

$$SS = \sum_{i=1}^n (|Z_i^*| - |\hat{Z}_i^*|)^2 \quad (6)$$

for the impedances at the  $n$  different frequencies in each spectrum.

The analytic components of the software are bundled to process run-time data passed from the impedance spectrum acquisition routine, or to read and process data files from earlier experiments, providing identical output in either case. In the former mode, the analyses are automatically performed immediately after acquisition of each spectrum. Graphic displays of the results afford a means to track changes in the loci of the impedance and its transforms and in the equivalent circuit parameters of each monitored body segment throughout the course of an experiment.

#### METHODS

After providing informed consent, each of four male human volunteers was fitted with ECG electrodes for bioimpedance monitoring of the left calf and thigh. Drive electrodes were placed on the lateral aspect of the anterior superior iliac spine and on the dorsum of the metatarsus. Calf pickup electrodes were placed laterally above the lateral malleolus of the fibula and below the fibular head. Thigh pickup electrodes were placed just above the lateral epicondyle of the femur and on the lateral aspect of the greater trochanter of the femur.

Effects of body position on the dielectric properties of the monitored segments were then characterized at 5 min intervals during three successive periods during which the subject was in the normal seated rest position (30 min), in a supine, 6° or 10° head-down tilt (HDT) position (90 min), and again in the seated rest position (60 min). Each impedance spectrum required about 70 s to acquire and consisted of measurements taken at 50 discreet frequencies distributed logarithmically from 3 to 150 kHz.

#### RESULTS

Fitted equivalent circuit parameters exhibited systematic changes in response to changed orthostatic stress that were consistent among all subjects. The changes in the two monitored segments of each subject followed different patterns, particularly during the HDT period, reflecting the different levels of orthostatic stress in the segments. Results are typified by those shown in Figure 2 for one subject maintained at -6° tilt during the HDT period.

The observed decreases in the calf shunt resistance,  $R_e$ , with assumption and maintenance of the seated position reflect the pooling of blood and other fluid in this segment. However, thigh  $R_e$  increased somewhat, indicating fluid loss from this segment that was less evident or absent in other subjects maintaining this position.

Rapid changes in  $R_e$  following each subsequent change in body

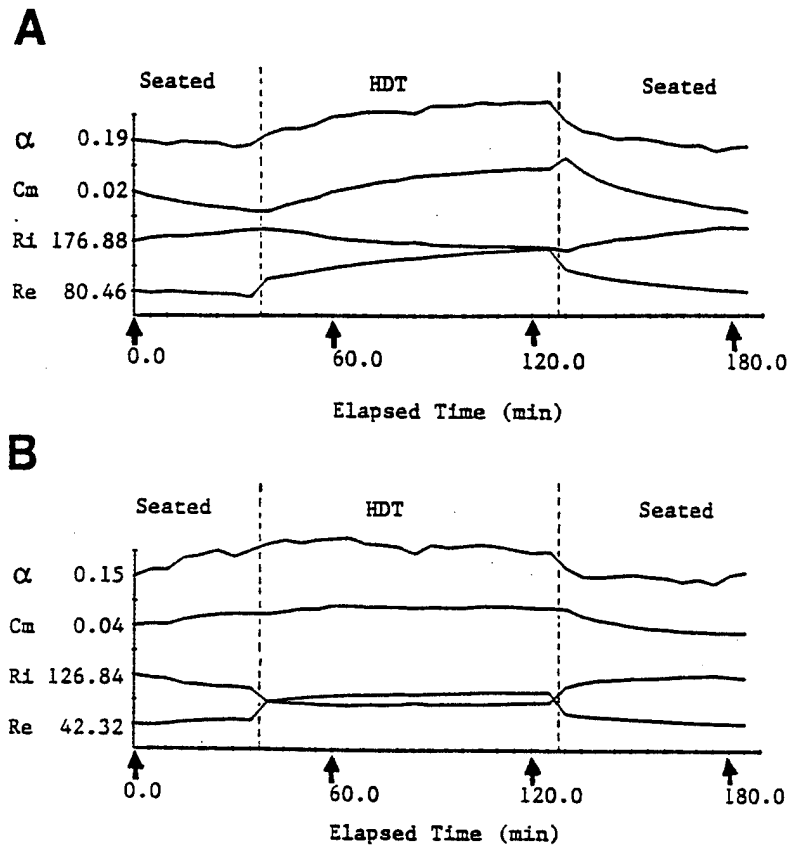


Figure 2. Fitted equivalent circuit parameters during the course of a single run for: (A) the left calf, and; (B) the left thigh of a subject. Each parameter is shown vs. elapsed time in "strip chart" format, with the abscissa scaled such that the major ticks above and below the first value shown at  $t=0$  represent + and - 20% deviation, respectively, from that value.  $R_e$  and  $R_i$  are in Ohms,  $C_m$  is in micro-farads and  $\alpha$  is dimensionless.

position correspond to the emptying or filling of segmental capacitance vessels, while the slower, more progressive changes in this parameter during maintenance of the different body positions reflect fluid movement out of or into the segmental interstitial space. Thus, with assumption and maintenance of the HDT position, initial large increases



in both calf and thigh  $R_e$  reflect the exsanguination of capacitance vessels, while the increases in these parameters continuing throughout HDT indicate interstitial fluid loss. The latter was more pronounced in the calf than the thigh.

Changes in the  $R_i$  and  $C_m$  parameters illuminate changes in the volumes and ionic concentrations of the segmental intracellular spaces. The decreases in calf  $R_i$  that accompanied assumption and maintenance of the HDT position indicate that the average volume and/or the electrolyte concentration of the intracellular space increased. The former interpretation is supported by the observed coincident increases of calf  $C_m$ . Increases in this parameter are plausibly interpreted to arise from decreases in the segmental average cell membrane thickness, such as would accompany increases in average cell volume. The indication that cells in the calf swell when the body is under anti-orthostatic stress is in accord with evidence that calf interstitial osmotic pressure decreases during HDT [6]. Similar but attenuated indications obtained for the compartmental responses in the thigh.

Changes observed during HDT reversed during the subsequent seated recovery period in all subjects.

#### CONCLUSIONS

Results show that impedance spectra of the human calf and thigh undergo systematic and dynamic changes in response to changes in orthostatic stress. The changes are reversible and, when related to the redistribution of fluid between segmental intracellular and extracellular fluid compartments by lumped-parameter equivalent circuit analysis, differ between the two segments in each subject in accord with the orthostatic dependence of the segments. EIS promises to provide a noninvasive means to quantify the kinetics of fluid shifts and compartmental fluid redistribution on a segmental level under conditions where high temporal resolution is desired.

#### ACKNOWLEDGEMENT

This research was supported by a contract from the U.S. Navy Bureau of Medicine, Contract No. N00014-87-C-0166.

#### REFERENCES

- [1] J.J. Ackmann and M.A. Seitz, "Methods of complex impedance

measurement in biologic tissue," CRC Critical Reviews in Biomedical Engineering, vol. 11, p. 281, 1984.

- [2] H. Kanai, S. Katsuyuki and M. Haeno, "Electrical measurement of fluid distribution in human legs: Estimation of extra- and intracellular fluid volume," J. Microwave Power, vol. 18, p. 233, 1983.
- [3] L.A. Geddes, et al., "Hazards in the use of low frequencies for the measurement of physiological events by impedance," Med. & Biol. Engng., vol. 7, p. 289, 1969.
- [4] D.W. Marquardt, "An algorithm for least-squares estimation of nonlinear parameters," J. Soc. Indust. Appl. Math., vol. 11, p. 431, 1963.
- [5] K.S. Cole and R.H. Cole, "Dispersion and absorption in dielectrics. I. Alternating current characteristics," J. Chem. Phys., vol. 9, p. 341, 1941.
- [6] A.R. Hargens, et al., "Fluid shifts and muscle function in humans during acute simulated weightlessness," J. Appl. Physiol.: Respirat. Environ. Exercise Physiol., vol. 54, no. 4, p. 1003, 1983.

## APPENDIX C.5

TECHNICAL NOTE

NONINVASIVE MEASUREMENT OF CHANGES IN  
SEGMENTAL FLUID COMPARTMENTALIZATION AND HEMODYNAMICS

Wayne A. Gerth, Ph.D.<sup>1</sup>  
Leslie D. Montgomery, Ph.D.<sup>2</sup>  
Yi-Chang Wu, M.D.<sup>3</sup>

F.G. Hall Hypo-Hyperbaric Center  
Duke University Medical Center  
Durham, NC 27710

Running Title: Fluid Shifts and Hemodynamics

Key Words: Bio-Impedance, Impedance Spectroscopy, Fluid  
redistribution, Hemodynamics, Head-down tilt,  
Intracellular volume, Extracellular volume

Send correspondence and reprint requests to:

Wayne A. Gerth, Ph.D.  
Box 3823  
Duke University Medical Center  
Durham, NC 27710  
Ph. (919) 684-5902

<sup>1</sup> Medical Research Assistant Professor of Physiology and Anesthesiology  
Department of Cell Biology, Division of Physiology  
Department of Anesthesiology  
Duke University Medical Center; Durham, NC 27710

<sup>2</sup> LDM Associates; 1764 Emory Street; San Jose, CA 95126

<sup>3</sup> Department of Cell Biology, Division of Physiology  
Duke University Medical Center; Durham, NC 27710

## ABSTRACT

An Electrical Impedance Spectroscopic (EIS) system is described that extends the capabilities of conventional fixed frequency impedance plethysmographic (IPG) methods to allow examination of the redistribution of fluids between the intracellular and extracellular compartments of the monitored body segments. The combination of EIS and IPG techniques was evaluated in studies of the human calf, thigh and torso during 90 min of 6° head-down tilt bedrest (HDT). The calf and thigh segments lost conductive volume while the torso gained volume during HDT. Hemodynamic responses calculated from pulsatile IPG data also showed a segmental pattern consistent with vascular fluid loss from the lower extremities and vascular engorgement in the torso. Lumped-parameter equivalent circuit analyses of EIS data for the calf and thigh indicated that overall volume decreases in these segments arose from decreases of extracellular volume that were not completely balanced by intracellular volume increases. The combined use of IPG and EIS techniques enables noninvasive tracking of volumetric and hemodynamic responses to environmental and physiological stresses with both temporal and anatomic resolution greater than attainable by other methods.

## INTRODUCTION

Redistributions of body fluids between different body segments, and between the intra- and extracellular compartments within these segments, are important physiological features of shock and other clinical disorders [4] and of response and adaptation to various orthostatic and anti-orthostatic stresses, including microgravity [2,6-9,11,16,17]. These redistributions affect cardiovascular function, water balance and perhaps skeletal muscle function through physiological mechanisms that may be better understood with simultaneous characterization of both the fluid redistributions themselves and of associated changes in cardiovascular and hemodynamic parameters. Fixed frequency bioelectrical impedance plethysmographic (IPG) techniques have emerged as valuable noninvasive tools that provide information about overall segmental volumes and hemodynamic status with a high degree of temporal resolution [12,14,15,22]. However, these techniques cannot provide information about relative redistributions of fluids between the intra- and extracellular compartments of the monitored segments. Bioelectrical impedance spectroscopy, coupled with computer-aided equivalent circuit analysis, can monitor such compartmental changes while retaining the other advantages of the IPG methods.

Tissues are ionic conductors of electric current which, by virtue of their structural heterogeneity, exhibit dielectric relaxation phenomena that give rise to frequency dependent variations of the impedance to such conduction [1]. In the 1 - 150 kHz range, the resultant dielectric dispersions arise principally from the capacitive reactances of cell membranes. At low frequencies in this range, high cell membrane reactances prohibit current flux through cells, so that tissular impedance is governed by properties of the

extracellular fluid. At high frequencies, membrane reactance is negligible, allowing current to pass through both the extra- and intracellular spaces. Tissue impedance is then governed by the combined properties of the two compartments. Time series of tissue impedances measured as a function of frequency consequently embody tissue structural information that can illuminate changes in the relative distributions of fluid between the tissue intra- and extracellular compartments [1,10].

An Electrical Impedance Spectroscopic (EIS) system that measures the in vivo dielectric properties of tissue has been developed and used in combination with conventional fixed frequency bioimpedance plethysmographic instrumentation to allow assessment of compartmental fluid redistribution and hemodynamic changes that occur in response to environmental or physiological stress. Performance of this combined system was evaluated on human volunteers during short term simulations of microgravity using 6° head-down tilt.

## EXPERIMENTAL PROCEDURES

### System Overview

The combined system was implemented using tandem operation of separate EIS and IPG instruments.

Electrical Impedance Spectroscopy (EIS). The EIS system consisted of a Schlumberger Technologies, Inc., Solartron 1260 Impedance/Gain-Phase Analyzer controlled via an IEEE-488 interface by a Digital Equipment Corporation

VAXstation 3200 computer. The entire system, excepting a laserprinter for hardcopy data and graphics output, was mounted in one full EIA standard cabinet rack on castors for portability in the laboratory.

An impedance spectrum of a body segment was obtained by measuring the voltage developed across the segment in response to sinusoidal electric current excitation at each of a series of discrete frequencies from 3 to 150 kHz. A signal generator and current amplifier in the 1260 provided the excitation signal which was passed through the segment and terminated at a current input channel on the 1260, where the amplitude and phase of the current actually transmitted through the segment was measured. Electric response of up to two segments in the excitation current path was measured across independent voltage input channels. Tetrapolar electrode configurations were used to minimize electrode impedance effects on measured voltages. System software configured the analyzer for spectrum acquisition, setting appropriate values for all analyzer functions, including the excitation current and the frequencies to be swept. The analyzer was operated in differential mode on each of its two channels with the shields for all output and input leads floated from ground at the analyzer chassis. Shields of all leads were also brought to equal potential at a single point near the electrode ends of the leads.

The excitation current was either kept fixed at about 0.5 mA or increased as a function of frequency from about 0.3 mA to a maximum of 5.0 mA (3.0 V max). The latter procedure maximizes signal-to-noise ratios and measurement accuracy in animal or human applications where maximum safe drive currents decrease with decreasing frequency. As the measurement frequency increased during each sweep from about 2.5 kHz to 150 kHz, the drive current was adjusted



upward using the log-log relationship:  $\ln I = m \ln f + b$ ; where  $I$  is the current at frequency  $f$ . Values of the parameters  $m$  and  $b$  were conservatively set according to data provided by Geddes and Baker for the frequency dependence of the threshold for current sensation in the human thorax [5]. A minimum current of 0.3 - 1.0 mA was used when this relationship gave smaller values and a limit of 5.0 mA was imposed at higher frequencies. Measurement results were passed in binary form from the analyzer to the computer for immediate processing and storage on disk or magnetic tape.

Impedance Plethysmography (IPG). A tetrapolar, multi-channel impedance plethysmograph (UFI Inc., No. 2994) was used to measure baseline resistances ( $R_0$ ) and pulsatile resistance changes ( $\Delta R$ ) in each monitored body segment. The IPG operated at a constant current, fixed excitation frequency of 50 kHz (0.1 mA, rms). A UFI Cardiotach was used to monitor a Lead I ECG. The seven analog outputs (6 impedance, 1 ECG) were each sampled at 200 Hz and recorded in digital form using a 286-series IBM-compatible personal computer with an 8-channel differential A/D convertor (Data Translation, Inc., DT-2811L) running under control of a commercially available high-speed data acquisition system (DataQ, Inc., CODAS).

### Data Analysis

EIS. Each impedance spectrum consisted of a series of discrete impedances  $Z^*$  computed from the measured voltage  $V^*$  and current  $I^*$  at each of the separate frequencies in the sweep. Each impedance is given by:

$$Z^* = V^*/I^* = R + Xj ; \quad (1)$$

where  $j = \sqrt{-1}$ ,  $R$  is the equivalent series resistance and  $X$  is the equivalent series reactance.

A simple lumped-parameter equivalent circuit model representing idealized conductance paths through the monitored body segment was fitted to each measured spectrum using a nonlinear least squares routine based on Marquardt's algorithm [13]. The circuit, schematized in Figure 1, models the segment as a uniform isotropic bidomain conductor [18] with an extracellular compartment having average resistance  $R_e$ , and an intracellular compartment having average resistance  $R_i$  and average capacitance  $C_m$ . The value of  $R_i$  is governed by both membrane and cytoplasmic properties, while  $C_m$  is governed principally by membrane properties. The complex admittance  $Y^*$  of the circuit is given by

$$Y^* = \frac{1}{Z^*} = \frac{1}{R_e} + \frac{1}{R_i} - \frac{1/R_i}{1 + j\omega\tau^\circ(1-\alpha)} , \quad 0 < \alpha < 1 ; \quad (2)$$

where  $\omega$  is the angular frequency given by  $2\pi f$ ,  $\tau^\circ$  is the time constant given by the product  $R_i \cdot C_m$ , and the quantity  $\alpha\pi/2$  is the angle between the real axis and a radius of the admittance locus passing through either of its two real axis intercepts. The  $(1-\alpha)$  exponent in Eq. (2) is included to account for the typical failure of tissular impedance loci to be centered on the real axis. This behavior is consistent with the presence in tissue of a practical infinitude of parallel R-C elements each with different time constants with values distributed about a mean at  $\tau^\circ$  [1,3,10]. By definition,  $\alpha=0$  when the center of the locus lies on the real axis. Increasing values of  $\alpha$  from 0 towards unity indicate a widening of the distribution of time constants, with

increasing standard deviation of the distribution about  $\tau^0$ .

Marquardt's algorithm was implemented using the norm of each observed impedance,  $|Z^*|$ , and that of the corresponding fitted impedance,  $|Z^*|$ . The algorithm adjusted the model parameters to minimize the sum of squares, SS,

$$SS = \sum_{i=1}^n (|Z_i^*| - |\hat{Z}_i^*|)^2, \quad (3)$$

for the impedances at the  $n$  different frequencies in each spectrum. The analytic components of the software were bundled to process run-time data passed from the impedance spectrum acquisition routine, or to read and process data files from earlier experiments, providing identical output in either case. In the former mode, the analyses were automatically performed immediately after acquisition of each spectrum. Graphic displays of the results afforded a means to track changes in measured and computed dielectric properties of each monitored body segment throughout the course of each run.

IPG. Impedance plethysmographic data were analyzed on a pulse-by-pulse basis using an interactive software package that included a graphic user interface to facilitate selection and specification of the impedance waveform landmarks shown in Figure 2. Times and differential resistances at these landmarks were used with basal resistances to calculate the following indices of segmental volume, blood flow and vascular compliance:

Segmental conductive volumes ( $V_e$ ) were calculated from segmental base resistances as described by Montgomery (15).

Blood flow index, BFI. BFI is a function of the maximum amplitude of the impedance pulse, the subject's heart rate and the basal resistance [14];

Dicrotic index, DCI.  $DCI (=B/A)$  is defined as the ratio of the amplitude of the pulse waveform at the height of the incisure (B) to the maximum pulse amplitude (A). DCI increases proportionally with general arteriolar compliance [22];

Anacrotic index, AI.  $AI (=a/T)$  is the ratio of the duration of the anacrotic phase of the pulse wave ( $a$ ) to the duration of the entire cardiac cycle (T). This ratio is the relative systolic filling time of a given body segment during the cardiac cycle and is consequently considered to reflect the compliance of the larger arteriolar vessels. AI decreases as the local arteriolar compliance increases [21];

Pulse transit time, PTT. PTT is the time interval in seconds between the onset of the ECG QRS complex and the onset of the impedance pulse waveform. PTT is a measure of the time required for the pressure profile of the cardiac pulse to be transmitted from the heart to the monitored segment. As the pulse conduction path becomes more rigid, the pressure pulse is transmitted more quickly between the two locations. PTT is therefore an index of the general, overall vascular compliance of the body [20].

### System Evaluation During HDT

Four men in good health between the ages of 27 and 50 volunteered to take part in a short-term 6° head-down tilt protocol for test and evaluation of system performance. The protocol consisted of three successive periods during which the subject was in the seated upright position for 30 min, in a supine, 6° head-down tilt (HDT) position for 90 min, and again in the upright seated position for 60 min. Except for rising to stand and move from one position to the next, the subject was at rest and asked to minimize limb movement and muscle flexure throughout the protocol. Each run was made in a room at  $21.0 \pm 0.5^\circ\text{C}$  average ambient temperature where air movement, bright light, noise, and other stimulation was kept minimal.

After providing informed consent, each subject was fitted with noninvasive ECG electrodes (3M, Ag/AgCl Red Dot) for bioimpedance monitoring of the left calf, thigh and torso. Calf pickup electrodes were placed laterally above the lateral malleolus of the fibula and below the fibular head. Thigh pickup electrodes were placed just above the lateral epicondyle of the femur and on the lateral aspect of the greater trochanter of the femur. Torso pickup electrodes were placed on the left iliac crest and the left clavicular line. Geometric lengths between the pickup electrodes for each segment were measured for calculation of segmental conductive volumes [15]. Drive electrodes were placed on the dorsum of the metatarsus and on the lateral aspect of the anterior superior iliac spine. An electrode positioned on the back of the left hand was used in place of the latter for IPG monitoring in order to include the torso in the current path. Each subject was also instrumented with standard sternal and biaxillary ECG electrodes for monitoring heart rate.

EIS was used at five min intervals to characterize the dielectric properties of the monitored segments. Each impedance spectrum required about 70 s to acquire and consisted of measurements taken at 50 discrete frequencies distributed logarithmically from 3 to 150 kHz. At run elapsed times of 0, 40, 65, 115, 130 and 185 min, electrodes were disconnected from the EIS system and connected to the IPG system. Two-minute periods of IPG measurements of baseline resistance ( $R_0$ ) and pulsatile resistance changes ( $\Delta R$ ) were then made of the calf, thigh, and torso body segments.

Statistical results show the repeatability of the measurements in different individuals. Paired t-tests of significance of changes in measured and calculated parameters throughout the protocol show trends that may be expected to emerge more substantially in a more extensive investigation.

## RESULTS

Calf, thigh and torso conductive volume changes during the HDT period are shown in Figure 3. The changes are shown in percent relative to the first value obtained after start of the HDT period; i.e., the value obtained at 40 min total elapsed time or 8-10 min after initial assumption of the HDT position. By minute 65 (approx. 33 min HDT), the calf segment had lost approximately 3% of its conductive volume ( $P < 0.05$ ), the thigh had lost about 2% volume and the torso had gained about 1.5% volume. After 90 min HDT, the volumes of all three body segments had changed significantly ( $P < 0.05$ ) relative to the first measurement during HDT. The calf and thigh had lost approximately

8 and 4% volume, respectively, and the torso volume had increased by approximately 3%.

An impedance spectrum is visualized as a locus of points in the complex plane by plotting the imaginary vs the real parts of the impedance (reactance vs resistance) at each frequency in the spectrum. Impedance loci of the calf and thigh of one subject at the end of each of the three periods in the test protocol are shown in Figure 4. Typifying the results for all subjects, the loci were widened and shifted towards higher  $R$  and more negative  $X$  values at the end of the HDT period in both segments. At the end of the post-tilt period, the locus for each segment resembled that obtained at the end of the pre-tilt period.

Grouped mean values of the fitted equivalent circuit parameters for the calf and thigh at the various elapsed times in the protocol are shown in "strip chart" format in Figure 5. Both the amplitudes and the time courses of the parametric changes during HDT followed somewhat different patterns in the two segments. In both segments, the  $R_e$  and  $R_i$  parameters showed large rapid changes at the outset of HDT that were not evident in the behavior of the  $C_m$  parameter. The tendencies for the resistance parameters to continue changing and for  $C_m$  to increase throughout the remaining period of HDT was more pronounced in the calf than in the thigh. At the end of the HDT period, mean calf  $R_e$  values had increased 35%, mean calf  $R_i$  values had decreased 24% and mean calf  $C_m$  values had increased 33% from their values at the end of the pre-tilt period. Parametric changes in the thigh were similar but attenuated. Mean thigh  $R_e$  increased 26%, mean thigh  $R_i$  decreased 14% and mean thigh  $C_m$  increased 12% over the same interval.

The magnitudes of the above  $R_e$  and  $R_i$  changes during HDT substantially exceeded those for the corresponding segmental conductive volume changes in Figure 3. These two sets of results are properly compared, however, only after reducing the  $R_e$  and  $R_i$  parameter pairs from each impedance spectrum to a mutual resistance,  $R_m$ , using the parallel relation:  $R_m = 1/(1/R_e + 1/R_i)$ . Changes in resultant  $R_m$  values during HDT then show excellent agreement with those in calculated segmental conductive volumes. For example, over the interval in Figure 3 spanned by the results at an elapsed time of 115 min, calf and thigh  $R_m$  increased 9 and 5%, respectively, compared to the 8 and 4% changes in respective conductive volumes.

Figures 6 - 10 present the grouped mean values ( $\pm$  S.E.) of the calculated segmental hemodynamic indices at the indicated elapsed times during the test protocol. Results are shown normalized and reduced to percent parametric change for each segment relative to the initial pre-tilt value (@  $t=0$ ). The grouped mean heart rate (Figure 6) decreased approximately 10% during the HDT period, and returned to pre-tilt values within minutes of assuming the seated recovery position. The blood flow index (Figure 7) increased 50, 115 and 30% in the calf, thigh and torso segments, respectively, during the first 30 minutes HDT. After 90 min HDT, the index for the thigh segment remained elevated, while indices for the calf and torso showed respectively greater tendencies to decrease toward their pre-tilt values.

The dicrotic index (Figure 8) decreased in the calf and thigh throughout the HDT period. In contrast, this index for the torso increased during the first 30 min of HDT and decreased to its pre-tilt value after 90 min HDT. The



anacrotic index (Figure 9) increased between 20 and 40% in the calf and thigh but decreased approximately 10% in the torso during HDT. Finally, segmental pulse transit times (Figure 10) increased in the lower body segments and decreased in the torso during the HDT period. Changes in each of these separate segmental hemodynamic indices indicate that vascular compliance increased in the calf and thigh but decreased in the torso during HDT.

## DISCUSSION

Results provide a detailed multi-segmental description of the volumetric and hemodynamic changes that occur during the initial 90 min of antiorthostatic bed rest. This environmental stressor is widely used to simulate the cardiovascular effects of microgravity and has known effects on fluid distribution and cardiovascular performance [2,7,9,10,12]. In conformance with these known effects, cardiovascular, hemodynamic and volumetric parameters provided by the present techniques exhibited systematic and dynamic changes during HDT that were reversible and showed patterns among the monitored segments that varied in accord with the orthostatic dependence of the segments. More generally, this study demonstrates the broad scope of information that comprehensive applications of impedance spectroscopic and plethysmographic techniques can provide in other experimental contexts as well.

The IPG results indicate that the calf and thigh segments lost conductive volume while the torso gained volume during HDT. This pattern is typical of a general cephalad shift of fluids, where the volume gain in the torso represents a portion of the fluid displaced from the lower segments. Observed segmental

volume changes are consistent with those determined in a similar fashion in other studies and shown to agree well with the volume changes determined from simultaneous anthropometric, capacitance band and strain-gauge plethysmographic measurements [15]. The agreement between the changes in mutual resistance calculated from the EIS results and the changes in segmental conductive volumes determined from the IPG data thus provides an important cross-validation of the two techniques: The segmental fluid shifts evident in the IPG results are also evident in the EIS results.

Significantly, the EIS results provide additional insights into how the segmental intra- and extracellular compartments participate in the fluid shifts. Because the equivalent circuit model as presently applied ignores the inequalities of the transverse and longitudinal resistivities of muscle masses in the monitored segments, calculated compartmental resistance and capacitance values have only limited absolute significance [18]. However, for a given electrode orientation, fractional changes in these values, as presented in Figure 5, accurately reflect actual changes in compartmental properties, provided that the processes leading to such changes uniformly affect all the monitored tissue. Thus, with assumption and maintenance of the HDT position, large initial increases in both calf and thigh  $R_e$  reflect the exsanguination of capacitance vessels, while the more gradual increases in these parameters continuing throughout HDT indicate interstitial fluid loss. The latter was more pronounced in the calf than in the thigh, indicating, in accord with the different antiorthostatic stresses in the segments, that interstitial fluid loss in the thigh was small compared to that in the calf. These results are consistent with previously reported decreases of interstitial and transcapillary pressures in the calf soleus muscle that continued throughout 8

hr of 5° HDT [7]. Upon resumption of the seated position, the fluid movement pattern reversed, with rapid return of the vascular volume in both segments followed by a gradual recovery of the respective interstitial volumes.

Changes in the  $R_i$  and  $C_m$  parameters illuminate changes in the volumes and ionic concentrations of the segmental intracellular spaces. The decreases in calf  $R_i$  that accompanied assumption and maintenance of the HDT position indicate that the average volume and/or electrolyte concentration of the intracellular space increased. The former interpretation is supported by the observed coincident increases of calf  $C_m$ . Increases in this parameter are plausibly interpreted to arise from decreases in the segmental average cell membrane thickness and increases in membrane area, such as would accompany increases in average cell volume. The indication that cells in the calf swell when the body is under anti-orthostatic stress is in accord with evidence that calf interstitial osmotic pressure decreases during HDT [7]. Similar but attenuated indications were obtained for the compartmental responses in the thigh.

The EIS results consequently augment the IPG results by providing evidence that HDT-induced losses of conductive volume from the calf and thigh arise from rather large losses of extracellular fluid that are not completely balanced by cellular imbibition of fluid. Similar conclusions have been forwarded by other workers for humans during chair rest and water immersion, where significant decreases of serum osmolality were observed [6], and during horizontal bed rest [8]. Hargens, et al., [7] also reported increases of cellular area in connective tissue of soleus muscle biopsied from human subjects after 8 hr HDT, although a net intracellular to extracellular fluid

shift -- opposite that presently indicated -- was concluded to have occurred on the basis of increased potassium and decreased creatinine urinary excretion. It is of interest that decreases of serum osmolality, the most probable cause of intracellular fluid accumulation, evidently occur in astronauts during spaceflight [11]. Notwithstanding the controversy about the direction of compartmental fluid shifts induced by anti-orthostasis, the presently indicated shifts are surprisingly large. The relative diminution of the shifts in the thigh with respect to those in the calf suggest that the net whole-body shift must be smaller, but the mechanism for such segmental differentiation is unknown. Further validation of the method is required to determine to what extent the effects might be quantitatively overestimated as a result of nonuniformities of current flow in the monitored segments and changes therein that could be caused by changes in the relative fluid contents of the composite tissues.

As observed for the segmental volumetric responses, the hemodynamic parameters calculated from the pulsatile IPG data also showed segment-specific responses to changes in orthostatic stress. Both the calf and thigh manifested hemodynamic responses to HDT that would have tended to minimize intravascular fluid loss from those segments. Decreases in the dicrotic index, and increases in the anacrotic index and pulse transit time indicate that the overall calf and thigh vascular compliance increased during HDT. These changes tended to be more pronounced in the calf than in the thigh, reflecting the same orthostatic dependence evident in the segmental fluid shifts. Conversely, hemodynamic parameters in the torso exhibited changes during HDT that would have tended to minimize vascular engorgement in this segment. Thus, segmental hemodynamic changes during HDT appear to have been coordinated to limit or reduce the

transfer of intravascular fluid from the legs to the torso and head. This counterregulatory pattern is consistent with that found by other investigators in human subjects under similar antiorthostatic stresses [9,12,19], and probably arises from both active changes in arteriolar tone and passive volume-related changes in compliance.

Segmental blood flow changes during HDT were generally consistent with the indicated changes in vascular compliance, reflecting the overall efficacy of the latter at redistributing an increased central venous return. Blood flow increased and remained elevated in the thigh during the HDT period. It should be noted that these flows include throughput for perfusion of the calf, where flow was also increased. Blood flow in the torso increased at the beginning of HDT, but tended to decrease toward the pre-tilt value during the latter stages of HDT. Heart rate determined from the ECG remained decreased throughout HDT. Given the increased torso blood flow, this result indicates that cardiac stroke volume increased during HDT. Results are generally in accord with earlier indications that cephalad shifts of blood during HDT cause increased end-diastolic volume and cardiac output, with the latter causing segmental blood flow increases [2,16,17]. The presently observed tendency for return of the cardiovascular parameters to pre-tilt values after an initial HDT-induced transient is also consistent with results of other studies, although the present time course for such adaptation appears longer than in other work [2].

## CONCLUSIONS

The combination of fixed and swept frequency bioimpedance monitoring has provided a detailed characterization of the human body's regional volume, hemodynamic and blood flow responses to a short term head down tilt simulation of microgravity. Observed responses are within the ranges of those reported from other studies, while regional patterns of the responses indicate that studies of this type should include examination of the relevant parameters to at least the segmental level of anatomic resolution. The present techniques provide such resolution augmented by a high level of temporal resolution using only simple superficial electrodes. Occlusion cuffs, displacement fluids, confining garments or invasive procedures are not required, making the methods suitable for applications under either laboratory or field operational conditions. These techniques afford a useful noninvasive means to monitor a variety of physiological parameters central to the physiology of fluid control in aerospace and clinical environments.

## ACKNOWLEDGEMENT

This research was supported in part by a contract from the U.S. Navy Bureau of Medicine, Contract No. N00014-87-C-0166. The authors thank Dr. Richard W. Montgomery of Management Analytical Associates, Inc., Corvallis, OR, for assistance in software development and Dr. Marc Maddou of SRI International, Menlo Park, CA, for technical advice during the initial phases of this work.

## REFERENCES

1. Ackmann JJ, Seitz MA. Methods of complex impedance measurement in biologic tissue. CRC Critical Reviews in Biomedical Engineering, 1984; 11:281-311.
2. Butler, GC, Xing H, Hughson, RL. Cardiovascular response to 4 hours of 6° head-down tilt or of 30° head-up tilt bed rest. Aviat. Space Environ. Med. 1990; 61:240-6.
3. Cole KS, Cole RH. Dispersion and absorption in dielectrics. I. Alternating current characteristics. J. Chem. Phys. 1941; 9:341-52.
4. Gauer OH, Henry JP, Behn C. The regulation of extracellular fluid volume. Ann. Rev. Physiol. 1970; 32:547-95.
5. Geddes LA, Baker LE. Hazards in the use of low frequencies for the measurement of physiological events by impedance. Med. & Biol. Engng. 1969; 7:289-96.
6. Greenleaf JE, Shavartz E, Kravik S, Keil LC. Fluid shifts and endocrine responses during chair rest and water immersion in man. J. Appl. Physiol.: Respirat. Environ. Exercise Physiol. 1980; 48(1):79-88.
7. Hargens AR, Tipton CM, Gollnick PD, Mubarak SJ, Tucker BJ, Akeson WH. Fluid shifts and muscle function in humans during acute simulated weightlessness. J. Appl. Physiol.: Respirat. Environ. Exercise Physiol. 1983; 54(4):1003-9.

8. Johnson PC, Driscoll TB, Carpentier WR. Vascular and extravascular fluid changes during six days of bedrest. *Aerospace Med.* 1971; 42(8):875-8.
9. Kabesheva TA, Kopanev SV, Panferova NY, Zavadovskiy AF. Vascular mechanisms of adaptation to antiorthstatic position. *Kosmich. Biol. Aviak. Med.* 1985; 19(2):35-9.
10. Kanai H, Katsuyuki S, Haeno M. Electrical measurement of fluid distribution in human legs: Estimation of extra- and intracellular fluid volume. *J. Microwave Power*, 1983; 18:233-43.
11. Leach CS. Fluid control mechanisms in weightlessness. *Aviat. Space Environ. Med.* 1987; 58(9, Suppl.):A74-9.
12. Maksimov DG, Domracheva MV. Changes in central and peripheral hemodynamics during prolonged antiorthostatic hypokinesia as weightlessness models. *Kosmich. Biol. Aviak. Med.* 1976; 5:52-7.
13. Marquardt DW. An algorithm for least-squares estimation of nonlinear parameters. *J. Soc. Indust. Appl. Math.* 1963; 11:431-41.
14. Montgomery LD, Hanish HM, Marker RA. An impedance device for study of multisegmental hemodynamic changes during orthostatic stress. *Aviat. Space Environ. Med.* 1989; 60:116-22.
15. Montgomery LD. Body volume changes during simulated weightlessness: An overview. *Aviat. Space Environ. Med.*, 1987; 58(9, Suppl.):A80-5.



16. Nicogossian AE, Parker Jr. JF. Space physiology and medicine. National Aeronautics and Space Administration. 1982; NASA SP-447:141-52.
17. Nixon JV, Murray RG, Bryant C, Johnson Jr. RL, Mitchell JH, Holland OB, Gomez-Sanchez C, Vergne-Marini P, Blomquist CG. Early cardiovascular adaptation to simulated zero gravity. J. Appl. Physiol.: Respirat. Environ. Exercise Physiol. 1979; 46(3):541-8.
18. Plonsey R, Barr RC. A critique of impedance measurements in cardiac tissue. Annals of Biomed. Engng. 1986; 14:307-22.
19. Skagen K. Sympathetic reflex control of blood flow in human subcutaneous tissue during orthostatic maneuvers. Danish Medical Bulletin, 1983; 30(4):229-41.
20. Strandness DE, Sumner DS. Hemodynamics for Surgeons. New York: Grune and Stratton, 1975: pp. 187-96.
21. Usochev VV, Shinkarevskaya IP. Functional changes in systemic and regional (intracranial) circulation accompanying low acceleration. Kosmich. Biol. Aviak. Med. 1973; 19(1):59-64.
22. Yarullin KK, Krupina TN, Vasil'yeva TD, Buyvolova NN. Changes in cerebral, pulmonary, and peripheral blood circulation. Kosmich. Biol. Aviak. Med. 1972; 6(4):33-9.

## FIGURE LEGENDS

1. Equivalent circuit used to interpret measured segmental impedance spectra.
2. Impedance plethysmographic pulse waveform with landmarks for calculation of hemodynamic parameters.
3. Grouped mean segmental conductive volumes vs elapsed time. An asterisk (\*) indicates that the value differs significantly ( $P < 0.05$ ) from the initial head-down tilt value. A plus (+) indicates that the value differs significantly ( $P < 0.05$ ) from that at 65 min elapsed time.
4. Complex impedance loci of one subject's: (A) calf and (B) thigh at (a) the end of the pre-tilt seated period; (b) after 90 min HDT, and; (c) at the end of the 30 min seated recovery period. Each locus consists of points from measurements at 50 discrete frequencies from 3 to 150 kHz. Individual points are obscured by connecting straight lines. The lowest frequency impedance is at the right-most or highest resistance end of each locus.
5. Grouped mean values of fitted equivalent circuit parameters vs run elapsed time for: (A) the left calf, and; (B) the left thigh of the four subjects in the study. Parameter values are shown in "strip chart" format, with the ordinate scaled such that the major ticks above and below the first value shown at  $t=0$  represent + and - 20% deviation, respectively, from that value.  $R_e$  and  $R_i$  are in Ohms,  $C_m$  is in micro-farads and  $\alpha$  is dimensionless.

6. Grouped mean heart rates vs elapsed time. An asterisk (\*) indicates that the value differs significantly ( $P < 0.05$ ) from that during the pre-tilt seated position. A plus (+) indicates that the value differs significantly ( $P < 0.05$ ) from the preceding value.
7. Grouped mean blood flow indices vs elapsed time. Symbols indicate significant differences as in Figure 6.
8. Grouped mean segmental diastolic indices vs elapsed time. Symbols indicate significant differences as in Figure 6.
9. Grouped mean segmental anastotic indices vs elapsed time. Symbols indicate significant differences as in Figure 6.
10. Grouped mean pulse transit times vs elapsed time. Symbols indicate significant differences as in Figure 6.

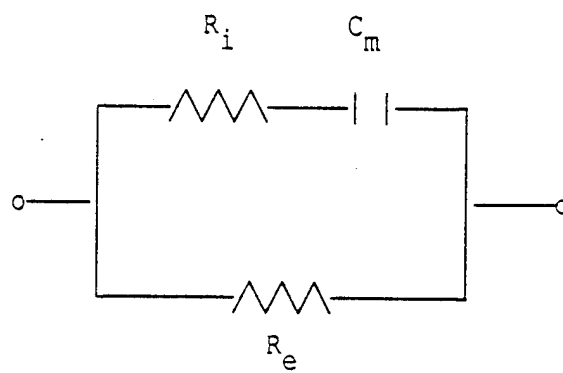
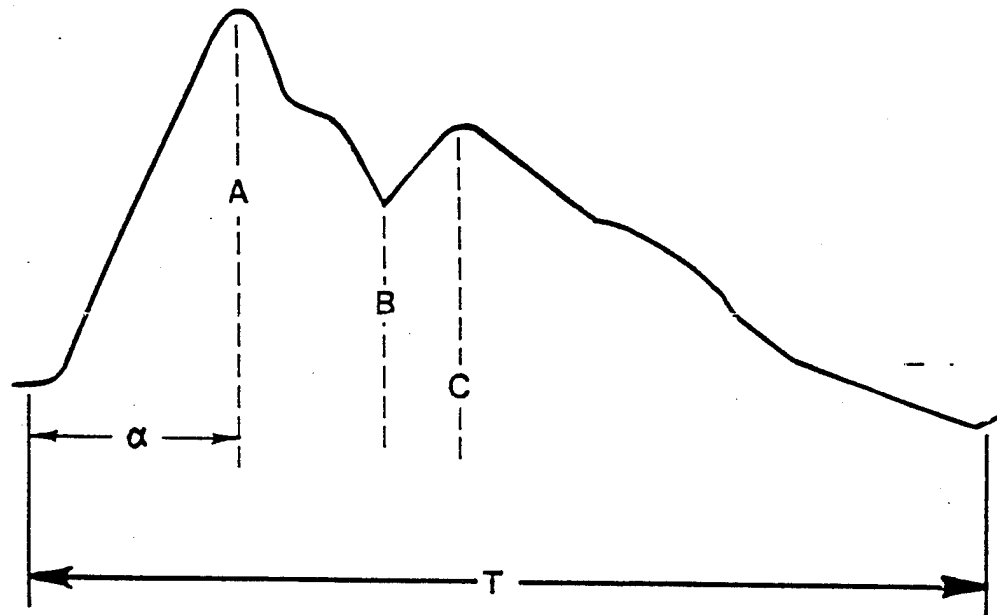


Figure 1.



$\alpha$  = DURATION OF ANACROTIC PHASE OF EACH PULSATILE WAVE (s)

T = DURATION OF TOTAL CARDIAC CYCLE (s)

A = MAXIMUM LEVEL OF THE IMPEDANCE WAVE (mm)

B = AMPLITUDE AT THE POSITION OF THE DICROTIC NOTCH (mm)

C = AMPLITUDE AT THE LEVEL OF THE PEAK OF THE DICROTIC WAVE (mm)

Figure 2.

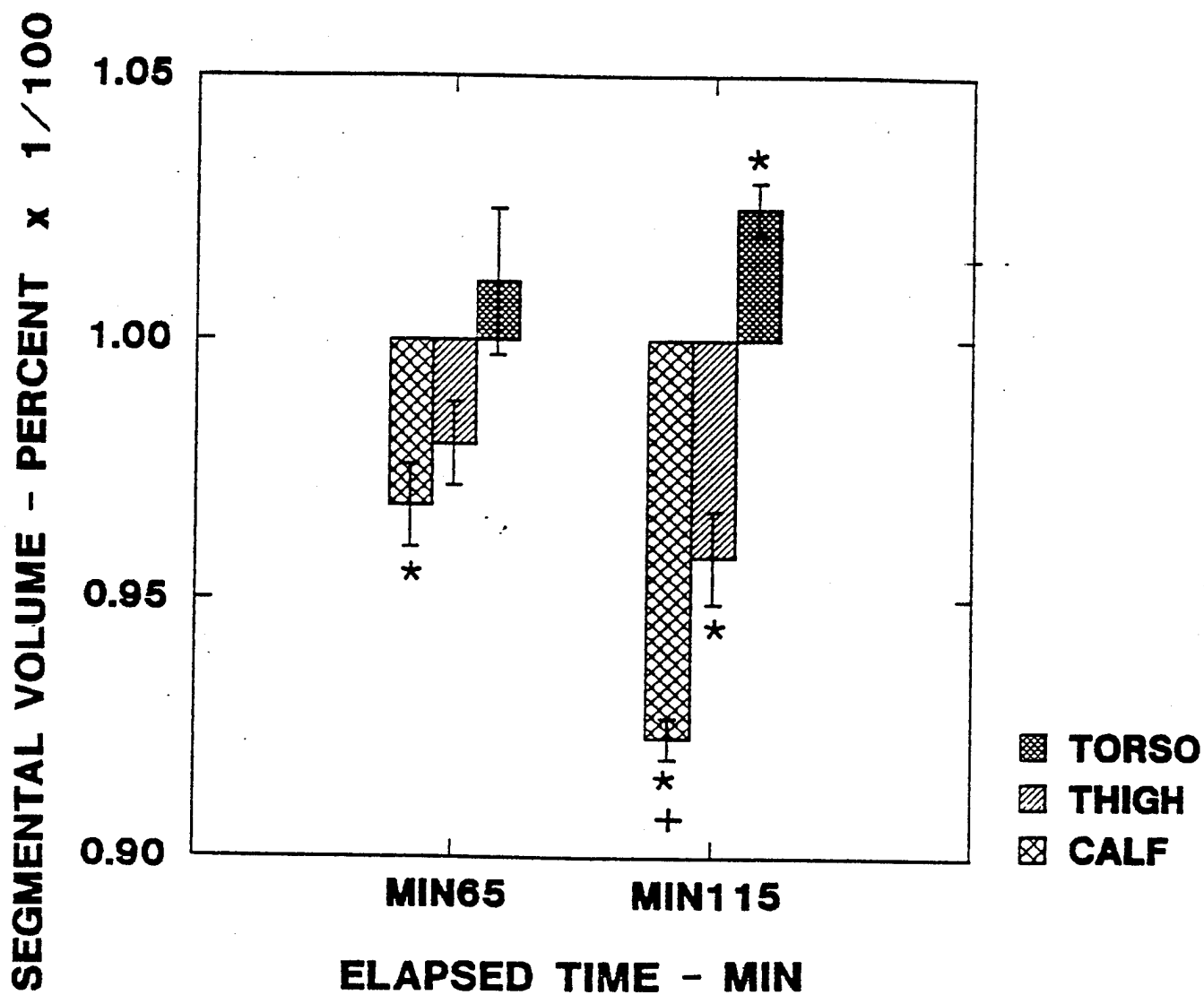


Figure 3.

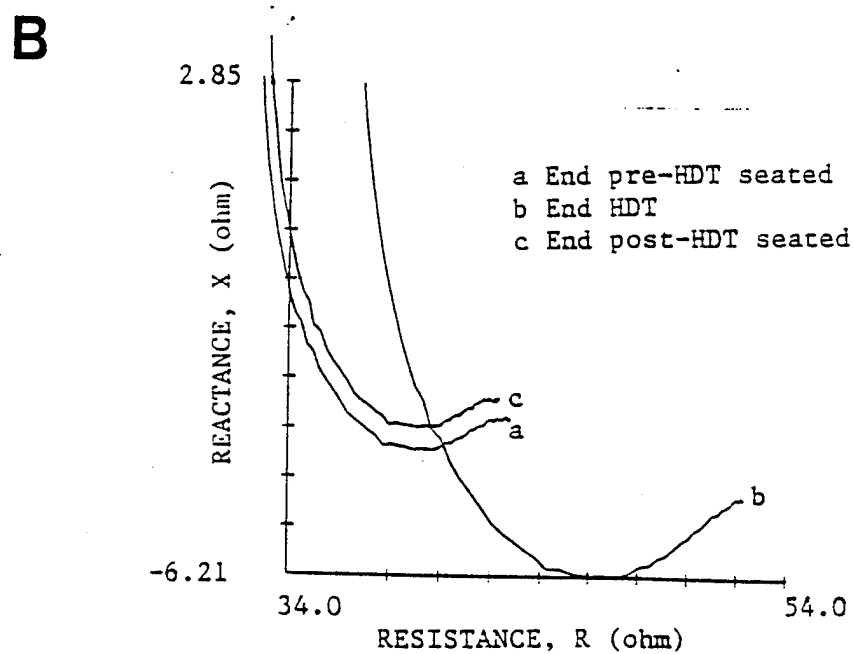
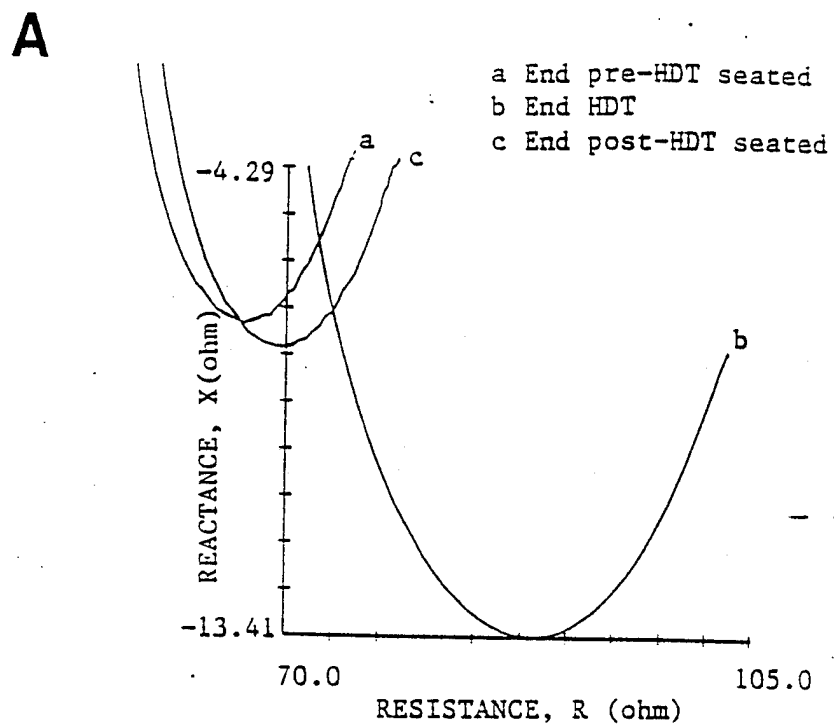


Figure 4.

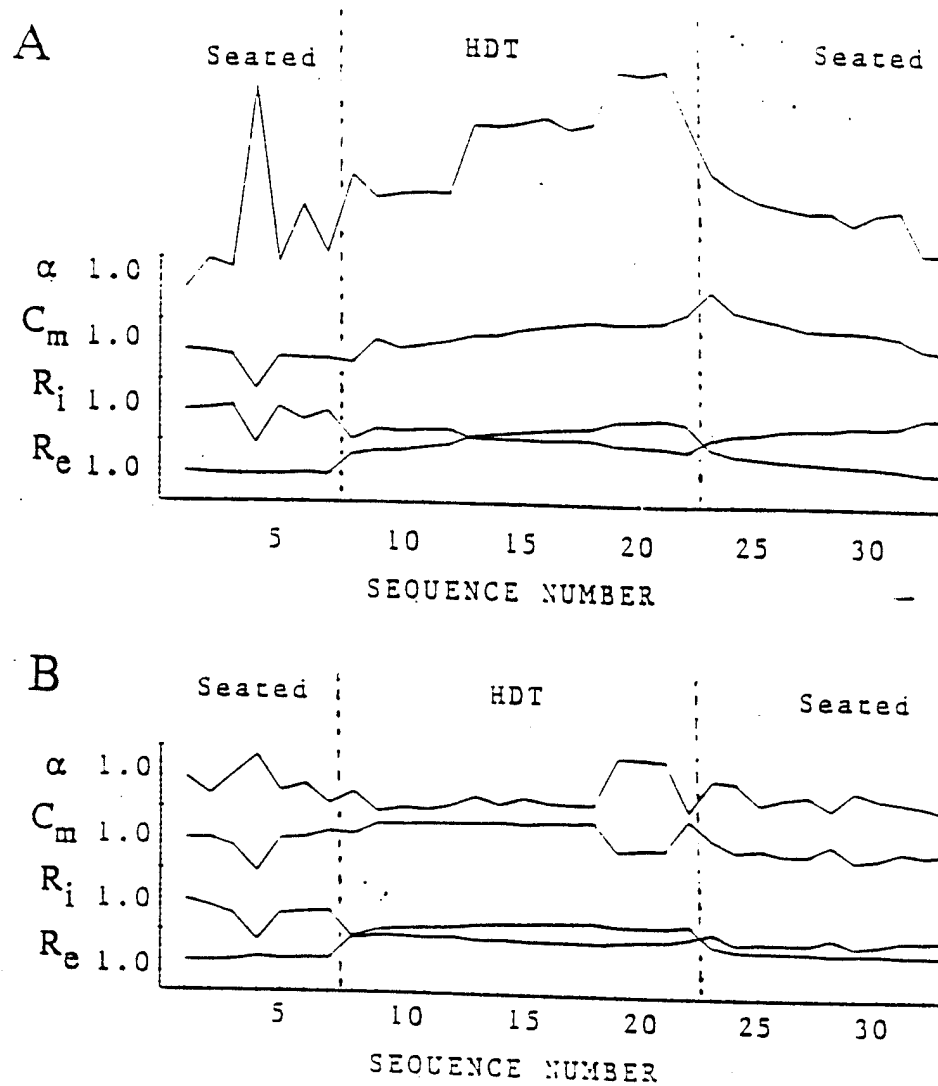


Figure 5.



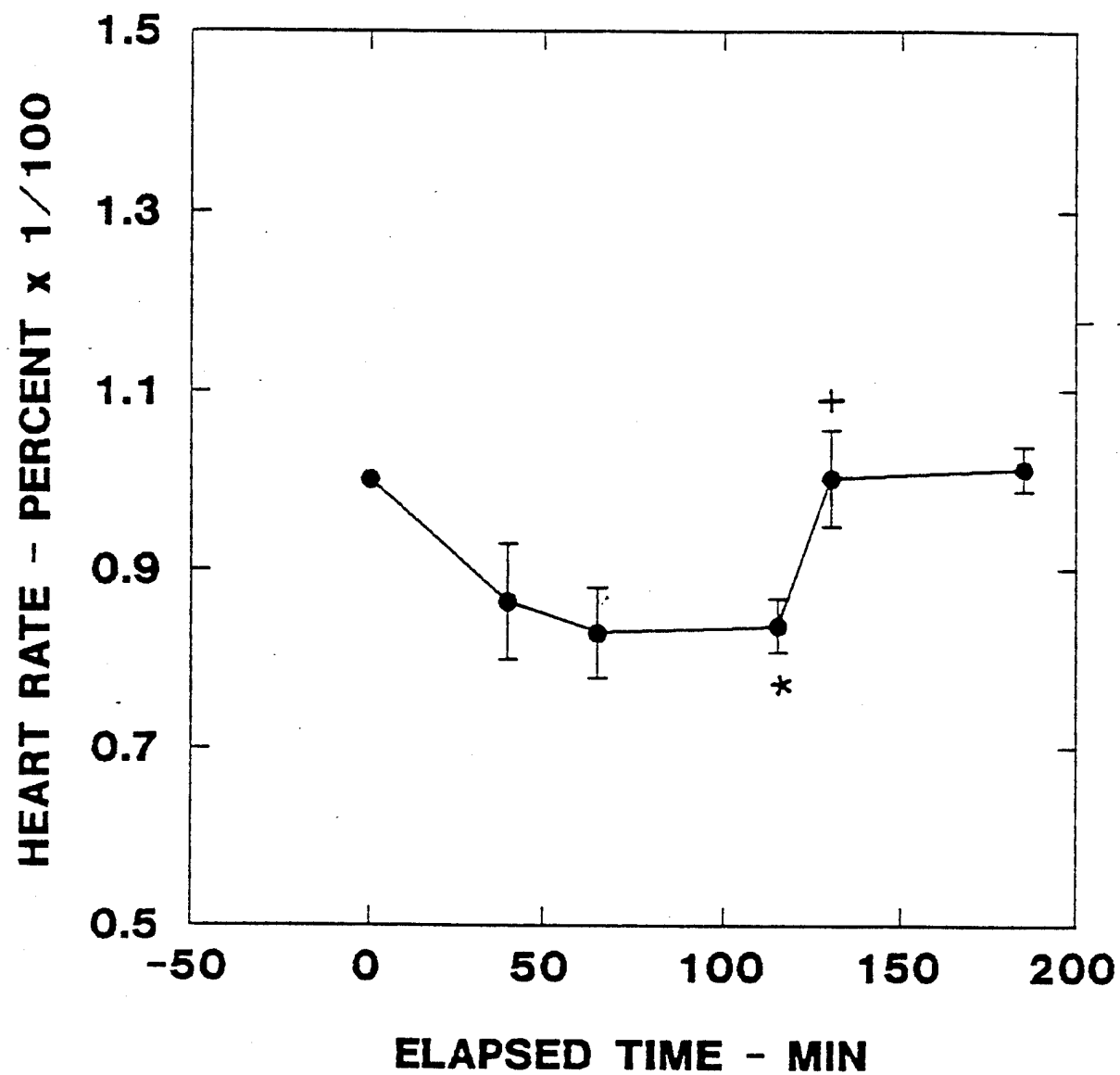


Figure 6.

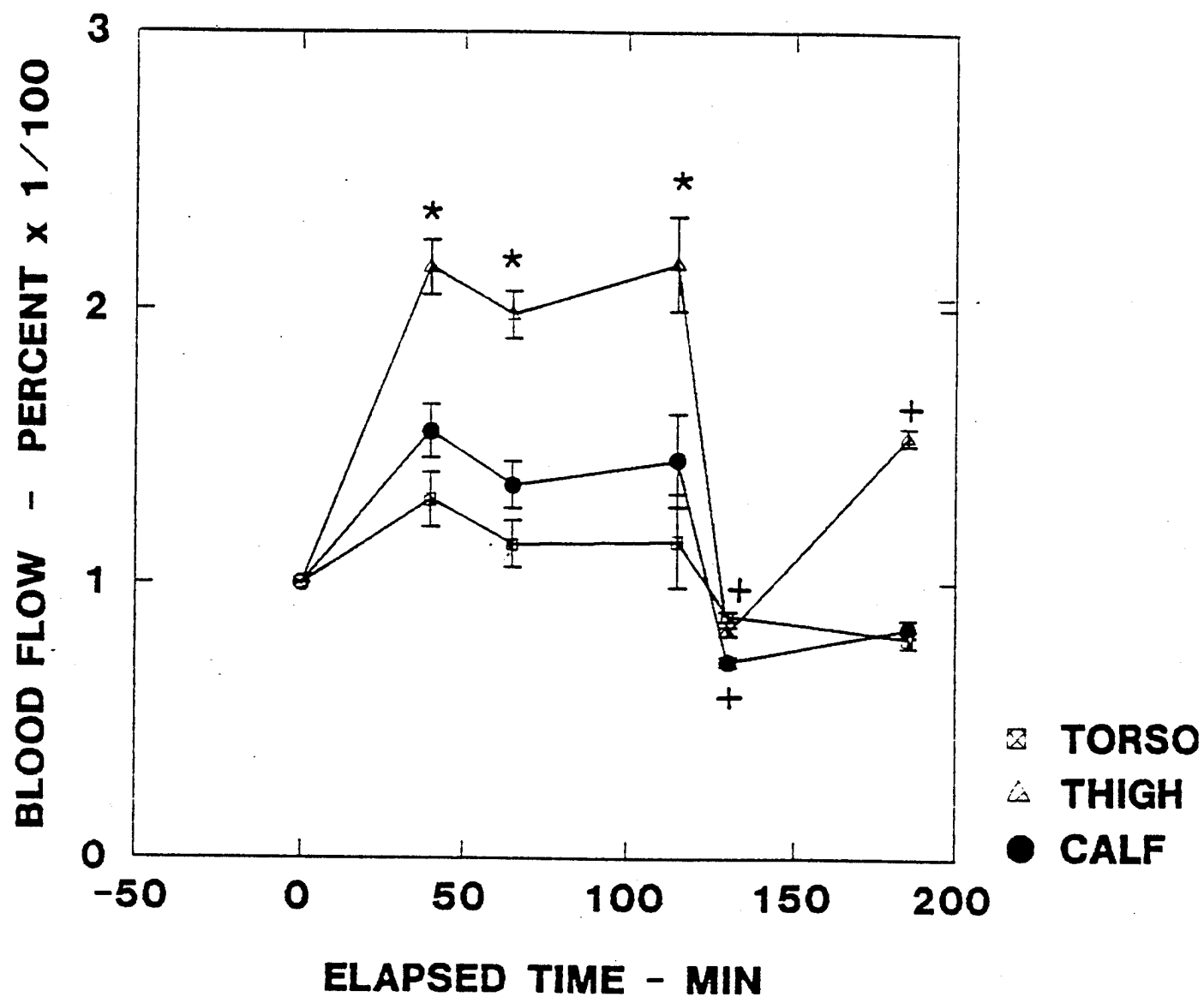


Figure 7.

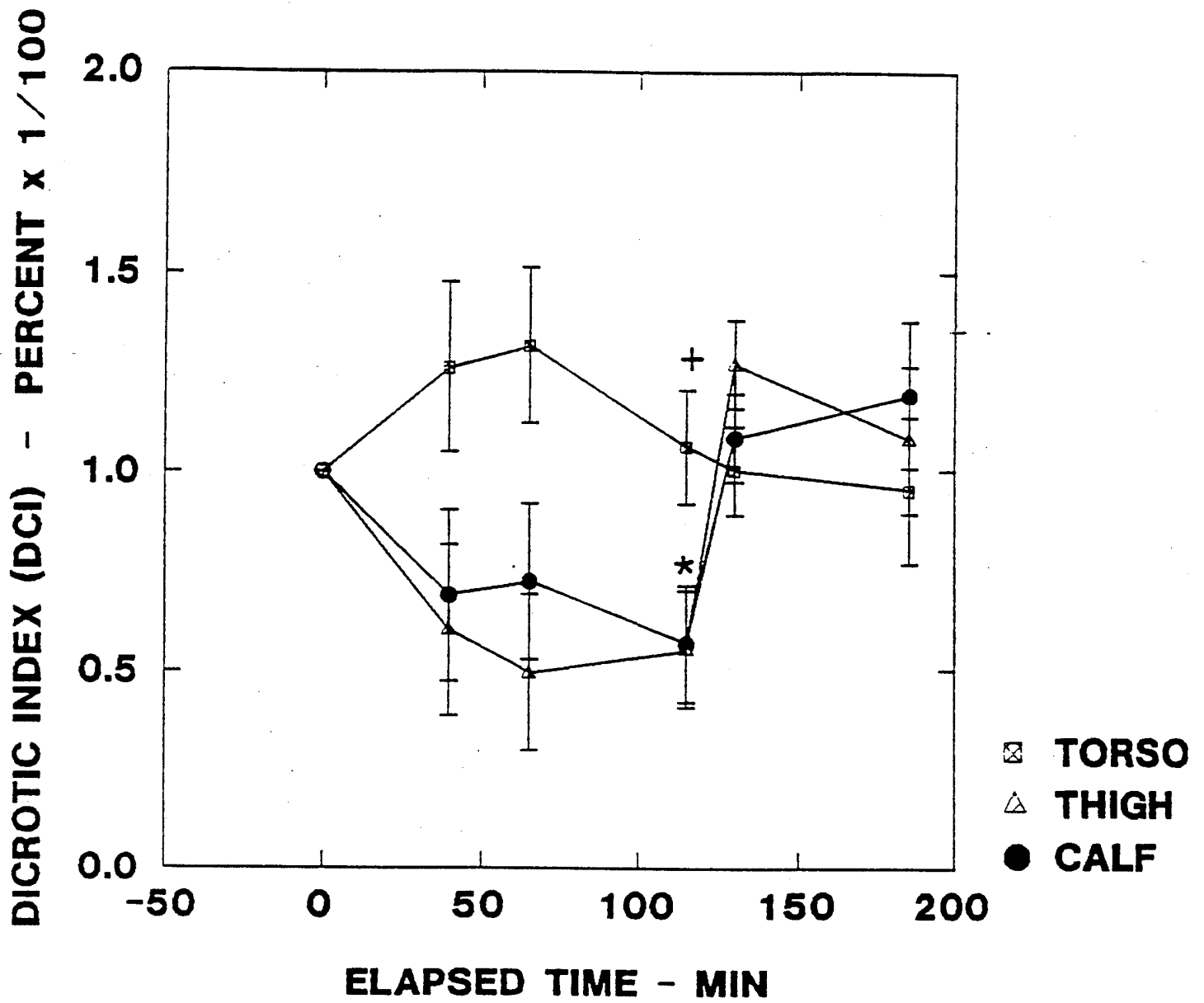


Figure 8.

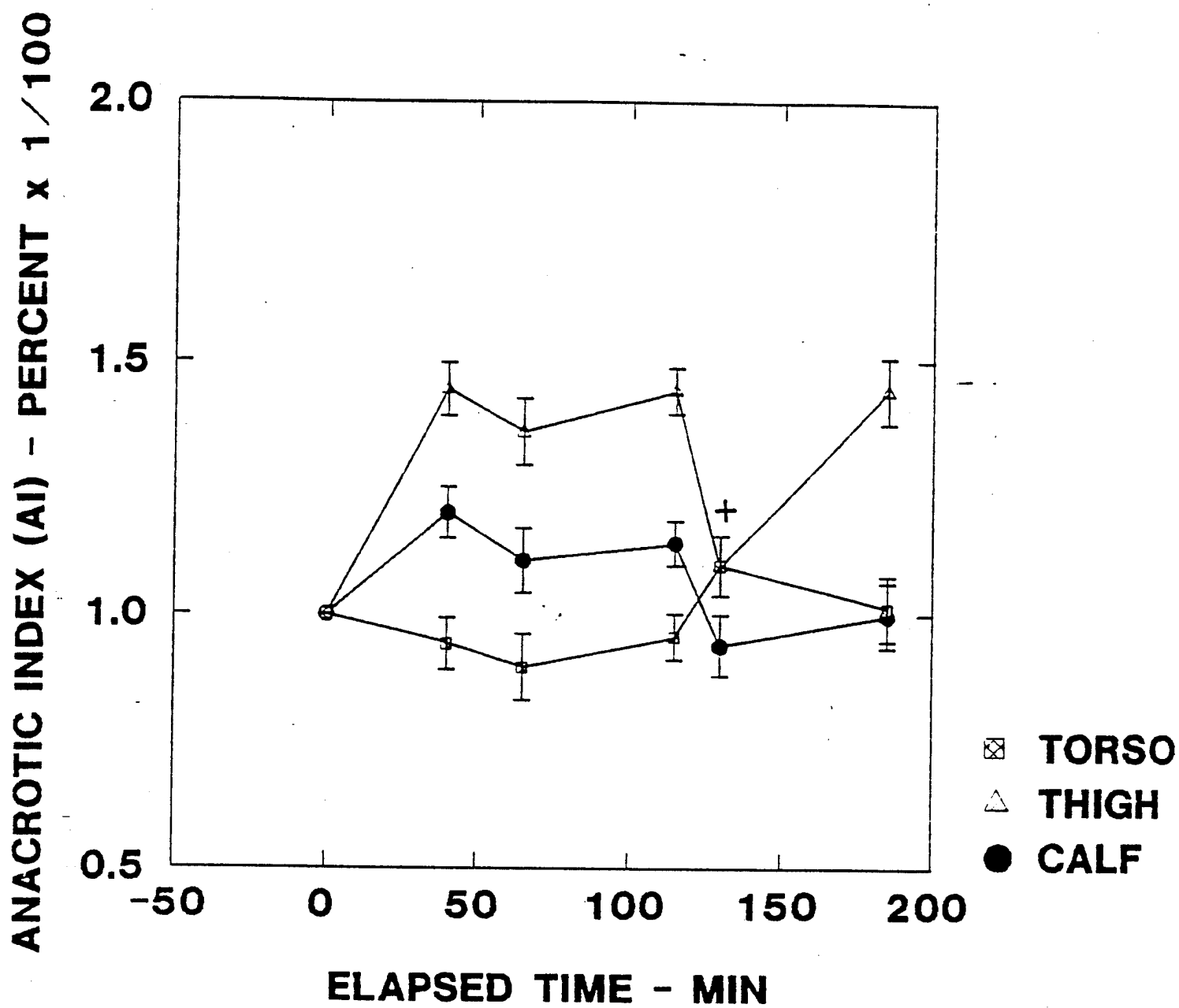


Figure 9.

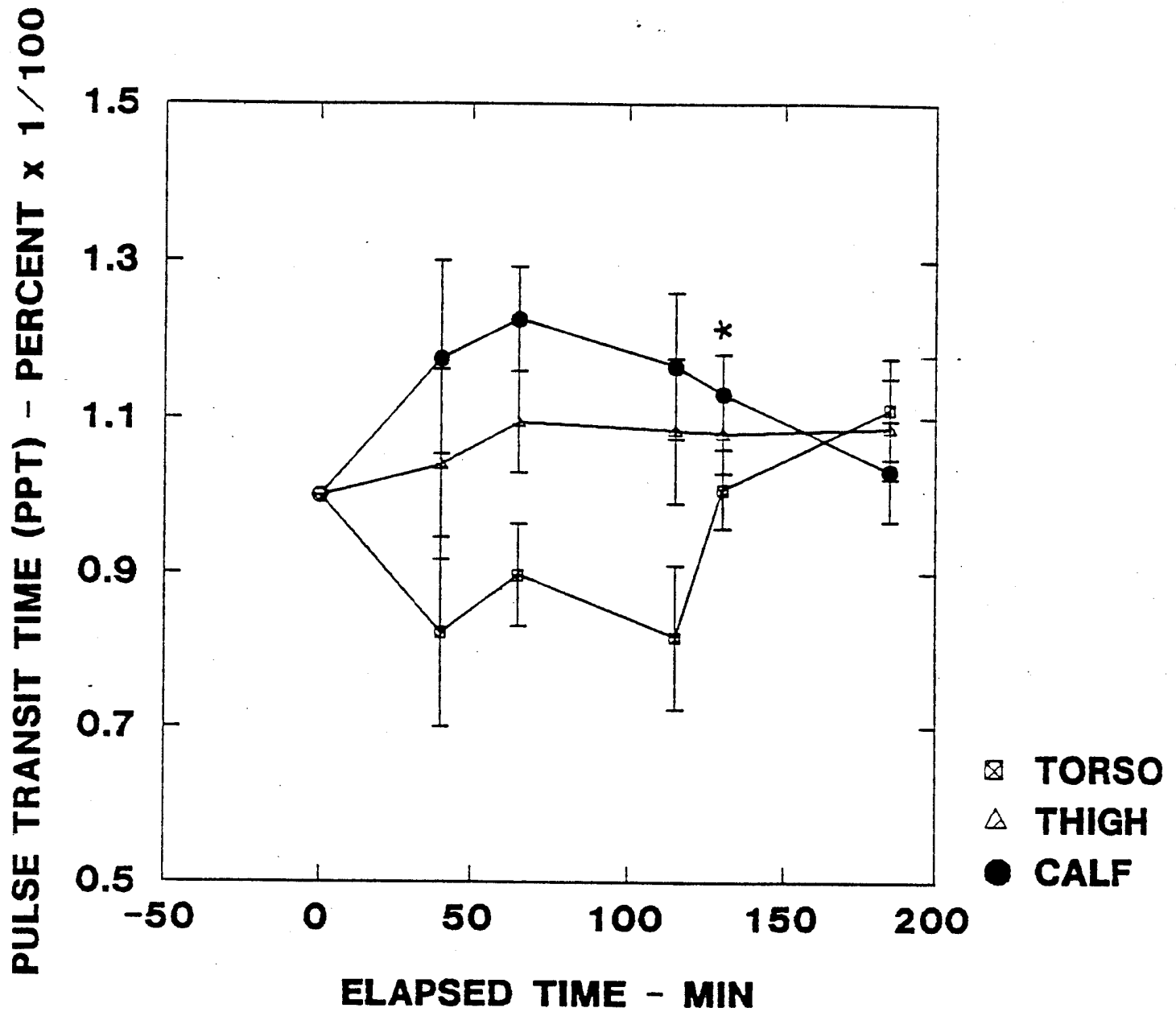


Figure 10.

## APPENDIX C.6

MONITORING OF SEGMENTAL  
INTRA- AND EXTRACELLULAR VOLUME CHANGES  
USING ELECTRICAL IMPEDANCE SPECTROSCOPY

David C. Sasser<sup>1</sup>, Wayne A. Gerth<sup>2,3,4</sup> and Yi-Chang Wu<sup>2,3</sup>

<sup>1</sup>Duke University School of Medicine,

<sup>2</sup>Department of Cell Biology, Division of Physiology,

<sup>3</sup>F.G. Hall Hypo-Hyperbaric Center, and

<sup>4</sup>Department of Anesthesiology

Duke University Medical Center  
Durham, North Carolina 27710

Running Title: Electrical Impedance Spectroscopy and Fluid Shifts

Correspondence and reprint requests to:

Wayne A. Gerth, Ph.D.  
Box 3823  
Duke University Medical Center  
Durham, NC 27710  
Ph. (919) 684-5902

ABSTRACT

Osmotically induced cellular volume changes in the perfused rat hindlimb were used to validate the use of Bioelectrical Impedance Spectroscopy (EIS) as a method for observing fluid shifts between the intracellular and extracellular spaces. Electrical impedance spectra were measured as cell volumes were manipulated by perfusion with Krebs-Henseleit solutions having different concentrations of NaCl. A simple equivalent circuit model of current conduction through the monitored tissue was fit to each measured spectrum to obtain segmental average values of the intracellular resistance ( $R_i$ ), membrane capacitance ( $C_m$ ) and extracellular resistance ( $R_e$ ). These parameters are governed in principle by variations in the average area and/or thickness of the cell membranes, and in the average cross-sectional areas and ionic concentrations of the intra- and extracellular fluid spaces. Accordingly, these parameters changed systematically and reversibly in conformance with both the magnitudes and directions of the perfusate concentration changes and the resultant cell volume changes. When cellular volume increases were induced by decreasing the perfusate concentrations,  $R_i$  decreased while  $C_m$  and  $R_e$  increased. Accompanying increases of the mean perfusion pressure due to constriction of the vascular space were observed in conformance with the cell volume increases indicated by the EIS results. When cellular volume decreases were induced by perfusion of more concentrated solutions,  $R_i$  increased whereas  $C_m$  and  $R_e$  decreased. Perfusion pressures that had previously been elevated by osmotic cellular swelling decreased during these periods due to cell shrinking and release of the vascular impingement. Results indicate that EIS, coupled with computer-aided equivalent circuit analysis, can be used to monitor segmental intercompartmental fluid shifts at minute resolution.

---

Key Words: Bio-Impedance, fluid redistribution, perfusate, osmolarity



## INTRODUCTION

Assessment of body fluid volumes and the distribution of these volumes between intracellular and extracellular compartments is a central and sometimes critical problem in the management of the severely ill patient. Such assessment presently depends upon subjective clinical impressions or results of indicator dilution measurements using multiple injectable tracers which distribute differentially between the body fluid compartments. The latter are not only invasive and time-consuming, but, depending upon the choice of tracers, occasionally provide inaccurate results due to imperfect equilibration of tracer substances throughout the desired compartments (3). Additionally, such measurements are not repeatable at frequencies sufficient to illuminate the time courses of changes in these volumes that are of greatest clinical and basic interest. Bioelectrical Impedance Spectroscopy (EIS), coupled with computer-aided equivalent circuit analysis, can monitor such changes at minute resolution.

Tissues are ionic conductors of electric current which, by virtue of their structural heterogeneity, exhibit dielectric relaxation phenomena that give rise to frequency dependent variations of the impedance to such conduction. In the 3.5 - 250 kHz range, the resultant dielectric dispersions arise principally from the capacitive reactances of cell membranes. At low frequencies in this range, high cell membrane reactances prohibit current flux through cells, so that tissue impedance is governed by properties of the extracellular fluid. At high frequencies, membrane reactance is negligible, allowing current to pass through both the extra- and intracellular spaces (see Figure 1). Tissue impedance is then governed by the combined properties of the two compartments. Time series of tissue impedances measured as a function of frequency consequently embody tissue structural information that can illuminate changes in the relative distributions of fluid between the intra- and extracellular compartments.

In the present study, electrical impedance spectra of intact perfused tissue preparations were measured as the cell volumes in the tissue were experimentally manipulated by changing the osmolarity of the perfusate. Measured spectra were found to be accurately correlated by a simple equivalent circuit model which idealized the monitored tissue as an isotropic bidomain conductor. Parameters of the model varied in a fashion that systematically reflected the known cell volume changes.

## MATERIALS AND METHODS

EIS system. The EIS system consisted of a Solartron 1260 Impedance/Gain-Phase Analyzer (Schlumberger Technologies, Ltd., Farnborough, England) controlled via an IEEE-488 interface by a Digital Equipment Corporation VAXstation 3200 computer. All aspects of system operation, including Analyzer setup, data acquisition, data processing and data display, occurred under control of system software written for this work.

Each impedance spectrum was obtained by measuring the voltage developed across the monitored tissue in response to sinusoidal electric current excitation at each of a series of 25 discrete frequencies from 3.5 to 250 kHz. A signal generator and current amplifier in the 1260 provided the excitation signal (0.5 mA max) which was passed through the tissue and

terminated at a current input channel on the 1260, where the amplitude and phase of the transmitted current was measured. Electric response of the tissue in the excitation current path was measured across one of two independent voltage input channels. Tetrapolar electrode configurations were used to minimize electrode impedance effects on measured voltages. The analyzer was operated in differential mode with the shields for all output and input leads grounded to the analyzer chassis. Shields of all leads were also brought to equal potential at a single point near the electrode ends of the leads. Measurement results were passed in binary form from the analyzer to the computer for immediate processing and storage on disk or magnetic tape.

Perfusates. The perfusates were modified Krebs-Henseleit (KH) solutions made from reagent grade chemicals and altered to have ideal osmolarities from 150 to 600 idmosm by varying the NaCl concentration as shown in Table I. Because each solution tended to be alkalotic on intitial formulation, the pH was adjusted to 7.40  $\pm$  0.05 by HCl titration. In some experiments bovine serum B-albumin was omitted. In all experiments, the solutions were at room temperature and air-saturated when perfused.

Subjects and surgical preparation. Experiments were performed on 6 healthy, male, Sprague-Dawley rats (Charles River Labs) weighing from 300-450 grams. After being anesthetized with sodium pentobarbital (50 mg/kg IP), each rat was placed supine with its head in a small head tent ventilated with 100% oxygen. A mid-line incision of the abdomen was made and the aorta and inferior vena cava were identified and dissected out from the retroperitoneum. The aorta was then ligated using 3-0 silk distal to the renal arteries and proximal to the iliolumbar arteries. A PE-50 polyethylene catheter (0.58mm i.d.) was inserted through a small incision made distal to the ligature, pushed to within approximately 0.5 to 1.0 cm of the common iliac bifurcation and secured in place with another 3-0 silk tie. At this time 1000 units of heparin were infused via the catheter followed by 2cc of standard Krebs-Henseleit solution. The vena cava was then ligated at the level of the aortic ligature with 3-0 silk and an incision made distally to allow free drainage of the venous outflow from the rat's hindquarters. A vacuum suction tube was placed intra-abdominally for constant removal of the venous outflow and prevention of fluid accumulation. Another 10cc of Krebs-Henseleit was perfused slowly over the ensuing 5-10 minutes while the EIS electrodes were placed.

EIS electrode placement. Stainless steel hypodermic needles (25 gauge) were used for both the drive and pick-up electrodes, positioned on the left leg as shown in Figure 2. The output drive electrode was inserted into the foot between the 2nd and 3rd metatarsals and the input drive electrode was placed in the muscular layer of the lower left abdomen. The pick-up electrodes were placed to span the bulk of the leg musculature; one inserted percutaneously into the distal gastrocnemius/soleus muscle, and the other inserted percutaneously into the proximal hamstring musculature.

Experimental procedure. Following surgical preparation and electrode placement, the aortic catheter was connected to a variable-speed peristaltic perfusion pump (Harvard Apparatus Co.). A blood pressure monitor (Winston Electronics Co., Model VT-1) was connected in parallel with the catheter for monitoring mean perfusion pressure. Perfusion with standard Krebs-Henseleit solution was then begun at a fixed rate of 2.5cc/min ( $\pm$  0.05), with

adequacy of the perfusion confirmed by blanching of the subject's hindlimbs and tail. The EIS system was then engaged. Spectra were taken every two minutes and perfusion pressures were measured every 3-5 min throughout the remainder of each run.

Within 5 min of beginning data acquisition, the anesthetized rat was euthanized by changing the breathing gas from 100% oxygen to 100% nitrogen. Apnea occurred within 30 s and asystole within 3-4 min. After establishing baseline behavior during the ensuing 10-15 min, the perfusate was changed with minimal interruption of flow by switching a stopcock to cause the pump to draw from another source beaker. Care was taken not to effect this change during an EIS data acquisition period. The perfusate volume in the tubing between the source and catheter ranged from 8-9cc depending on the source beaker. Dead volume clearance at a perfusion rate of 2.5cc/min occurred in approximately 3-4 min. The first perfusate was then followed by others of different composition, in sequences and for durations which varied from run to run. The perfused hindlimbs were dissected after several runs to observe gross anatomical appearance.

Data Analysis. Each impedance spectrum consisted of a series of discrete complex impedances ( $Z^*$ ) that were computed from the measured complex voltage ( $V^*$ ) and complex current ( $I^*$ ) at each of the separate frequencies in the sweep according to the relation:

$$Z^* = V^*/I^* = R + Xj ; \quad (1)$$

where  $j = \sqrt{-1}$ ,  $R$  is the equivalent series resistance and  $X$  is the equivalent series reactance.

A simple lumped-parameter equivalent circuit model representing idealized conductance paths through the monitored body segment was fitted to each measured spectrum using a nonlinear least squares routine based on Marquardt's algorithm [6]. The circuit, schematized in Figure 3, models the segment as a uniform isotropic bidomain conductor [ ] with an extracellular compartment having average resistance,  $R_e$ , and an intracellular compartment having average resistance,  $R_i$ , and average capacitance,  $C_m$ . The value of  $R_i$  is governed by both membrane and cytoplasmic properties, while  $C_m$  is governed principally by membrane properties. The complex admittance  $Y^*$  of the circuit is given by

$$Y^* = \frac{1}{Z^*} = \frac{1}{R_e} + \frac{1}{R_i} - \frac{1/R_i}{1 + j\omega\tau^\circ(1-\alpha)} , \quad 0 < \alpha < 1 ; \quad (2)$$

where  $\omega$  is the angular frequency given by  $2\pi f$ ,  $\tau^\circ$  is the time constant given by the product  $R_i \cdot C_m$ , and the quantity  $\alpha\pi/2$  is the angle between the real axis and a radius of the admittance locus passing through either of its two real axis intercepts. The  $(1-\alpha)$  exponent in Eq. (2) is included to account for the typical failure of tissular impedance loci to be centered on the real axis. This behavior is consistent with the presence in tissue of a practical infinitude of parallel R-C elements each with different time constants with values distributed about a mean at  $\tau^\circ$  [ ]. By definition,  $\alpha=0$  when the center of the locus lies on the real axis. Increasing values of  $\alpha$  from 0 towards unity indicate a widening of the distribution of time constants, with

increasing standard deviation of the distribution about  $\tau^\circ$ .

Marquardt's algorithm was implemented using the norm of each observed impedance,  $|Z^*|$ , and that of the corresponding fitted impedance,  $|Z^*|$ . The algorithm adjusted the model parameters to minimize the sum of squares, SS,

$$SS = \sum_{i=1}^n (|Z^*| - |\hat{Z}^*|)^2, \quad (3)$$

for the impedances at the  $n$  different frequencies in each spectrum. The analytic components of the software were bundled to process run-time data passed from the impedance spectrum acquisition routine, or to read and process data files from earlier experiments, providing identical output in either case. In the former mode, the analyses were automatically performed immediately after acquisition of each spectrum. Graphic displays of the results afforded a means to track changes in measured and computed dielectric properties of the monitored tissue throughout the course of each run.

EIS system performance was validated by fitting Eq. (2) to measured impedance spectra from electric circuits hardwired with components of known resistances and capacitances as in Figure 3. The spectra were measured using the same cabling as in the experimental applications. All circuit components were resolved from the measured spectra to within 0.1% of their known values, well within the  $\pm 10\%$  ratings of the individual circuit components. Results showed that the influence of stray capacitance was minimal over the experimental frequency range. Drive electrode impedance, modeled by inserting R-C circuits in series with the circuit under test, was shown not to affect parameters calculated from measured spectra.

## RESULTS

An impedance spectrum can be visualized as a locus of points in the complex plane by plotting the complex vs the real part of each impedance in the spectrum. Tissue impedance loci from a typical run are shown in Figure 4. Locus A is an impedance spectrum obtained during a period of hypertonic perfusion. Locus B was obtained during subsequent hypotonic perfusion. The locus is right-shifted toward higher resistances, with widening of the span between low and high frequency real axis intercepts and lowering of the minimum reactance. Locus C, measured after the perfusate had been changed back to the hypertonic solution, illustrates the return of spectral properties to initial values with restoration of the initial perfusate composition.

The spectral changes evident in the graphic renditions are more quantitatively summarized by the changes in the corresponding fitted equivalent circuit parameters. As illustrated in Figure 5, residuals of the model fits to different loci showed patterns that remained within  $\pm 0.2\%$  of each other for all spectra measured in any given run. Changes in the spectra throughout the runs were consequently fully "captured" by changes in the equivalent circuit parameters.

All parameters remained relatively stable during the initial periods of isotonic KH perfusion and varied systematically and reversibly in response to

subsequent changes in perfusate osmolarity. From run to run these variations generally exhibited kinetics typical of perfusion-limited washin and washout with an initial phase of rapid change followed by an asymptotic approach to steady state.

Equivalent circuit parameters and mean perfusion pressures from a typical experiment in which the perfusates contained albumin are shown plotted vs elapsed time in Figure 6. With change of the perfusate to a hypertonic KH solution (600 idmosm) at 11 min, the segmental average membrane capacitance ( $C_m$ ) and the extracellular resistance ( $R_e$ ) decreased while the intracellular resistance ( $R_i$ ) increased. This pattern was typical of periods following increases of the perfusate NaCl concentration and was typically reversed after the perfusate was changed to a less concentrated solution. This reversal is evident in the run shown after perfusion of hypotonic KH (150 idmosm) was commenced at 17 min. Although the mean perfusion pressure had remained essentially unchanged prior to this perfusion, it increased 13% during the ensuing 13 min.

Parametric responses were graded according to the magnitudes of perfusate concentration changes. In the illustrated run, the perfusate osmotic concentration was increased to 318 idmosm at 30 min. During the ensuing 11 min,  $C_m$  and  $R_e$  decreased at an average rate of  $2.0\% \text{ min}^{-1}$  and  $1.1\% \text{ min}^{-1}$ , respectively, and  $R_i$  increased at  $0.6\% \text{ min}^{-1}$ . At 41 min elapsed time the perfusate concentration was increased further to 600 idmosm. The parameters continued changing in the same directions but at increased rates.  $C_m$  and  $R_e$  decreased at  $5.8\% \text{ min}^{-1}$  and  $4.3\% \text{ min}^{-1}$ , respectively, and  $R_i$  increased at  $3.5\% \text{ min}^{-1}$ . By the end of the latter perfusion the mean perfusion pressure had returned to the initial baseline level.

Similar gradations of response occurred with perfusate concentration decreases. At 47 min into the illustrated run, perfusion of a 318 idmosm KH solution was begun. During the following 10 min,  $C_m$  and  $R_e$  each increased at an average rate of about  $1.1\% \text{ min}^{-1}$ , while  $R_i$  decreased at about  $0.6\% \text{ min}^{-1}$ . With a further decrease of perfusate concentration to 150 idmosm at 57 min, the parameter changes accelerated and  $C_m$  and  $R_e$  then increased at rates of  $7.75\% \text{ min}^{-1}$  and  $5.25\% \text{ min}^{-1}$ , respectively, and  $R_i$  decreased at  $3.75\% \text{ min}^{-1}$ . The mean perfusion pressure increased to approximately 6% above baseline during this latter perfusion.

As the illustrated results show, decreases in  $R_e$  during hypertonic perfusions were readily and completely reversed by hypotonic perfusions when the perfusates contained albumin. However, in other runs in which the perfusates lacked albumin,  $R_e$  tended to decrease gradually throughout the runs with attenuated increases during hypotonic challenges that failed to completely reverse the effects of preceding hypertonic perfusions. Post-run dissections of the perfused hindlimbs in the latter experiments revealed large amounts of subcutaneous and interstitial edema with marked weeping of clear fluid from cut surfaces. In contrast, dissections following experiments in which the perfusates contained albumin showed normally appearing, dry anatomy without evidence of significant edema.

## DISCUSSION

Cells behaving as perfect osmometers change volume in response to

changes in the osmolarity of their bathing fluid. The present work exploited this principle to test the correspondence between changes in measured dielectric properties of an intact tissue and experimentally induced changes in cell volume. Interstitial osmotic pressures were manipulated to effect cell volume changes by varying the concentration of NaCl in the perfusates. This solute has a high capillary permeability (7) and rapidly equilibrates between the intravascular and interstitial spaces. The observed perfusion pressure variations that accompanied perfusate changes confirmed that each perfusate caused its intended change in cell volume. Pressure increases during hypotonic perfusion indicated increased vascular resistance from cell swelling and attendant constriction of the vascular space. Similarly, pressure decreases during subsequent hypertonic perfusions indicated reversal of this trend with decreased vascular resistance. However, perfusion pressures during hypertonic perfusions never decreased below the steady-state levels observed during the initial isotonic perfusion, indicating that the vasculature was maximally dilated at the onset of the experiments.

The isotropic bidomain model fitted to measured impedance spectra approximates the extracellular and intracellular spaces of the monitored tissue as separate, continuous and uniform volumes separated by a capacitance. All transmitted currents and potentials are consequently averaged over a region of many cells in extent. The extracellular and intracellular spaces are assumed to be wholly resistive, while the electrical resistance of the membranes is assumed to be wholly reactive; i.e., due only to their capacitance. Plonsey and Barr (8) showed that if the spacing between pickup electrodes is sufficiently large, the total tissue resistance is given by that of the extracellular and intracellular compartments in parallel as modeled here. However, the convenience of defining these two compartments as lying in the same region; namely, that occupied by the entire tissue; is not adopted here. Rather, the extracellular, intracellular and membrane regions are considered to have conductive properties related to average but separate geometric and concentrative properties of the respective regions through the following relations:

$$R = \rho L/A \quad (4)$$

$$C = \epsilon \epsilon^0 A/T. \quad (5)$$

where subscripts indicating the compartment; intracellular, extracellular or membrane; are omitted. Each resistance ( $R$  in  $\Omega$ ) is governed by the specific resistivity of the compartmental contents ( $\rho$  in  $\Omega \cdot \text{cm}$ ), the length of the compartment ( $L$  in cm) and its cross-sectional area ( $A$  in  $\text{cm}^2$ ). The capacitance ( $C$  in  $\mu\text{Farads}$ ), assumed embodied wholly in membranes, is governed by the dielectric constant ( $\epsilon$ ), area ( $A$ ), and thickness ( $T$ ) of the membranes. The validity of this model is confirmed by the variance of its parameters in conformance with known cellular volume changes.

The segmental average intracellular resistance  $R_i$  provides information about the volume and ionic concentration of intracellular fluid. Assuming that the length of the monitored segment remains unchanged, the cross sectional area of this compartment must increase with its volume and thereby cause  $R_i$  to decrease. Accordingly, this parameter was always observed to decrease during hypotonic perfusions when cell volumes were increasing. Significantly, increases in cytoplasmic ion concentrations that can generally also account for decreased  $R_i$  could not have occurred in the present

experimental context. The osmotic influxes of water underlying the present cell volume increases must have instead caused the intracellular ion concentrations to decrease and the corresponding intracellular specific resistivities to increase. While the observed  $R_i$  decreases must consequently have been attenuated by the influence of the latter, the evidence is clear that geometric effects of cell swelling predominated. Ambiguity over the relative importance of these two factors in other contexts potentially may be resolved by the accompanying changes in the average cell membrane capacitance.

Cell volume increases must increase the segmental average cell membrane area and/or decrease the segmental average cell membrane thickness. Provided that other membrane properties governing membrane dielectric constant remain unchanged, the segmental average membrane capacitance  $C_m$  must consequently increase. Observed changes in  $C_m$  were in accord with this expectation. This parameter increased under conditions known to cause cell swelling and decreased under conditions known to cause cell volume decreases. Thus, in the present experiments, enlargement of the intracellular compartment was unequivocally indicated by the concurrence of increases in membrane capacitance and decreases in intracellular resistance.

The segmental average extracellular resistance is governed by volumetric and concentration factors analogous to those governing the intracellular resistance. The extracellular resistance must consequently increase with decreasing extracellular (intravascular and interstitial) ionic concentration and/or volume. The observed  $R_e$  increases during hypotonic perfusion were consistent with both the decreased electrolyte concentration in the perfusate and the possible depletion of interstitial fluid volume from water flux into the cells.

The graded response of the equivalent circuit parameters to perfusates of varying degrees of hypo- or hypertonicity is a manifestation of basic osmotic principles. Larger and more rapid volume changes occur as the differences between intracellular and extracellular salt concentrations increase and produce greater changes in osmotic pressures (4).

The reversibility of the  $R_i$  and  $C_m$  parameters with reversal of perfusate concentration changes further supports model validity. However, the persistent decreases of  $R_e$  that occurred when the perfusates lacked albumin strongly indicated the development of marked extracellular edema. Post-run dissections supported this indication by revealing the expected edematous changes. When albumin was incorporated and  $R_e$  was more readily controlled, dissections showed normal dry anatomy without signs of edema. An intravascular oncotic agent is evidently required to prevent transudation and accumulation of perfusates in the interstitial and subcutaneous spaces, particularly in preparations such as the present where lymphatic drainage was probably negligible.

In summary, EIS has been shown to be a convenient, high-resolution method of monitoring segmental fluid shifts between the intracellular and extracellular fluid compartments, and can be readily employed noninvasively with use of adhesive skin electrodes. Osmotically induced changes in segmental intracellular volumes result in systematic changes in the parameters of a simple equivalent circuit model that conform with the theoretical dependence of these parameters on the average area and/or

thickness of the cell membranes, and the average cross-sectional areas and ionic concentrations of the intra- and extracellular fluid spaces in the monitored tissue. In addition, it was recognized that alteration of both the volume and ionic concentration of the extracellular/interstitial fluid resulted in similarly consistent and predictable changes. Quantification of the response of these parameters to osmotic challenges is still required, but this system already promises to be helpful in the characterization of fluid shifts in response to such clinical conditions as acute intravenous fluid therapy, diuretic treatment, edema formation, hemodialysis, hypoxia and shock.

#### ACKNOWLEDGEMENTS

The development of the Electrical Impedance Spectroscopic System used in this work was supported by USN contract N00014-87-C-0166. The authors are grateful to Dr. Claude Piantadosi and Mr. Craig Marshall for technical advice and support.



REFERENCES

1. Cole, K. S., and R. H. Cole. Dispersion and absorption in dielectrics. *J. Chem. Phys.* 9: 341-352, 1941.
2. Gerth, W. A., L. D. Montgomery, and Y. C. Wu. A computer-based bioelectrical impedance spectroscopic system for noninvasive assessment of compartmental fluid redistribution. In: *Proceedings Third Annual IEEE Symposium on Computer-Based Medical Systems*. Los Alamitos, CA, IEEE Computer Society Press, 1990, pp. 446-453.
3. Guyton, A. C. *Textbook of Medical Physiology*. Philadelphia, W. B. Saunders Company, 1986, pp.382-392.
4. Gilles, R. Mechanisms of osmoregulation: Maintenance of cell volume. New York, John Wiley and Sons, Ltd., 1979, pp. 3-45.
5. Kanai, H., S. Katsuyuki, and M. Haeno. Electrical measurement of fluid distribution in human legs: Estimation of extra- and intracellular fluid volume. *J. Microwave Power.* 18: 233-243, 1983.
6. Marquardt, D. W. An algorithm for least-squares estimation of nonlinear parameters. *J. Soc. Indust. Appl. Math.* 11: 431-441, 1963.
7. Pappenheimer, J. R. Passage of molecules through capillary walls. *Physiol. Rev.*, 33: 387-423, 1953.
8. Plonsey, R., and R. C. Barr. A critique of impedance measurements in cardiac tissue. *Ann. of Biomed. Engng.* 14: 307-322, 1986.

Table I. Modified Krebs-Henseleit Solutions

Solute	Concentration (gm/L)		
	1	2	3
NaCl	7.95	16.18	3.03
KCl	0.20 →		
CaCl <sub>2</sub>	0.26 →		
MgCl <sub>2</sub>	0.10 →		
NaHCO <sub>3</sub>	1.00 →		
NaH <sub>2</sub> PO <sub>4</sub>	0.09 →		
Dextrose	0.98 →		
β-albumin	60.00 →		
Ideal Osmolarity (X 10 <sup>-3</sup> )	318.4	600.0	150.0

FIGURE LEGENDS

1. Schematic representation of high vs. low frequency current paths through tissue (from Ref. 5).
2. Electrode placement on the rat left hind limb for Electrical Impedance Spectroscopic measurements:  $I_1$ : current output electrode;  $I_2$ : current input electrode;  $V_1$  and  $V_2$ : pickup electrodes.
3. Equivalent circuit model of current conduction through tissue. The tissue is modeled as two parallel conductance paths; one through an extracellular compartment having average resistance  $R_e$ , and the other through an intracellular compartment having average resistance  $R_i$  and capacitance  $C_m$ .
4. Complex impedance loci of the rat hindlimb: (A) during a period of hypertonic perfusion; (B) during an ensuing hypotonic perfusion; and; (C) after restoration of the initial hypertonic perfusion. Each locus consists of points from measurements at 50 discrete frequencies distributed logarithmically from 3.5 to 250 kHz. Individual points are obscured by connecting straight lines. The lowest frequency impedance is at the right-most or highest resistance end of each locus.
5. Residuals vs frequency of the equivalent circuit model fits to the impedance loci shown in Figure 4.
6. Fitted equivalent circuit parameters vs run elapsed time for a typical serial perfusion experiment. Parameter values are shown in "strip chart" format, with the ordinate scaled such that the major ticks above and below the first value shown at  $t=0$  represent + and - 20% deviation, respectively, from that value.  $R_e$  and  $R_i$  are in Ohms,  $C_m$  is in  $\mu$ Farads and  $\alpha$  is dimensionless. Perfusate changes are marked by vertical lines and labelled with a 1 for 318.4 idmosm isotonic KH, 2 for 600 idmosm hypertonic KH, and 3 for 150 idmosm hypotonic KH. Corresponding mean perfusion pressures in mm-Hg are plotted in the lower panel.

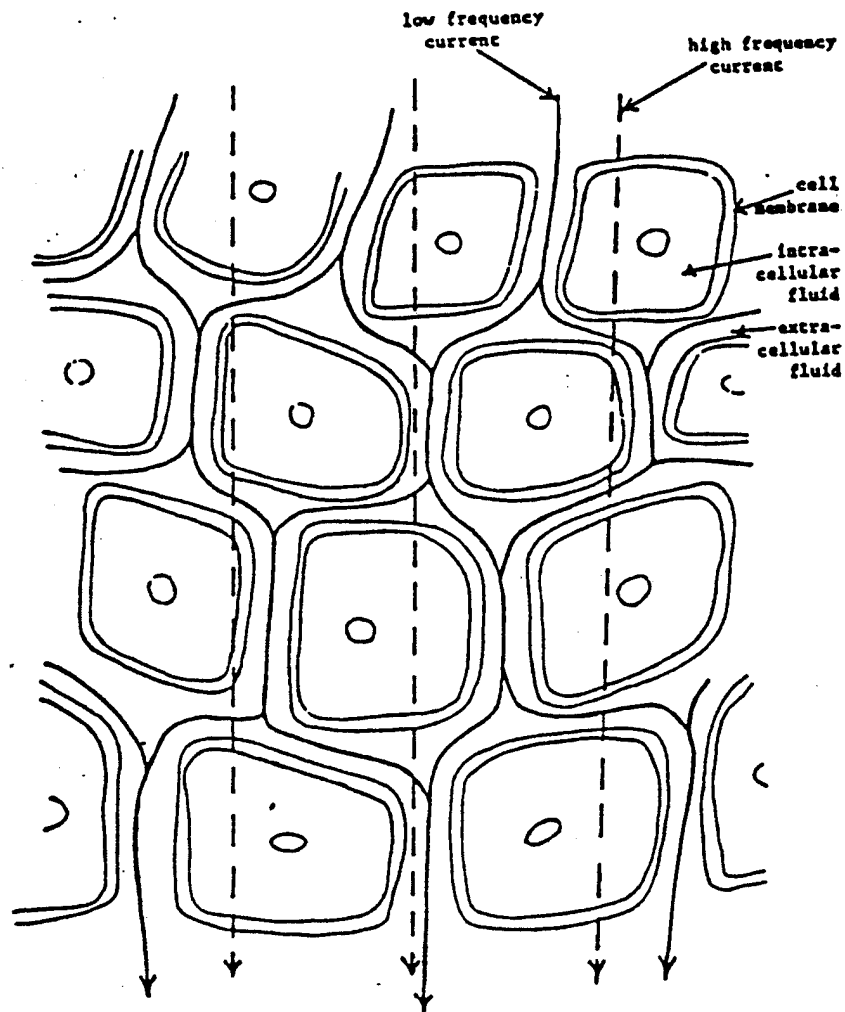


Figure 1.

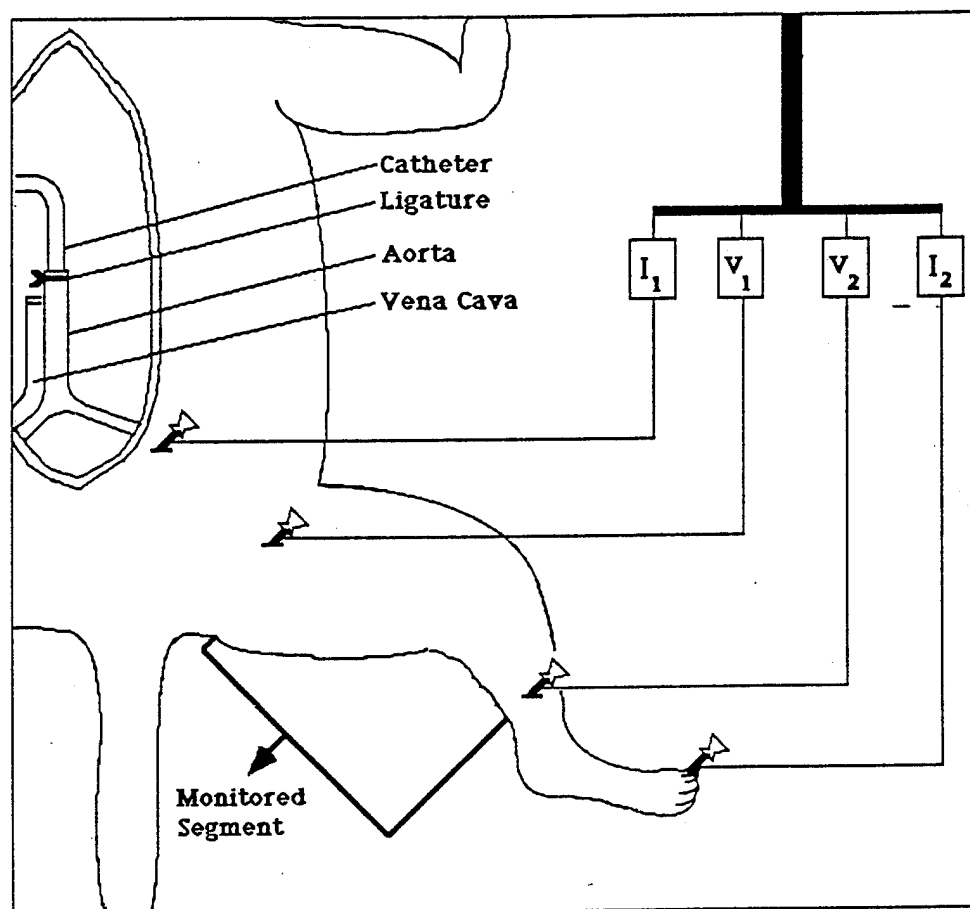


Figure 2.

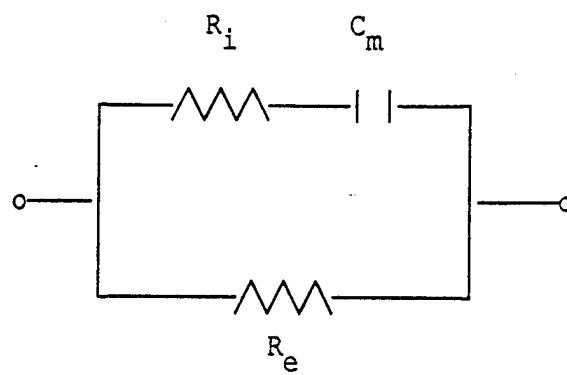


Figure 3.

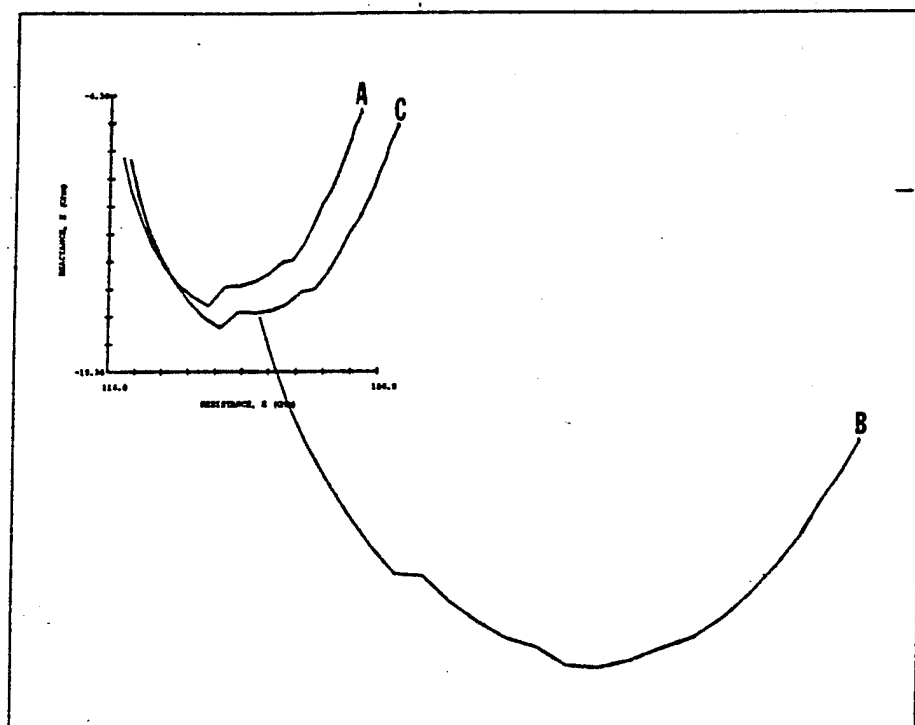


Figure 4.

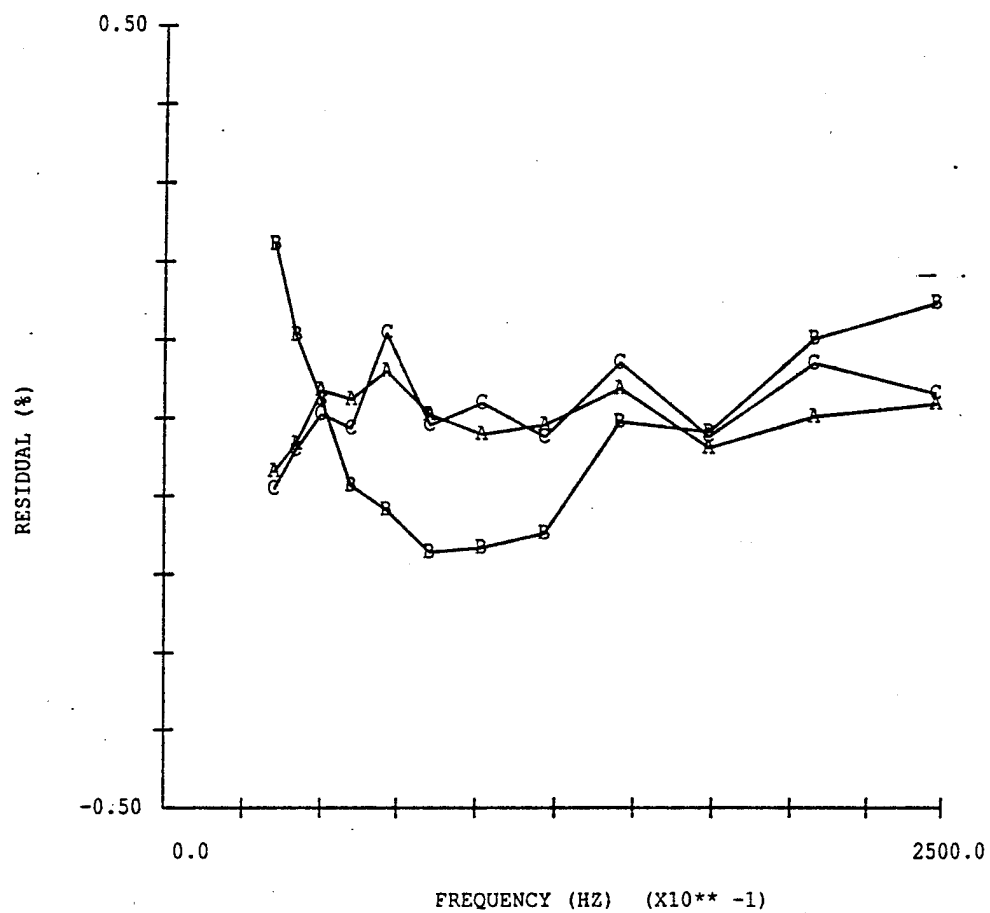


Figure 5.



Figure 6.

